



**FRICITION AND HEAT GENERATION IN
ROLLING/SLIDING CONTACTS IN THE
ELASTOHYDRODYNAMIC LUBRICATION REGIME**

By

Salem Almail

Thesis submitted in candidature
of the degree of Doctor of Philosophy
at Cardiff University

Institute of Mechanics and Advance Material
Cardiff School of Engineering
Cardiff University

June 2020

Summary

This thesis presents both experimental and theoretical investigations to study the friction and heat generation in the rolling/sliding contacts in the elastohydrodynamic lubrication (EHL) regime, using a twin-disc test rig that was previously built and used for this purpose.

An experiment was carried out, where the data recorded were analysed using a numerical model that was developed during this work to find the heat transfer coefficient h and the heat partition β , and to compare the results of this numerical model with those measured during the EHL experiment. The downhill simplex method for error minimisation was used in this work, which was able to calculate the minimum total error between measurement and model temperatures of both discs for the same given (β, h_s) combination, rather than for each disc individually.

Some uncertainties showed up during these analyses, which led to extensive investigations made by modifying the numerical model and re-designing some test rig hardware (shafts and thermocouple amplifiers). The differences between model and measured temperatures were analysed to identify whether or not the individual thermocouple measurements were consistent with each other and the fundamental conduction equation. This showed that at least two measurements were unreliable on each disc. Synthesised experiments were then constructed using the model and measured lower boundary temperatures from the EHL experiments. These were used to assess the influence of noise in the data on the results, to find the optimum position of thermocouples, and to investigate the resolution of the thermocouples and logging recorders.

The test rig was also subjected to further developments. Firstly, new integral shafts and test discs were designed in order to replace the existing components in order to eliminate the uncertainty of thermal asymmetry in the shaft and disc configurations. Secondly, new on-shaft thermocouple amplifiers were commissioned to adapt the test rig so as to overcome the uncertainties revealed in the previous investigations.

Acknowledgements

Primarily, all praise and thanks to God for everything, and for the wisdom he bestowed upon me, the strength, peace of my mind and good health in order to complete this thesis.

I would like to express my great appreciation to my three supervisors, Professor Pwt Evans and Dr Alastair Clarke for their continuous supervision, advice, support, and useful suggestions during my study at Cardiff University, and Dr Khayri Sharif for his help and giving me the opportunity to study at Cardiff University. I could not have imagined having better supervisors for my PhD studies.

I would like to especially thank Professor Pwt Evans, for his willingness to spare me his time and guide me to complete this thesis. I have learned a lot from him. He was the backbone of this thesis by providing wise advice and valuable instructions.

This PhD would not have been possible without the support of the Kuwaiti Ministry of Defence, thank you for the sponsorship and funding me to complete my studies.

I must also thank the technical staff of the School of Engineering for their support and help, especially Mr Denley Slade for his help in the electronic work. I am also highly indebted to my colleagues in the Tribology group, Othman Alshatti, Dr Simon Hutt, Dr Dewi Griffiths, Dr Ben Cahill, Paul Revill and William Britton for their help and support.

I must not forget to thank my cousin Mr Abdullah Al-qallaf who encouraged me and convinced me that I should pursue my Master and Doctoral degrees. I am also very grateful to Eng Adel Al-jarallah Al-kharafi for his help to make it possible.

My parents, I wish there was some way of showing my deep gratitude for all you have done for me throughout my studies and my life, thank you for your endless support and continuous encouragement. My deepest gratitude goes to my beloved and supportive wife, I cannot find words to express my feeling and gratitude for supporting me emotionally and mentally during my studies.

Finally, I want to thank everyone who has been involved directly or indirectly throughout this work supported and prayed for me.

Contents

Summary	ii
Acknowledgements	iii
Nomenclature	ix
Chapter 1 Introduction and literature review	1
1.1 Introduction	1
1.2 Introduction to Tribology	1
1.3 Introduction to lubrication	4
1.4 Introduction to elastohydrodynamic lubrication (EHL)	5
1.5 Thermal analysis of EHL	7
1.5.1 Experimental scuffing tests using a twin disc machine	11
1.5.2 Use of scuffing test results to investigate heat partition at the contact	15
1.6 Insights on temperature measurements in EHL contacts	17
1.6.1 Temperature measurement by thermocouples	18
1.6.2 Radiation detection techniques	23
1.7 Infrared measurements of EHL lubricant films.	28
1.8 Disc testing	35
1.8.1 LaMCoS twin disc machine	36
1.8.2 FZG disc testing	42

1.9	Development of Patching test rig to measure the heat partition	46
1.10	Aims and objectives	51
Chapter 2	A twin-disc test rig for investigating the friction and heat generation in the EHL regime	54
2.1	Introduction	54
2.2	Description of the twin-disc test rig	54
2.3	Test discs	60
2.4	History of the test rig	62
2.4.1	Experimental procedure	62
2.4.2	Modifications for heat partition measurement	64
2.4.3	Further modifications	69
Chapter 3	Theory and development of numerical model for the thermal behaviour of the test discs	72
3.1	Introduction	72
3.2	The governing partial differential equation	72
3.2.1	The amount of heat conducted into the element	75
3.2.1.1	Heat flow in the radial direction	75
3.2.1.2	Heat flow in the axial direction	76
3.2.1.3	Heat flow in the circumferential direction	78
3.2.1.4	Net heat conducted into the element	79
3.2.2	The amount of heat generated inside the element	79

3.2.3	The amount of heat stored in the element due to the rise of temperature	79
3.2.4	The amount of heat change due to disc rotation	80
3.2.5	Conduction partial differential equation	81
3.3	Finite difference numerical method	81
3.3.1	Introduction to the method	81
3.3.2	Derivation of finite difference approximations using Taylor's theorem	82
3.4	Two-dimensional transient model of bulk temperature	84
3.4.1	Simplification of the conduction partial differential equation	84
3.4.2	The explicit method	85
3.4.3	The implicit method	87
3.4.4	The implicit method by Crank-Nicolson	88
3.4.5	Finite difference approximations within the test disc	89
3.4.6	Boundary conditions	91
3.4.6.1	Boundary condition at the outer radius	92
3.4.6.2	Boundary condition at the Inner radius	94
3.4.6.3	Boundary condition at the insulated disc faces	95
Chapter 4	Numerical modelling of the EHL heat partition test	97
4.1	Introduction	97
4.2	Data filtering	97
4.2.1	Disc temperature filtering process	99

4.2.2	Friction force filtering process	105
4.2.3	Oil/surrounding temperature filtering process	109
4.3	Mesh sensitivity test	111
4.4	Analysing an experiment	123
4.4.1	Analysis method	123
4.4.2	Relationship between h_s and h_f	126
Chapter 5	Development of the test modelling approach	138
5.1	Introduction	138
5.2	Total error variation (with β and h)	138
5.3	Downhill simplex method for non-linear minimisation	144
5.3.1	Basics of the Downhill Simplex method	144
5.4	Determining n using Simplex method values for error	155
5.5	Inconsistencies in temperature measurements	160
5.6	Optimum positioning and required accuracy of thermocouples	169
5.6.1	Synthesised experimental data	169
5.6.2	Synthesised experiment	171
5.6.3	Thermocouple position investigation	178
5.6.4	Synthesised experiments based on Clarke data	183
5.6.5	Thermocouples accuracy investigation	186
5.7	Conclusion on requirements	190
Chapter 6	Test rig development design	191

6.1	Introduction	191
6.2	Integral shaft and disc	191
6.3	Developing on-shaft thermocouple amplifiers	198
6.4	Conclusion on requirements	210
Chapter 7	Conclusions and recommendations for future research	211
7.1	Summary of the work	211
7.2	Conclusions	212
7.3	Recommendations for future work	214
	References	216

Nomenclature

Symbol	Definition	Units
a	Minor axis of Hertzian contact	m
A	Area	m ²
b	Major axis of Hertzian contact	m
c_p	Specific heat capacity	Jkg ⁻¹ K ⁻¹
h	Heat transfer coefficient	Wm ⁻² K ⁻¹
h_f	Heat transfer coefficient of the fast disc	Wm ⁻² K ⁻¹
h_s	Heat transfer coefficient of the slow disc	Wm ⁻² K ⁻¹
K	Thermal conductivity of the test disc	Wm ⁻¹ K ⁻¹
K_c	Thermal conductivity of the ceramic washers	Wm ⁻¹ K ⁻¹
Nu	Nusselt number	---
p_0	Maximum Hertzian contact pressure	Nm ⁻²
q_{fr}	Frictional heat flux	Wm ⁻²
r	Radial co-ordinate in the thermal model	m
Re	Reynolds number	---
T	Temperature	°C
t	Time	s
T_{fl}	Fluid/surrounding temperature	°C
u_1	Speed of the fast surface	ms ⁻¹
u_2	Speed of the slow surface	ms ⁻¹
u_s	Sliding speed	ms ⁻¹
u_r	Mean entraining speed	ms ⁻¹
ν	Kinematic viscosity of fluid	m ² s ⁻¹
w	Width of the test disc	m
w_c	Width of the ceramic washers	m
z	Axial co-ordinate in the thermal model	m
α	thermal diffusivity	m ² s ⁻¹
β	Heath partition parameter	---
θ	Angular co-ordinate in the thermal model	rad
ρ	Density	kgm ⁻³
χ	Ratio of heat transfer coefficients	---
σ	Wavelength	---
ω	Angular velocity	s ⁻¹

Chapter 1 Introduction and literature review

1.1 Introduction

This chapter illustrates experimental as well as theoretical analysis of thermal behaviour of the elastohydrodynamic lubrication regime in rolling and sliding contacts. It starts with a brief overview of tribology, lubrication and elastohydrodynamic lubrication followed by a review of relevant literature along with the aims and objectives of the thesis.

1.2 Introduction to Tribology

According to a Department of Education and Science report in 1966 (The Jost Report), tribology is defined as, “The science and technology of interfacing surfaces in relative motion and practices related thereto”. The word ‘Tribology’ is originated from ‘Tribos’ a Greek word, which means rubbing (Bhushan, 2013). The literal translation of tribology could be the science of rubbing. In English, it is known as science of lubrication, friction, and wear. According to Bhushan (2013), tribology is the art of employing operational analysis to issues related to economic consequences, mainly wear of technical equipment, maintenance and reliability; the scope of tribology is extremely broad right from household equipment to spacecraft. To understand tribology and its highly complex surface interaction requires knowledge of different disciplines such as rheology, materials science, heat transfer, thermodynamics, fluid mechanics, solid mechanics, applied mathematics, chemistry, physics, machine design, lubrication, reliability and performance. According to Dowson (1998), the word tribology is relatively new but the operation or study of tribology is older than the records. During Palaeolithic period, drills made for drilling

holes were fixed with bearings, usually these bearings were made from either bones or antlers. Also stones for grinding cereals as well as potters' wheels must have had some sort of bearing arrangements (Davidson, 1957). Near Lake Nimi, Rome, a ball thrust bearing was found which dates from about AD 40. It is found that, our ancestors were using wheels since 3500 BC and they were concerned with reducing friction during translational motion.

Figure 1-1 shows a drawing of a harvest cart with studded wheels, circa AD (1338). Ancient knowledge of lubrication and frictional devices is demonstrated by devices such as water lubricated sleds used to transport large stone blocks for buildings as well as monuments.



Figure 1-1 Drawing of two wheeled harvest cart with studded wheel, folio-173v, circa 1338 AD (Bhushan, 2013)

Figure 1-2 shows the sledge is being used to transport a substantial statue by Egyptians, circa 1880 BC. It can be observed that in the image, 172 slaves are dragging a huge statue weighing approximately 600 kN on a wooden trail. A man standing in front of the sled is supporting the sculpture, maybe he was one of the

earliest lubrication technicians. According to Dowson (1998), 800 N was the pull exerted by each slave, accordingly the total effort equal to frictional force would be 800×172 N. Therefore, the estimated coefficient of friction would be 0.23. The evidence of use of lubrication and lubricants thousands of years ago was found in a tomb in Egypt. Animal fat lubricant was found in a chariot's wheel bearing in this tomb.

Tribological principles were used by military engineers to design war machinery as well as methods of reinforcements during and after Roman Empire. Artist and engineer Leonardo da Vinci (1452-1519) was first to propose a systematic approach towards friction. Leonardo da Vinci deduced the rules governing the motion of a rectangular block sliding over flat surface.

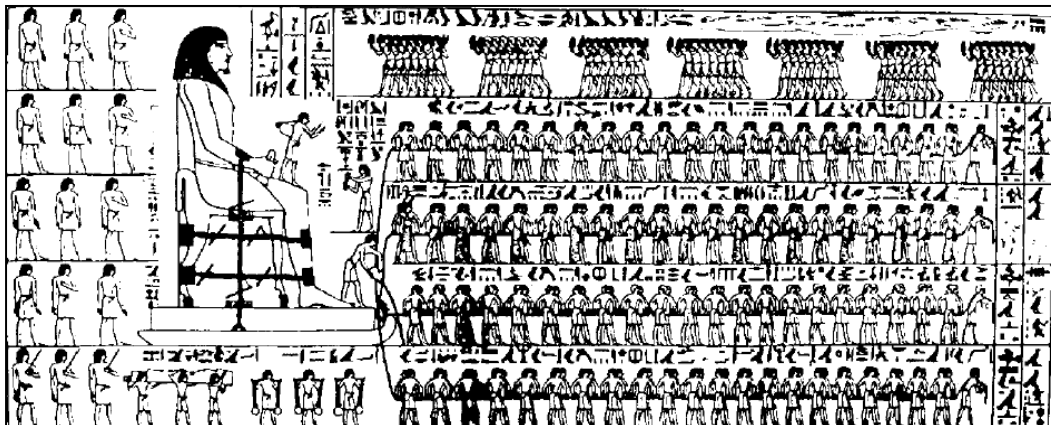


Figure 1-2 Egyptians moving colossus by using Lubrication, El- Bersheh, circa 1880 BC (Bhushan, 2013)

He introduced the ratio of friction force to normal load which was the main concept of friction coefficient. There is no historical evidence available of influence of his theory, this could be since the work of da Vinci was unpublished for many years. The French physicist Guillaume Amontons, rediscovered the laws of friction in 1699 through the analysis of dry sliding of two flat surfaces (Amontons, 1699). He deduced that frictional force is directly proportional to the normal load, and resists the sliding at an

interface. He also proposed that the sum of the friction force does not depend on the visible or apparent contact area. Another French Physicist, Charles Augustine Coulomb confirmed the observation noted by Guillaume Amontons. Coulomb contributed the third law of friction, which is that once motion starts then the force of friction is independent of velocity. Coulomb differentiated in this way between kinetic and static friction (Coulomb, 1785).

1.3 Introduction to lubrication

According to Maione and D'Elia (2005), wear as well as friction between two or more contact faces that are moving relative to each other can be reduced by means of applying lubricants with suitable properties. There is a difference between the terms friction and wear, friction corresponds to the force that opposes the motion that would be caused by the total force applied. The friction force corresponds to the force required to break the bond between surface micro-asperities and the deformation force necessary to make potential grooves when solid bodies move against each other. Frictional force is associated with energy consumption and heat production. On the other hand, wear is a process of the ongoing loss of surface material caused by motion of two surfaces. This may happen for various reasons, such as abrasion, tearing of asperities, adhesion, corrosion and fatigue etc. These factors may cause modification to the surface structure, dimensions and mass of the body. It is not always necessary or recommended to reduce wear and friction together, sometimes reducing wear alone may be beneficial such as in oil bath clutches, or in some cases friction needs to be reduced without wear, for example in grinding and polishing operations. In many applications it is desired to reduce both friction and wear and this can be achieved by means of lubrication. Lubrication can have an essential impact on the dynamic behaviour of mechanical structures and machines due to the

phenomena involved. Proper lubrication helps machinery, equipment, and mechanisms to function properly with enhanced performance, optimized energy utilization and reduction in wear. In contrast, poor lubrication will result in failure of the lubrication film to effectively separate the surfaces, leading to premature failure of machine parts and equipment and hence added cost to the owner. Economic benefits can be enjoyed if lubrication is well applied such as, conservation of materials, energy saving, reduction in frequent maintenance as well as a positive effect on the environment. Total energy consumption can be reduced by reducing friction, and the authors estimate that the total energy consumption can be reduced in industrialized countries by 4.5%. Elementary practices of the lubrication process have been known since ancient times and the proof of the same are found during archaeological study. Modern lubrication has emerged since the second half of the 19th century due to rapid industrialization. The first governing equations of hydrodynamic lubrication were defined during this era. Since then, substantial research effort has been carried out continuously to understand and develop the science of lubrication. During recent studies it was found that different areas are yet to be investigated with promising potential applications. It is clear that research in the field of lubrication is still on going and has huge scope.

1.4 Introduction to elastohydrodynamic lubrication (EHL)

According to Zakaria (2010), many lubricated machine parts that do not fit conformally to each other have small highly pressurised lubricated areas carrying the total load applied to the parts. The area of lubrication for two surfaces in a non-conformal combination is normally three orders of magnitude less than that of conformal combination. In other words, whilst the area of lubrication between non-conformal faces enlarges significantly with the load it is still much smaller than the area of

lubrication between the two conformal contacting surfaces. Examples of non-conformal surfaces would be: cam and follower, gear teeth transmitting load, rolling element bearings and others. One of the most complicated applications of tribology is gear tooth contacts. There are many types of gears in use but the most common are, spur, bevel, worm and helical gears. Load in these gears is transmitted by means of Hertzian lubricated contacts which are called elastohydrodynamic contacts (EHL).

When loaded non conformal surfaces have relative motion against each other with lubrication between them, the concentrated load leads to high contact pressures which can result in elastic deformation of the contacting surfaces and a near-parallel lubricant film. This mechanism is called elastohydrodynamic lubrication. Partial or full separation of contacting surfaces prevents machine parts wearing whilst reducing friction considerably. By considering a cylinder loaded against a plane, a solution was given by Martin (1916) for the gear teeth lubrication contact problem. Martin used rigid surfaces in combination with Reynolds equation for an incompressible isoviscous lubricating fluid. The oil film predicted was extremely thin at the operating load and much smaller than the surface roughness of the gear. It is difficult to consider this thin film realistic when looking at the long life of gears running without any damage. The major limitation of using the customary assumption of rigid surfaces in modelling was when applying these models to non-conformal contacts with heavy loading (Martin, 1916). Hertz (1881) analysed elastic deformation in optical lenses pressed together and discovered his now widely used contact theory. His work proved to be pioneering in the field of contact mechanics. Nowadays contact stress as well as analysis of elastic deformation of loaded non-conformal contacts is based on Hertzian contact theory (Johnson, 1987).

According to Popova and Popov (2014), elastohydrodynamic lubrication was first considered by Alexander Mikhailovich Ertel. Ertel used Reynolds's equations of

lubrication to solve problems related to hydrodynamic lubrication; full film lubrication was predicted considering combined effects of elastic distortion of surfaces (Hertzian contact theory) and the effect of pressure on the lubricant's viscosity. The work of Ertel was published in a renowned paper according to Cameron (1985) and Morales-Espejel and Lugt (2011). Dowson and Higginson (1959) obtained the full mathematical elastohydrodynamic solution for the line contact problem. These calculations gave pressure distributions for severely loaded contacts which were close to Hertzian and film thickness similar to the solution derived by Grubin (1949). The solution derived by Dowson and Higginson has new characteristic features of elastohydrodynamic solution at the contact's outlet, such as the exit film constriction and pressure spike. Later on, widespread research and new effort has been conducted on elastohydrodynamic lubrication by using different methods of numerical solution using modern computer technology. Different scenarios and aspects are taken in to consideration for the problems related to contacts (Bhushan, 1995), rheological models (Chang, 1991), thermal effects (Habchi, 2010) and surface roughness (Holmes, 2005).

The following subsection will concentrate on the temperature rise and heat division in elastohydrodynamic lubrication.

1.5 Thermal analysis of EHL

In many lubricated machine parts the components have relative, sliding contact with each other and this relative motion raises the temperature of the machine parts. This is a significant factor that has to be considered in the machine's operation along with wear and damage to its parts. Extreme high temperature in elastohydrodynamic contacts leads to considerable decrease in the fluid viscosity along with elastic distortion of the bodies in contact. Depending upon the relative movement between

the parts in contact, fluid within the contacts is subjected to compression and shearing. Heat is generated within the fluid film due to this compressive and shearing action of the lubricant separating the contacting bodies. This heat from the fluid film is dissipated to the bodies or machine parts in contact with the lubricant film. Therefore, researchers have focussed on the rise of temperature and heat division between the contacting surfaces in elastohydrodynamic lubrication. Dry contact analysis was used for thermal studies of contacting surfaces in the early era. It is necessary to categorize the solid temperature of the surface in two types of motion before presenting the thermal analysis study. One is the steady state or bulk temperature and other is transient 'flash' temperature. The bulk temperature can be thought of as the mean temperature of the surfaces and the flash temperature is the local rise in temperature due to the passage of the surface through the contact. Both of these temperatures in a lubricated contact are related to the fluid film between the contacting surfaces. Early analysis was carried out by Blok (1937) on the rise of temperature in dry sliding contacts. Blok considered two lubricated surfaces and concluded that high temperature rise occurs at the surface of contact when two surfaces with lubrication slide over each other with high speed. Blok's work helps to explore rise in temperature of a contacting surface resulting from moving and stationary heat sources small in dimension compared to the bodies they were heating, this case is of a semi-infinite body. Heat sources of different geometries and with various kinds of heat distribution were considered for understanding the temperature rise in sliding surfaces in contact. Blok invented the method to calculate rise in flash temperature by using the solution for a concentrated source of heat moving across the surface of a semi-infinite solid. By using the hypothesis to analyse partition of heat between contacted surfaces, Blok suggested that if two surfaces are in physical contact then the maximum flash temperature of both contacting surfaces is the same. The work by Blok (1937) and Jaeger (1942) together forms the foundation of the gear

tooth temperature calculations. To calculate bulk temperature, Blok used the theory of a thermal network (Blok, 1970), and total contact temperature was found through adding the bulk temperature to the flash temperature component. Olver (1991) gave a number of different approximate solutions for skin temperature or bulk temperature calculations for multiple shapes of disc testing machines and then carried on to calculate flash temperature by using Blok's theory.

An analytical approach to compute flash temperature was presented by Tian and Kennedy (1994) for different ranges of heat source distribution and contact shape which is based on the work of Jaeger & Carslaw. Carslaw and Jaeger (1959) applied their improved method of 'Blok postulate', for the division of heat to a full range of contacts. As this Blok method is limited to match maximum temperature within the surface contact, it is not possible to meet the condition of these two physically contacting surfaces being at equal temperature, as these high temperatures take place at different points on the surface of contact due to the speed difference.

Bos and Moes (1995) developed an algorithm to calculate distribution of flash temperature and heat partition of two contacting surfaces by matching the temperature of the surfaces at all positions within the contact. A singular integral equation is required to find the solution for this condition. Bos and Moes considered a number of closed form functions for different geometries and for distribution of heat flux. The results showed a good match with the numerical method's results for corresponding geometries. Kennedy (1984) summarised different methods of calculations of flash temperature along with discussion of the methods of handling the heat partition issues for dry contacts. All these methods of calculation made some assumptions such as dry and physical contact between contacting surfaces, as well as flash temperature determination and heat division either by matching the temperature at the entire contacting interface or by achieving the same maximum

contact temperature for both the contacting surfaces. When considering lubricated contacts then neither of these approaches are strictly applicable. Elastohydrodynamic lubrication is used to achieve heavily concentrated fluid film lubrication. Substantial increase in viscosity is observed along with elastic distortion due to pressure developed within the lubricant. Heat is produced within the film of fluid during sliding of these contacts due to compressive and shear heating of the lubricating film. In this scenario, conduction is the governing heat transfer mechanism and it is perpendicular to the film of lubrication. The highest temperatures are found to be developed within the film when the heat generated is throughout the film thickness. The surfaces to which heat is transferred by conduction are usually at lower or different temperatures, this surface gradient is required to transfer the heat from the lubricant film to contacting surfaces. There is no physical reason why the surfaces should be at the same temperature within the contact, which is the common approach taken by the dry contact work outlined here. Different methodologies have been tested previously to find the temperatures of the surface of lubricated contacts.

To estimate the rise of temperature within rolling and sliding contacts, Crook (1962) developed a method to analyse and measure the effect of film thickness, traction and temperature of the surfaces, which were considered on the basis of the hypothesis of equal heat partition between contacting bodies.

For heavily loaded line contacts, Manton *et al.*, (1967) developed a mathematical model which considered the lubricating film. The analysis carried out by Manton *et al.*, (1976) was based on the hypothesis of Hertzian semi-elliptical distribution of pressure as well film thickness based on the well-known formula derived by Dowson and Higginson, rather than a full elastohydrodynamic investigation. The procedure of analysis considered the bulk temperatures as an inlet boundary conditions and assumed that these can be estimated or known. From these assumption and known

parameters contact temperature and heat partition were calculated. It was observed that the amount of heat which passed into the slower moving surface was higher than that of the faster moving surface. Temperature profiles were compared with those idealized by (Merritt, 1962) to understand experimental readings of heat division between test discs. This showed the heat absorbed by the faster moving disc was more than that absorbed by the slower disc.

Wang and Cheng (1981) used a model of a pair of spur gears in which simplified elastohydrodynamic lubrication analysis was used. Squeeze film effects were considered on the gear lubricant film along with Hertzian pressure distribution in this analysis. In this paper the authors assume that lubricant shear takes place predominantly at the mid-plane and that the temperature profile is linear between the surface temperature and the mid film maximum temperature. This was the basis for their heat transfer analysis of the gear tooth and was used to compute flash temperatures at the contacting teeth over the meshing cycle.

1.5.1 Experimental scuffing tests using a twin disc machine

The twin disc test rig used for the research described in thesis was built and commissioned for scuffing tests by Patching *et al.*, (1995). It is capable of high speeds with recirculating power and was used to explore failure in ground and superfinished discs due to scuffing under conditions usually found in gas turbine gearing.

Figures 1-3, 1-4 and 1-5 show the rig, the test head and drive arrangements, and the test head schematic respectively. The diameter of discs used was 76.2 mm and the discs were crowned so that the Hertzian contact area was elliptical with an aspect ratio of 1:4. The radius of relative curvature of the disc contact in the rolling/sliding direction replicates the contact conditions between involute gears on 150 mm centres.

The crowning ensured that the Hertzian contact's major axis was parallel to axis of the disc so that the contact was self-aligning and did not experience edge effects at the face boundaries of the contact. The discs were mounted on parallel shafts in the test head which were connected by belts and gears to transmit power at the rolling/sliding contact to achieve specific slide/roll ratios. Fixed bearings held the faster shaft, whereas the slower shaft was installed on bearings mounted on a swinging yoke. A hydraulic ram acting on this yoke was used to apply load to the contact.

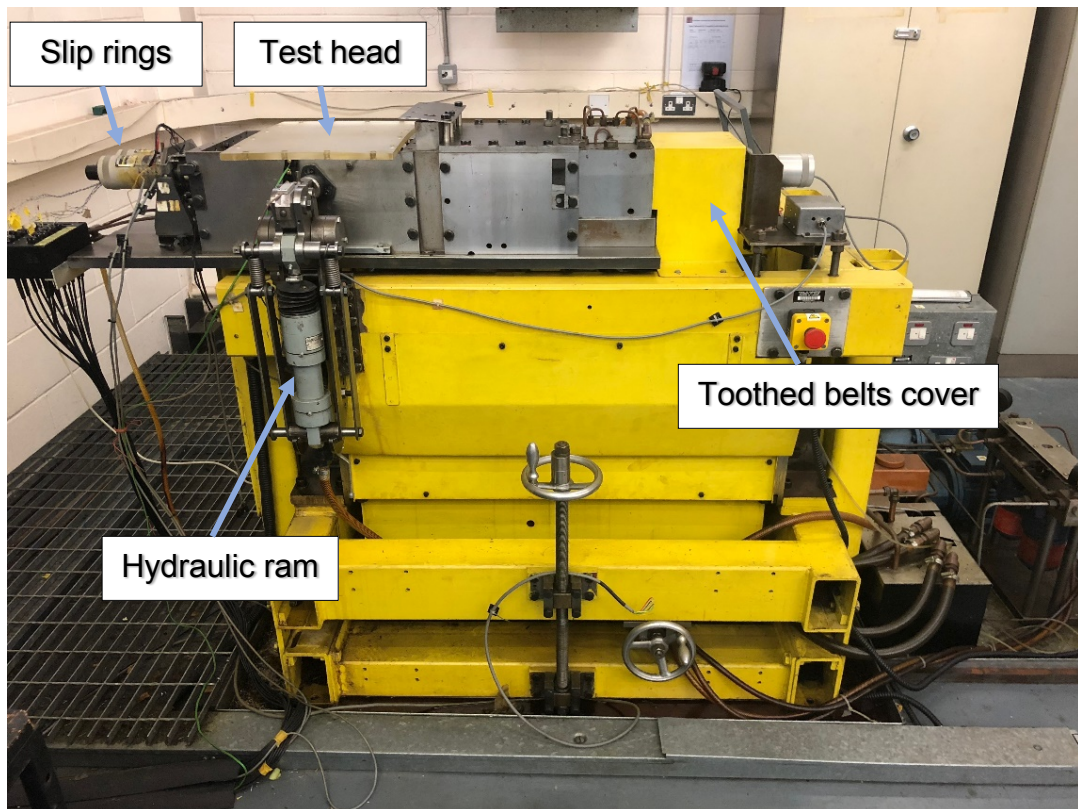


Figure 1-3 Twin-disc test rig

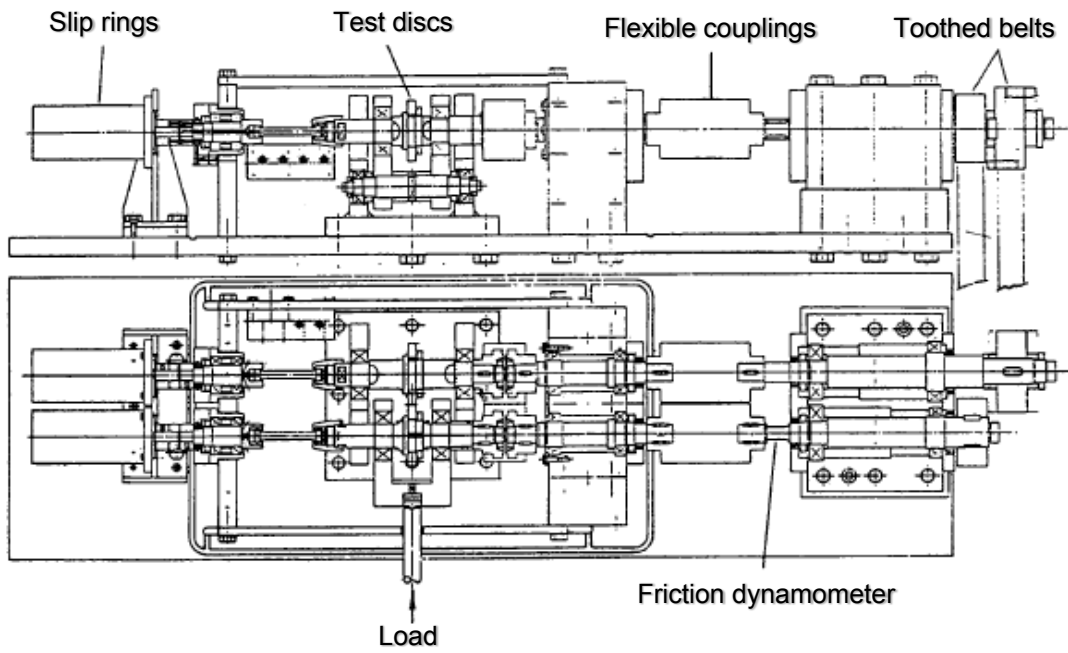


Figure 1-4 Drawing of the test head and drive arrangement of the test rig (Patching, 1994)

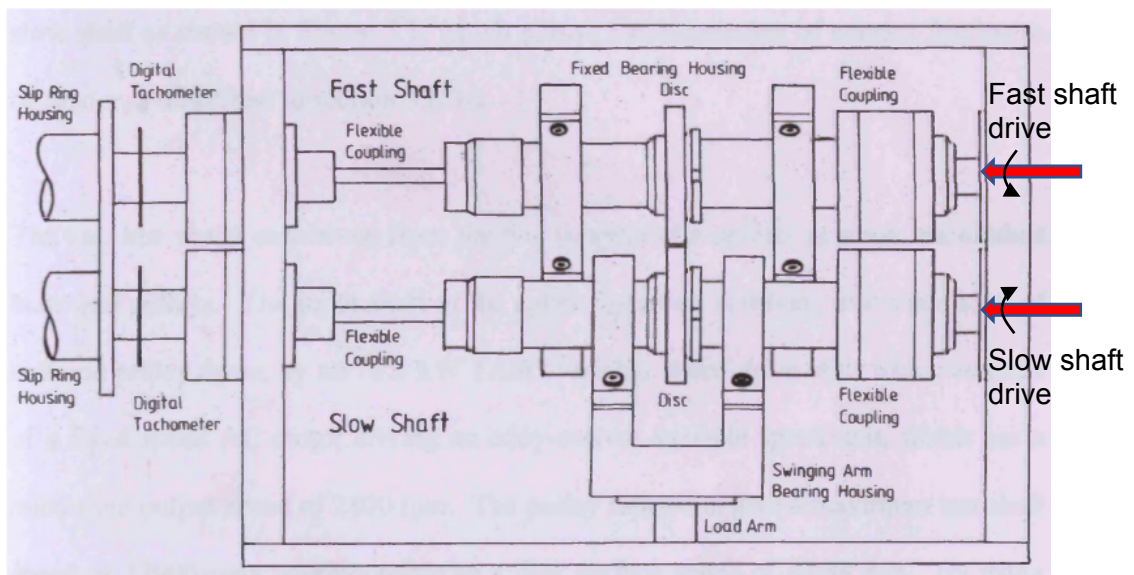


Figure 1-5 Test head schematic (Patching, 1994)

The test discs were equipped with thermocouples, located 3.2 mm below the surface of disc at centre line of the track. For continuous measurement of the developed

torque in the shaft and friction at the point of the contact of disc, a strain gauged section of shaft was used to measure torque on the shaft (drive) of slow disc. This developed torque was due to frictional traction between sliding discs and friction at the bearings on which slow shaft was installed. To enable the traction between the discs to be calculated, the bearing friction was carefully measured with the test rig operating under pure rolling conditions so that the frictional traction was effectively zero. Friction in bearings is primarily a function of load and speed and these measurements were carried out over a range of loads and speeds. The friction in the bearings could then be removed from the friction measurements in the rolling/sliding contact tests so that the frictional traction at the contact could be obtained. The friction and disc temperatures were recorded continuously. Spray lubrication was used on the test disc, where a constant flow rate jet was directed at the contact between the discs. The lubricant used was a synthetic turbine oil, Mobil Jet 2, which was circulated to the test head at a controlled temperature of 100°C and directed by separate jets to the inlet and outlet of the disc test contact and to each of the bearings supporting the shafts.

Discs in contact were running at constant speed during each test. At the beginning of every test, oil was distributed through the test head and discs were run with very light load until stabilization of the temperature in the entire system occurred. The initial load was applied and held constant for three minutes, the load applied was equivalent to maximum Hertzian contact pressure $P_0 = 0.6$ GPa. The load was then increased to give $P_0 = 0.7$ GPa, also held for three minutes. The process was repeated until the discs were at the maximum load $P_0 = 1.7$ GPa. The load was increased in Hertzian maximum pressure steps of 0.1 GPa and held constant for 3 minutes for each step until the disc scuffed. The trace of temperature and friction force record of a typical experiment is shown in Figure 1-6 below.

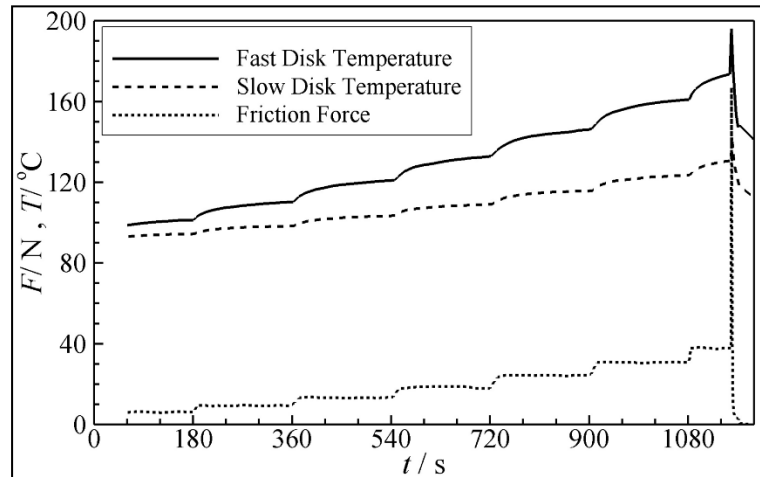


Figure 1-6 Typical traces corresponding to Patching's experiment (Clarke, 2009)

This series of scuffing experiments was carried out using this test rig to examine scuffing failure of the surface, typically in gas turbine auxiliary drive gearing under a range of sliding speeds and loads.

1.5.2 Use of scuffing test results to investigate heat partition at the contact

Clarke *et al.*, (2007) used the temperature and friction measurements obtained in scuffing tests to develop a heat conduction thermal model of disc and shaft assemblies. Their objective was to find a way to infer the surface temperature of the discs from the measured thermocouple temperature 3.2 mm from the surface. This objective was found to depend on knowing the way in which heat division occurred between the contacting surfaces and led to exploration of the heat partition at the contact which was operating in the elastohydrodynamic regime (EHL).

A transient heat conduction 2D model was developed to calculate the average temperature in the heat generating area of the disc as well as the shaft. This model overlooks any circumferential dissimilarity. Frictional heat generated at the contact

along with convective heat losses from the surface of shaft and disc to circulated spray mixture in the test head is used as an input. EHL contacts have very thin lubricant films in the Hertzian contact area where the frictional heat is dissipated. Consequently, the amount of heat convected from the contact area by the lubricant is negligible and almost all the heat passes into the disc surfaces by conduction. The complete frictional heat measured during the tests of experiments was separated between the contact surfaces according to a factor β , where $0 \leq \beta \leq 1$, which is defined as the fraction of the total frictional heat which passes into the faster disc. The remaining portion $(1 - \beta)$ passes into the slower disc. It should be noted that this definition of β is reversed in the current work, where β represents the proportion of heat passing into the slower disc. In the thermal model the Hertzian pressure distribution was used to distribute heat input to every disc. The β factor was tuned until the measured temperature at the positions of the thermocouples matched with the ones recorded during the experiment. It was assumed that β remained constant over the period of each three minute loading stage, but it was allowed to vary between stages of load in the experiment. The heat transfer coefficient for different surfaces was calculated from expressions in the literature for forced convection for cylindrical surfaces and rotating planes to ensure balance of temperature within disc was maintained (Clarke *et al.*, 2006). This method was used to model 9 different tests, five out of nine used ground discs whereas the others used super finished discs. Figure 1-7 shows the calculated temperature trace for an experiment. The graph shows good agreement with the measured thermocouple temperatures recorded in the experiment shown in Figure 1-6. Figure 1-7 also shows the mean circumferential temperatures calculated for the centre line of the running track surface. As adjustments were made to eliminate bearing friction, the friction trace shown in Figure 1-7 is different from the one shown in Figure 1-6.

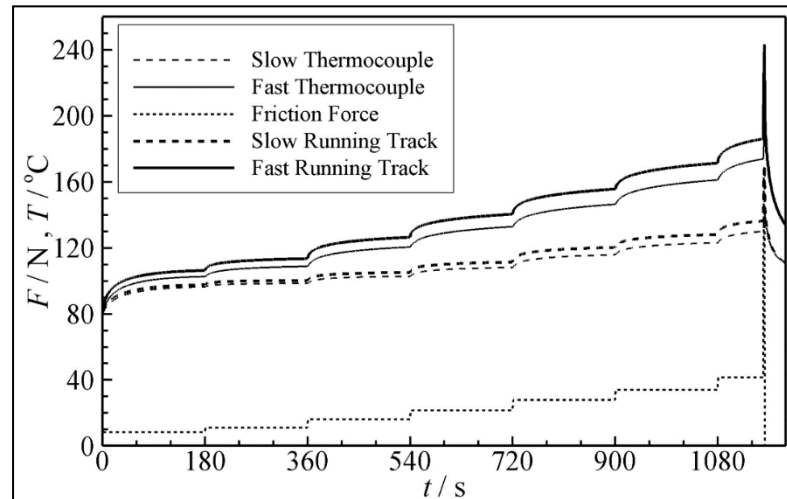


Figure 1-7 Calculated temperatures from 2D transient model for experimental test (Clarke, 2009)

1.6 Insights on temperature measurements in EHL contacts

Different tribological applications as well as processes have frictional motion between the lubricated parts. These parts generate heat due to friction between them. Heat produced due to friction may cause changes in structure as well as properties of parts and oxidation of the surfaces (Bhushan, 2000). High temperatures due to friction may affect the performance of the parts; also, it might affect the wear and frictional behaviour of the parts. Therefore, to prevent machine parts from failure from heat generated due to friction and to improve the performance of the systems, it is required to measure the amount of heat generated between the frictional contacts of the machine. According to Stachowiak and Batchelor (2004), accurate temperature measurement is one of the most difficult tasks in tribology. The difficulties are listed as,

- Small area of heated surface due to rise of transient temperature
- Surface temperature within dynamic contact and adjacent to dynamic contact
- Ambient temperature of lubricant in the lubricated contacts

There are different methods which are used to measure temperature in tribological applications, but in this section two major methods will be reviewed which are being used especially in elastohydrodynamic lubrication contacts namely thermocouples and infrared temperature mapping.

1.6.1 Temperature measurement by thermocouples

Thermocouples are made up of two wires of dissimilar metals, with ends of these two wires connected to measure rise in thermal Electro Motive Force (EMF). The EMF is a function of the temperature at the junction and temperature rise is independent of the gradient within the wires.

Embedded thermocouple

By using empirically derived calibration tables, comparison of the EMF can be made which is obtained through keeping one junction at cold junction in other words 'reference temperature' and the other at the measuring junction (Reed, 1982). A small hole is drilled within a fixed component of a sliding pair. The hole is slightly below the sliding surface of which the temperature is to be measured. As shown in Figure 1-8, the thermocouple is inserted through this drilled hole in a way that the measuring junction is at or just below the sliding surface.

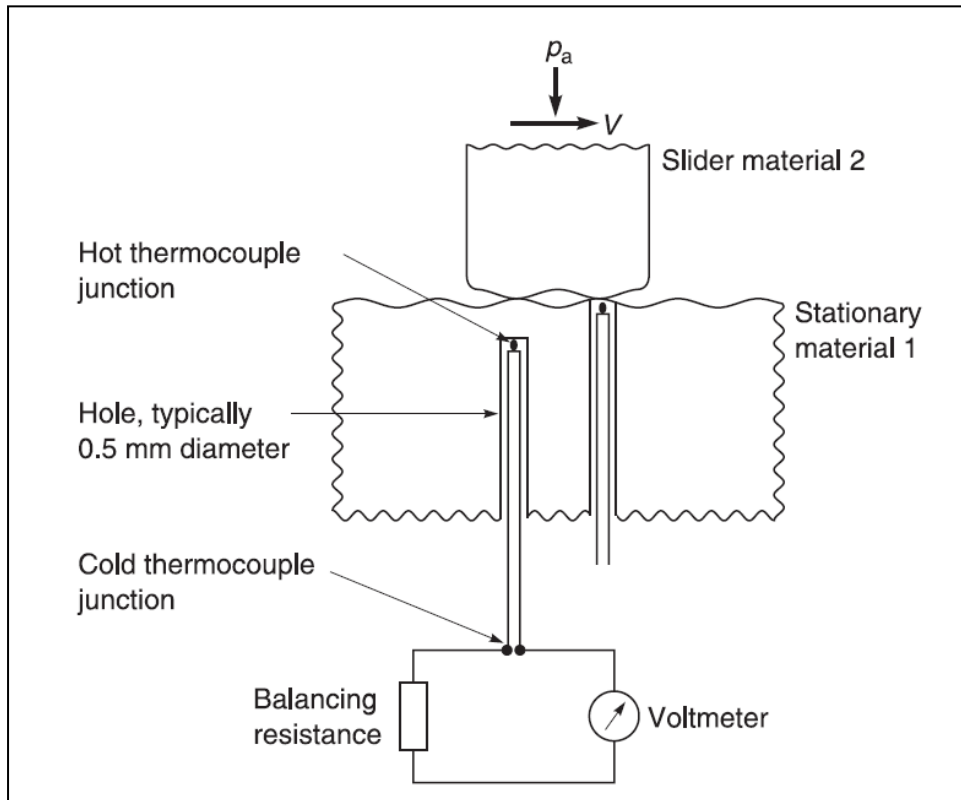


Figure 1-8 Schematic representation of two embedded thermocouples one fixed below the surface and the other at sliding surface (Bhushan, 2013)

To bond the thermocouple into the hole, inorganic cement or an epoxy can be used. This also helps to insulate the thermocouple wire from adjacent material. A set of embedded thermocouples can be used at different distances from the surface of contact to measure thermal gradients. Better measures of transient changes during frictional heating as well as relative measures of coefficient of friction are given by thermocouples (Bhushan, 2013). On the other hand, it is difficult to measure actual flash temperatures by using thermocouples due to the distance between the measuring junction from the contact and the finite material mass between the contact and the measuring junction. High thermal gradients can be observed perpendicular to sliding contact. It is possible to place the thermocouple exactly at the surface of contact by extending the hole until the surface, and grinding the thermocouple even with the surface, even though the flash temperature measured by thermocouple may

vary due to the thermal properties of the thermocouple, also the thermocouple measures the average temperature of total finite mass at the point of contact (Spurr, 1980).

Dynamic Thermocouple

The measurement of thermal EMF of metallic contacts can directly indicate the temperature rise between them. Figure 1-9 shows how the sliding surface and stationary material together can form a thermocouple junction. By using slip ring/ bush arrangement or mercury cup, electrical connections can be made for the moving component.

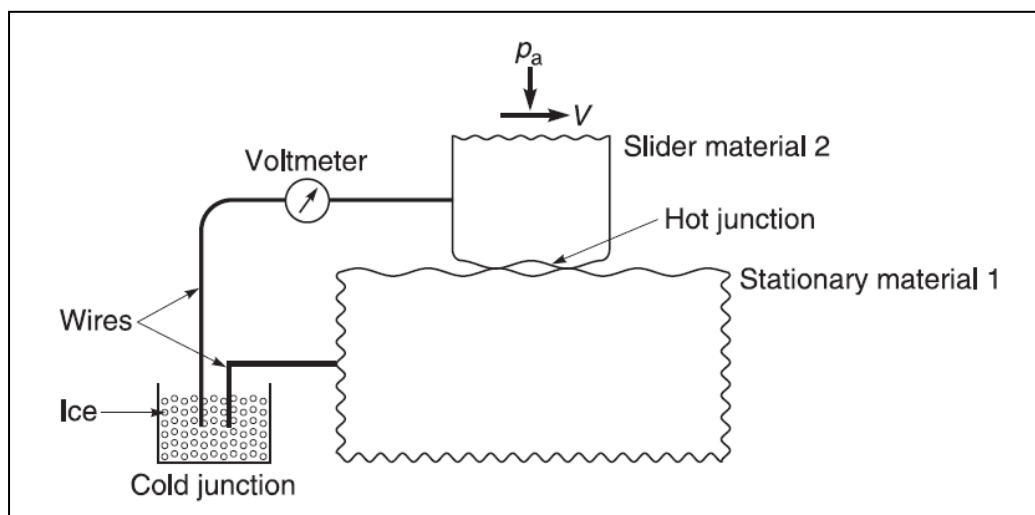


Figure 1-9 Schematic representation of the dynamic thermocouples technique used for measuring temperature of the surface of two dissimilar metals (Bhushan, 2013)

The EMF can be converted into a temperature rise by calibration of the sliding pair with a standard thermocouple. The process of calibration usually involves measuring of the EMF potential of heated sliding pair as well as a standard thermocouple in a molten lead bath (Shaw, 2005). This dynamic thermocouple technique was invented in order to measure contact temperature during metal cutting operations (Shore,

1925) (Shaw, 2005) (Chandrasekar and Bhushan, 1990). Good average surface temperature measurement can be made using the dynamic thermocouple technique. Dynamic thermocouples can be very sensitive to changes in surface temperature due to the very thin junction. Dynamic thermocouples are used in applications where higher values are to be obtained as well as for the faster transient response as compared to embedded thermocouples. This technique of temperature measurement of lubricated contacts is limited to metallic pairs of dissimilar metals only and it requires external electrical connections for the sliding pair.

Thin film temperature sensors

This technique involves deposition of vapour to develop thin film temperature sensors on the surface. A very small size of thin film sensor measures the temperature rise accurately for small regions. The first vapour deposited thermistor temperature sensors were used to measure the temperature of a surface on the flanks of gear teeth (Kannel *et al.*, 1972). Figure 1-10 shows the thin film sensors with titanium coated thin strip on insulator made up of alumina on a surface of one of the meshing teeth pair. Sensitivity of titanium strip's resistance is dependent on temperature as well as pressure; hence variation in transient temperature and pressure can be measured due to any change in resistance of the titanium strip.

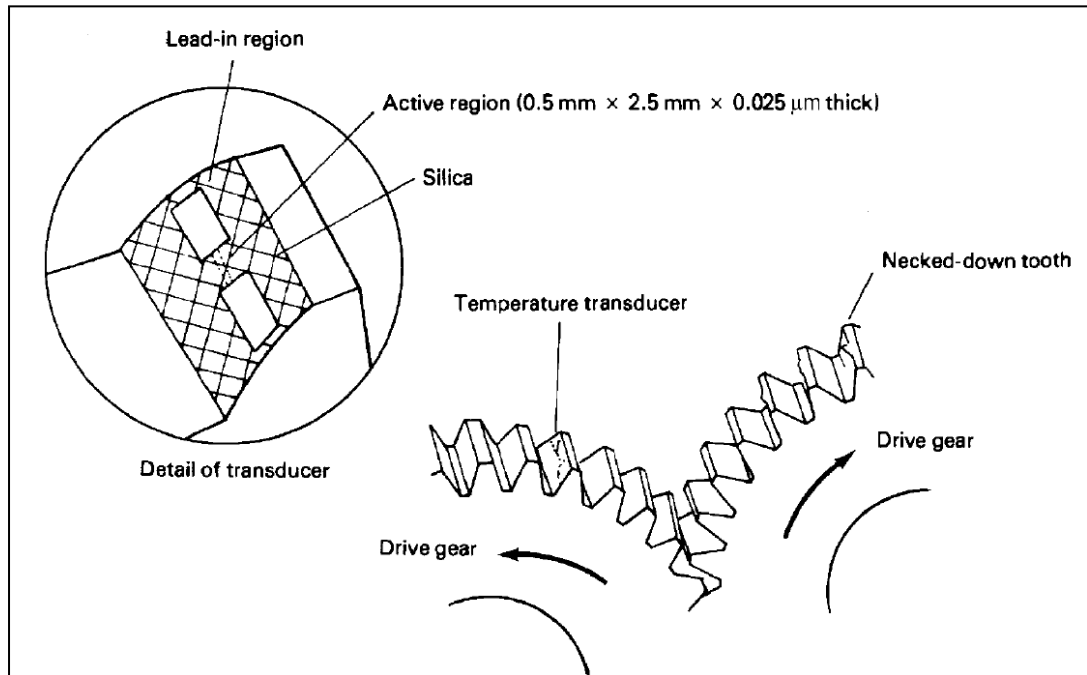


Figure 1-10 Schematic representation of thin film temperature sensor (thermistor) for temperature measurement of gear teeth (Kannel *et al.*, 1972)

Magneto-resistive (MR) sensors are used in read heads in magnetic recording media (Bhushan, 1971). A thin strip of ferromagnetic alloy is used as a sensor. Magneto-resistive strips are sensitive to temperature variation due its resistance changing with temperature. To measure flash temperature of the interface at magnetic head medium interface, MR sensors have been used.

To produce thin film thermocouples, micro-fabrication techniques have been employed (Marshall *et al.*, 1966). Vapour deposition techniques are used in these thermocouples to produce pairs of thermocouples from thin films of dissimilar metals for example copper and nickel sandwiched between layers of dielectric materials such as alumina. Figure 1-11 shows the development of a thin film thermocouple for sliding contact measurement of temperature and its cross-section (Tian *et al.*, 1992). To insulate the thermocouple from the material substrate underlying a protective top layer is used. The total thickness of the sensors could be as small as 1 μm and the

actual measuring junction can be 10-100 μm^2 with a thickness of 0.5 μm . The sensitivity of thin film temperature sensors is higher due to their small thermal mass and they can measure flash temperature more effectively than traditional wire thermocouples.

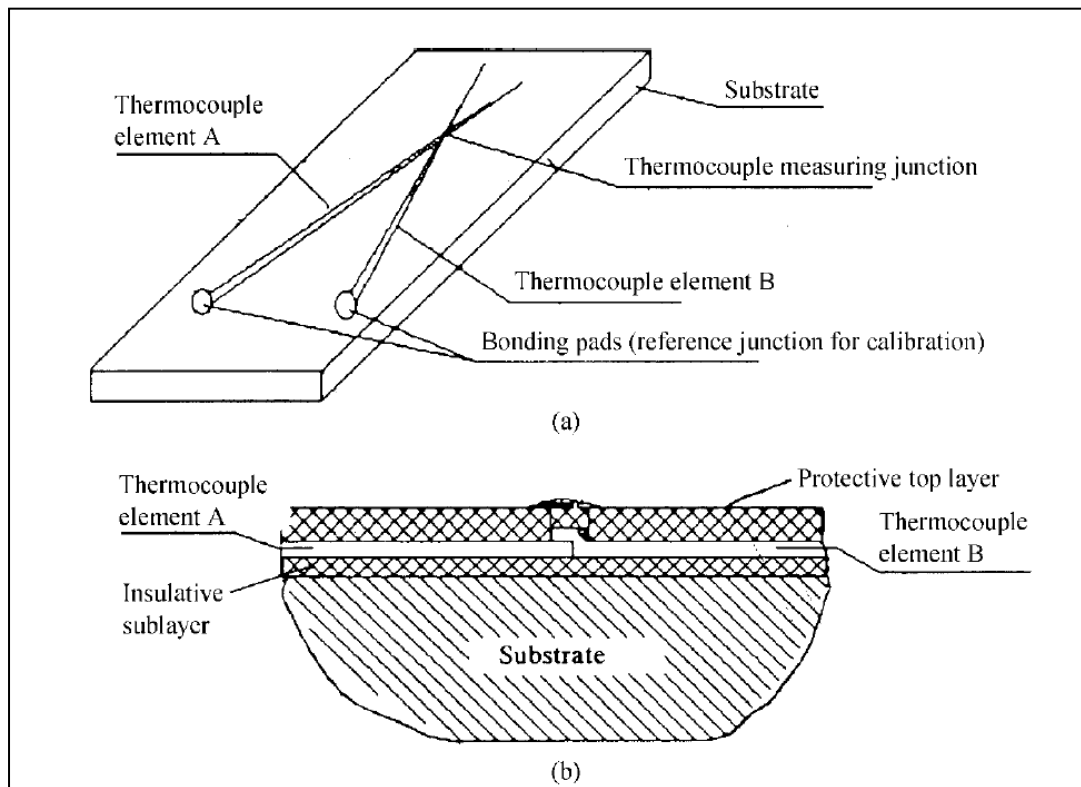


Figure 1-11 Schematic representation thin film thermocouple (a) Surface (b) Cross-section (Tian *et al.*, 1992)

1.6.2 Radiation detection techniques

Each material emits radiation based on the structure of the material and surface temperature, known as thermal radiation. The configuration must be known to determine properties of heat transfer of specific material and radioactive features of the material. It is possible to deduce the temperature by measuring the emitted thermal radiation once all the factors have been measured. To measure flash

temperature, radiation detection techniques have been applied successfully. This technique requires one of the surfaces to be translucent to detect radiation. For these studies, a useful material is sapphire as it is transparent when operated within the infrared regions, also the mechanical as well as thermal properties of sapphire resemble the properties of steel (Bhushan, 2013).

Infrared detection

Infrared- radiometric (IR) microscopes are used for temperature measurement of local surfaces. The detector is equipped with optics to restrict the field of view to a small spot size to allow spatial resolution (Nagaraj *et al.*, 1978) (Gulino *et al.*, 1986). Winer and coworkers used a high resolution infrared radiometric microscope with liquid nitrogen cooled indium antimonide detector along with optics which have reflective properties which can allow spatial resolution up to 38 μm . A photometer is usually used as a detector which measures radiation coming from an object in the range of 1.8 to 5.5 μm wavelength. The output of the detector is the combined value of the range of radiation received over the period. The difference between radiant energy coming from the object and infrared energy is measured by IR microscope. It is possible in DC mode by cutting the radiation coming from the object area whereas in AC mode it forms due to thermal fluctuations. To measure temperature of the surface where the detector is focused on the area of the contacts or through the sapphire on to the contact of sapphire and the sample, the IR microscope technique is successfully employed. Figure 1-12 shows a ray diagram to calculate contribution of radiation coming from the sample in contact with a block of sapphire. There are three sources through which radiation can enter neglecting double reflections (Gulino *et al.*, 1986) and those are: Radiation from environment, Radiation passing through the top surface and Radiation produced by the sample, Note: sapphire emits minor radiation, ϵ is 0.11 for the sapphire with thickness 3.2 mm.

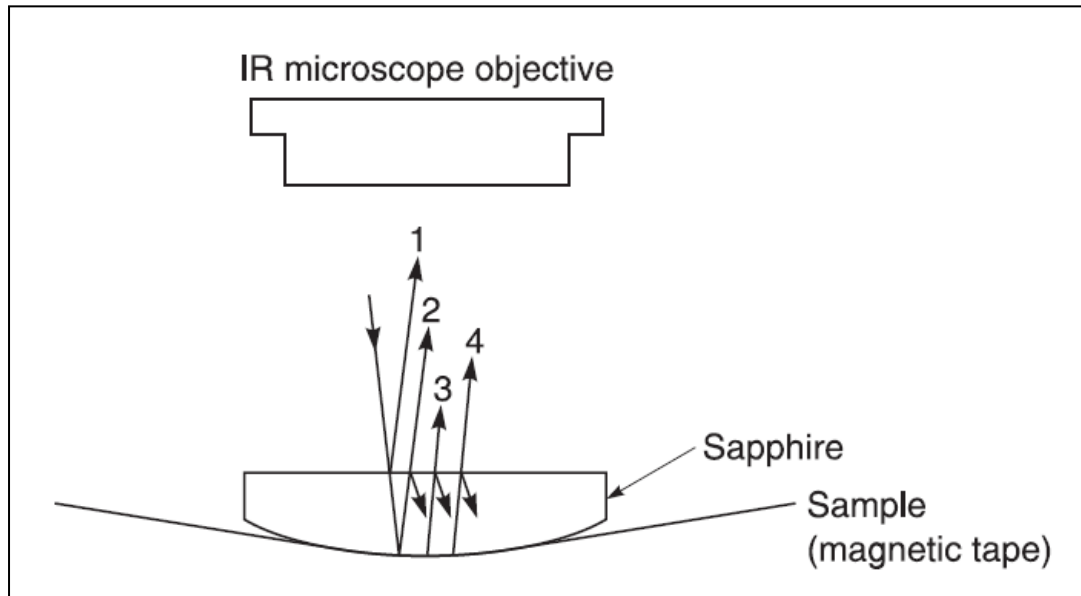


Figure 1-12 Schematic representation of IR microscope objective (Bhushan, 2013)

Reflectivity of sapphire is 0.063 for a thickness of 4 mm (Union carbide, 1972). It is required to measure properties of the material such as emissivity, reflectivity as well as transmittance of the sample in order to calculate the surface temperature. Surface temperature can be calculated after proper calibration (Nagaraj *et al.*, 1978) (Gulino *et al.*, 1986). Weighted intensities average over the targeted area are used to derive the temperature from output signal. The minimum spot size is the targeted area at the focus. The minimum spot size for a specific objective with air as the transmitting medium is supplied by the manufacturer and must be adjusted because of sapphire within the optical path which increases the diameter of the spot. The experiment was carried out by Gulino *et al.*, (1986), in which the diameter of the spot is increased up to four times for a value of 120 μm for the 15x objective lens. Peak flash temperature could not be measured accurately due to the larger minimum size of the spot as well as the time constant when compared to the usual duration and size of contact for typical engineering interfaces. The maximum temperature rise in a steel ball in lubricated sliding contact with a sapphire disc was reported as 100 to 200 $^{\circ}\text{C}$ (Nagaraj

et al., 1978). It is possible that the IR microscope may miss several events of contacts occurring at other parts of the contact area, due to the limitation of the field of measurement to a single spot. An IR camera which has ability to scan can be used to overcome this limitation, for example the AGA Thermocision, Lindingo, Sweden (Gulino *et al.*, 1986) (Meinders *et al.*, 1983) (Griffioen *et al.*, 1986). The camera has a detector which is similar to an IR microscope and it operates as a scanning device. Thermal energy due to radiation during scanning is converted into an optical pattern which is shown on a video display screen. In the line scan mode, a fixed line which may be several millimetres in length is scanned continuously, with a maximum rate of scan of up to 2500 lines every second with one frame comprising 100 lines. The size of these devices is very large for minimum spot size. To scan 1.5 mm in length the time taken is of the order of milliseconds. It has the capacity to scan a large region and to capture many flash temperatures. It is been observed that flash temperature rise is underestimated by the scanning type instruments (Griffioen *et al.*, 1986). Low surface temperatures resulting from elastomeric contact are due to large surface contact that decreases the energy dissipated per unit area. The spectral distribution of the radiation produced by two separate detectors can be used to obtain peak flash temperature rise (Bair *et al.*, 1991). The radiations produced are chopped between two detectors to pass through different band pass filters which are placed in front of each detector thereby measuring power radiated in two different wavelength ranges. The two measured values are a function of temperature and hot spot area. The maximum temperature within the view can be obtained from the ratio of detected power with two wavelengths. Once temperature is calculated then the hot spot area can be determined. The optical setup is shown in Figure 1-13 whereas typical results of this method in graphical form are shown in Figure 1-14.

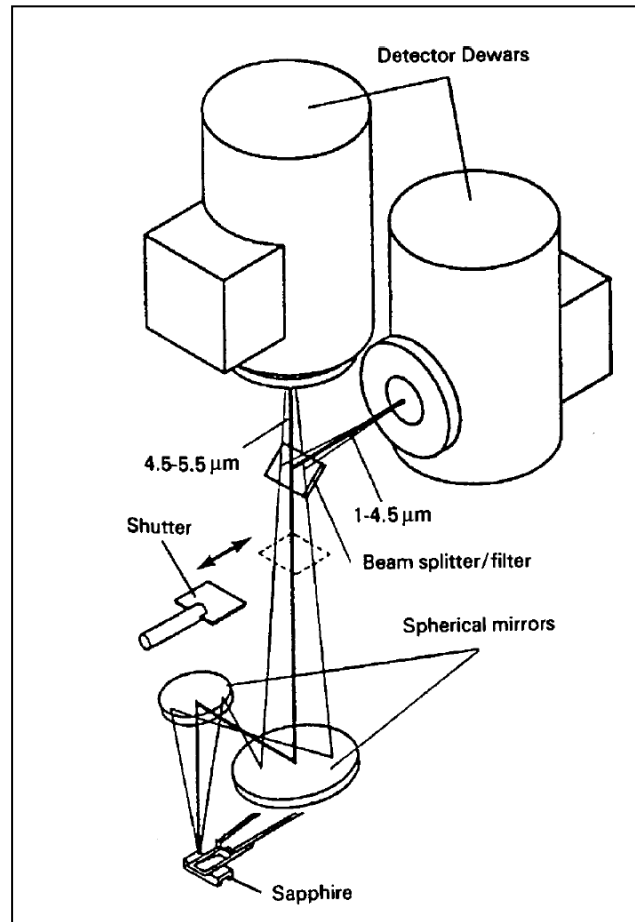


Figure 1-13 Optical arrangement of IR measurement system (Bair *et al.*, 1991)

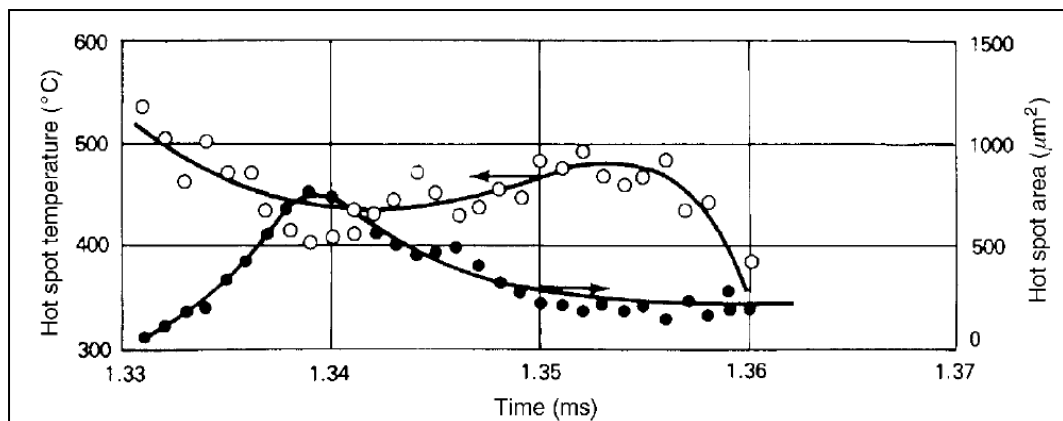


Figure 1-14 Example of hot spot area and temperature measured by means of Optical arrangement of IR measurement system (Bair *et al.*, 1991)

It is possible to make field of view very large which allows detection of flash temperature over an area of interest. During the process of sliding determination of

temperature can lead to inaccuracy due to uncertainty about the emissivity of the surface of contact, this may happen with any of the IR techniques. Considering, wear, oxidation and changes in surface characteristics may lead to variation of the total emissivity of the metallic as well as non metallic surfaces. By keeping the spectral distribution of emissivity constant it is possible to overcome the difficulty of varying emissivity by using the two detector measurement technique as measured temperature is then independent of the emissivity.

1.7 Infrared measurements of EHL lubricant films.

Infrared temperature measurements of EHL lubricant films have been developed over the last 20 years. Those that are published in the literature are generally obtained using ball on disc contacts where a steel ball is in contact with the plane side of a sapphire disc. This configuration enables EHL film thicknesses to be measured by interferometry of collimated light and has been a major experimental tool in studying EHL since it was first developed in the 1960s. The optical access provided to the lubricant film allows temperature measurements to be taken of the lubricant film.

Yagi *et al.*, (2006) carried out experiments using a ball-on-disc test rig to study the temperature distribution of a longitudinally grooved steel ball and sapphire disc under EHL contact conditions. The surface temperatures of the steel ball and sapphire disc were measured as well as the oil film using an infrared method that was developed by the authors. The rolling/sliding contact condition was achieved by driving the steel ball (50.8 mm in diameter) and the sapphire disc (96 mm in diameter) independently, where the load was applied using an air cylinder and measured by means of a load cell. Different balls were subjected to cutting process to create longitudinal grooves at different depth below the surface (1.5, 2 and 4 μm) with 120 μm separation, the

profile of these grooves is shown in Figure 1-15, where A represents the depth of 4 μm .

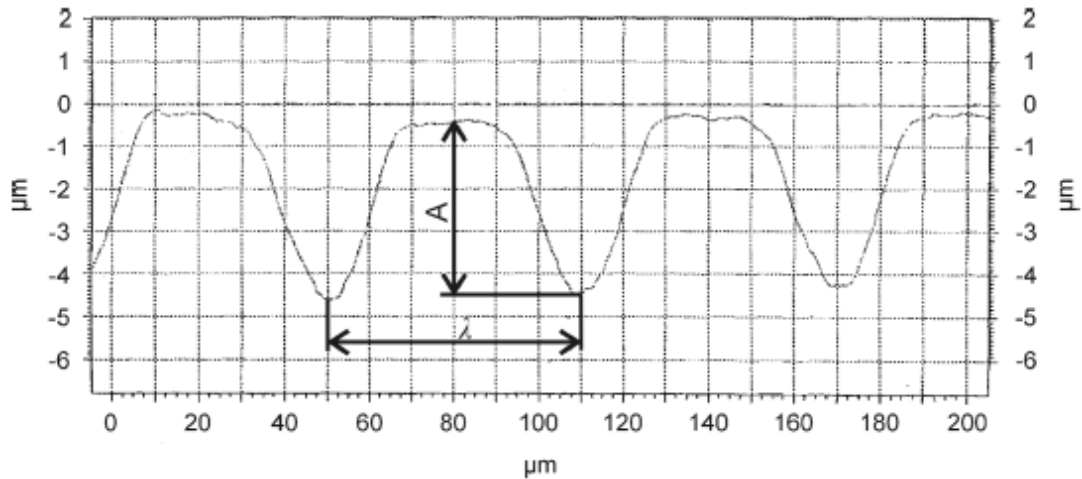


Figure 1-15 Longitudinal grooves profile $A=4 \mu\text{m}$, $\lambda=120 \mu\text{m}$ (Yagi *et al.*, 2006)

Their infrared technique was able to measure the correct temperature distribution of the longitudinal surfaces in the thin film areas as well as estimating the heat transfer within the grooved zones. As summary of the experimental results, they concluded that increasing the sliding speed as well as the depth of the grooves on the surface leads to decrease in film thickness which has a good agreement with the theoretical results by Lubrecht *et al.*, (1988). Also, the grooved surfaces have a higher temperature distribution than the non-grooved surfaces, and have a similar shape of temperature distribution compared to the oil film. With higher sliding speeds, the temperature of the non-grooved surfaces remains almost constant whereas it increases with the grooved surfaces.

To estimate the temperature, pressure and viscosity distributions in line contact under EHL conditions for a given film thickness, Chu *et al.*, (2009) proposed a thermal EHL inverse approach. It was able to overcome the issue of fluctuations in temperature

rise and pressure distribution, and to generate more accurate results of the temperature rise and pressure from fewer measured points of film thickness which reduced the computational load significantly. Figure 1-16 shows the influence of measured points of a given film thickness on (a) the temperature rise and (b) the pressure using the direct inverse approach.

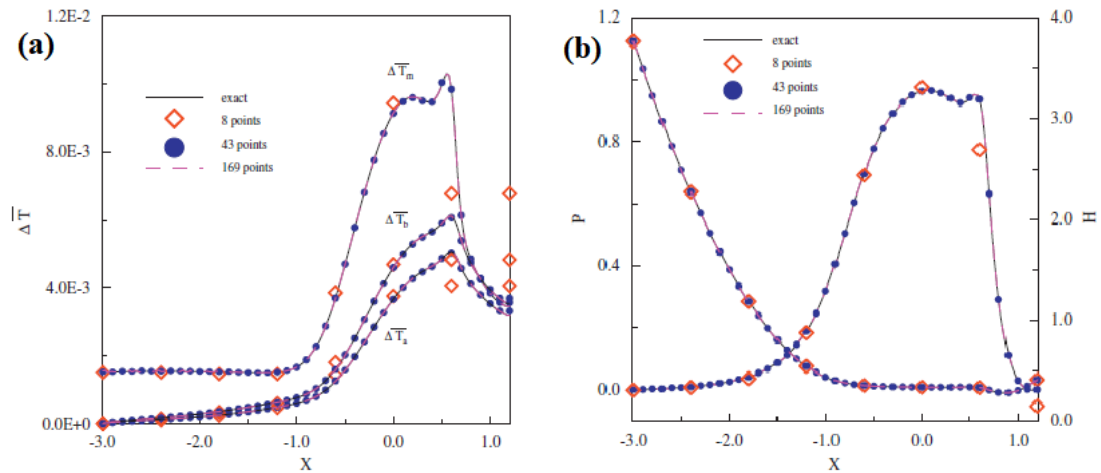


Figure 1-16 Using the direct inverse approach with different measured points of the film thickness: (a) Temperature rise distribution and (b) pressure distribution (Chu *et al.*, 2009)

From the figure, with the highest number of measured points (169 points), the result of the estimated values of the temperature and pressure approaches the exact numerical solution, where using the smallest measured points (8 points) leads to different estimated values of temperature and pressure. Using the 43 measured points, the result shows correct temperature and pressure values in the inlet and outlet region, however, the spikes of the temperature and pressure in the dimple region are incorrect. To overcome this issue, the inverse approach was used where the domain is divided into three regions (the inlet, the outlet and the Hertzian contact region). This approach obtained accurate estimated values using only 31 measured points. The results using this approach are shown in Figure 1-17 for (a) the temperature rise and (b) pressure.

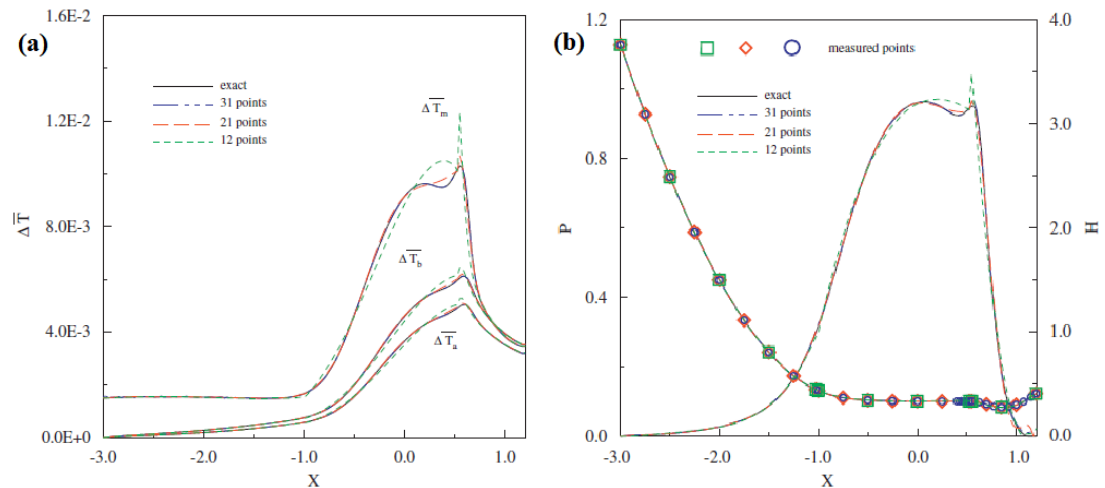


Figure 1-17 Using the inverse approach with different measured points of the film thickness: **(a)** Temperature rise distribution and **(b)** pressure distribution (Chu *et al.*, 2009)

These correct results were obtained for a given film thickness. The resolution in film thickness measurement can be affected by errors that occur in the optical interferometry measurement, hence, resulting in errors in the solution. The inverse approach still gives correct result with a minor error within the three regions in apparent viscosity, where the direct inverse approach gives a larger error in apparent viscosity (Chu *et al.*, 2009)

Lu *et al.*, (2018) developed a new method that was able to measure the thermal behaviour of lubricant and surfaces in the rolling/sliding contacts under EHL conditions using infrared microscopy with two band pass filters, and using Planck's law to convert the radiation measurement into temperatures. Their method spatially analyses the temperature of the oil film in 3D, and requires the emissivity of the oil film to be measured. The contact was achieved by loading a rotating steel ball against a sapphire disc as illustrated in Figure 1-18.

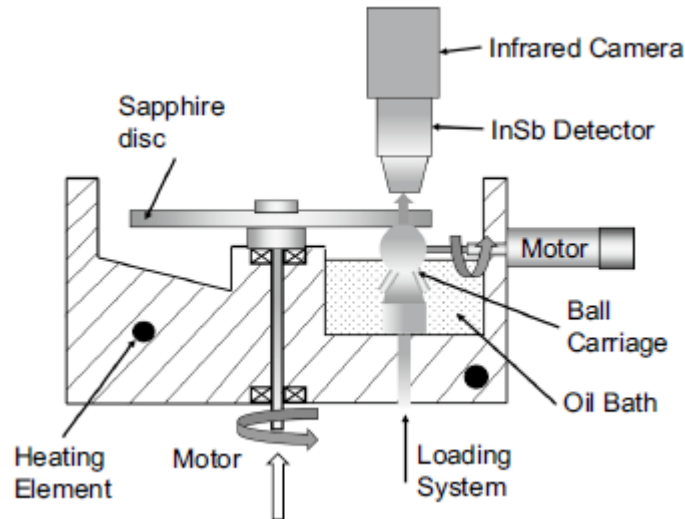


Figure 1-18 Schematic diagram of the of the experimental device (Lu *et al.*, 2018)

According to Lu *et al.*, (2018), the emissivity of the oil film is dependant on film thickness and temperature, and should be considered when measuring the oil temperature as it decreases with temperature rise and decreasing film thickness. For a given speed, they carried out different experiments using different sliding/rolling ratios, when the sapphire disc is moving faster than the steel ball it is called positive sliding/rolling ratio where the negative sliding/rolling ratio is *vice versa*. They found that the temperature of the sapphire disc surface was higher than that of the steel ball surface in all cases of sliding/rolling ratios except pure rolling. Also, within the oil film, the highest temperature of oil was found close to the sapphire disc when having negative slide/roll ratio, this is because the steel ball was moving faster, hence more heat is removed by convection. Figure 1-19 shows the surfaces and oil temperatures, and the film thickness along the central line of the contact. Figure 1-20 shows the temperature profiles of the different cases, the solid line represents the temperatures at the positive sliding/rolling ratios where the dashed line represents those at the negative sliding/rolling ratios (Lu *et al.*, 2018).

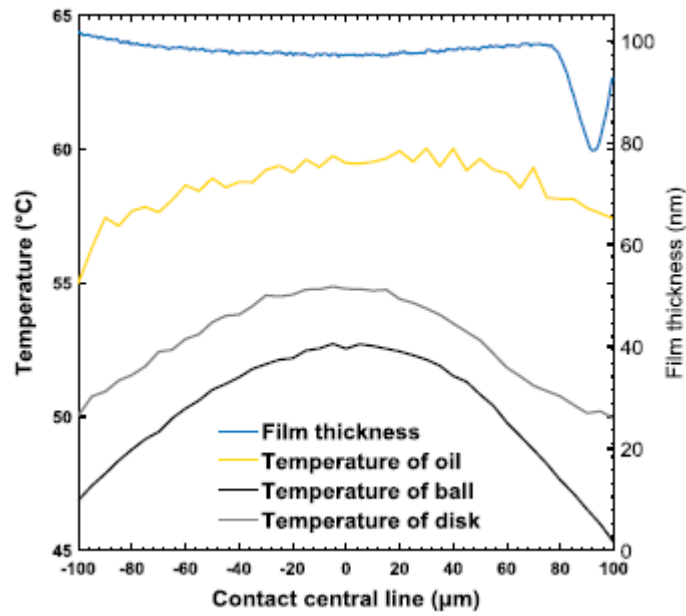


Figure 1-19 Oil and surfaces temperatures and film thickness along the centre of the contact (Lu *et al.*, 2018)

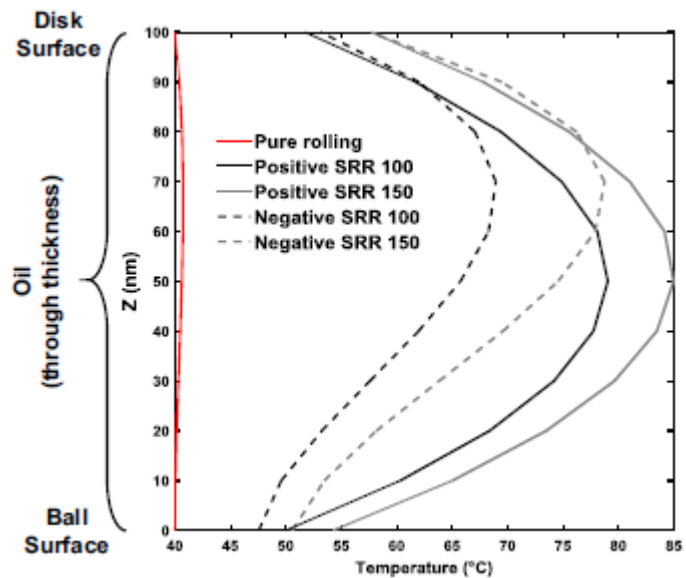


Figure 1-20 Temperature profiles of the different cases of sliding/rolling ratios (Lu *et al.*, 2018)

Further investigations carried out by Lu *et al.*, (2020) that were an extension of Lu *et al.*, (2018), the authors used the same test rig in order to study the influence of thermal properties of surfaces and the lubricants on the rheological behaviour of fluids. Two

lubricants (Santotrac 50 and PAO4), and three balls of different materials (steel, silicon, nitride and zirconia) were used to extend the range of thermal diffusivity and conductivity values. Table 1-1 shows the lubricants and the ball specimens thermal and mechanical properties.

Table 1-1 Thermal and mechanical properties of lubricants and ball specimens (Lu *et al.*, 2020)

	Steel	Si3N4	Zirconia	Sapphire	Santotrac 50	PAO4
Young's Modulus	210	310	210	345		
Poisson ratio	0.3	0.27	0.32	0.3		
Load	20	12	20			
Hertz contact diameter μm	100	80 μm	100 μm			
Conductivity (W/m.K)	21	30	3	23.1	0.104	0.17
Heat Capacity (J/kg.k)	420	760	278	753	1867	2219
Density (kg/m ³)	7860	3440	5680	3985	889	820
Diffusivity (mm ² /s)	6.36	11.47	1.90	7.7	0.06	0.09

Their experimental tests and theoretical calculations showed that these properties are a significant factor in controlling the film temperature and the friction in EHL conditions. On the other hand, the accurate relationship between the thermal properties and the system response is complicated (Lu *et al.*, 2020). They showed that shear localisation is also affected by these properties, for the zirconia ball which has very low thermal diffusivity and conductivity it occurs close to its surface. For the silicon nitride ball which has high thermal diffusivity and conductivity compared to the sapphire disc, the shear localisation is observed close to the sapphire disc. And for the steel ball which has thermal diffusivity and conductivity that is similar to the

sapphire disc, the shear localisation occurs at the centre point within the oil film. Figure 1-21 presents the temperature distribution of the oil within the oil film.

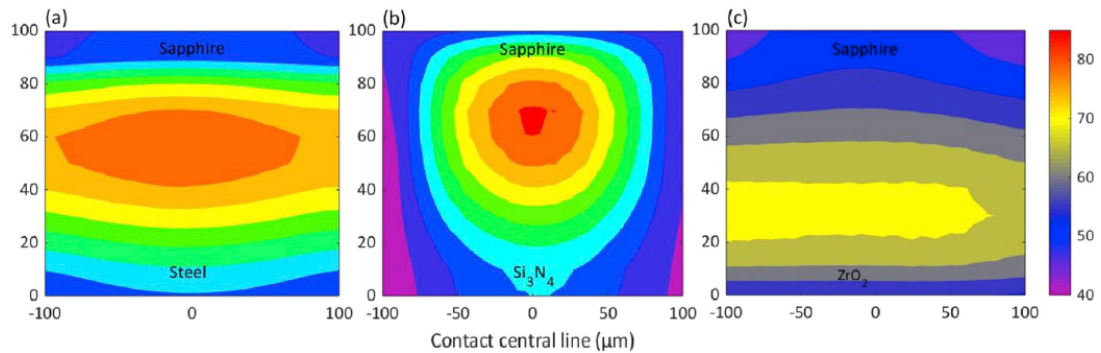


Figure 1-21 Temperature maps through film thickness for (a) steel ball, (b) silicon nitride ball and (c) zirconia ball lubricated by Santotrac 50 (Lu *et al.*, 2020)

The detailed temperature profiles shown in Figure 1-20 show that this film temperature method is now becoming capable of providing data from which the heat flux at the solid/lubricant boundary can be determined. If this can be integrated over the whole of the contact area, then it will provide a measurement of the heat partition. However, that requires accurate knowledge of the thermal conductivity of the lubricant at both surfaces, which is pressure and temperature dependant. The asymmetry in the results for positive and negative slide roll ratios also identifies the problem of using a transparent surface which has different thermal properties to the counterface. There are also significant differences in the cooling mechanism for the ball, which is immersed in a temperature controlled bath, and the disc that is rotating in air.

1.8 Disc testing

Olver and Spikes (1998) developed a simple model to calculate the traction in EHL contacts. Their method was based on viscoelastic (Maxwell-Eyring) rheology, including the evaluation of lubricant's rheological properties at the mean contacting pressure and temperature of oil film. To calculate the temperatures, they assume that

the film shears on the central plane, and model the film and solid bodies as a series of thermal resistances as shown in Figure 1-22 using thermal network theory. This gives a simple iterative solution for the oil temperatures and the traction coefficient. However, their assumption led to roughly equal total heat input for lower sliding speed that they considered. Their method is based on the average behaviour over the Hertzian contact length and presumes that the heat is dissipated over at the mid lubricant plane. The conclusion from detailed thermal EHL analyses by Clarke *et al.*, (2007) is that the lubricant behaves according to a non-Newtonian limiting shear stress model with slip occurring at or near the higher temperature surface. The central dissipation assumption made by Olver and Spikes (1998) is very influential in determining the heat partition outcome so that calculations using this simple model are not capable of predicting the observed behaviour in high speed disc tests.

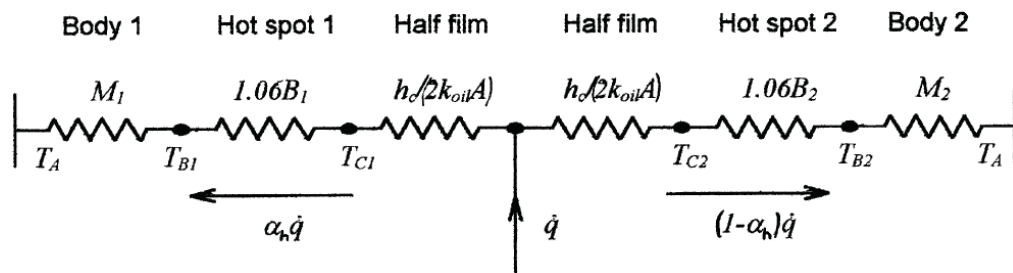


Figure 1-22 Thermal network model of two bodies and oil film (Olver and Spikes, 1998)

1.8.1 LaMCoS twin disc machine

A thermal investigation on scuffing using a twin disc machine was carried out by LaMCoS, INSA-Lyon (Isaac *et al.*, 2018). The author conducted an experiment by using a twin disc machine and thermal model by using network methodology to validate the hypothesis.

Figure 1-23 shows the test rig used for the experiment. The contact conditions between the gear teeth or ring and rolling element are simulated in this rig. The rig has two discs, one cylindrical and the other crowned. The radius of curvature of the crowned disc is 200 mm. The elliptical contact between the two discs has been achieved by the radius of curvature. To allow sliding conditions, these discs are driven by two independent motors. Oil is injected by a nozzle located above the two discs. A heating bath is used to maintain a constant temperature of the lubrication throughout the test which can be controlled from ambient temperature to more than 100 °C.

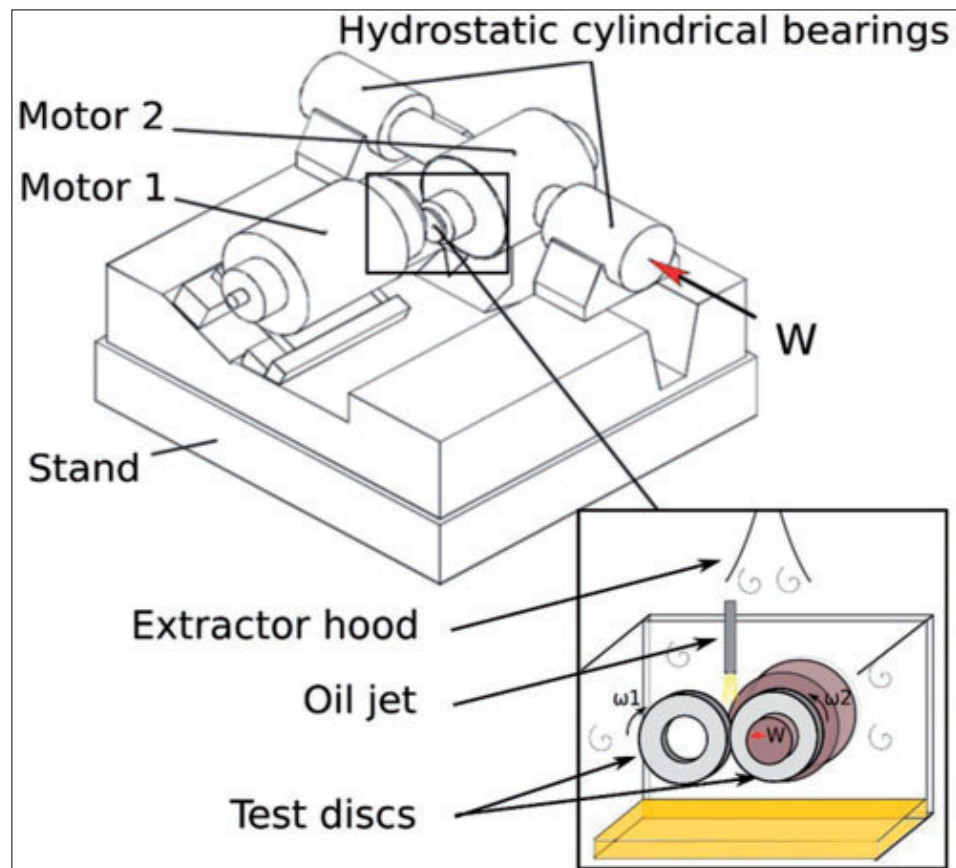


Figure 1-23 Schematic representation of twin disc setup (Isaac, 2018)

The thermal network methodology comprises separate nodal analysis which associates the heat generation due to the loss of power to the thermal dissipations. The author has subdivided the twin disc machine into 18 isothermal elements. Each

isothermal element represents a part of the twin disc machine as shown in table 1-2 below.

Table 1-2 List of elements (Isaac, 2018)

Number	Element Reference
1	The air outside the housing
2	Oil inlet
3-4	Rolling bearing
5	The air inside the housing
6	Oil Jet
7	Oil outlet
8	Contact
9-10	Discs
11-16	Housing
17-18	Shafts

They are connected through the characteristics of thermal resistance, and each resistance represents the type of heat transfer at the specific location for an example, conduction, convection, or radiation as shown in Figure 1-24.

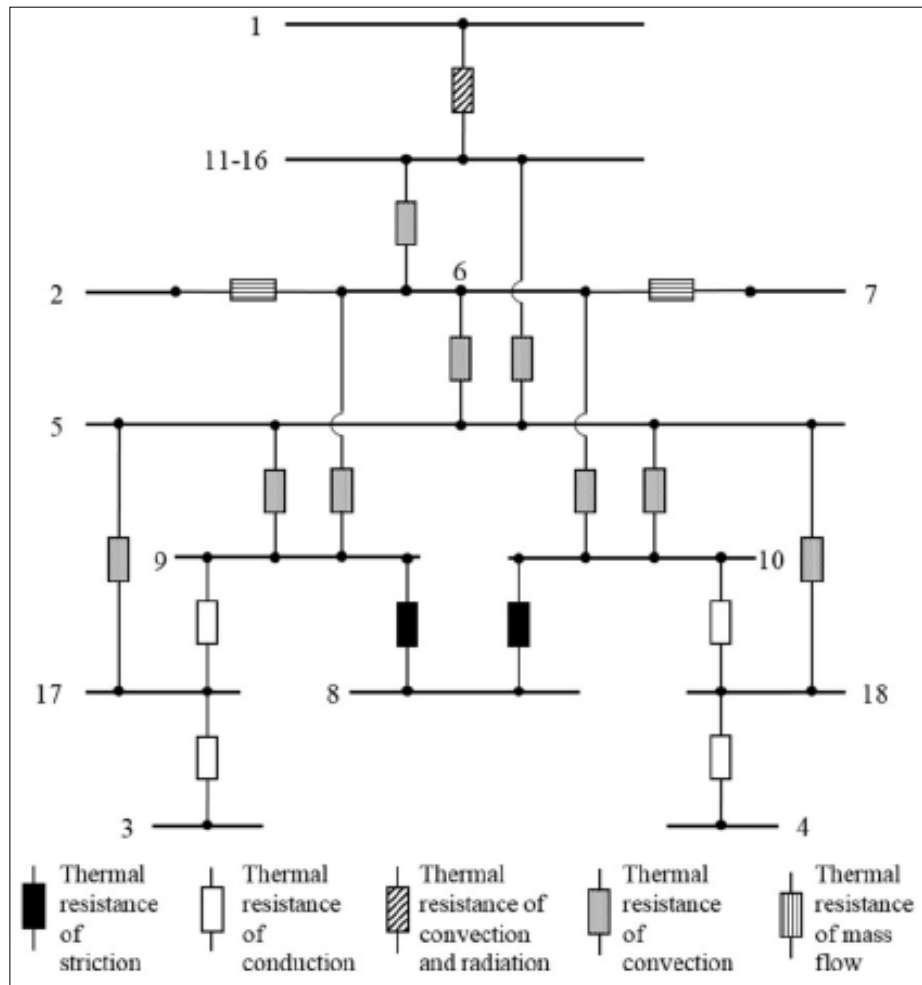


Figure 1-24 Thermal network of twin disc machine (Isaac, 2018)

Figure 1-25 shows the evolution of the temperature during the traction tests (Isaac *et al.*, 2018). The tests were carried out using the twin disc machine testing rig with the pressure applied during the test. The experiment was carried out for three traction tests using the following conditions: polished discs ($R_a = 0.05 \mu\text{m}$), oil inlet temperature was set to 80°C , mean rolling speed was set to 30 m/s , Slide-to-Roll Ratio (SRR) varied between 0% and 20%, whereas Hertzian pressure for three tests was maintained at 1.1, 1.5 and 1.8 GPa respectively. For the sake of clear understanding, the author has presented the disc bulk, oil outlet and inlet temperatures only on the graph. The evolution of the bulk temperature confirms and

shows a good agreement with those simulated using the thermal network methodology that has a much reduced computational time.

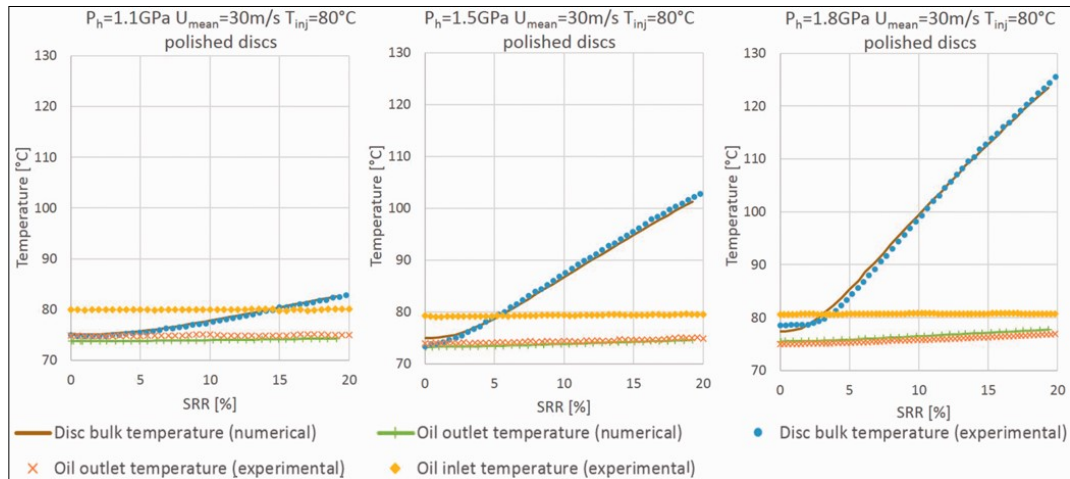


Figure 1-25 Temperature evolution during traction tests (Isaac, 2018)

From Figure 1-25, the oil outlet temperature is lower in all the three tests as compared to the oil inlet temperature. This is because of the housing size and the large amount of heat exchanged with ambient air, where forced convection between the casing and flow of oil is generated due to the oil projected by the discs. Also, forced convection is caused by the air extractor between the casing and ambient air which causes the cooling effect on the housing.

The results of the traction tests in Figure 1-26 show that thermal flow can have a significant influence on the measured coefficient of friction even at low SRR. Due to shearing within the contact, the heat transfer occurs from the oil to the discs. The discrepancies were observed between the traction test performed in sequence and the existing applications such as gear transmission due to the heat transfer. According to the author, Diab's frictional calculation correlates well with the experimental finding when disc bulk temperature is used instead of oil inlet temperature.

Diab's friction model:

$$T_{Contact} = T_{Bulk} + \Delta T_{Flash}$$

T_{Flash} = Temperature rise inside the contact

T_{Bulk} = Bulk temperature of the concerned element

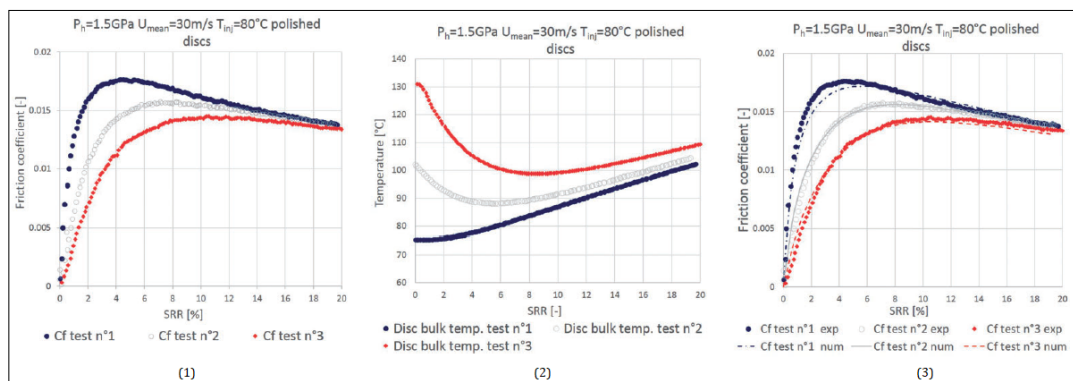


Figure 1-26 (1) Evolution of friction with slide to roll ratio (2) Evolution of the calculated disc temperature with slide to roll ratio (3) Evolution of friction using the calculated disc bulk temperature (Isaac, 2018)

Three scuffing tests were carried out and shown in Figure 1-27. The two tests in Figure 1-27 (1) have identical operating conditions: a Hertzian pressure set to 1.5 GPa, 22 m/s rolling speed, oil inlet temperature set to 80 °C, and rough disc ($R_a = 0.4 \mu\text{m}$) located perpendicular to the sliding direction, where the third test in Figure 1-27 (2) and (3) has a different oil inlet temperature that is set to 100 °C. The hypothesis made for the experiment is that ‘scuffing should appear sooner for a hotter oil injection’. However, thermal analysis of the scuffing test shows opposite results. There is no relation between the determination of scuffing and the oil inlet temperature. However, the difference between the oil inlet temperature and the bulk temperature are very important when the power losses at the contact are significant.

Therefore, in this situation, use of inlet temperature to determine the thickness of film within the contact is not characteristic.

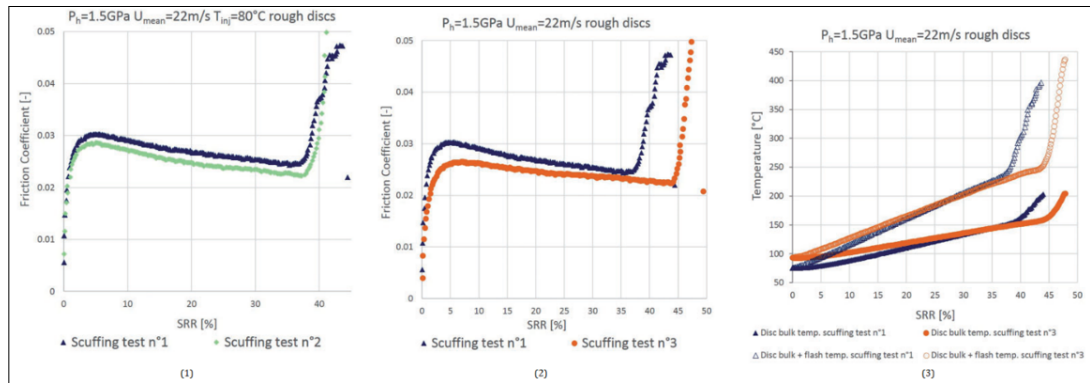


Figure 1-27 (1) Evolution of friction during identical scuffing test (2) Comparison of scuffing test with different oil temperature (3) Evolution of disc bulk temperature with side to side roll (Isaac, 2018)

1.8.2 FZG disc testing

Miyata *et al.*, (2008) used an FZG twin-disc test rig shown in Figure 1-28 to measure the temperature distributions in an elliptical contact area within EHL sliding/rolling conditions such as those in Continuously Variable Transmission (CVT) using thin-film sensors.

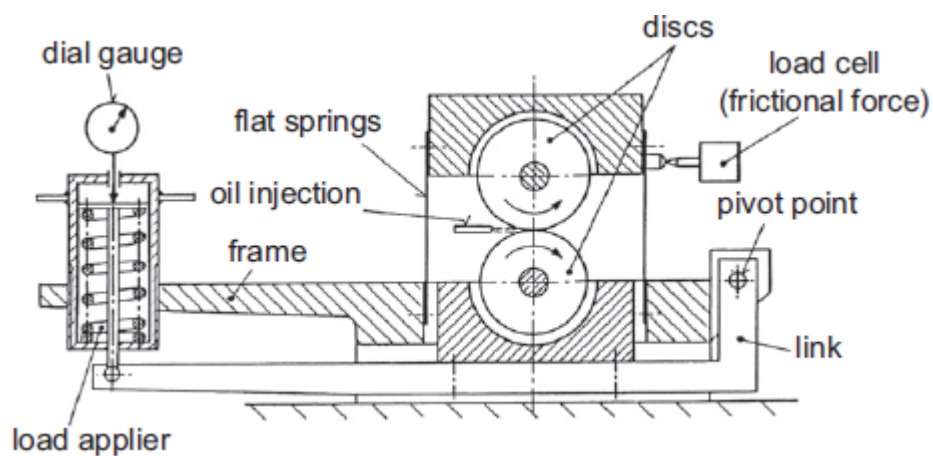


Figure 1-28 Schematic of the FZG test rig (Miyata *et al.*, 2008)

Two discs made of case-carbonised steel were press-fitted onto each shaft, these shafts were driven independently by electric motors, and the desired slip ratio achieved by means of CVTs mounted between the motors and the shafts. The velocity of each disc, frictional force and the normal force were measured. A traction fluid, Santotrac 50 was used as lubricant and its temperature was maintained with a constant temperature at the inlet of the contacting zone. Figure 1-29 shows a photograph and drawing of the thin-film sensor on the disc surface which was used to measure the temperature distribution in an elliptical contact under the EHL conditions.

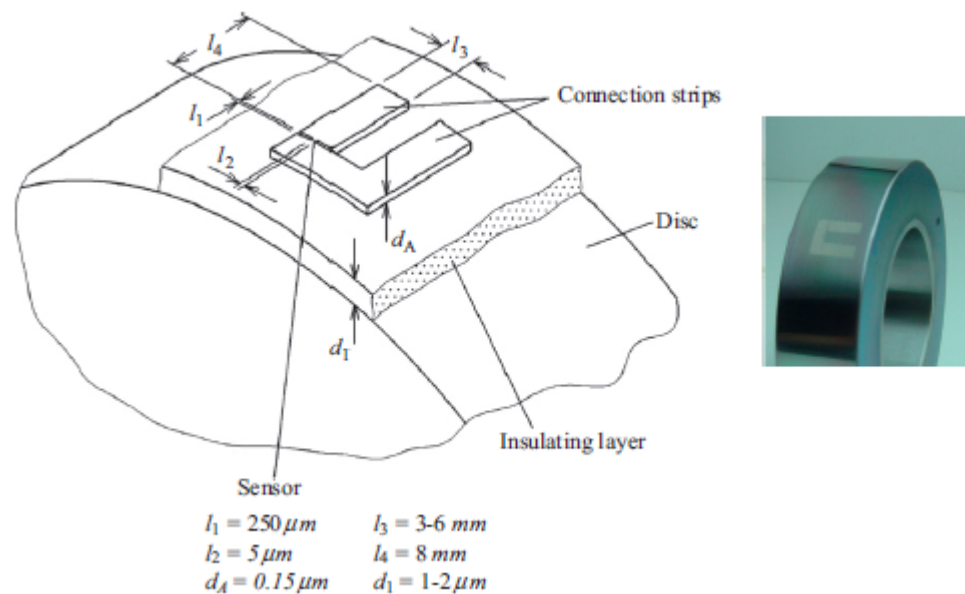


Figure 1-29 Photograph and drawing of thin-film sensor on the disc (Miyata *et al.*, 2008)

Figure 1-30 shows a drawing of the disc configurations tested. Disc combination (a) was used for the test under no-spin motion conditions, and disc combination (b) was used for the test under spin motion conditions. The spin motion conditions were achieved by using the conical design (V shape) of the disc with angle of 30° and only the radial force was generated where the axial force was neglected

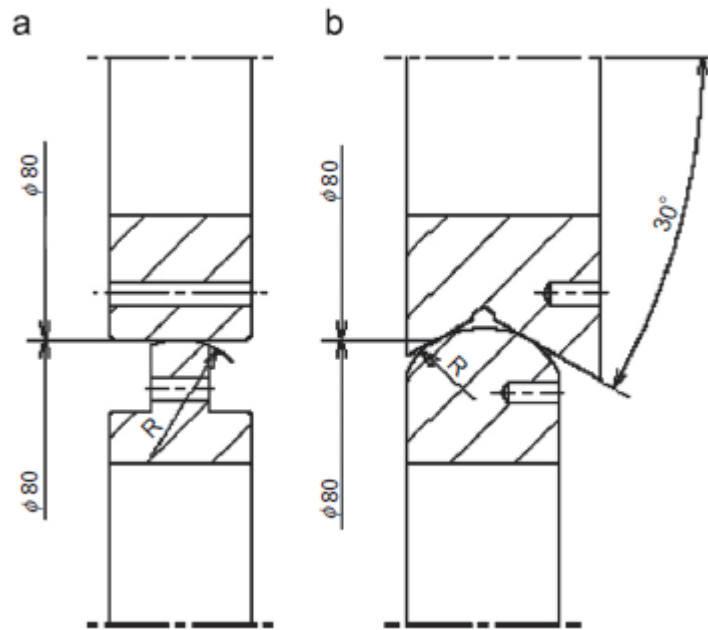


Figure 1-30 Drawing of the disc combinations (Miyata *et al.*, 2008)

Platinum Resistance Thermometers (PRTs) were used to measure the bulk temperature of the discs. Different maximum Hertzian pressure values of 980, 1260 and 1500 MPa were used during the experiments with different sliding speeds 5, 10 and 12 m/s.

They found that in an elliptical contact, the increase in temperature is growing in proportion with pressure, slip and circumferential speed. Also, with slow sliding speed conditions, the increase in temperature is more significant under spin motion, where with faster sliding speed conditions the difference in temperatures between them is decreased (Miyata *et al.*, 2008).

Ebner *et al.*, (2018) used the same twin-disc test rig to measure the temperature under the EHL conditions using the thin-film sensor in order to investigate the thermal insulation effects within the EHL contacts. In these tests, the frictional force and speed of the surfaces were measured, the bulk temperature of the lower disc was measured

by a resistance temperature sensor located 5 mm below the disc surface. The contact region was lubricated using an oil delivery point located close to the discs. The upper test disc was replaced with a ceramic sensor disc either made from Zirconium dioxide (ZrO_2) or Aluminum Oxide (Al_2O_3), and thin film sensors made from Platinum were installed on the surface of this disc. The lower disc which is paired with the upper disc was made from case-carburized steel with or without a Diamond-like Carbon (DLC) coating. The drawing and configuration of these discs are shown in Figure 1-31.

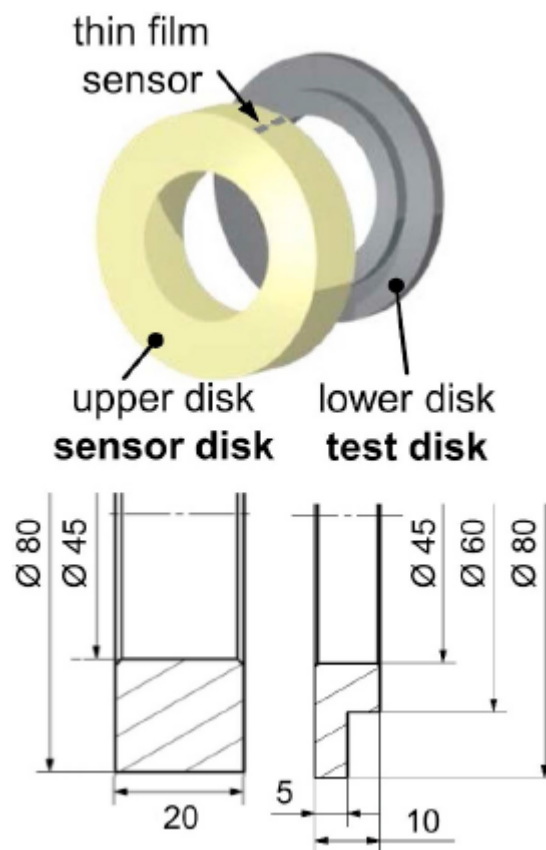


Figure 1-31 Drawing and configuration of the sensor and test discs (Ebner *et al.*, 2018)

The experiments were carried out under line contact conditions at two maximum Hertzian pressures, 600 or 1000 MPa, and sliding speeds of 8 or 16 m/s. As a summary of their work, significant different thermal inertias were shown by changing

the sensor disc material which is paired with the uncoated or DLC-coated steel test discs. This showed that the thermal insulation effects using different sensor disc materials has an influence on the measured temperature and the fluid friction during the EHL experiment. The data obtained from the EHL experiment were analysed using a Thermal EHL (TEHL) simulation model, and the results showed a good agreement between these simulated data and those measured during the EHL experiment. The model confirmed the importance of the thermal insulation effects and clarified the significance of the position and dimension of the sensor. For the considered disc pairs, the thin film sensor reflects the temperature near the surface of the sensor disc, which explains why that the DLC-coated discs do not considerably influence on the temperature measured during the EHL experiment. Nevertheless, due to the DLC coating, the thermal insulation effects are still present and were shown by the TEHL model, which showed a good agreement with the temperatures measured during the EHL experiment in an absolute and relative terms (Ebneret *al.*, 2018).

1.9 Development of Patching test rig to measure the heat partition

Clarke (2009) carried out an investigation on heat partition in elastohydrodynamic sliding contacts under full film lubrication conditions. The aim of this work was to explore the generation of frictional heat divided between the contacting bodies by shearing of lubricant at rolling/sliding elastohydrodynamic contacts. Due to the effects of temperature increase on viscosity of the lubricant at the inlet zone which has a consequent effect on the film thickness, it is necessary to have knowledge of the surface temperatures of the contacting bodies (Clarke, 2009).

Previously used to study scuffing, a two-disc test rig was modified in order to allow the measurement of the temperature of the disc at six sub surface locations in each

disc. This was achieved by using embedded thermocouples which were calibrated carefully. To understand the heat partition behaviour of elastohydrodynamic lubrication contacts, it was required to make these changes and modifications to the original test rig used by Patching (1994). The brief outline of some changes is given below.

- 1) Each disc is fitted with additional thermocouples giving a total of 6 thermocouples per disc at different positions near the running track. Using additional thermocouples removes the need to thermally model the whole disc and shaft assembly while computing the heat partition parameter β , which was necessary when simulating the earlier experiments of Patching (Clarke, 2009).
- 2) Insulating washers are fitted to each side of the test discs, this minimises the axial heat flow from the sides of the discs. The modelling of the heat transfer boundary conditions becomes easier as the flow of heat is reduced by the washer from the sides of the disc. Due to this arrangement it is required to determine only one heat transfer coefficient and that is from the running track of the disc, this achieved by using a run-down test which is measured and shown in Figure 1-32 below.

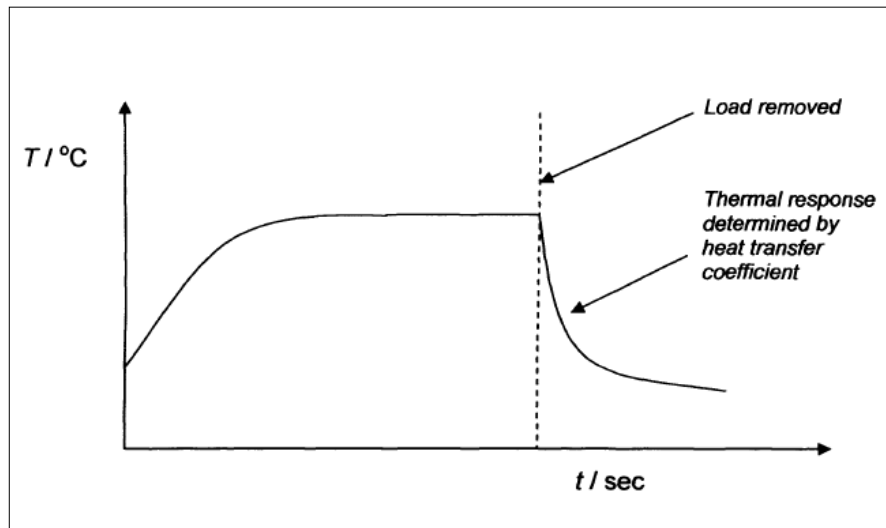


Figure 1-32 Run-down test to establish heat transfer coefficient (Clarke, 2009)

- 3) New computer-based data acquisition and control system has been developed and installed.

By using synthetic gas turbine oil (Mobil Jet 2), a series of tests were conducted at a range of maximum Hertzian contact pressures between 1 and 1.6 GPa and sliding speeds from 10 to 20 m/s, at a slide/roll ratio of 1.24. The speed was fixed in each experiment and then load was applied. The discs were run together under the specified loading until they reached steady state temperature conditions. The load was then removed and the discs brought out of contact by small separation, which gives independent convective heat transfer from the running track of each disc. The frictional heat input to the discs stops after the removal of the load so there is no heating during the cooling of the discs. The discs were allowed to run until they cooled to the surrounding temperature. The data obtained during these experiments were analysed by using a two-dimensional conduction model for the outside region of the disc, this attempted to achieve the best similarity between the measured and calculated temperatures. To achieve this objective the partition of heat between the discs was adjusted along with the level of forced convection from the disc surface

until the temperature of the loaded phase and cooling phase of the test are closest to experimental measurements. The analysis showed that the heat partition favours the faster disc, and around 60% of the total frictional heat dissipated into the faster disc (Clarke, 2009).

During a range of thermal elastohydrodynamic analyses performed by using different rheological and viscosity models, it was determined that the heat partition predicted by the thermal elastohydrodynamic analysis approached that obtained during experiment only when the maximum heat was dissipated by slip or near to the fast surface (Clarke, 2009). These circumstances only happened when a limiting shear stress rheological model was used in combination with the Barus viscosity model. However, it was found that the results of the fast disc were inconsistent. This was validated during the numerical analysis of the results of fast disc. According to Clarke (2009), significant work needed to be carried out to eliminate these inconsistencies as fast disc temperatures were not reliable. Clarke had conducted various tests to find out the source of error, repeat tests were performed along with corrections in instrumentation used such as connections of fast discs temperature were swapped with computer using slow disc instrumentation and vice versa. The results of these repeat test showed that the slow disc continued to be consistent which affirmed that the instrumentation was not the cause of the error but the origin of the error lay in the thermocouples or in the slip rings and wiring within the shaft and disc (Clarke, 2009). The investigation by Clarke suggested that the problems with the fast disc measurement, could be eliminated by the combination of the thermal elastohydrodynamic modelling, modified suitable instrumented disc machine and detailed heat partition analysis. This offers a means of analysing rheological as well as traction behaviour of the lubricants used in elastohydrodynamic lubrication contacts. According to Clarke (2009), the approach developed has a tremendous

potential to become an essential technique for comparing elastohydrodynamic lubrication rheological models as compared to the simple conventional approach of friction measurement in elastohydrodynamic lubrication in sliding and rolling contacts, which fails to adequately discern between different rheological and piezoviscous models.

Al-Hamood (2015) conducted similar experiments to analyse heat generation and partition between contacting bodies under sliding and rolling elastohydrodynamic lubrication contacts. The test rig previously used by Clarke was re-commissioned and used for the test work. The test machine consists of 76.2 mm crowned and super finished test discs which were fixed on the parallel shafts. Similar to the model used in Clarke, these test discs were equipped with 6 thermocouples to measure the temperature during rolling/sliding elastohydrodynamic lubrication condition. To minimize the heat transfer over flat surface of the disc, a ceramic washer was fixed on the plane sides of each disc. To acquire data from the sensors installed on the rig, a LabVIEW data acquisition system was used. Several test runs are carried out on the test rig in order to obtain the results of elastohydrodynamic lubrication experiment which showed that the slow disc has significantly lower bulk temperature than the fast disc. A transient two-dimensional numerical model was constructed to determine the average circumferential temperature distribution by using three thermocouples within the disc as boundary conditions (Al-Hamood, 2015). It was observed that for each disc the best fit to experiment was obtained when the heat partition factor as well as convection heat transfer coefficient were varied steadily in the model. Linear relationships between the convective heat transfer coefficient h_f and heat partition factor β for the fast disc, and h_s and $1-\beta$ for slow disc were determined. On the other hand, to carry out transient modelling, the mechanism for unloading was developed to ensure quick separation of the discs. This helps to improve the trend of temperature

in the cooling stage. A micro switch was used in the experimental set up to provide accurate monitoring of the disc contact and separation. Also, the arrangement of thermocouples within the discs was modified after careful assessment. A hot oil bath was used for an immersion test which determined the dynamic response of the thermocouples. Significant lag in measurement was found during the modelled test. It was analysed by Al-Hamood (2015) that the system identification method was required to recognise the dynamic characteristics of the temperature measurement system to compensate for time lagging. The cause behind the uncertainties in measurement was suggested to be circumferential variation in the interfacial pressure along the interference fit between the shaft and the discs. The pressure variation resulted in a substantial circumferential change in the thermal conductance along the fit (Al-Hamood, 2015).

1.10 Aims and objectives

The need to determine the heat partition β in the EHL rolling/sliding contacts is the main purpose of this work. The heat transfer coefficient for the slow disc h_s and the fast disc h_f should be known in order to identify the heat partition β from an experiment. The surface temperatures and the surface heat flux are found as part of the solution in a thermal EHL analysis. Hence, the heat partition β is not imposed, but is a result of the analysis that depends on the rheological behaviour of the lubricant. If the heat partition β can be identified independently of the EHL analysis, it can be used to validate thermal EHL analyses and to identify the actual rheological properties of the lubricant within the contact. Finding β from experiments shows that the lubricant behaves according to a non-Newtonian limiting shear stress model, and this is demonstrated by Clarke *et al.*, (2007)

The initial aims and objectives:

- 1) To study the thermal behaviour of a twin-disc test rig in EHL rolling/sliding contact conditions and the concept of heat partition between the discs.
- 2) To develop the test rig further so as to remedy some of its difficulties and perform heat partition experiments with a range of lubricants.
- 3) To develop a thermal model of the test discs to interpret the experimental results and calculate heat partition.
- 4) To conduct EHL simulations and compare with experimental results.

During the development of the test rig to achieve the second point of the aims and objectives, practical difficulties with the instrumentation were encountered which led to re-design of the electrical processing of temperature measurements using on-shaft thermocouple amplifiers. However, this was not resolved due to technical staff changes which reduced the availability of electrical support.

This led to greater emphasis on the third point of the initial aims and objectives so that the final aims and objectives became:

- 1) To study the thermal behaviour of a twin-disc test rig in EHL rolling/sliding contact conditions and the concept of heat partition between the discs.
- 2) To develop the test rig further, by designing new integral shafts and test discs, new on-shaft processing of thermocouple signals, and modifying the position of the slip rings.
- 3) To develop a thermal model of the test discs to interpret the experimental results and calculate heat partition.
- 4) To develop a robust method to deduce the experimental heat partition and heat transfer parameters based only on the experimental temperature distribution.

- 5) To determine the effects of thermocouple noise and resolution on the results and identify the requirements for effective on-shaft processing of thermocouple signals.

Chapter 2 A twin-disc test rig for investigating the friction and heat generation in the EHL regime

2.1 Introduction

In this chapter, a general overview of the twin-disc test rig is described, followed by the history of construction and development of this test rig, which was used by Patching (1994) to carry out an investigation of scuffing failure of a surfaces in rolling sliding contact for conditions replicating those in gas turbine auxiliary gearing applications. The procedure for carrying out an experiment is also described. Then it outlines the modifications and developments made by Clarke (2009) and Al-Hamood (2015) to carry out experiments to investigate the heat partition and thermal behaviour in the EHL contact rather than the scuffing failure of a surface.

2.2 Description of the twin-disc test rig

Initially, the rig was designed in collaboration with Rolls-Royce, with the aim of replicating the typically found aerospace gear meshes such as side/roll ratios, entraining speeds and contact pressure. The initial rig specification is illustrated in Table 2-1 below:

Table 2-1 Specification of the rig from (Patching, 1994)

Sliding Speed	25 m/s maximum
Hertzian contact pressure	1.7 GPa maximum
Oil feed temperature	100°C typical, 200°C maximum
Lubricant	Mobil Jet 2 (synthetic)
Disc material	Case-carburizing alloy steel to Rolls-Royce specification 6010
Heat treatment	Case-carburized, hardened and tempered to Rolls-Royce specification (RPS 371)
Surface finish	Final grinding to 0.4 μm Ra, transverse to direction of entrainment

A general overview of the test rig is shown in Figure 2-1 below, also the test rig layout along with associated drives is shown in Figure 2-2, where Figures 2-3 and 2-4 show the isometric projection and the test head layout respectively.

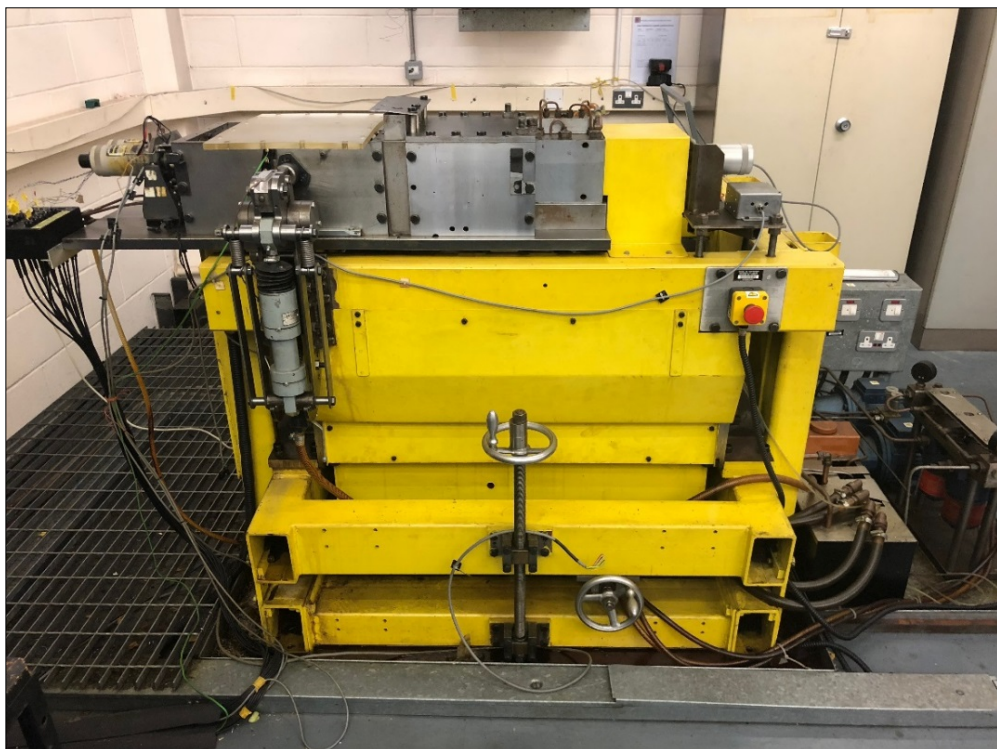


Figure 2-1 Photograph of the test rig

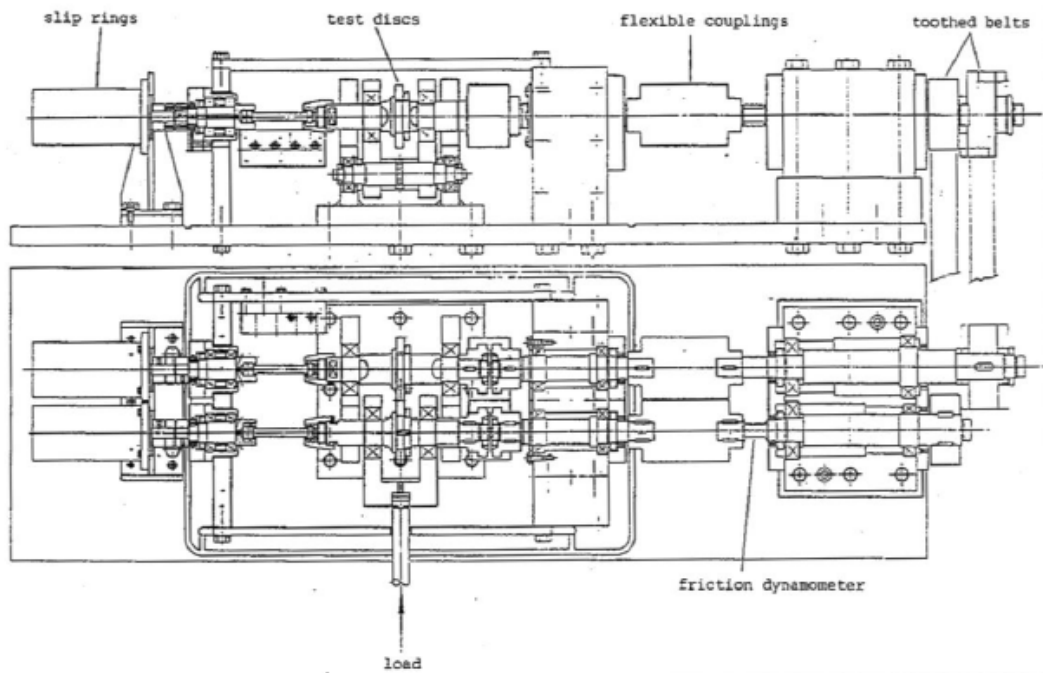


Figure 2-2 Test head layout with associated drive (Patching, 1994)

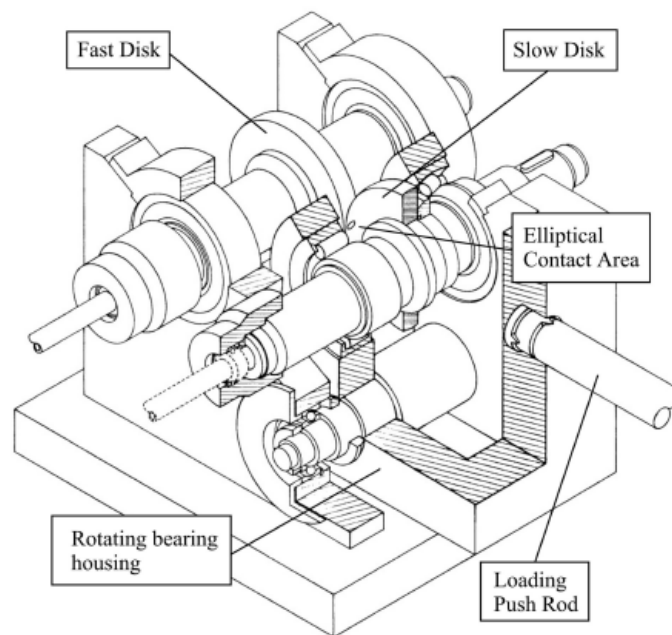


Figure 2-3 Isometric view of test head (Patching, 1995)

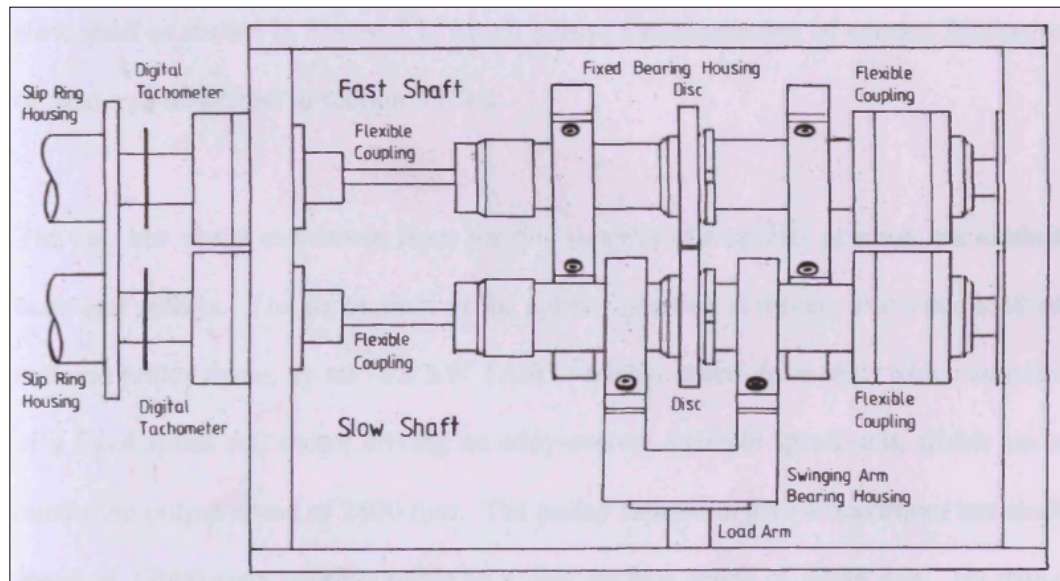


Figure 2-4 Test head layout (Patching, 1994)

The test rig was constructed to examine scuffing failure of a surface, typically in gas turbine auxiliary drive gearing under a range of sliding speeds and loads. A series of scuffing experiments has been conducted using this test rig (Snidle & Evans, H.P., 1990). The rig has the capability to avoid damaging edge effects due to the self-aligning crowned disc configuration adopted, and also has the capability to operate under high load and sliding conditions.

As the rig operates at high speeds, rolling element bearings are used to support the shafts that carry the test discs to minimize the frictional losses. Double row spherical roller bearings are installed for each shaft at one end to provide axial and radial restraint. At the other end of the shaft, cylindrical roller bearings are used to provide radial restraint. This arrangement allows high radial load capacities with axial thermal expansion of the shafts. The shafts are manufactured from EN36C steel, which is case hardened to 680 Hv. To ensure higher concentricity, these shafts were ground finished between the dead centres. Depending on the manufacturing tolerances, a heavy diametral interference fit is used to press the discs onto the shaft. In addition,

a locking nut is used to ensure the discs are constrained should the frictional forces exceed the restraining action of the interference fit. The shafts are drilled with central and radial holes where the thermocouples pass through to measure the temperature of the discs. The original discs were fitted with one thermocouple per disc to measure and monitor the approximate bulk temperature, which are located on the centre line of the running track, approximately 3 mm below the surface of the discs. The slow shaft is equipped with a friction dynamometer as shown in Figure 2-2. The friction dynamometer measures the torque in the shaft which enables the contact friction to be determined. A splitter gearbox is used to drive these two shafts by means of toothed belts and pulleys. These belts and pulleys are driven by a variable speed TASC drive unit (18.5 kW), which has a fixed speed AC motor to drive an eddy current variable speed unit with maximum speed of 2800 rpm. A maximum test shaft speed up to 12000 rpm can be reached by the available pulley ratios, which corresponds to a disc surface speed of 47.88 m/s.

The test shaft speed ratios available vary between 1 (pure rolling) and 4.24. These are achieved by using different pulleys on the connection between the test shafts and the splitter gearbox. The two disc surfaces move in the same direction as a result of rotating their shafts in opposite directions.

When two surfaces are subjected to rolling/sliding motion where their velocities are u_1 and u_2 , the sliding speed is then:

$$u_s = u_1 - u_2$$

Also, the mean entraining (or rolling) velocity is expressed as:

$$u_r = \frac{u_1 + u_2}{2}$$

Therefore, the sliding/rolling ratio can be written as:

$$\frac{u_s}{u_r} = \frac{2(u_1 - u_2)}{(u_1 + u_2)}$$

The previous equation can be re-written in terms of the gear ratio G (at the splitter gearbox) between the shafts as:

$$\frac{u_s}{u_r} = \frac{2(G - 1)}{(G + 1)}$$

In this work, the highest gear ratio delivered by the combination of the pulleys in the test rig is 4.24, which gives a sliding/rolling ratio of 1.24.

The maximum load applied at the contact is equal to 4 kN, this is a Hertzian contact pressure of 1.7 GPa for the test discs. A hydraulic cylinder delivers that load by the mean of a bell-crank system and a push rod as shown in Figure 2-5 below. The slower shaft is attached to a swinging arm (yoke) and the load is transmitted to this arm via the push rod. Crossed knife edges are used to apply the load to the yoke with a controlled line of action as shown in Figure 2-4. The applied load is measured by a load cell that is fixed on the bell-crank lever system.

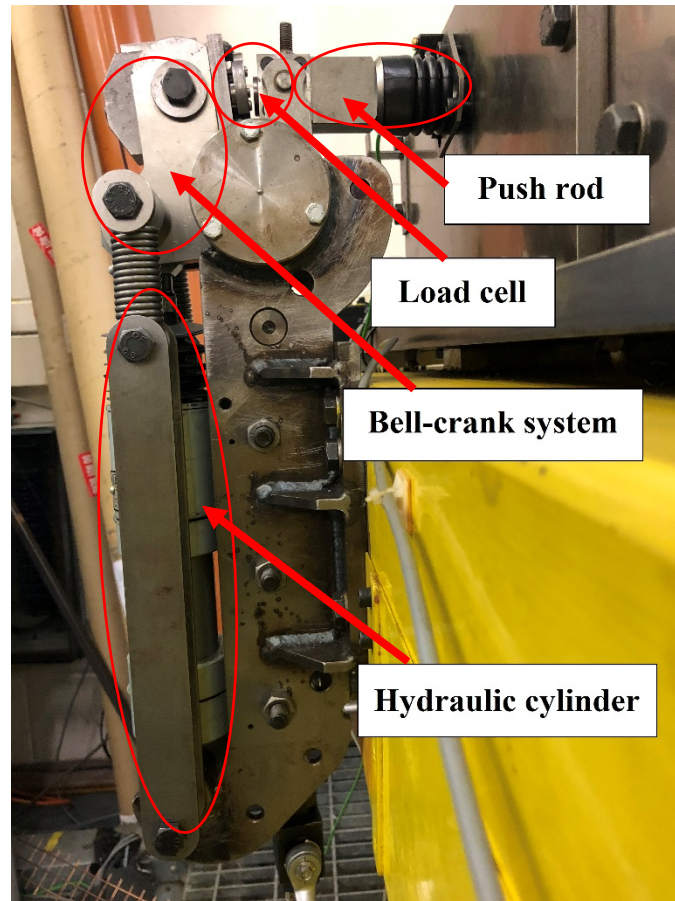


Figure 2-5 Hydraulic system for loading

A constant displacement pump delivers the lubricating oil to the test discs and support bearings in the test head. This oil is kept in a reservoir that is electrically heated and can be controlled to maintain the oil temperature at set values from above ambient temperature up to 200 °C. The oil supply line is fitted with a 1 μm filter.

2.3 Test discs

The test discs that are mounted on the shafts of this test rig are 76.2 mm (3") in diameter and 9.53 mm in width, they have a 304.8 mm (12") crown radius, which is the standard geometry used in most of the disc machines at Cardiff University. Figure 2-6 below shows the drawing of the test discs.

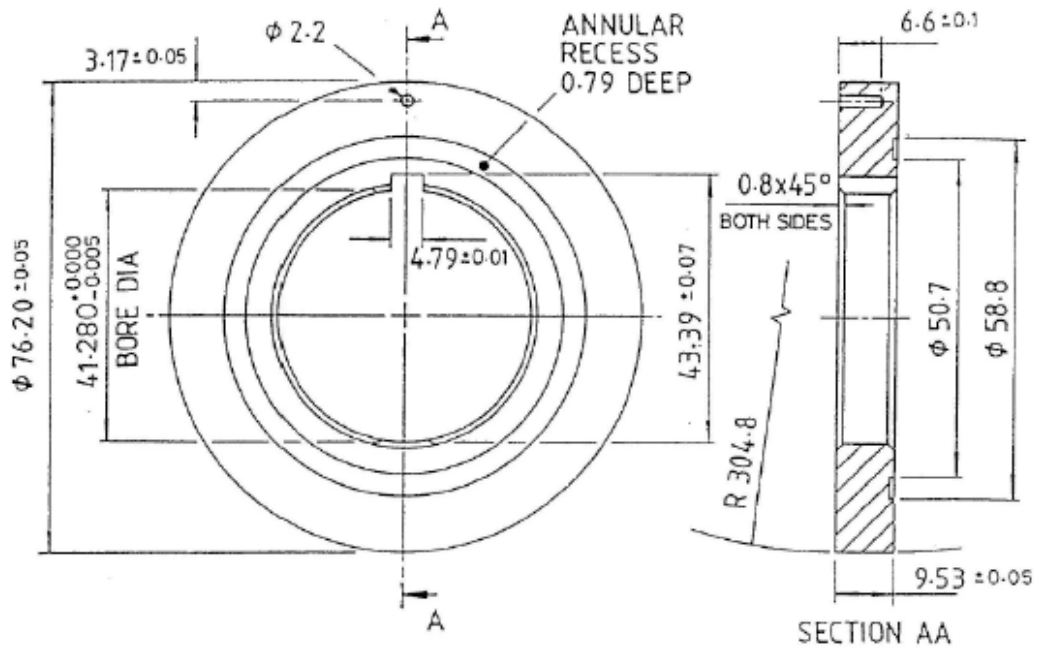


Figure 2-6 Dimensions of the test in mm (Patching, 1994)

The composition of the discs that are made from Rolls-Royce RR6010 steel is listed below in Table 2-2. The discs are subjected to heat treatment that is a standard aerospace specification, and then they are ground and to a standard roughness (R_a) of $0.04 \mu\text{m}$. Some discs are super finished following the final grinding to provide smooth surfaces for comparative studies of roughness effects.

Table 2-2 Composition of RR6010 steel (% mass)

Element	C	Si	Mn	P	S	Ni	Cr	Mo
Max	0.18	0.35	0.55	0.015	0.012	4.30	1.40	0.30
Min	0.14	0.10	0.25	0.0	0.0	3.80	1.00	0.20

2.4 History of the test rig

As mentioned previously, the test rig used in this work was built and commissioned by Patching *et al.*, (1995). He carried out a series of experiments to examine scuffing failure of surface of aerospace gears. His experiments are fully described in Patching *et al.*, (1995), where an unexpected heat partition behaviour between two surfaces in EHL contact is observed. This motivated Clarke *et al.*, (2006) to carry out investigations on the heat partition and thermal analysis between these surfaces by using the available scuffing test results. Clarke developed to the test rig to carry out these investigations, the modifications by Clarke are fully described in Section 2.4.2. Later, the test rig was subjected to further modifications by Al-Hamood (2015) which are outlined in Section 2.4.3 where he carried out another series of experiments and examined the thermal behaviour between these two surfaces.

2.4.1 Experimental procedure

In this work, the test rig was used again to study the behaviour of the surface temperature of the discs and how the heat is partitioned between these surfaces. A repeat of an EHL experiment reported by Al-Hamood (2015) was carried out. The data obtained from this repeat EHL experiment were analysed to investigate the heat partition β , the heat transfer coefficient for the slow disc h_s and the fast disc h_f , and to compare the results obtained with Al-Hamood's experimental results. The temperature measurements obtained during this repeat EHL experiment were also compared with those obtained by Al-Hamood.

Before starting the repeat EHL experiment, the oil was heated and maintained at 80 °C by means of the oil heaters and stirrers in the rig's lubricant supply system. Once the pre-set operating temperature is reached, the oil was then pumped into the oil

supply network with a constant displacement pump and circulated to the rig components. Thermocouples in the oil tank were used to measure and monitor these temperatures. A warm-up period of between 50 and 60 minutes was adopted to allow the test head temperatures to reach a steady state. Each oil delivery point was visually checked during this period to ensure the lubrication of all bearings.

At the end of the warm-up period, the shafts were brought up to the required test speeds with a small clearance and under zero load. The selected EHL experiment had a 4.24 speed ratio with a speed of 1546 rpm for the slow shaft, and 6555 rpm for the fast shaft, which gave a contact entrainment speed of 20 m/s. The temperatures of the six thermocouples per disc were monitored at this point. Their values changed as a new thermal equilibrium was established for the un-loaded rotating discs. Once the temperatures had stabilised, the EHL experiment could be started.

To begin the experiment data recording was started and the two discs were left running with no load for around 60 seconds. The load was then applied by means of the hydraulic ram. The load was set to 1850 N for the test and once the load was applied, the temperatures within the discs increased rapidly. The load was maintained for 1100 seconds. The load was then removed using the quick release process that ensured that the discs were fully separated. At this point, a rapid drop in the disc temperatures was observed as they cool. The cooling phase continued for a further 1000 seconds over which the disc temperatures returned to steady-state conditions. At this point, the EHL experiment was complete and all the data had been recorded in the data acquisition software. The recorded temperature, load and friction measurements provide the test record and could then be used as input to the numerical model in order to find the heat partition coefficient, β , and the heat transfer coefficients for the slow disc, h_s , and the fast disc, h_f .

2.4.2 Modifications for heat partition measurement

Clarke (2009) carried out modifications to adapt the test rig for investigating the thermal behaviour and heat partition in the EHL contact instead of investigating the surface failure of the discs.

The test discs were subjected to some modifications. Five additional J-type thermocouples (iron/constantan) were fitted to each disc at different positions near the running track, the total number of thermocouples became six per disc instead of the previous single one. Originally, the two J-type thermocouples were fitted to the test discs using copper ferrules, Clarke concluded that using ceramic cement which is an electrical insulator is the most efficient in terms of thermal conductivity and electric connectivity as it is specially made for thermocouple installation. Figure 2-7 shows the schematic layout of the shaft and test disc configuration which shows the new arrangement of the six embedded thermocouples. The central thermocouple in the upper row is at the previous single thermocouple position.

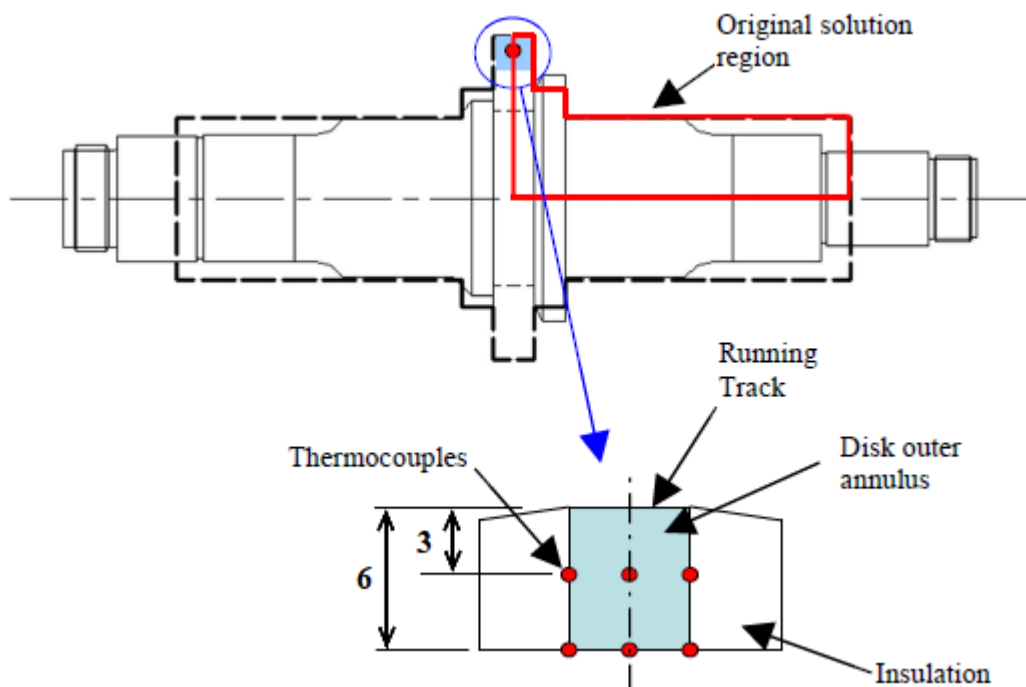


Figure 2-7 Schematic of the shaft and disc showing the thermocouples arrangement (Clarke, 2009)

In each disc, the six thermocouples were fitted in two rows of three as shown in Figure 2-7. The upper row holes are located at 3 mm below the surface of the test disc and the lower row holes are located at 6 mm below the surface. Each row has a middle thermocouple located at the centre line of the running track of the test disc, where the other two thermocouples are approximately 2 mm away from the side surfaces of the test disc.

The position and the depth of the thermocouple holes are shown in Figure 2-8 below, which shows twelve holes per disc. This is to fit a replacement thermocouple in case of failure of any existing thermocouples during the EHL test. It can be noticed also that the holes are located at different circumferential positions, this is to minimise any disturbance caused by the holes to heat conduction in the test disc.

Another modification was made was to install insulating ceramic washers as shown in Figure 2-9. They are fixed on both sides of the test discs in order to minimise the losses of heat in the axial direction from the side faces of the test discs, hence the modelling for the heat transfer boundary condition at the side faces becomes simpler and more accurate. The insulating washer diameter is 76 mm which is slightly smaller than that of the test discs, 76.2 mm. This is to avoid any contact between the insulating washers of one disc with the other ones on the other disc. They insulating discs are attached to the test discs using M3 bolts.

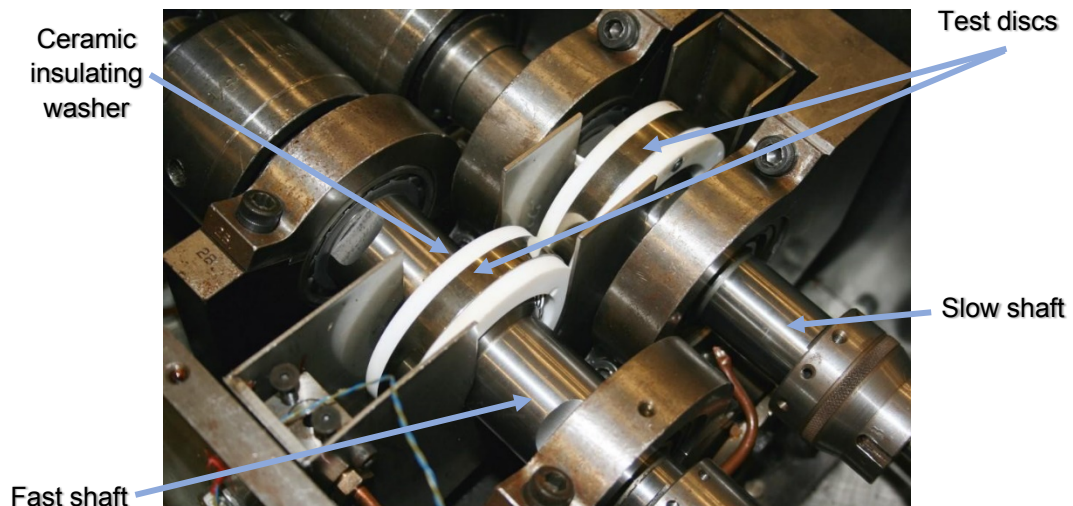


Figure 2-9 Photograph of the test head after installing the ceramic washers (Clarke, 2009)

With regards to signal conditioning of the thermocouples, the test rig was fitted with a 5B-series signal conditioning modules supplied by Analog Devices, where each module is used to condition only one signal as they provide galvanic isolation for the input and output. Figure 2-10 and 2-11 show the thermocouple signal conditioning module and the configuration of 5B-series modules used for the test rig.



Figure 2-10 5B module for thermocouple signal conditioning

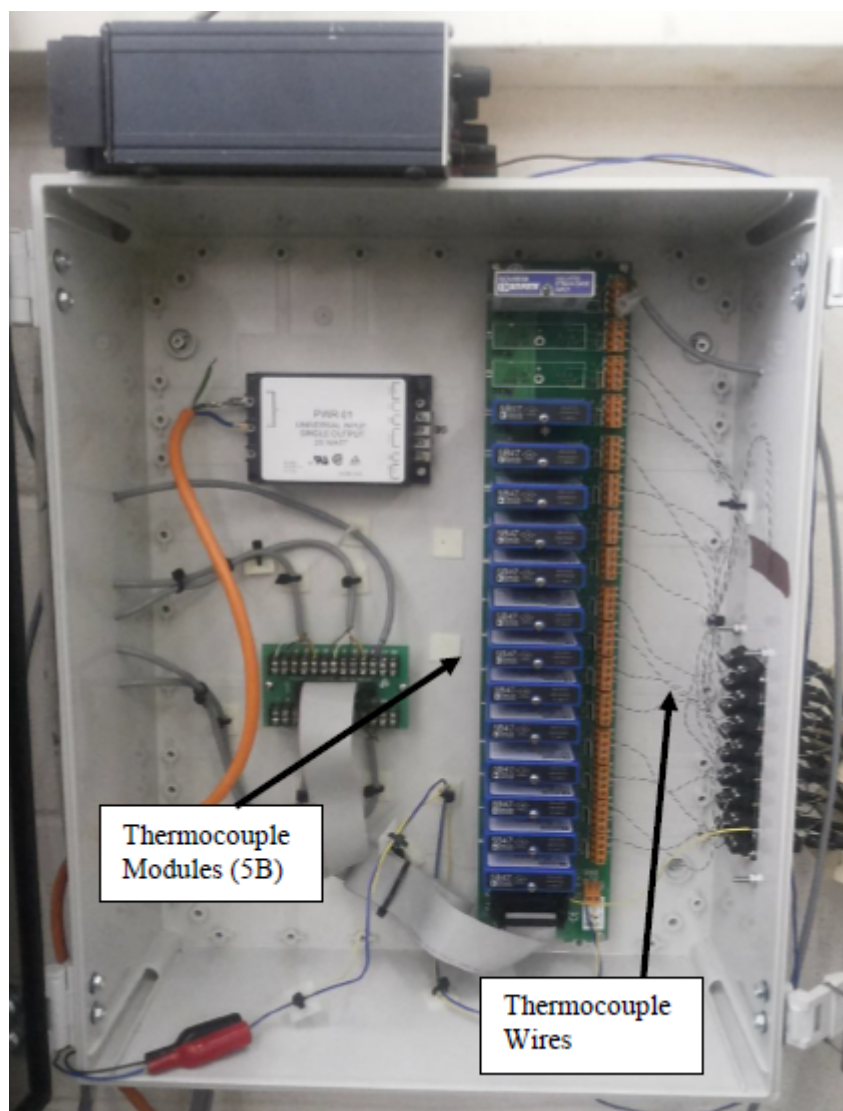


Figure 2-11 Photograph of 5B-series thermocouple signal conditioning modules (Al-Hamood, 2015)

The data acquisition and control systems were also modified, a new PC-based system was developed and installed for the test rig using LabVIEW 7 to write the data acquisition system, which is specifically configured for development of the data acquisition and control systems. The data are recorded and logged using a data acquisition card (National Instruments 6030-E) which is used for interfacing the electronic instruments on the test rig with the PC. Figure 2-12 below, shows the inputs and outputs used in the system.

Signal	Type	Description
Disk Temperatures (12 channels)	Thermocouple Analogue Input	6 J-Type thermocouple signals per disk
Disk oil delivery temperature	Thermocouple Analogue Input	J-Type thermocouple
Applied Load	Voltage Analogue Input	Load Cell
Friction	Voltage Analogue Input	Strain gauge torque transducer
Fast shaft speed	Digital Input	TTL signal from Optical Sensor
Slow shaft speed	Digital Input	TTL signal from Optical Sensor
Motor speed control	Analogue Output	Signal to control TASC drive unit
Load control	Analogue Output	Signal to control hydraulic proportional valve

Figure 2-12 Inputs and outputs to Data acquisition system (Clarke, 2009)

2.4.3 Further modifications

Further developments were carried out by Al-Hamood (2015) on the test rig. He carried out investigations on the unloading process and improved the mechanism to

ensure a faster separation of the test discs in the unloading stage. This was important as he used the cooling phase in his analyses and the time at which the load was removed was an important parameter in the modelling approach. Figure 2-13 below shows a drawing of the hydraulic loading/unloading system after this modification.

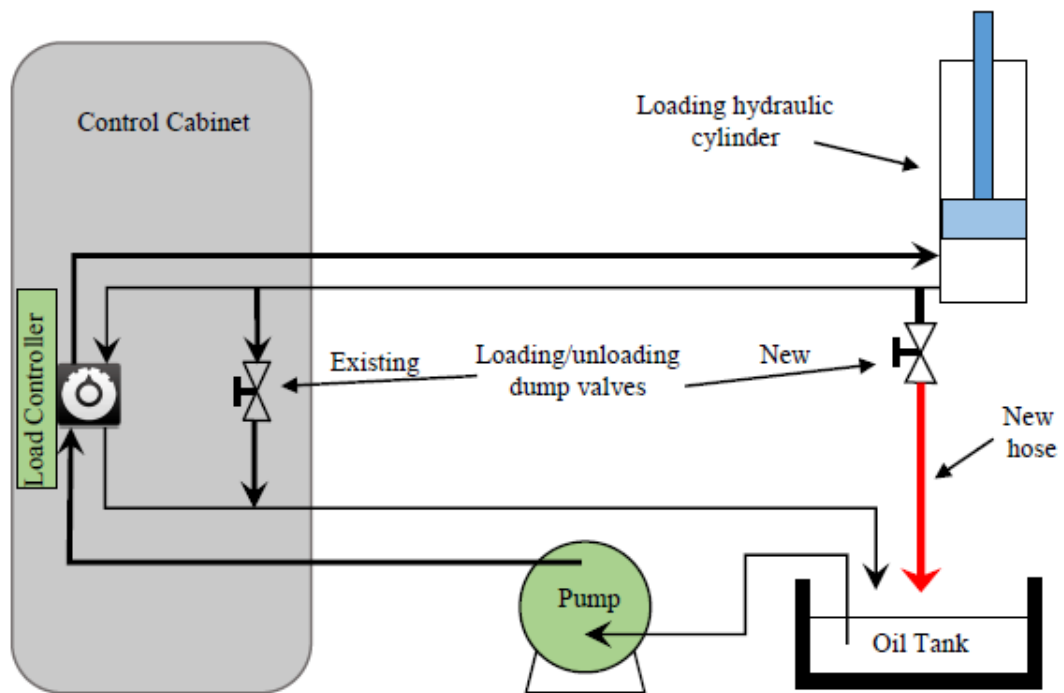


Figure 2-13 Schematic drawing of the hydraulic loading/unloading system (Al-Hamood, 2015)

Also, monitoring the separation of the discs was improved by upgrading the detection microswitch which gave a more consistent indication of separation time.

An additional hardware development was carried out for the data acquisition system, where the new National Instrument NI9213 module has been introduced and fitted to NI cDAQ-9174 Four-slot USB chassis to allow more measurements to be logged during the EHL experiments.

The most important improvement made by Al-Hamood, was the thermocouple installation developments. Firstly, he showed that a 1.3 mm hole diameter for the thermocouples is the optimal diameter rather than the 2.2 mm size used previously. Secondly, he showed that fitting an additional thermocouple per test disc near the surface in the centre line of the running track will give a higher range of temperature variation and better temperature discrimination, which can be adopted for error minimization in the conduction modelling. Finally, the thermocouples' arrangement within the test discs was modified compared to the previous investigations, where thermocouple at position *e* in Figure 2-14 was relocated at the new centre line position 1.25 mm from the surface of the test disc. As this surface is subjected to high load during the EHL tests, it is necessary when making the new holes to consider the expected point at which the plastic yielding first occurs. Accordingly, the best position of the new 1.3 mm diameter hole was calculated to be with its centre 1.25 mm below the surface. Figure 2-14 shows the final arrangement of the thermocouples within the test disc made by Al-Hamood. Also, in the current work, this configuration was used for the repeat experiment. Further analyses aimed at optimising the positions of thermocouple are described in Chapter 5.

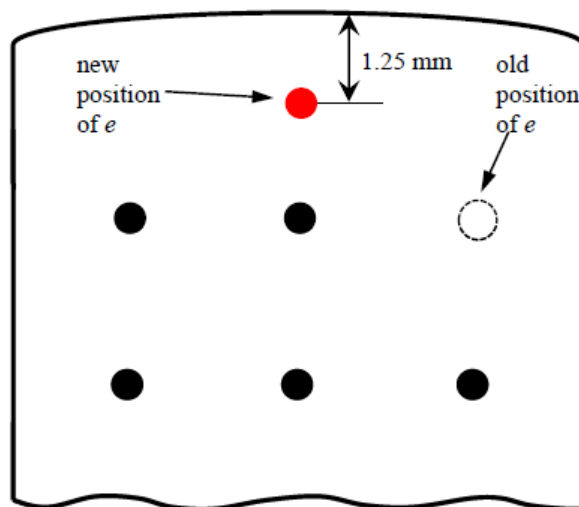


Figure 2-14 The arrangement of the thermocouples within the test disc (Al-Hamood, 2015)

Chapter 3 Theory and development of numerical model for the thermal behaviour of the test discs

3.1 Introduction

Previous work had used a numerical model to find the heat partition coefficient, β , and the heat transfer coefficients for the slow disc, h_s , and the fast disc, h_f , by analysing each disc individually and selecting the values of β and h to obtain the best fit to the measured temperatures of the experiment. This work is discussed in more detail in Chapter 4. However, in the current work, the objective was to analyse both discs at the same time and to develop an approach for determining the best fit of the three problem parameters (β , h_s and h_f) to the experimental results for both discs. Hence, a new numerical model was produced and developed.

The derivation of the partial differential equation which governs the temperature distribution within the test discs is outlined in this chapter. The finite difference method is explained and used to derive the convenient finite difference form of the equation for this work. The numerical solution used in this work and the way the calculation proceeds are also covered. Thus, the heat partition behaviour can be determined by comparing the results of this numerical model to those measured during the EHL experiment where the two discs are in rolling/sliding contact.

3.2 The governing partial differential equation

The theoretical model of the thermal behaviour of the test discs is initiated by working out the governing partial differential equation. As the test discs have cylindrical shape, it is convenient to use the cylindrical coordinates structure (r, θ, z) . Figure 3-1 below

shows a sketch of the test disc used in this work, and a small element of the disc with this coordinates structure with dimensions Δr , Δz , $r\Delta\theta$. The disc's material is isotropic and homogeneous, in other words at all points within the disc the density, thermal conductivity and heat capacity are the same.

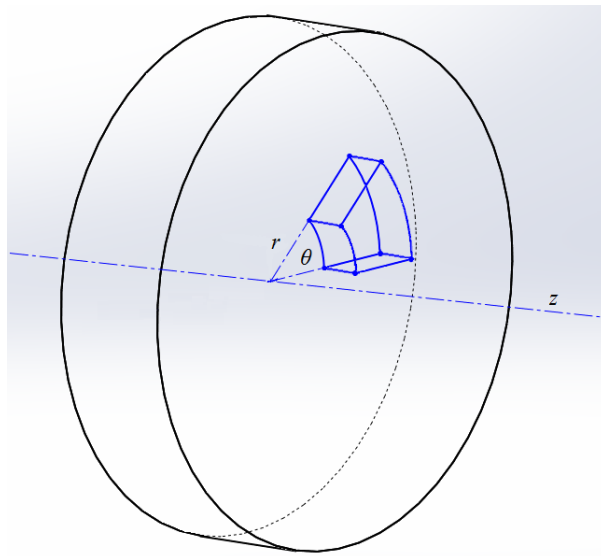


Figure 3-1 Element in the test disc

The small element in Figure 3-1 assumed to be fixed in space and that the disc material travels through this element while the disc rotates about the $0z$ axis. The central point of the element is located at (r, θ, z) as shown in Figure 3-2.

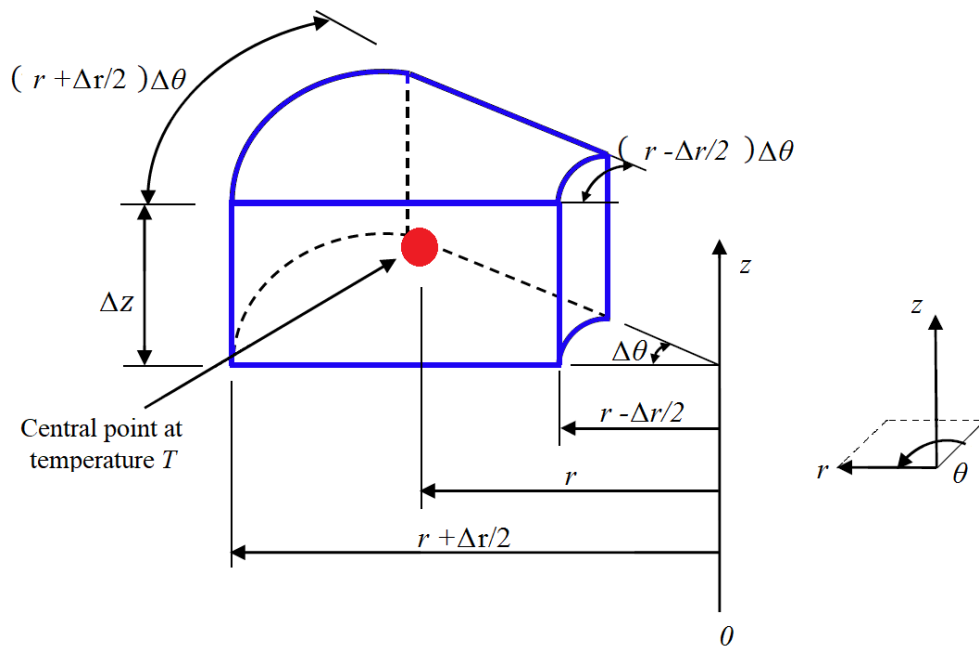


Figure 3-2 Element of the disc

The rate of change of the energy of the element consists of:

- a) The rate of change of energy transfer into the element.
- b) The rate of change of energy transfer out of the element.

That is to say, at time t the thermal balance equation of the element can be expressed as:

The amount of heat conducted into the element

+

The amount of heat generated inside the element

=

The amount of heat stored in the element due to the raise of temperature

+

The amount of heat leaving the element due to disc rotation.

And it can be expressed based on the conservation of energy as:

$$dQ_c + dQ_g = dQ_e + dQ_r \quad (3.1)$$

In the following sections, the derivation of each term in equation (3.1) is highlighted.

3.2.1 The amount of heat conducted into the element

The total amount of heat conducted into the element dQ_c can be determined from Fourier's law of heat conduction by adding the heat flow in the radial, axial and circumferential direction, and it can be written as follows:

$$Q_c = -KA \frac{\Delta T}{\Delta x} \quad (3.2)$$

Where: Q_c is the heat flow rate by conduction (J/s)

K is the thermal conductivity of body material (W/mK)

A is the cross-section area where the heat is flowing (m²)

$\frac{\Delta T}{\Delta x}$ is the temperature gradient in heat flow direction (K/m)

3.2.1.1 Heat flow in the radial direction

Using equation (3.2), at the face $r - \frac{\Delta r}{2}$, the heat flow that travel across the element in the radial direction is:

$$\begin{aligned}
 dQ_{r-\frac{\Delta r}{2}} &= -K \left(\left(r - \frac{\Delta r}{2} \right) \Delta \theta \Delta z \right) \frac{\partial T}{\partial r} \Big|_{r-\frac{\Delta r}{2}} \\
 &= -K \left(\left(r - \frac{\Delta r}{2} \right) \Delta \theta \Delta z \right) \frac{\partial}{\partial r} \left(T - \frac{\partial T}{\partial r} \frac{\Delta r}{2} \right) \\
 &= -K \left(\left(r - \frac{\Delta r}{2} \right) \Delta \theta \Delta z \right) \left(\frac{\partial T}{\partial r} - \frac{\partial^2 T}{\partial r^2} \frac{\Delta r}{2} \right)
 \end{aligned} \tag{3.3}$$

Similarly, the heat flow at the face $r + \frac{\Delta r}{2}$ gives:

$$\begin{aligned}
 dQ_{r+\frac{\Delta r}{2}} &= -K \left(\left(r + \frac{\Delta r}{2} \right) \Delta \theta \Delta z \right) \frac{\partial T}{\partial r} \Big|_{r+\frac{\Delta r}{2}} \\
 &= -K \left(\left(r + \frac{\Delta r}{2} \right) \Delta \theta \Delta z \right) \frac{\partial}{\partial r} \left(T + \frac{\partial T}{\partial r} \frac{\Delta r}{2} \right) \\
 &= -K \left(\left(r + \frac{\Delta r}{2} \right) \Delta \theta \Delta z \right) \left(\frac{\partial T}{\partial r} + \frac{\partial^2 T}{\partial r^2} \frac{\Delta r}{2} \right)
 \end{aligned} \tag{3.4}$$

Subtracting equation (3.4) from the equation (3.3) gives the net heat flow in the radial direction:

$$dQ_{cr} = dQ_{r-\frac{\Delta r}{2}} - dQ_{r+\frac{\Delta r}{2}} = -K r \Delta \theta \Delta r \Delta z \left(\frac{1}{r} \frac{\partial T}{\partial r} + \frac{\partial^2 T}{\partial r^2} \right) \tag{3.5}$$

3.2.1.2 Heat flow in the axial direction

Again, using the equation (3.2), at the face $z - \frac{\Delta z}{2}$, the heat flow in the axial direction

across the element is:

$$\begin{aligned}
 dQ_{z-\frac{\Delta z}{2}} &= -K (r \Delta \theta \Delta r) \frac{\partial T}{\partial z} \Big|_{z-\frac{\Delta z}{2}} \\
 &= -K (r \Delta \theta \Delta r) \frac{\partial}{\partial z} \left(T - \frac{\partial T}{\partial z} \frac{\Delta z}{2} \right) \\
 &= -K (r \Delta \theta \Delta r) \left(\frac{\partial T}{\partial z} - \frac{\partial^2 T}{\partial z^2} \frac{\Delta z}{2} \right)
 \end{aligned} \tag{3.6}$$

The same way at $z + \frac{\Delta z}{2}$ can be expressed as:

$$\begin{aligned}
 dQ_{z+\frac{\Delta z}{2}} &= -K (r \Delta \theta \Delta r) \frac{\partial T}{\partial z} \Big|_{z+\frac{\Delta z}{2}} \\
 &= -K (r \Delta \theta \Delta r) \frac{\partial}{\partial z} \left(T + \frac{\partial T}{\partial z} \frac{\Delta z}{2} \right) \\
 &= -K (r \Delta \theta \Delta r) \left(\frac{\partial T}{\partial z} + \frac{\partial^2 T}{\partial z^2} \frac{\Delta z}{2} \right)
 \end{aligned} \tag{3.7}$$

Subtracting equation (3.7) from the equation (3.6) gives the net heat flow in the axial direction as follows:

$$\begin{aligned}
 dQ_{cz} &= dQ_{z-\frac{\Delta z}{2}} - dQ_{z+\frac{\Delta z}{2}} = -K (r \Delta \theta \Delta r) \left(\frac{\partial T}{\partial z} - \frac{\partial^2 T}{\partial z^2} \frac{\Delta z}{2} \right) + K (r \Delta \theta \Delta r) \left(\frac{\partial T}{\partial z} + \frac{\partial^2 T}{\partial z^2} \frac{\Delta z}{2} \right) \\
 &= K r \Delta \theta \Delta r \Delta z \left(\frac{\partial^2 T}{\partial z^2} \right)
 \end{aligned} \tag{3.8}$$

3.2.1.3 Heat flow in the circumferential direction

Finally, at the face $\theta - \frac{\Delta\theta}{2}$, the heat flow in the circumferential direction across the

element is:

$$\begin{aligned}
 dQ_{\theta - \frac{\Delta\theta}{2}} &= -K (\Delta z \Delta r) \frac{\partial T}{r \partial \theta} \Big|_{\theta - \frac{\Delta\theta}{2}} \\
 &= -K (\Delta z \Delta r) \frac{\partial}{r \partial \theta} \left(T - \frac{\partial T}{\partial \theta} \frac{\Delta\theta}{2} \right) \\
 &= -K \left(\Delta z \frac{\Delta r}{r} \right) \left(\frac{\partial T}{\partial \theta} - \frac{\partial^2 T}{\partial \theta^2} \frac{\Delta\theta}{2} \right) \tag{3.9}
 \end{aligned}$$

In the same manner, at $\theta + \frac{\Delta\theta}{2}$ it leads to:

$$\begin{aligned}
 dQ_{\theta + \frac{\Delta\theta}{2}} &= -K (\Delta z \Delta r) \frac{\partial T}{r \partial \theta} \Big|_{\theta + \frac{\Delta\theta}{2}} \\
 &= -K (\Delta z \Delta r) \frac{\partial}{r \partial \theta} \left(T + \frac{\partial T}{\partial \theta} \frac{\Delta\theta}{2} \right) \\
 &= -K \left(\Delta z \frac{\Delta r}{r} \right) \left(\frac{\partial T}{\partial \theta} + \frac{\partial^2 T}{\partial \theta^2} \frac{\Delta\theta}{2} \right) \tag{3.10}
 \end{aligned}$$

Subtracting equation (3.10) from the equation (3.9) gives the net heat flow in the circumferential direction:

$$dQ_{c\theta} = dQ_{\theta - \frac{\Delta\theta}{2}} - dQ_{\theta + \frac{\Delta\theta}{2}} = -K \left(\Delta z \frac{\Delta r}{r} \right) \left(\frac{\partial T}{\partial \theta} - \frac{\partial^2 T}{\partial \theta^2} \frac{\Delta\theta}{2} \right) + K \left(\Delta z \frac{\Delta r}{r} \right) \left(\frac{\partial T}{\partial \theta} + \frac{\partial^2 T}{\partial \theta^2} \frac{\Delta\theta}{2} \right)$$

$$= K r \Delta z \Delta r \Delta \theta \left(\frac{1}{r^2} \frac{\partial^2 T}{\partial \theta^2} \right) \quad (3.11)$$

3.2.1.4 Net heat conducted into the element

Adding equations (3.5), (3.8) and (3.11) together gives the total amount of heat conduction into the element dQ_c :

$$dQ_c = K r \Delta \theta \Delta r \Delta z \left[\frac{1}{r} \frac{\partial T}{\partial r} + \frac{\partial^2 T}{\partial r^2} + \frac{\partial^2 T}{\partial z^2} + \frac{1}{r^2} \frac{\partial^2 T}{\partial \theta^2} \right] \quad (3.12)$$

3.2.2 The amount of heat generated inside the element

The amount of heat generated inside the disc material can be considered as zero, therefore:

$$dQ_g = 0 \quad (3.13)$$

3.2.3 The amount of heat stored in the element due to the rise of temperature

The internal stored energy dQ_s in the element due to the rise of temperature during time period Δt is:

$$dQ_s = \rho c_p (r \Delta \theta \Delta r \Delta z) \frac{\partial T}{\partial t} \quad (3.14)$$

Where: ρ is the density of the material (kg/m³)

c_p is the specific heat capacity of the material (J/kg.K)

3.2.4 The amount of heat change due to disc rotation

The total amount of heat change as a result of the disc rotation is equal to the difference between the heat leaving and that entering the element. The material travels through this element within time period Δt is $\omega r \Delta t \Delta r \Delta z$. The material is entering and leaving the element at temperatures $T|_{\theta-\frac{\Delta\theta}{2}}$ and $T|_{\theta+\frac{\Delta\theta}{2}}$ respectively,

where the total amount of heat can be expressed as:

$$dQ_r = \rho c_p \omega r \Delta r \Delta z \left(T|_{\theta+\frac{\Delta\theta}{2}} - T|_{\theta-\frac{\Delta\theta}{2}} \right) \quad (3.15)$$

According to Maclaurin's theory, the temperatures $T|_{\theta+\frac{\Delta\theta}{2}}$ and $T|_{\theta-\frac{\Delta\theta}{2}}$ can be written

as:

$$T|_{\theta+\frac{\Delta\theta}{2}} = T + \frac{\Delta\theta}{2} \frac{\partial T}{\partial \theta} \Big|_{\theta} + \frac{\Delta\theta^2}{8} \frac{\partial^2 T}{\partial \theta^2} \Big|_{\theta} \quad (3.16)$$

$$T|_{\theta-\frac{\Delta\theta}{2}} = T - \frac{\Delta\theta}{2} \frac{\partial T}{\partial \theta} \Big|_{\theta} + \frac{\Delta\theta^2}{8} \frac{\partial^2 T}{\partial \theta^2} \Big|_{\theta} \quad (3.17)$$

Hence, subtracting equation (3.17) from the equation (3.16) gives:

$$T|_{\theta+\frac{\Delta\theta}{2}} - T|_{\theta-\frac{\Delta\theta}{2}} = \Delta\theta \frac{\partial T}{\partial \theta} \quad (3.18)$$

Therefore, the substitution of equation (3.18) and (3.15) leads to:

$$dQ_r = \rho c_p \omega r \Delta r \Delta z \Delta\theta \frac{\partial T}{\partial \theta} \quad (3.19)$$

3.2.5 Conduction partial differential equation

Substitution of the four energy expressions in equations (3.12), (3.13), (3.14) and (3.19) into equation (3.1) will lead to the overall governing partial differential equation for the temperature in the test disc, which can now be expressed as:

$$\rho c_p (r \Delta \theta \Delta r \Delta z) \frac{\partial T}{\partial t} = K r \Delta \theta \Delta r \Delta z \left[\frac{1}{r} \frac{\partial T}{\partial r} + \frac{\partial^2 T}{\partial r^2} + \frac{\partial^2 T}{\partial z^2} + \frac{1}{r^2} \frac{\partial^2 T}{\partial \theta^2} \right] + \rho c_p (\omega r \Delta r \Delta z \Delta \theta) \frac{\partial T}{\partial \theta} \quad (3.20)$$

Simplifying the equation (3.20) leads to:

$$\frac{\partial T}{\partial t} = \alpha \left[\frac{1}{r} \frac{\partial T}{\partial r} + \frac{\partial^2 T}{\partial r^2} + \frac{\partial^2 T}{\partial z^2} + \frac{1}{r^2} \frac{\partial^2 T}{\partial \theta^2} \right] + \omega \frac{\partial T}{\partial \theta} \quad (3.21)$$

Where $\alpha = \frac{K}{\rho c_p}$, and it is the thermal diffusivity (m²/s) of the disc material.

According to Croft and Stone (1977), equation (3.21) is known as the conduction partial differential equation of heat partition at all times in the disc material.

3.3 Finite difference numerical method

3.3.1 Introduction to the method

The equation (3.21) described in Section 3.2.5 is a complex equation, like most of other partial differential equations (PDEs) where solving them by using analytical solution is not applicable. Therefore, the finite difference method (FDM) is a simple numerical method that can be used for application to the solution of PDEs. When

using this method, the temperature derivatives in equation (3.21) will be replaced by a set of finite difference equations which approximate it at every mesh points. Therefore, this method brings equation (3.21) to a linear system problem which involves the temperatures at different points. Depending on the size of the problem, an iterative method or matrix inversion may be used to solve it.

3.3.2 Derivation of finite difference approximations using Taylor's theorem

Equation (3.21) now involves temperatures at different points. Therefore, it is convenient to use Taylor's theorem is used to obtain expressions for spatial derivatives. Figure 3-3 illustrates a function in which the values of w are measured at three equally spaced mesh points.

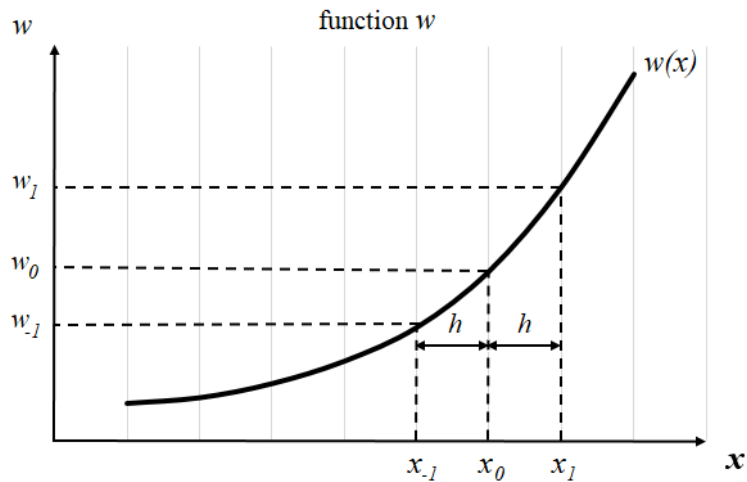


Figure 3-3 Values of w_{-1} , w_0 and w_1 for equally spaced points x_{-1} , x_0 and x_1

The value of w_1 can be found in terms of w_0 and its derivatives based on a truncated fourth order Taylor series theorem as follows:

$$w(x+h) = w_x + \frac{\partial w_x}{\partial x} h + \frac{\partial^2 w_x}{\partial x^2} \frac{h^2}{2!} + \frac{\partial^3 w_x}{\partial x^3} \frac{h^3}{3!} + \frac{\partial^4 w_x}{\partial x^4} \frac{h^4}{4!}$$

That is
$$w_1 = w_0 + \frac{\partial w_0}{\partial x} h + \frac{\partial^2 w_0}{\partial x^2} \frac{h^2}{2!} + \frac{\partial^3 w_0}{\partial x^3} \frac{h^3}{3!} + \frac{\partial^4 w_0}{\partial x^4} \frac{h^4}{4!} \quad (3.22)$$

The same approach of using w_0 and its derivatives is repeated to obtain the expression for w_{-1} :

$$w_{-1} = w_0 - \frac{\partial w_0}{\partial x} h + \frac{\partial^2 w_0}{\partial x^2} \frac{h^2}{2!} - \frac{\partial^3 w_0}{\partial x^3} \frac{h^3}{3!} + \frac{\partial^4 w_0}{\partial x^4} \frac{h^4}{4!} \quad (3.23)$$

Subtracting equations (3.22) and (3.23) and then adding them again give the following expressions respectively:

$$\frac{\partial w_0}{\partial x} = \frac{w_1 - w_{-1}}{2h} - \left[\frac{2h^2}{3!} \frac{\partial^3 w_0}{\partial x^3} \right] \quad (3.24a)$$

and
$$\frac{\partial^2 w_0}{\partial x^2} = \frac{w_1 + w_{-1} - 2w_0}{h^2} + \left[\frac{2h^2}{4!} \frac{\partial^4 w_0}{\partial x^4} \right] \quad (3.24b)$$

These two equations are known as the central difference equations, representing the first and the second order derivatives of the function $w(x)$. As noticed during the derivation, the terms $O(h^2)$ are neglected and hence the expressions are of second order accuracy.

On the other hand, there are simpler equations can be used for $\frac{\partial w_0}{\partial x}$, such as the forward and the backward difference equations. They are obtained straightway from equations (3.22) and (3.23) as follows:

$$\frac{\partial w_0}{\partial x} = \frac{w_1 - w_0}{h} - \left[\frac{h}{2!} \frac{\partial^2 w_0}{\partial x^2} + O(h^2) \right]$$

That is $\frac{\partial w_0}{\partial x} = \frac{w_1 - w_0}{h}$ Forward difference equation (3.25)

$$\frac{\partial w_0}{\partial x} = \frac{w_0 - w_{-1}}{h} + \left[\frac{h}{2!} \frac{\partial^2 w_0}{\partial x^2} + O(h^2) \right]$$

That is $\frac{\partial w_0}{\partial x} = \frac{w_0 - w_{-1}}{h}$ Backward difference equation (3.26)

Forward and backward difference equations are accurate to first order as the terms $O(h)$ in square brackets are neglected.

This is to say, it is more suitable to use the central difference equations rather than the forward and backward difference ones since they are more accurate for any given finite difference mesh.

3.4 Two-dimensional transient model of bulk temperature

3.4.1 Simplification of the conduction partial differential equation

The frictional heat flux conducted to the test discs may be assumed to be equally distributed at the circumferential surface of the test discs since the period required for the thermal equilibrium is not reached, and this is due to the fact that the test discs rotates in a shorter time than that needed for the thermal equilibrium. Hence, to determine the mean or the bulk temperature in the test discs, the change in the flash or circumferential temperature will be ignored.

The change in the flash or circumferential temperature occurs in thin layers of the test discs close to the circumferential surface. The arrangement of the thermocouples (6 mm and 3 mm below the surface) will not experience any change in temperature, this has been concluded by Qiao (2005), Al-Hamood (2015) and by Clarke (2009) who used steady-state three-dimensional flash temperature model.

Since the change in circumferential temperature is not being taken into account in this model, the problem is simplified to a two-dimensional transient conduction model where the conduction partial differential equation (3.21) can then be reduced to:

$$\frac{\partial T}{\partial t} = \alpha \left[\frac{1}{r} \frac{\partial T}{\partial r} + \frac{\partial^2 T}{\partial r^2} + \frac{\partial^2 T}{\partial z^2} \right] \quad (3.27)$$

In order to solve equation (3.27), two numerical methods can be used, which are the explicit and the implicit methods. In the following sections, each of these methods is highlighted.

3.4.2 The explicit method

This method uses a forward difference approximation where it converts the time derivative in equation (3.27) accordingly. The approximation needs the known temperature of each mesh point and its neighbouring mesh points at a previous time step in order to determine that of the current time step. This process is used to evaluate all temperatures at all points at the current time step using those of the previous time step, and it moves forward in time.

Figure 3-4 illustrates a typical explicit scheme, the temperatures at the previous time step (k) T_{i-1}^k , T_i^k and T_{i+1}^k are used to calculate the temperature T_i^{k+1} at a current

time step ($k+1$). The superscript k is the time step and the subscript i is the position of the mesh point.

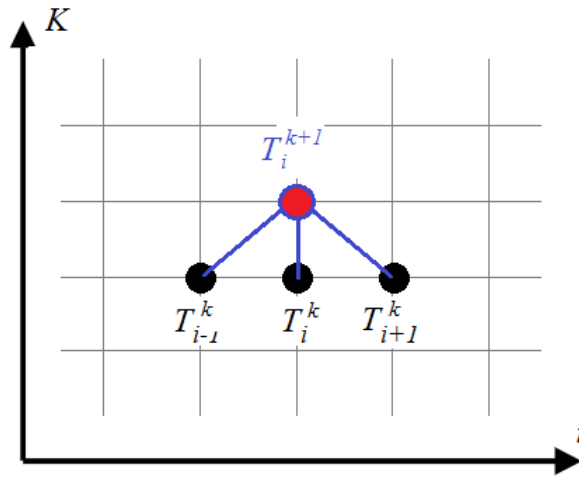


Figure 3-4 Schematic diagram of the explicit method

This numerical method is simple and computationally fast, however, in terms of stability it has a limitation where using a large time step ∂t will give instability in the result which grows with time leading to an incorrect solution. The discussion of Smith (1985) stated that the stable results are only achieved when the mesh ratio is $0 < \frac{\Delta t}{h^2} < 0.5$, where h^2 is the mesh size. Many authors discussed and showed how to use the stability criteria in order to calculate the mesh ratio e.g. Croft *et al.*, (1977) Consequently, achieving stability requires fine meshes and small time steps which take longer time to calculate. In addition, the approximation is first order accurate in time. Due to those disadvantages, the explicit method is not the most suitable method for the numerical solution of this work.

3.4.3 The implicit method

This method is contrary to the explicit method, it uses a backward difference approximation where it converts the time derivative in equation (3.27) accordingly. The approximation involves the temperature at the previous time step and that at each mesh point at the current time step which depends on the temperatures of the neighbouring mesh points also at the same time step which are unknown. Hence, for each mesh point, series of equations are produced and solved simultaneously in order to get the temperature at the current time step.

Figure 3-5 outlines a typical implicit scheme where it needs the known temperature at a previous time step T_i^k and those unknown at the current time step T_{i-1}^{k+1} , T_i^{k+1} and T_{i+1}^{k+1} . This is to say, at each time step, equations involving three unknowns must be solved in order to calculate the temperature at the next time step.

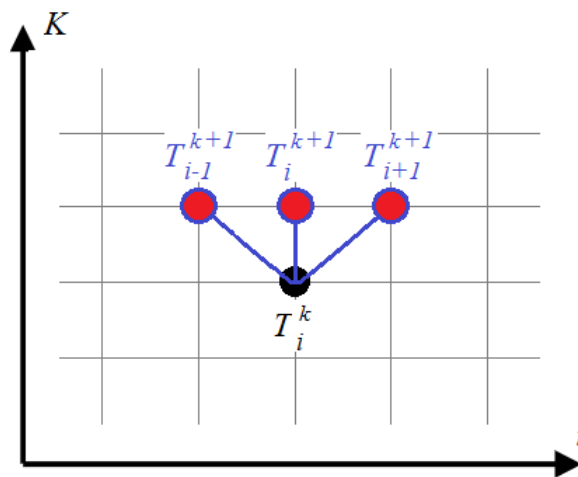


Figure 3-5 Schematic diagram of the implicit method

This method can replace the explicit one as it is numerically more stable when solving equations with large time step size, but it is computationally slow and requires more

time. Again, the approximation has first order accuracy in time, which means it generally leads to less accurate results.

3.4.4 The implicit method by Crank-Nicolson

This method was developed in the mid-20th century by John Crank and Phyllis Nicolson (Smith, 1985). It is the average of the explicit and implicit methods (combination of forward and backward difference approximations). The expression of the time derivative is obtained at the time midway between the previous time step k and the current time step $k+1$ using a central difference approximation. In addition, it uses finite difference approximations at both time steps k and $k+1$ to obtain the expression of the spatial derivatives on the right-hand side of equation (3.27). Figure 3-6 shows a typical Crank-Nicolson scheme.

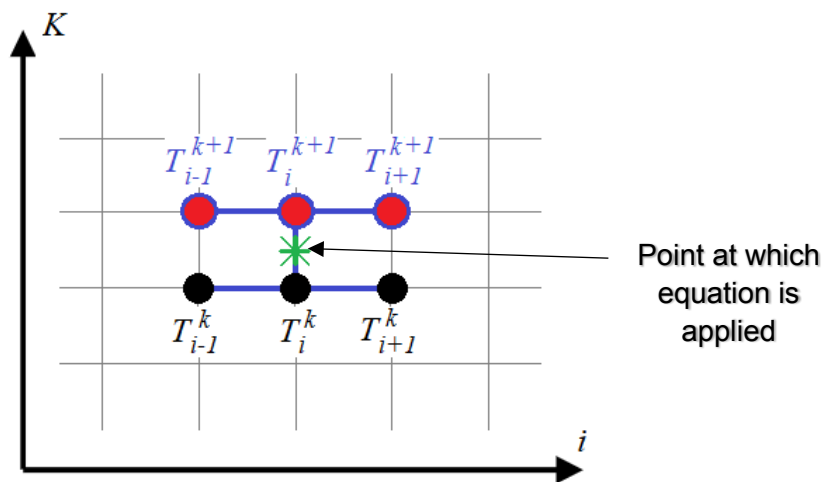


Figure 3-6 Schematic diagram of the Crank-Nicolson method

This numerical method is more accurate since it has second order accuracy in time and it is unconditionally stable. Hence, it is the most suitable numerical method to be used in this work.

3.4.5 Finite difference approximations within the test disc

Figure 3-7 illustrates a schematic mesh layout for the considered region within the test disc with the terminology used for the derivations of the finite difference approximations for both the interior and boundary points.

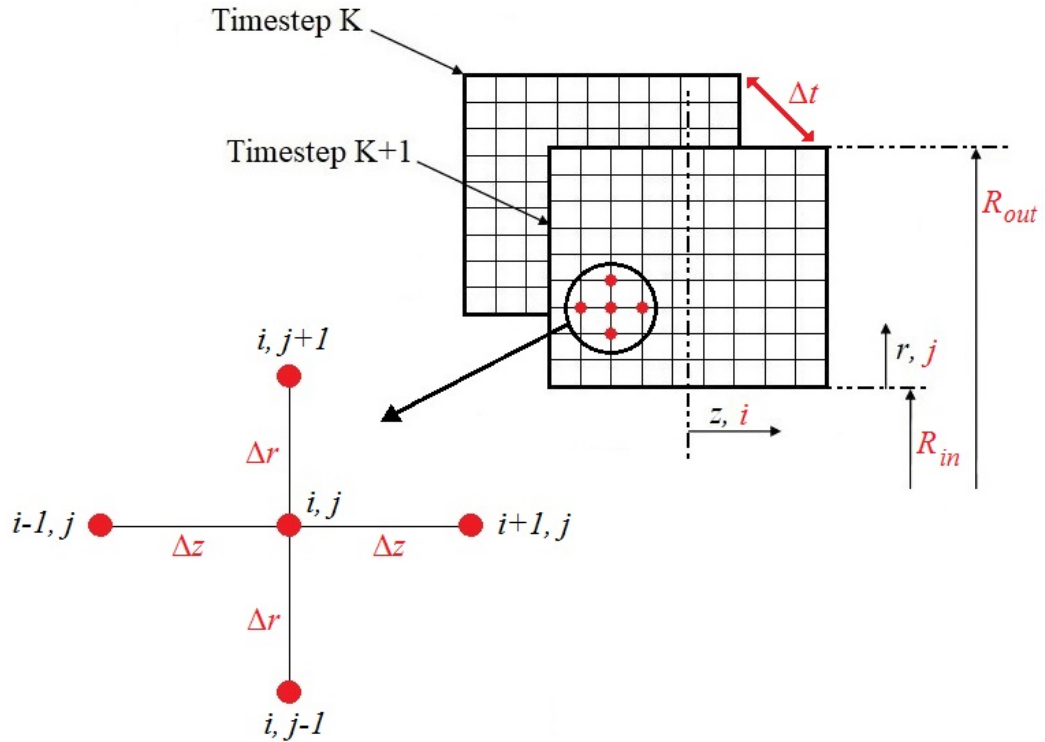


Figure 3-7 Schematic diagram of the mesh layout and terminology

By applying the Crank-Nicolson method in equation (3.27), it can be expressed in finite difference form as:

$$\frac{T_{i,j}^{(K+1)} - T_{i,j}^{(k)}}{\Delta t} = \frac{\alpha}{2} \left[\frac{1}{r} \frac{\partial T}{\partial r} + \frac{\partial^2 T}{\partial r^2} + \frac{\partial^2 T}{\partial z^2} \right]_{i,j}^{(K+1)} + \frac{\alpha}{2} \left[\frac{1}{r} \frac{\partial T}{\partial r} + \frac{\partial^2 T}{\partial r^2} + \frac{\partial^2 T}{\partial z^2} \right]_{i,j}^{(K)} \quad (3.28)$$

Where the spatial position and the time step are represented by the subscripts i, j and the superscript respectively. Substitute the following from equation (3.28):

$$\frac{\partial T}{\partial t} = \left\{ \frac{T_{i,j+1} - T_{i,j-1}}{2\Delta r} \right\} \qquad \frac{\partial^2 T}{\partial r^2} = \left\{ \frac{T_{i,j+1} + T_{i,j-1} - 2T_{i,j}}{\Delta r^2} \right\}$$

$$\frac{\partial^2 T}{\partial z^2} = \left\{ \frac{T_{i+1,j} + T_{i-1,j} - 2T_{i,j}}{\Delta z^2} \right\}$$

Leads to:

$$\begin{aligned} \frac{T_{i,j}^{(K+1)} - T_{i,j}^{(K)}}{\Delta t} = & \frac{\alpha}{2} \left[\frac{1}{r} \left(\frac{T_{i,j+1} - T_{i,j-1}}{2\Delta r} \right) + \frac{T_{i,j+1} + T_{i,j-1} - 2T_{i,j}}{\Delta r^2} + \frac{T_{i+1,j} + T_{i-1,j} - 2T_{i,j}}{\Delta z^2} \right]^{(K+1)} \\ & + \frac{\alpha}{2} \left[\frac{1}{r} \left(\frac{T_{i,j+1} - T_{i,j-1}}{2\Delta r} \right) + \frac{T_{i,j+1} + T_{i,j-1} - 2T_{i,j}}{\Delta r^2} + \frac{T_{i+1,j} + T_{i-1,j} - 2T_{i,j}}{\Delta z^2} \right]^{(K)} \end{aligned} \quad (3.29)$$

$$\text{Let: } \quad s_0 = \frac{\Delta t \alpha}{2\Delta r^2} \qquad s_1 = \frac{\Delta r}{2r_j} \qquad s_2 = \frac{\Delta r^2}{\Delta z^2}$$

Collecting terms at the different time steps together gives:

$$\begin{aligned} & \left[T_{i,j} (1 + 2s_0 + 2s_0s_2) - T_{i,j+1} (s_0s_1 + s_0) + T_{i,j-1} (s_0s_1 - s_0) - s_0s_2T_{i+1,j} - s_0s_2T_{i-1,j} \right]^{(K+1)} \\ & = \left[T_{i,j} (1 - 2s_0 - 2s_0s_2) + T_{i,j+1} (s_0s_1 + s_0) - T_{i,j-1} (s_0s_1 - s_0) + s_0s_2T_{i+1,j} + s_0s_2T_{i-1,j} \right]^{(K)} \end{aligned}$$

Let

$$RHS = \left[T_{i,j} (1 - 2s_0 - 2s_0s_2) + T_{i,j+1} (s_0s_1 + s_0) - T_{i,j-1} (s_0s_1 - s_0) + s_0s_2T_{i+1,j} + s_0s_2T_{i-1,j} \right]^{(K)}$$

The equation relating the temperatures at the five nodal points at time step k+1 is then:

$$\left[T_{i,j} (1 + 2s_0 + 2s_0s_2) - T_{i,j+1} (s_0s_1 + s_0) + T_{i,j-1} (s_0s_1 - s_0) - s_0s_2T_{i+1,j} - s_0s_2T_{i-1,j} \right]^{(K+1)} = RHS$$

Making $T_{i,j}$ the subject of this equation:

$$(1+2s_0+2s_0s_2) T_{i,j} = (s_0s_1+s_0) T_{i,j+1} - (s_0s_1-s_0) T_{i,j-1} + s_0s_2T_{i+1,j} + s_0s_2T_{i-1,j} + RHS$$

Equation (3.29) can now be re-written in the form:

$$T_{i,j} = C T_{i,j+1} + D T_{i,j-1} + A T_{i+1,j} + B T_{i-1,j} + G \quad (3.30)$$

$$\text{Where: } C = \frac{(s_0s_1+s_0)}{(1+2s_0+2s_0s_2)} \quad ; \quad D = -\frac{(s_0s_1-s_0)}{(1+2s_0+2s_0s_2)} \quad ; \quad A = B = \frac{s_0s_2}{(1+2s_0+2s_0s_2)}$$

$$\text{and } G = \frac{RHS}{(1+2s_0+2s_0s_2)}$$

In equation (3.30) all temperatures are at time step $(k+1)$. The term G involves the temperatures at time step (k) and can be written as:

$$G_{i,j} = H T_{i,j} + C T_{i,j+1} + D T_{i,j-1} + A T_{i+1,j} + B T_{i-1,j} + F \quad (3.30a)$$

$$\text{Where: } H = \frac{(1-2s_0-2s_0s_2)}{(1+2s_0+2s_0s_2)}$$

3.4.6 Boundary conditions

The region KLMN outlined in Figure 3-8 is the solution region, where different boundary conditions are applied, and they will be highlighted in the next sections.

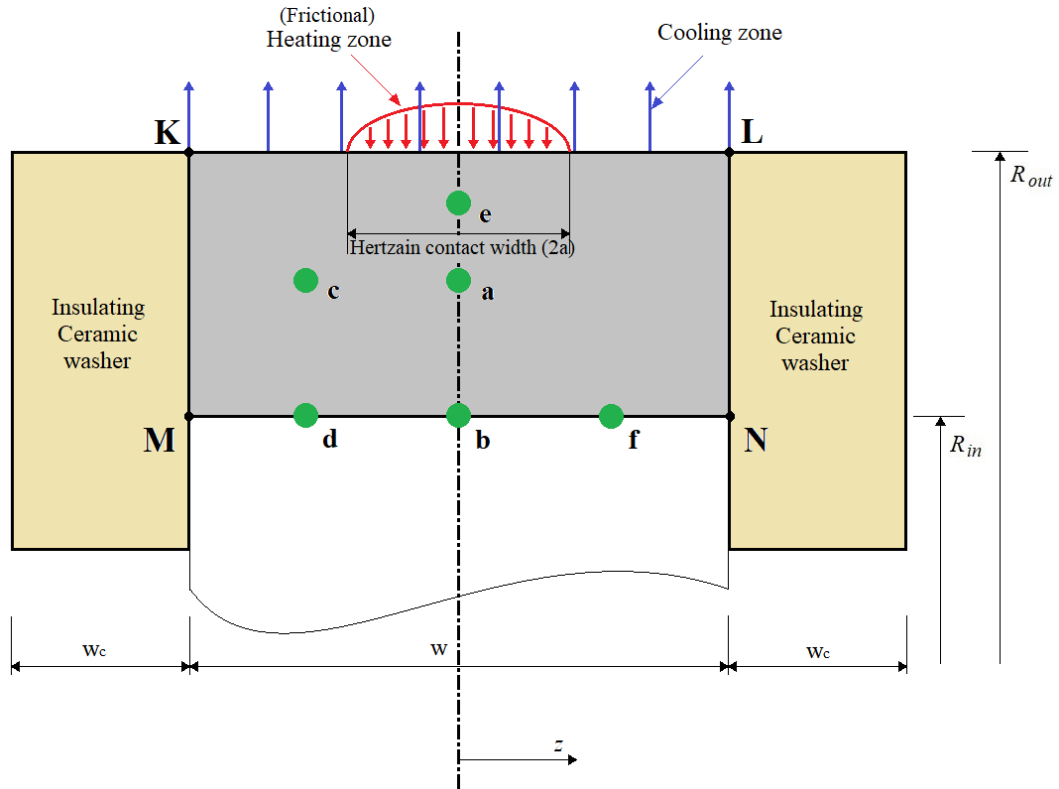


Figure 3-8 Two-dimensional model of the test disc and arrangement of thermocouples

Two groups of thermocouples are embedded in the discs ($e - c - a$) and ($d - b - f$) as shown in Figure 3-8. The former gives the temperatures to compare between the model and the experimental results, and the latter gives the measured boundary temperatures for the calculation.

3.4.6.1 Boundary condition at the outer radius

The line KL in Figure 3-8 represents the test disc's outer surface R_{out} . There are two zones at this boundary, the heating zone where the flow of heat generated due to the friction within the EHL contact and conducted into the Hertzian contact width ($2a$), and the cooling zone where the rotation of the test disc results in a flow of heat that is transferred to the surroundings by convection. Therefore, in equation (3.30) the

temperature expression $T_{i,j+1}$ is eliminated since it does not exist, the energy balance at this boundary is written as:

$$-K \frac{\partial T}{\partial r} = -K \frac{(T_{i,j+1} - T_{i,j-1})}{2\Delta r} = h(T_{i,j} - T_{fl}) - q_{fr} \quad (3.31)$$

Where: K is the thermal conductivity of the test disc

h is the convective heat transfer coefficient

q_{fr} is the conducted frictional heat flux

T_{fl} is the temperature of the fluid/surrounding

Re-arranging and substituting equation (3.31) into equation (3.30) will eliminate the temperature expression $T_{i,j+1}$ and make the coefficient $C = 0$. The value of h will be highlighted and described in chapters 4 and 5. The distribution of the frictional heat flux q_{fr} is supposed to be proportional to the contact pressure and applied over the running track of circumferential surface of the test discs in semi-elliptical shape due to the rolling/sliding between these surfaces, and it has a Hertzian contact width ($2a$). The power dissipation at the contact due to friction is equal to FU_s , where F is the frictional force measured during the experiment and U_s is the sliding speed. Imposing the heat partition coefficient β as the rate of the total fractional heat which flows to the slow disc, where $0 \leq \beta \leq 1$. Thus, leads to:

$$q_{fr} = 1.5 \bar{q} \left(1 - \frac{z^2}{a^2} \right) \quad \text{on } z = \pm a$$

Where:
$$\bar{q} = \frac{\beta FU_s}{4\pi R_{out} a} \quad \text{for the slow disc} \quad (3.32a)$$

$$\bar{q} = \frac{(1-\beta)FU_s}{4\pi R_{out} a} \quad \text{for the fast disc} \quad (3.32b)$$

In this work, the rate of the total frictional heat \bar{q} in equation (3.32a) is dedicated to the slow disc, and corresponds to the fast disc by changing β by $1-\beta$ (swapped compared to the work done by Clarke and Al-Hamood). In accordance with the above expressions of \bar{q} , the distribution of the total frictional heat flux between these discs is given by a parabolic shape in the z direction and equally distributed in the circumferential direction over the running track.

3.4.6.2 Boundary condition at the Inner radius

The line MN in Figure 3-8 represents the test disc's inner surface R_{in} , which is 6 mm below the surface. The thermocouples d , b and f are installed at this line as shown in the figure, thermocouple b is installed at the centre line of the test disc width, where d and f are installed 2 mm from each edge of the test disc. A boundary condition along the line MN is provided by applying the temperatures measured by those thermocouples during the experiment. Temperature distribution at all points along this boundary is represented by fitting a second-order polynomial to those measured temperatures with non-zero slope at the surfaces $z = \pm \frac{w}{2}$

$$T(z) = Az^2 + Bz + C \quad (3.33)$$

Figure 3-9 shows the boundary temperature distribution based on the three thermocouples readings obtained from an experiment of the slow disc (D3).

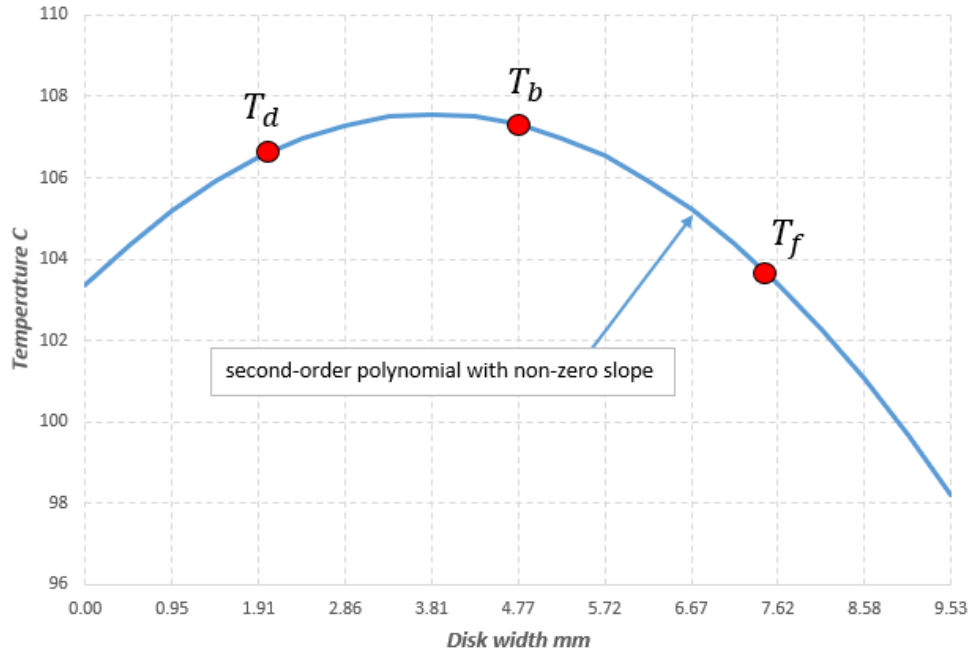


Figure 3-9 Temperature distribution at the inner radius of the slow disc

3.4.6.3 Boundary condition at the insulated disc faces

As described in chapter 2, both side faces of the test discs are insulated with ceramic washers, and they are represented in Figure 3-8 by the lines KM and LN. In equation (3.30), the temperature expressions $T_{i-1,j}$ and $T_{i+1,j}$ should be eliminated at KM and LN respectively as they do not exist. In addition, the temperature is assumed to be equal for the ceramic washers and the test disc as stated by the thermal balance at these boundaries where the heat conducted from the test disc should be equal to that conducted into the ceramic washers. While the outer face of the ceramic washers is assumed to be equal to the surrounding temperature T_{fl} which is measured continuously by a thermocouple fixed in the middle of the test area compartment. Hence, at the line LN:

$$-K \frac{\partial T}{\partial z} = -K \frac{(T_{i+1,j} - T_{i-1,j})}{2\Delta z} = -K_c \frac{(T_{fl} - T_{i,j})}{w_c} \quad (3.34)$$

Where: K_c is the thermal conductivity of the ceramic washer

w_c is the width of the ceramic washer

T_{fl} is the temperature of the fluid/surrounding

The term $T_{i+1,j}$ will be eliminated by re-arranging equation (3.34) and substituting in equation (3.30). Similarly, at the line KM, using the previous method to eliminate the term $T_{i-1,j}$.

The solution process of the numerical model is fully described in Chapter 4 and 5.

Chapter 4 Numerical modelling of the EHL heat partition test

4.1 Introduction

This chapter outlines the methods of modelling the experimental results of the EHL test that have been carried out using the twin-disc test rig described in Chapter 2 by applying the numerical model for the thermal behaviour of the test discs, which is described in Chapter 3. This investigation followed on from analysing an experiment where some uncertainty showed up in its results after applying the model to find the convection heat transfer coefficient h and the heat partition coefficient β . This led to an understanding that some developments and improvements were necessary for the numerical model approach and particularly to the test rig hardware (shafts and amplifiers).

4.2 Data filtering

The electrical noise is an undesirable signal in any experimental data and its existence introduces a typical source of uncertainty. This unwanted signal is usually logged with the desired original signal. It can be caused within the systems/circuit by factors such as loose connection, faulty component or poor design of the circuit, or from an external system such as vibration, change in environmental temperature or electromagnetic interference. Figure 4-1 shows an example of the presence of noise in an oil temperature reading from an EHL test.

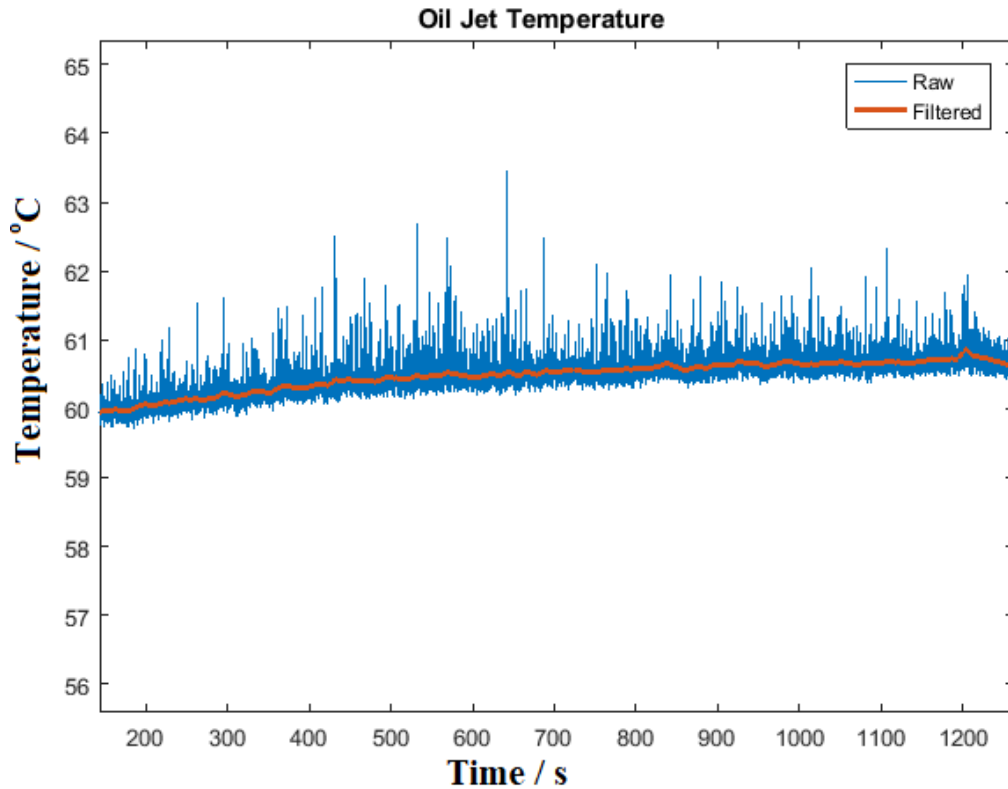


Figure 4-1 Typical noise from data

The EHL experiment data are always recorded by LabVIEW software, which is associated with the test rig, and they are written in a file that includes the readings of the six thermocouples of each test disc, load, friction force, oil and ambient temperatures. These data were filtered and curve fitted using the Gaussian filtering process available in the MATLAB software to eliminate the electrical noise from it, and then stored in spreadsheets as input files prepared so as to read the values using the Fortran 90 code written to obtain the results by analysing the experiment using the model described in Chapter 3.

4.2.1 Disc temperature filtering process

The temperatures are measured at a logging frequency of 75 Hz (so that successive measurements are $\Delta t \approx 0.012\text{s}$ apart) by six thermocouples that are embedded in each test disc as described in Chapter 4, then recorded by LabVIEW software. As a result of having these data acquired by electronic devices, they are subjected to electrical noise that comes from surrounding sources such as other devices in the laboratory or environmental sources such as changing in the surrounding temperature. In addition, this test rig is equipped with slip rings which may also cause electrical noise.

In order to remove the electrical noise and process the curve fitting for the six temperatures of each disc, these temperatures readings are firstly imported to MATLAB software. Then, a Numeric Matrix is created for each thermocouple's data versus time and saved into the Workspace in MATLAB. Plotting these data gives the curves shown in Figure 4-2.

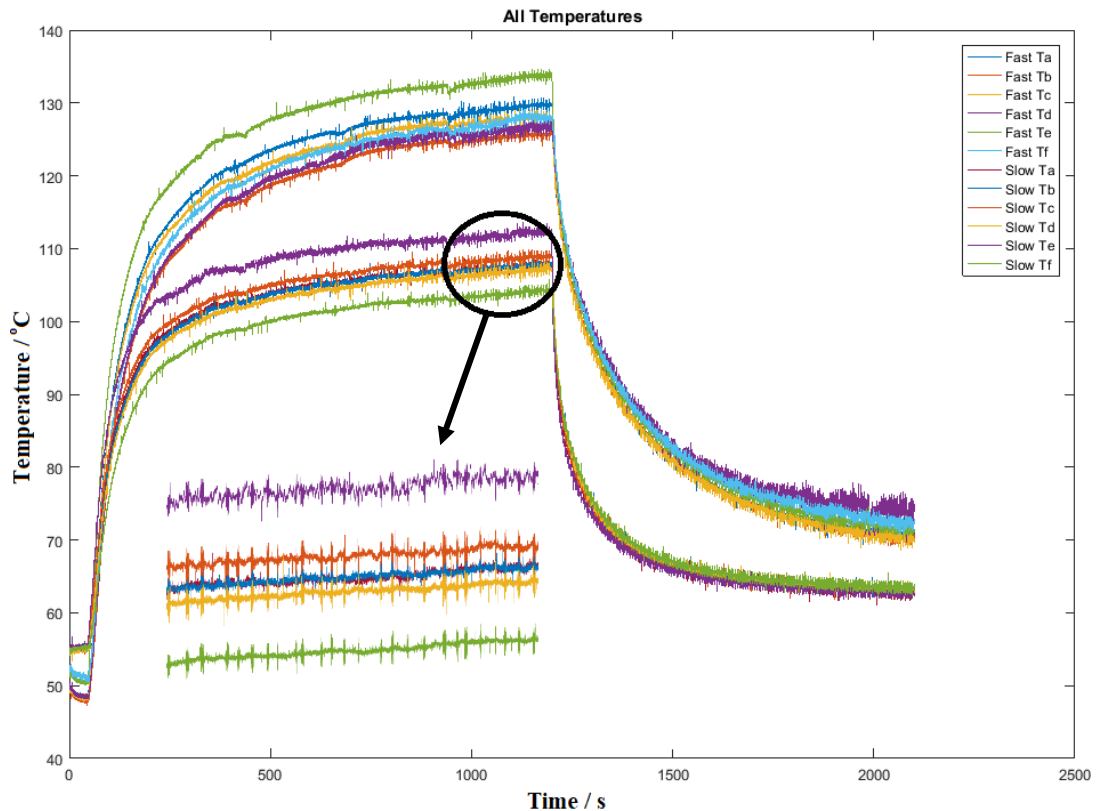


Figure 4-2 Raw data of the temperatures of the Fast and the Slow disc

The curves joining the measurements in Figure 4-2 represent the temperatures of the fast and slow discs during the EHL experiment. The lines are thick, and rapid changes in measurement values can be seen in all curves. The thermocouples measure the temperatures at specific depths below the surface, which means the measured temperatures are the mean circumferential temperatures at those positions. They can only be changing slowly (they should give smooth curves) due to their depth which ensures that they are not be affected by the highly transient temperature rise and fall at the surface in each disc revolution as it passes through the contact, as it does not penetrate to that depth. Consequently, the high frequency variation present in the measured temperatures cannot be correct and must be caused by electrical noise. This is to be expected as the thermocouple voltage is in the range 3 to 11 mV when

passed through the rig slip rings. A noise component of the order 0.1 mV introduced in the rig, at the slip ring contacts or in the shielded connecting cable to the signal processing unit will correspond to the ± 2 °C high frequency noise seen in the recorded temperatures.

The filter parameters were chosen so that the high frequency variation was removed but the low frequency variation was retained. The low frequency variation that corresponds to the real changes that are physical responses to the power input variations caused by changes in the measured friction. For these reasons, the filter parameters were chosen by comparing the filtered signals and this was a matter of judgement for each experiment.

The first step to remove this noise is by applying a MATLAB code that applies Gaussian filter processing to each thermocouple's readings. The filtered temperature values at a given time, t , are a weighted sum of the measured values obtained before and after that time. The weighting factors form a Gaussian distribution centred at the given time and extend by the filter wavelength, σ , before and after the time. The σ value is generally set to 250 for this work meaning that the Gaussian distribution is spread over the interval $(t-250 \Delta t, t+250 \Delta t)$. A higher value of wavelength σ means averaging over a longer period adding more filtering to the data. Hence, it gives a smoother filtered curve, whereas a lower value gives a filtered curve but with some electrical noise that has not been completely removed.

Figures 4-3, 4-4 and 4-5 illustrate comparisons between the raw data of a thermocouple reading and the filtered data after applying different values of wavelength in the filtering process $\sigma = 800, 20$ and 250 .

Firstly, a high value of wavelength $\sigma = 800$ is selected to see how the filtered data will behave when using a high value of wavelength. The result is obtained and plotted as shown in Figure 4-3 below.

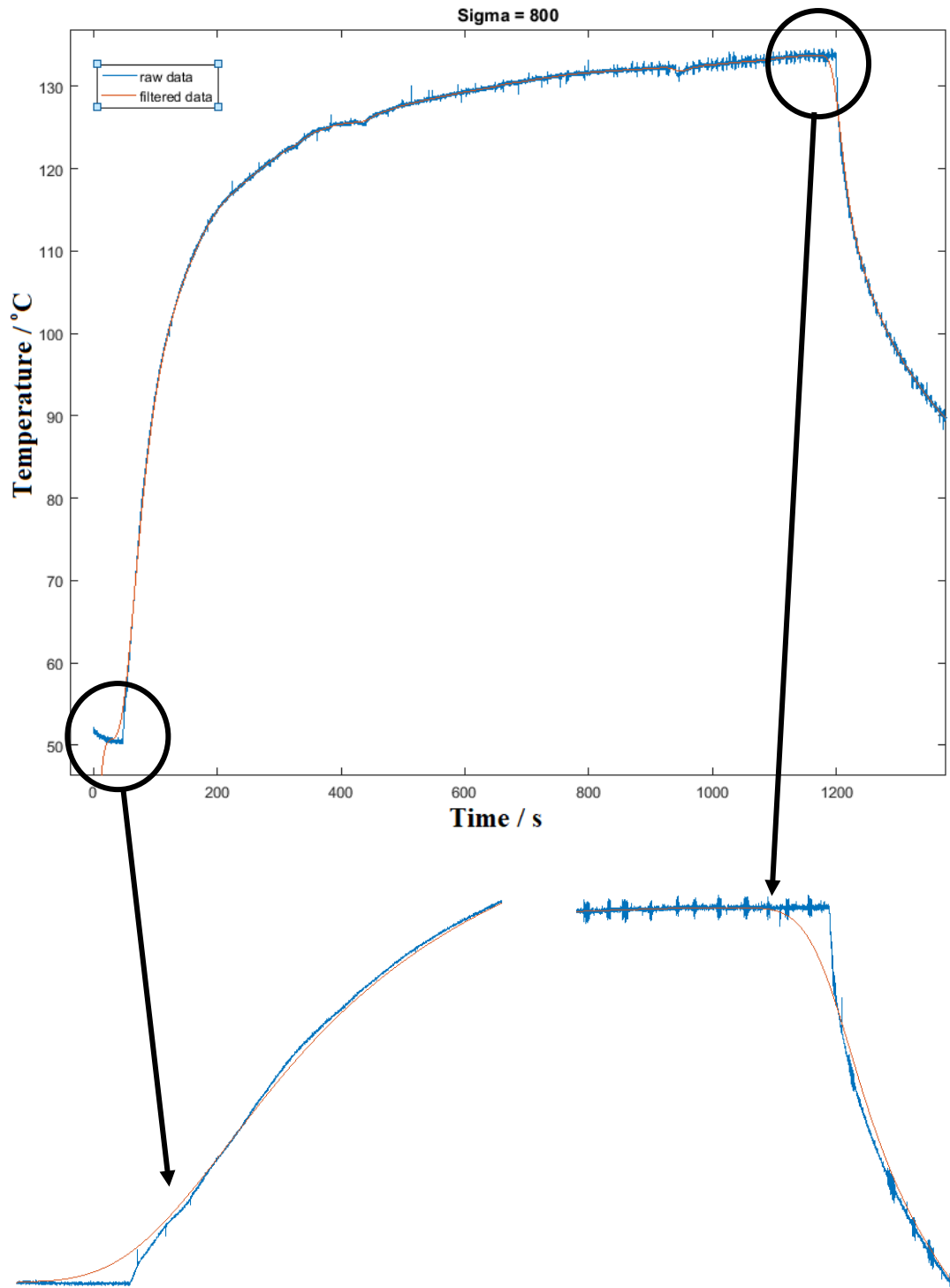


Figure 4-3 Temperature curve when using high wavelength $\sigma = 800$

Figure 4-3 shows a smooth filtered curve that generally follows the measured temperatures but with deviations and significant differences between the raw and the filtered data around the loading and unloading stage. The filtered data does not follow the original data, this gives incorrect values of temperature when comparing at a specific timestep between raw and filtered data. Hence, this value of wavelength is not appropriate because the averaging is taking place over too great a range.

Secondly, the wavelength is now changed to a much lower value, $\sigma = 20$, to observe the change in the temperature curves, Figure 4-4 below shows the result of this filtering process over 200s.

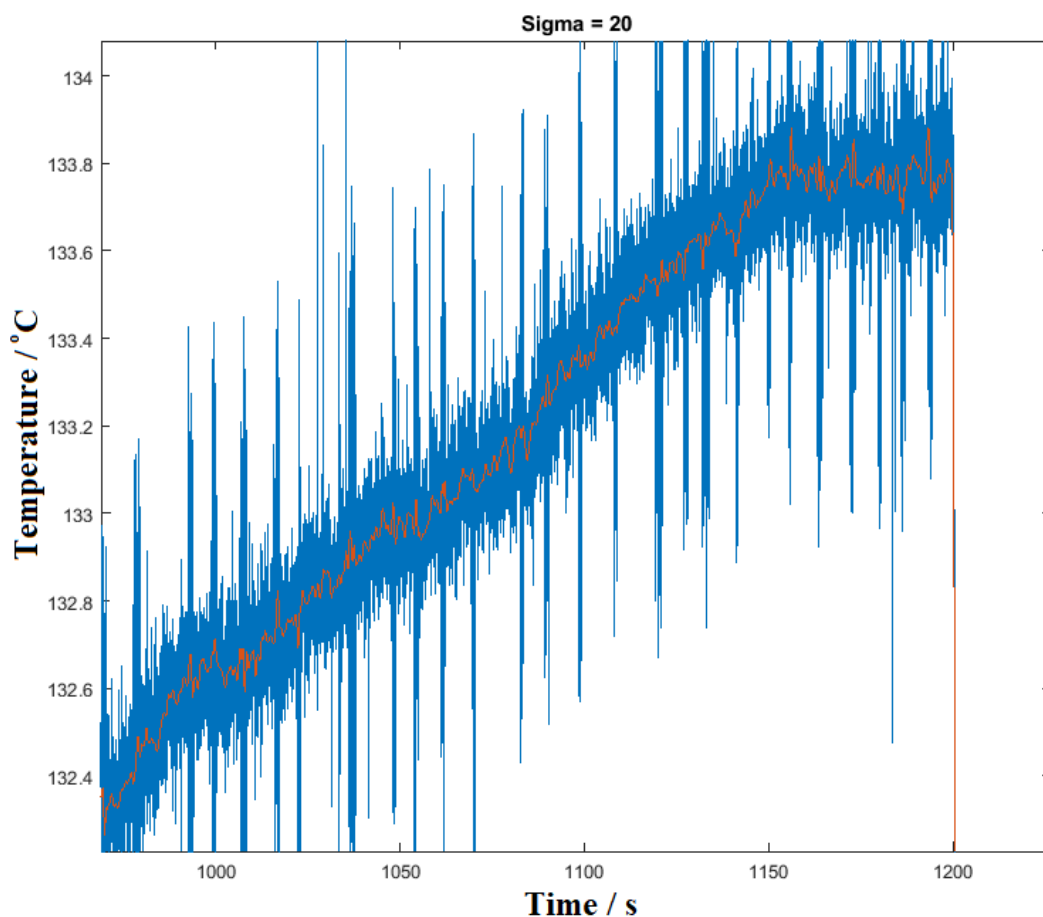


Figure 4-4 Close up view of temperature curve when using low wavelength = 20

In Figure 4-4 the filtered data has not smoothed the noisy signal enough, it follows the local average of the raw data and still contains the unwanted electrical noise but at lower amplitude. This curve needs to be filtered using a higher wavelength in the Gaussian filter processing.

Finally, after using many values of σ and making comparisons between them, a wavelength $\sigma = 250$ was found to be the most appropriate value for the filtering process in this work. The result showed a smooth filtered curve that behaves as the raw data and does not have electrical noise. It is able to follow minor undulations in the measured signal but has imposed sufficient smoothing to be consistent with the expected increase in the temperature measured at a point within the disc which has a high thermal mass.

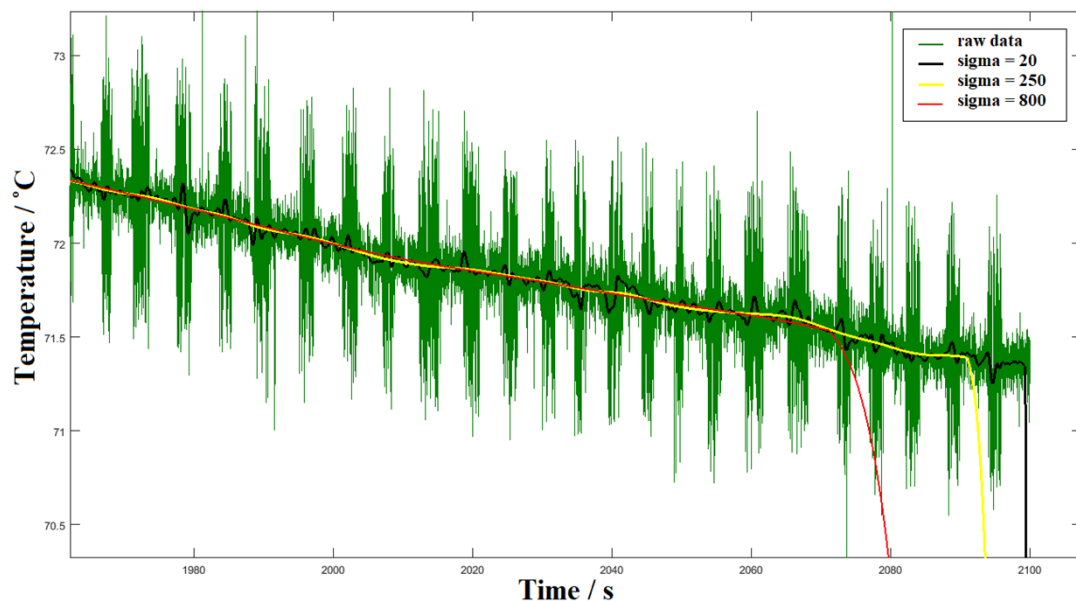


Figure 4-5 comparison between three values of σ

As shown in Figure 4-5 the black, yellow and red lines shows the filtered curves obtained with σ values of 20, 250 and 800 respectively where it is clear that the $\sigma =$

20 curve still has an electrical noise component as it follows the electrical noise recorded from the original data. On the other hand, the $\sigma = 800$ curve is extremely smooth but it does not follow when there is an increase or decrease in data values. Hence, the $\sigma = 250$ curve is the most accurate in terms of achieving a balance between smoothness and removing the noise and following the original data values.

4.2.2 Friction force filtering process

A friction dynamometer (transducer), which is attached to the slow shaft, is used to measure the friction force that includes bearing friction and windage losses as the shaft is rotating. It is also recorded by the LabVIEW software.

A schematic drawing of the shaft's layout including the bearings and their directions of rotation is shown in Figure 4-6 below.

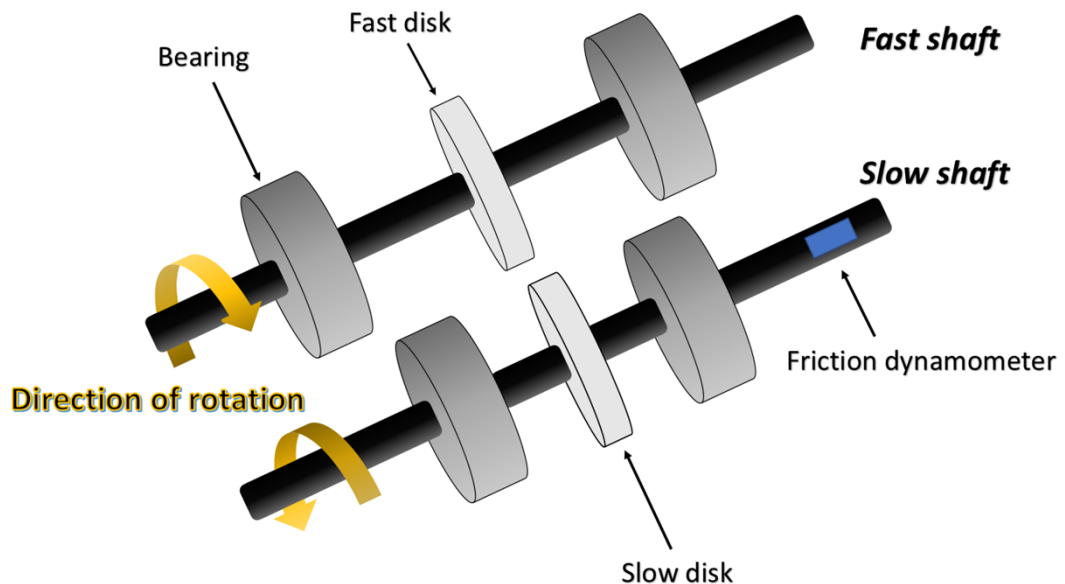


Figure 4-6 Schematic of the shafts and bearings arrangement

Before filtering the friction data and applying the process that has been used to filter the thermocouple's data, it is necessary to calculate and find the correct value of the traction force at the contact. In fact, the traction force is higher than that measured by the friction transducer due to the fact that the bearing friction and windage act in the opposite direction for the slow shaft. These traction forces are shown in Figure 4-7

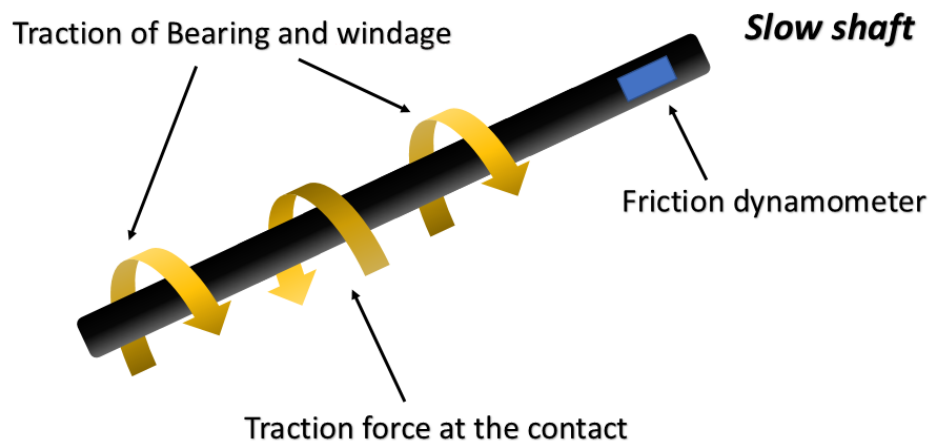


Figure 4-7 Friction torques on the slow shaft

Therefore, the bearing friction and windage should be added to the measured friction. To determine the bearing friction and windage, experiments were carried out and fully described by Clarke (2009) where a linear best fit between contact load and measured friction force was obtained and shown in Figure 4-8 (where y is total friction force and x is the bearing load). For these calibration experiments the gear connection between the shafts was disconnected. In this configuration there is no slip between the discs and therefore no friction at the contact, and both shafts turned at the same speed. The measured friction then corresponds to four shaft bearings running at the same speed. The best fit lines were used to adjust and calculate the correct traction force at the EHL test by inserting the applied load as the x in corresponding linear equation. This gives twice the additional friction force that needs to be added to that

measured by the friction transducer in the experiment when the discs are in rolling/sliding contact.

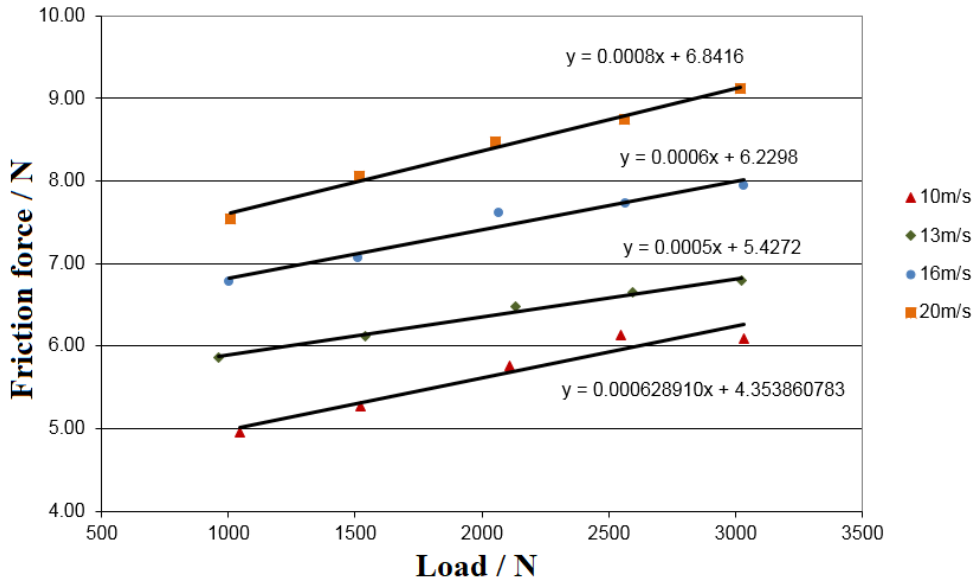


Figure 4-8 Bearing friction and windage in the slow shaft (Clarke, 2009)

Figure 4-9 shows the adjusted friction force. The friction scale is zeroed using the mean friction at the beginning and end of the test.

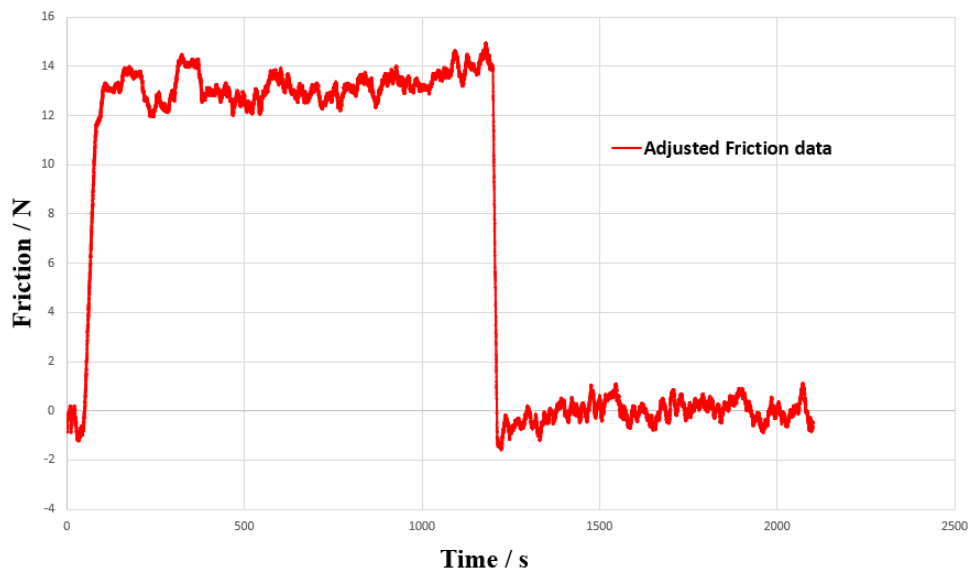


Figure 4-9 Adjusted friction force

After this step, the bearings' friction is added to the adjusted friction force for the loaded period as shown in Figure 4-10. The amount added is calculated using the slope of the appropriate line in Figure 4-8.

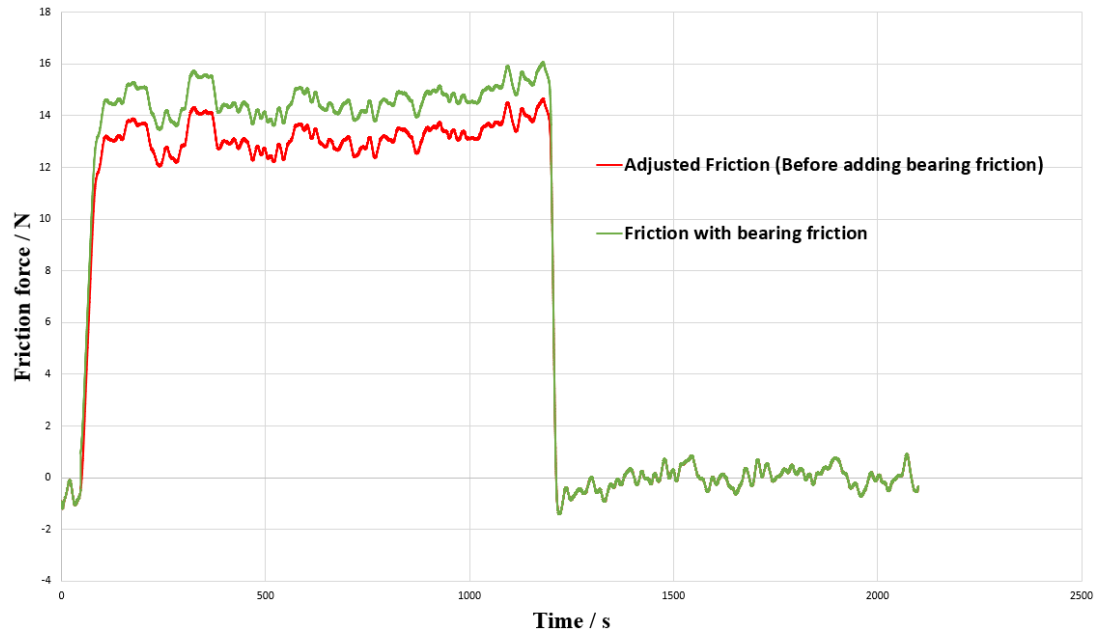


Figure 4-10 Adjusted friction force and friction force after adding bearing friction

Once the friction force is calculated, its data file is then imported into MATLAB software in order to filter and remove the electrical noise from it by using the same process as that for the thermocouple's readings. In this filtering process, the wavelength is set to $\sigma = 300$ as it was found to be the most appropriate value giving the best filtering quality for the dataset. After applying the MATLAB filtering code, the output data is plotted as shown in Figure 4-11 where a short section from this data was selected to zoom in, and this illustrates the difference between the original and the filtered data.

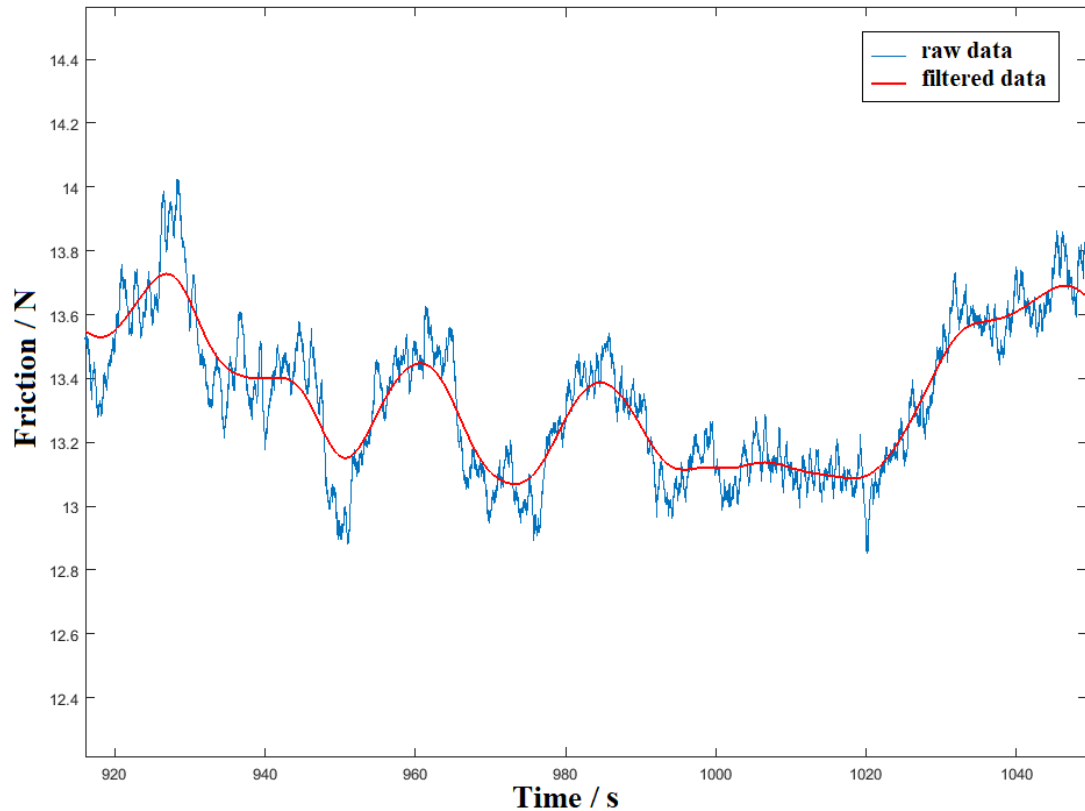


Figure 4-11 raw data and filtered data of the friction

4.2.3 Oil/surrounding temperature filtering process

The oil temperature of the surroundings in the vicinity of the discs is also included in the calculations of the numerical model, where it is known as the temperature of the fluid/surrounding T_{fl} . Therefore, it is necessary to filter the oil temperature data recorded by LabVIEW and remove the electrical noise.

There are three thermocouples placed inside the protection case that covers the two test discs during the EHL test, one is above the left edge of the fast disc, the second one is above the right edge of the slow disc and the third one is above the contact surfaces in the middle. Figure 4-12 illustrates this in a schematic drawing of the oil/surrounding thermocouples arrangement.

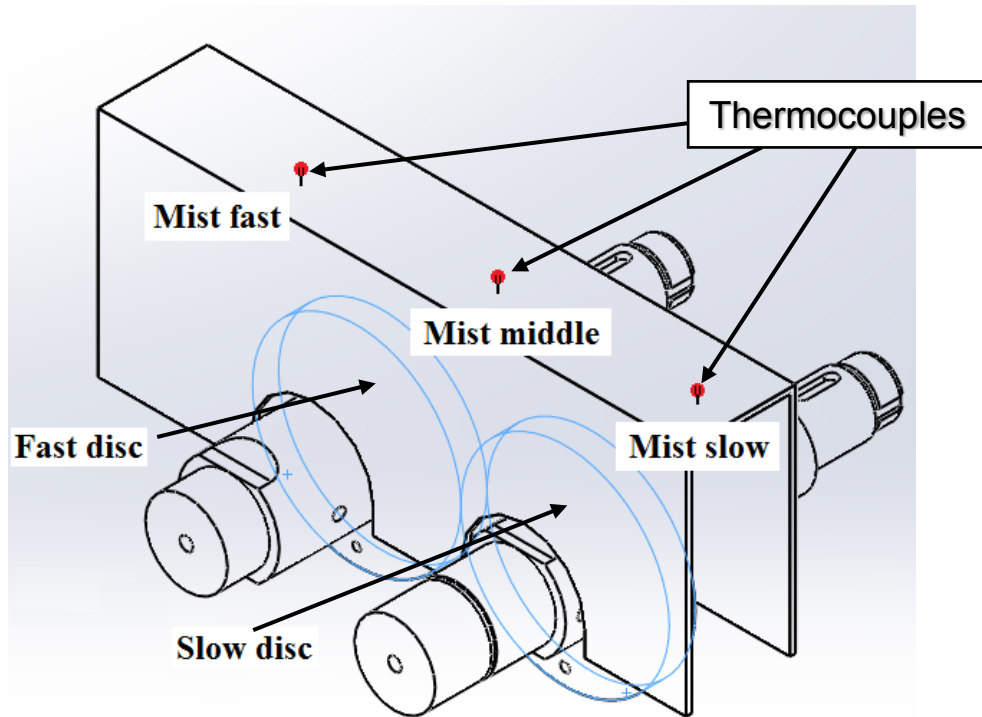


Figure 4-12 The three oil/surrounding thermocouples in the protection case of the test discs

The three thermocouples' measurements give almost the same temperatures at the same timesteps. However, the temperature measurement above the contact surfaces (Mist middle) is selected for the calculations of the numerical model in this work as it is the closest to the EHL contact surfaces hence it gives closer temperature readings of the surrounding temperature. The dataset of the oil/surrounding temperature (Mist Middle) is filtered and plotted as shown in Figure 4-13.

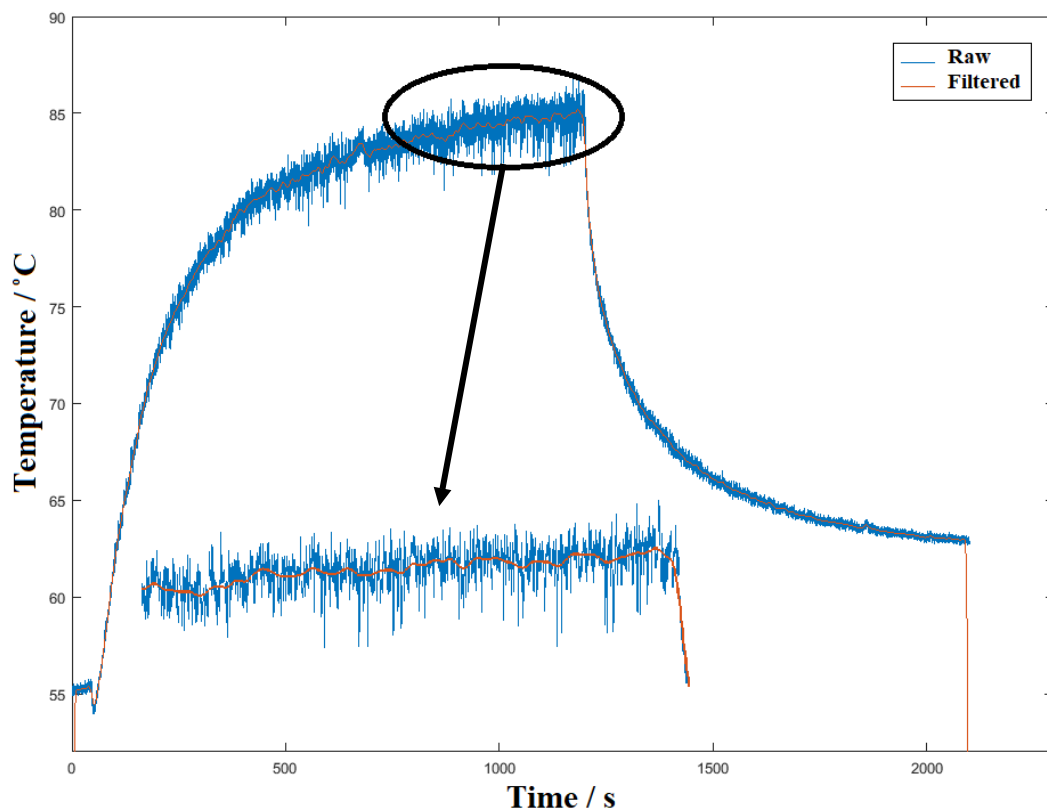


Figure 4-13 Raw and filtered oil/surrounding temperature

The data recorded by the thermocouple shown in blue colour contains an electrical noise with high amplitude, however after applying the filtering process, it has completely removed and the new filtered data shown in red colour can be then imported to the numerical model.

4.3 Mesh sensitivity test

The solution region KLMN outlined in Figure 4-14 is modelled with a rectangular regular $n \times m$ distribution of mesh points in accordance with the dimensions of this region (n in z the direction and m in the r direction), and a suitable time step is chosen to carry out the transient analysis. The model is axisymmetric about the disc axis so

that the transient effects modelled are the steady change in mean temperature at each mesh point over the duration of the experiment.

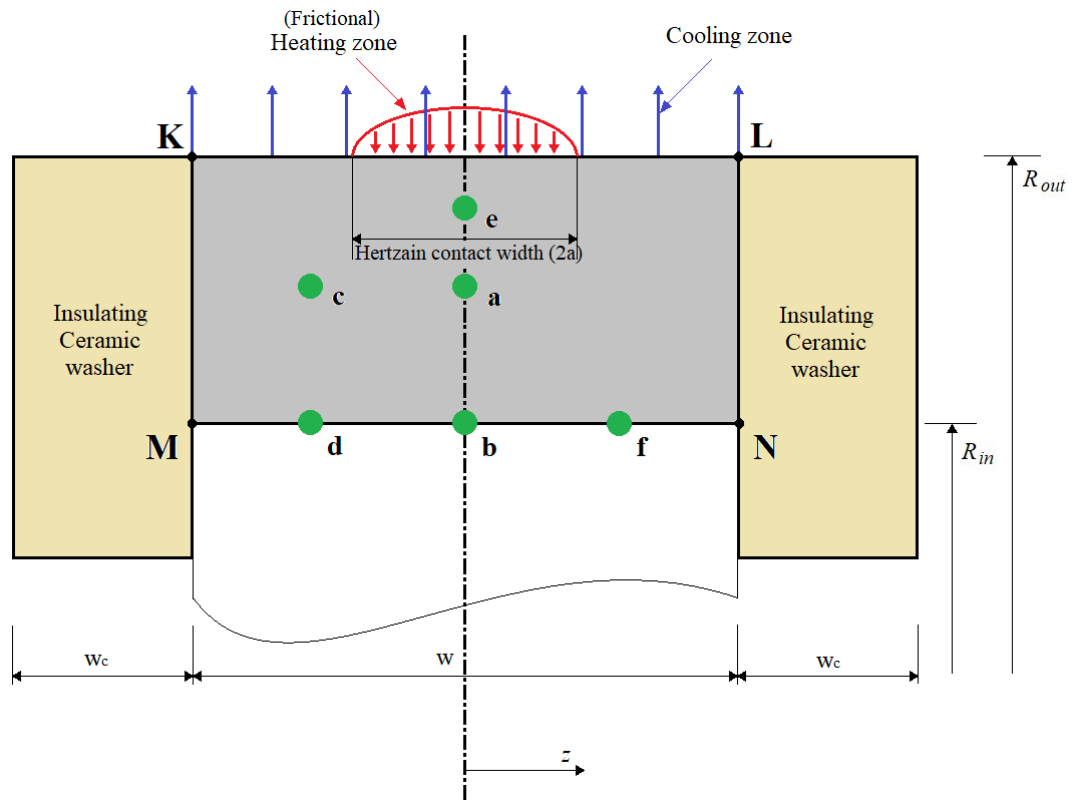


Figure 4-14 Two-dimensional model of the test disc and thermocouples positions

In this work, the mesh size is set to 21x15 in the transient analysis, and a 1 second time step was selected based on the studies conducted by Al-Hamood (2015) where he showed the difference between results for a test case with constant inner boundary temperature and a high value constant running track heat flux. Differences between the 0.4 s and 1 s results were only seen during the initial five seconds when the test case was highly transient.

The mesh points along the boundary line MN were selected as the boundary conditions which are time varying, and they were given by the measured thermocouple temperatures at *d*, *b* and *f* and by applying equation (3.33). All

remaining mesh points within the structure were solved at each time step by using the Gauss Seidel iteration method to solve the implicit formulation equation by iterative application of equation (3.30).

The temperature values at all points in the mesh are updated using equation (3.30) in a sweep through the mesh points that comprises one cycle. The Gauss Seidel iteration method uses the newly calculated temperatures once they have been calculated instead of waiting until the end of each cycle. This method is simpler, converges in fewer cycles and requires less computer storage. Hence, it is the most suitable to be used in this work.

A series of tests was carried out where the number of mesh points in the solution region $n \times m$ was changed for each test. Four tests were carried out and their mesh sizes are shown in Table 4-1.

Table 4-1 Mesh sizes tested for this work

Mesh test	Points in z direction	Points in r direction
A	11	8
B	21	15
C	41	29
D	81	57

Figures 4-15, 4-16, 4-17 and 4-18 below show the results obtained from mesh tests A, B, C and D respectively for the slow disc. Each figure represents the temperature distribution of the slow disc at the last time step $t = 1000s$. The contours obtained from the test with finest mesh (where n and m values are largest) is smoother than those obtained from coarser mesh (with smaller values of n and m). This is caused in part by the contour plotting algorithm.

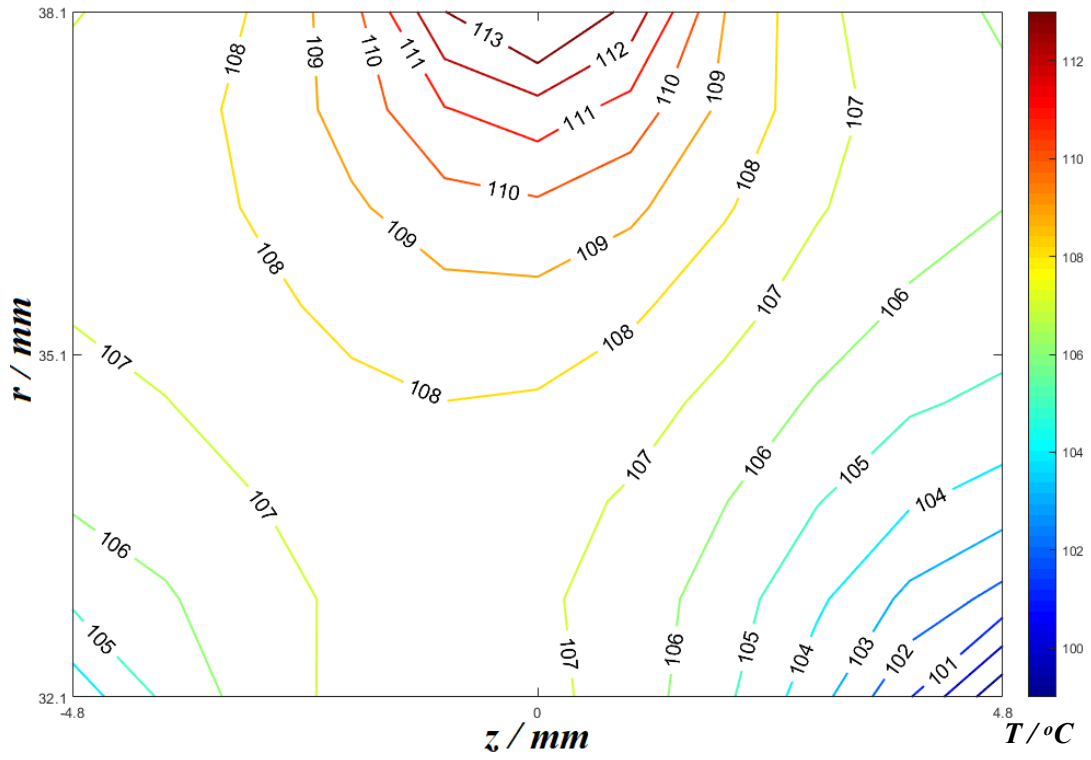


Figure 4-15 Temperature contour for the slow disc for test (A) mesh size 11x8, at time step 1000s

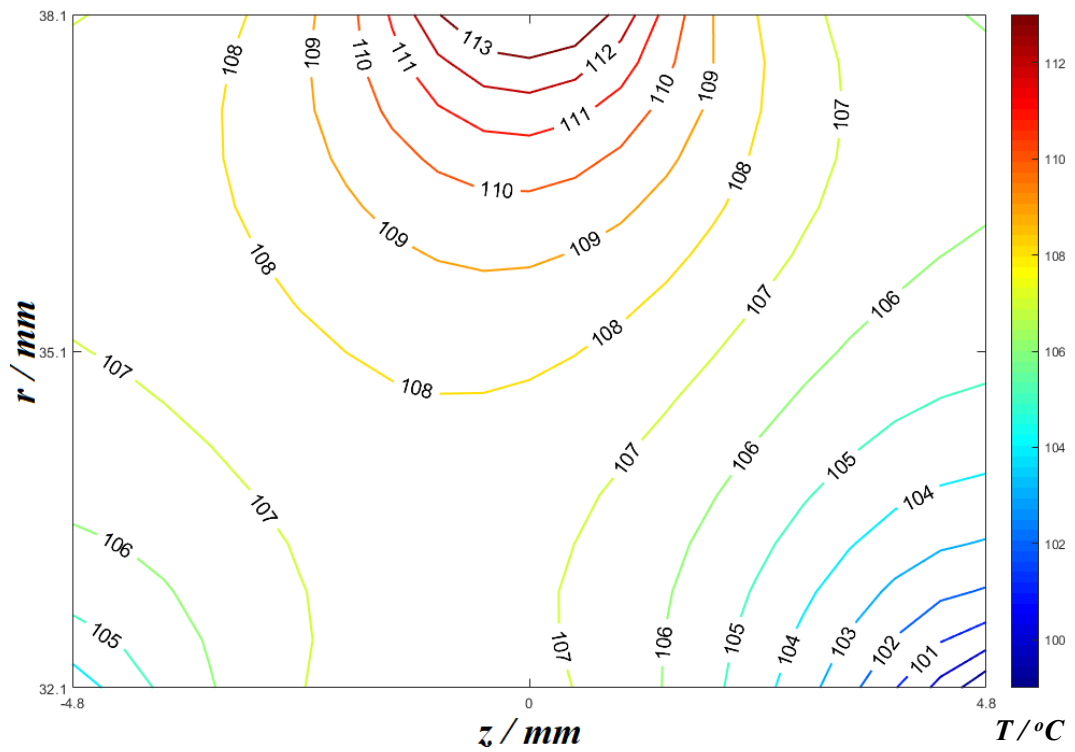


Figure 4-16 Temperature contour for the slow disc for test (B) mesh size 21x15, at time step 1000s

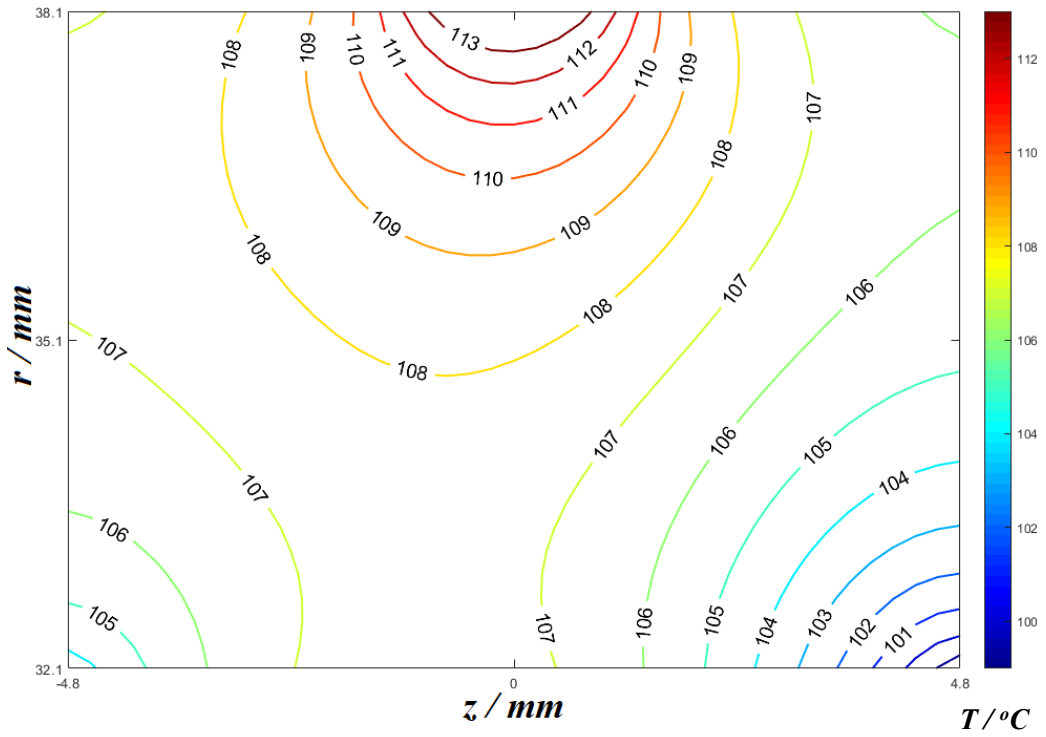


Figure 4-17 Temperature contour for the slow disc for test (C) mesh size 41x29, at time step 1000s

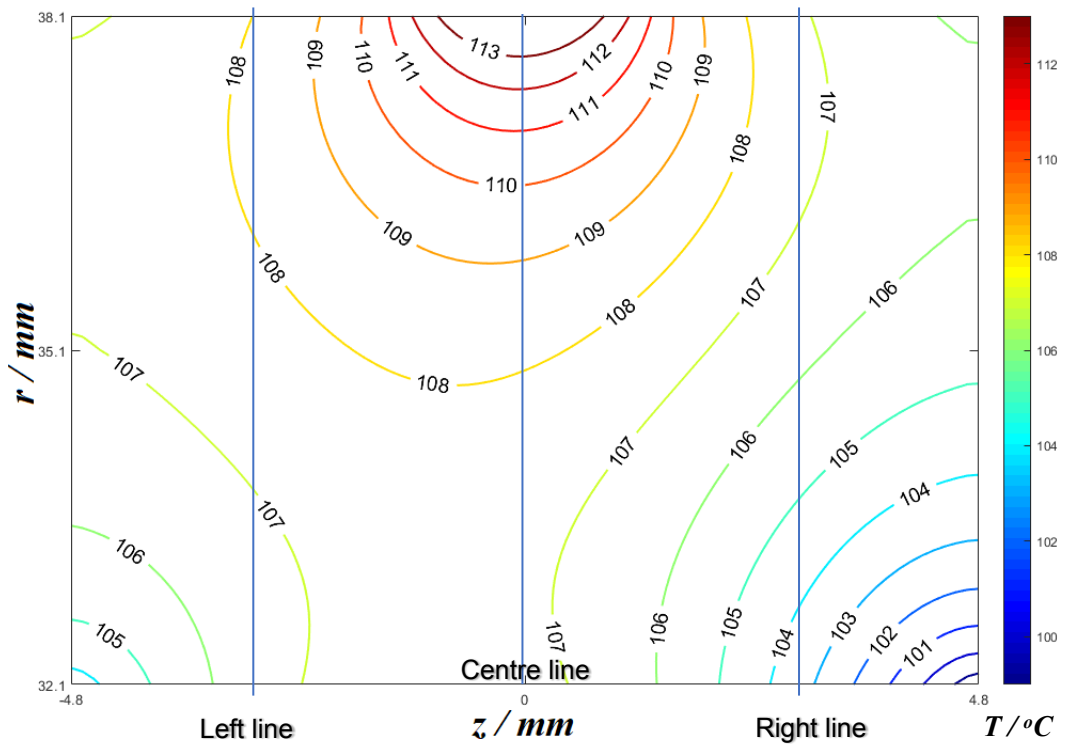


Figure 4-18 Temperature contour for the slow disc for test (D) mesh size 81x57, at time step 1000s

There are slight differences in the temperature distribution between the four previous contour plots. The difference in temperature distribution is most apparent in the upper half of the test disc within the region ($35.1 \text{ mm} \leq r \leq 38.1 \text{ mm}$), and it can be seen at the surface and at the top corners in the previous three figures.

The temperatures along the vertical centre line (shown in blue colour in Figure 4-18) of the slow disc at the time step $t = 1000\text{s}$ are also plotted for the four mesh tests to make a comparison between them as shown in Figure 4-19 below. Where it shows that there are slight differences in temperatures between the four mesh tests, the results obtained from the mesh tests (A), (B) and (C) have differences in temperature at the same position compared to each other, and for mesh test (C) and the finest mesh (D) the differences in temperature are negligible.

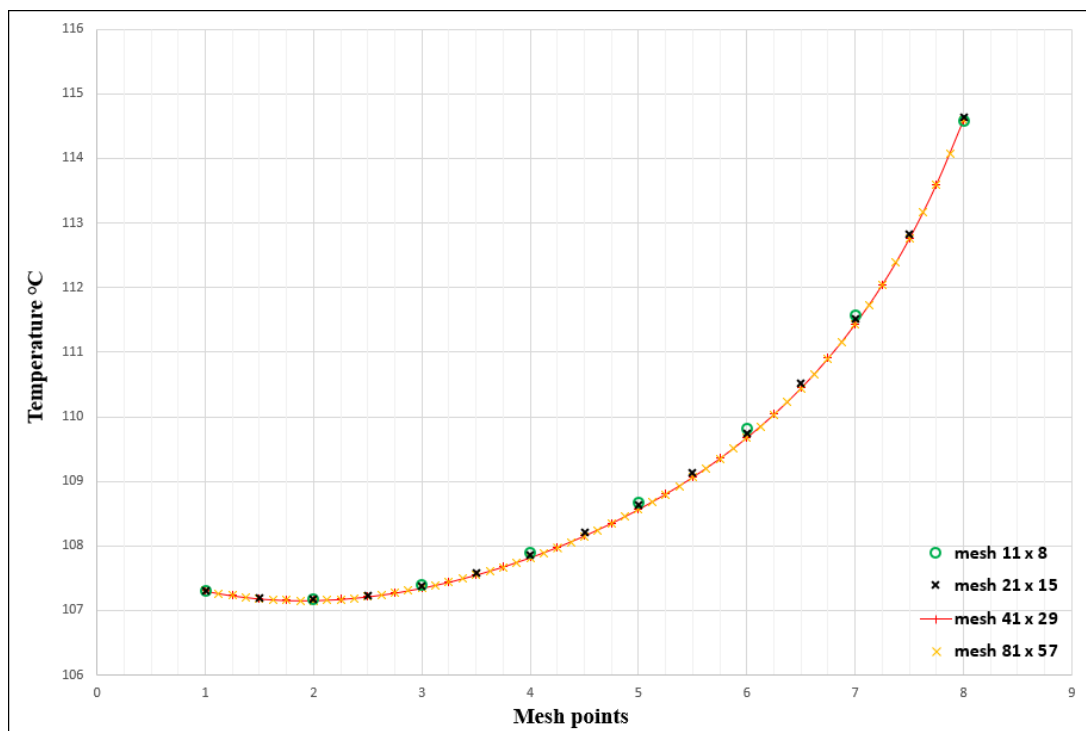


Figure 4-19 Temperatures at $t = 1000\text{s}$ along the vertical centre line for mesh test A, B, C and D

The temperature along the vertical left line and the vertical right line (shown in blue colour in Figure 4-18) are also plotted for the four mesh tests and shown in Figure 4-20 and 4-21 respectively. Again, mesh tests (C) and (D) have the same temperatures and the differences are negligible. However, mesh test (D) it is a time consuming process due to the large amount of data involved in the analysis. Hence, mesh (C) was used as the finest mesh during the mesh investigations.

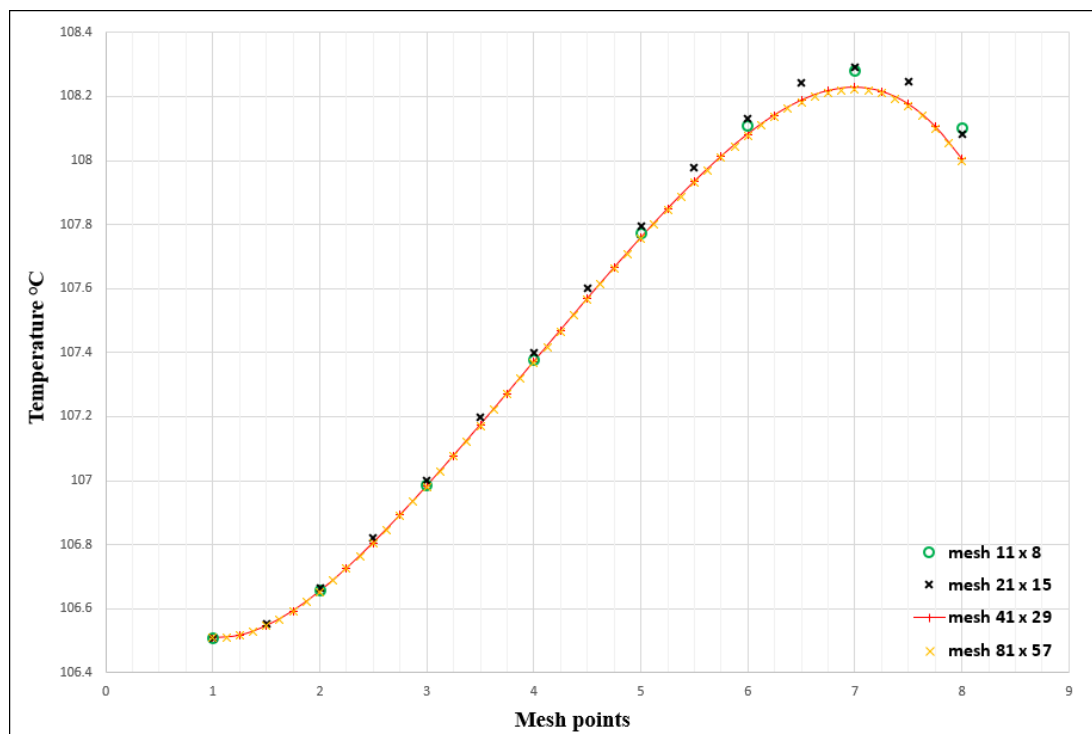


Figure 4-20 Temperatures at time step $t = 1000s$ along the vertical left line for mesh test A, B, C and D

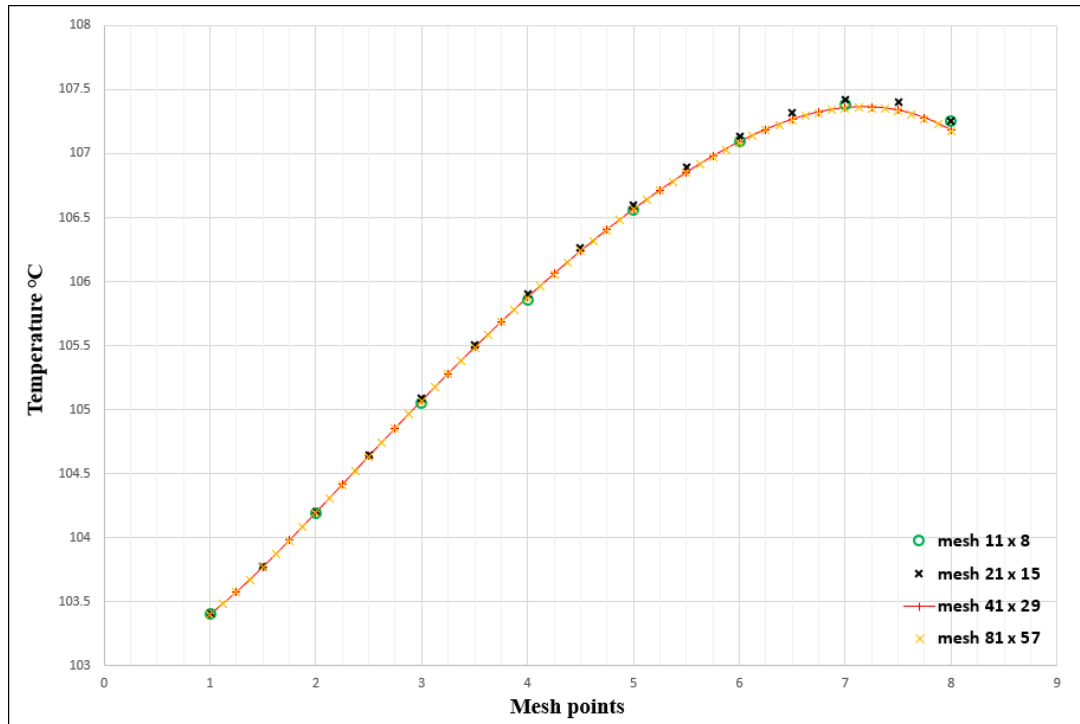


Figure 4-21 Temperatures at time step $t = 1000s$ along the vertical right line for mesh test A, B, C and D

The temperature plots along the three vertical lines (left, centre and right) shows that the temperatures at the lowest boundaries are exactly the same temperatures for the four mesh tests, this is because these temperatures were given by the three thermocouples located at the lower boundary. However, the temperatures change by small amounts as the disc surface is approached, This happens due to the fact that the temperatures near the surface are influenced by the frictional heat flux q_{fr} which is conducted to the disc at the surface and applied over the Hertzian contact width ($2a$), and this frictional heat flux is obtained with different values for each mesh test. The frictional heat flux q_{fr} at time step $t = 1000s$ is applied with a semi-elliptical distribution over the contact width. The way in which this is implemented for meshes A, B, and C is shown in Figure 4-22.

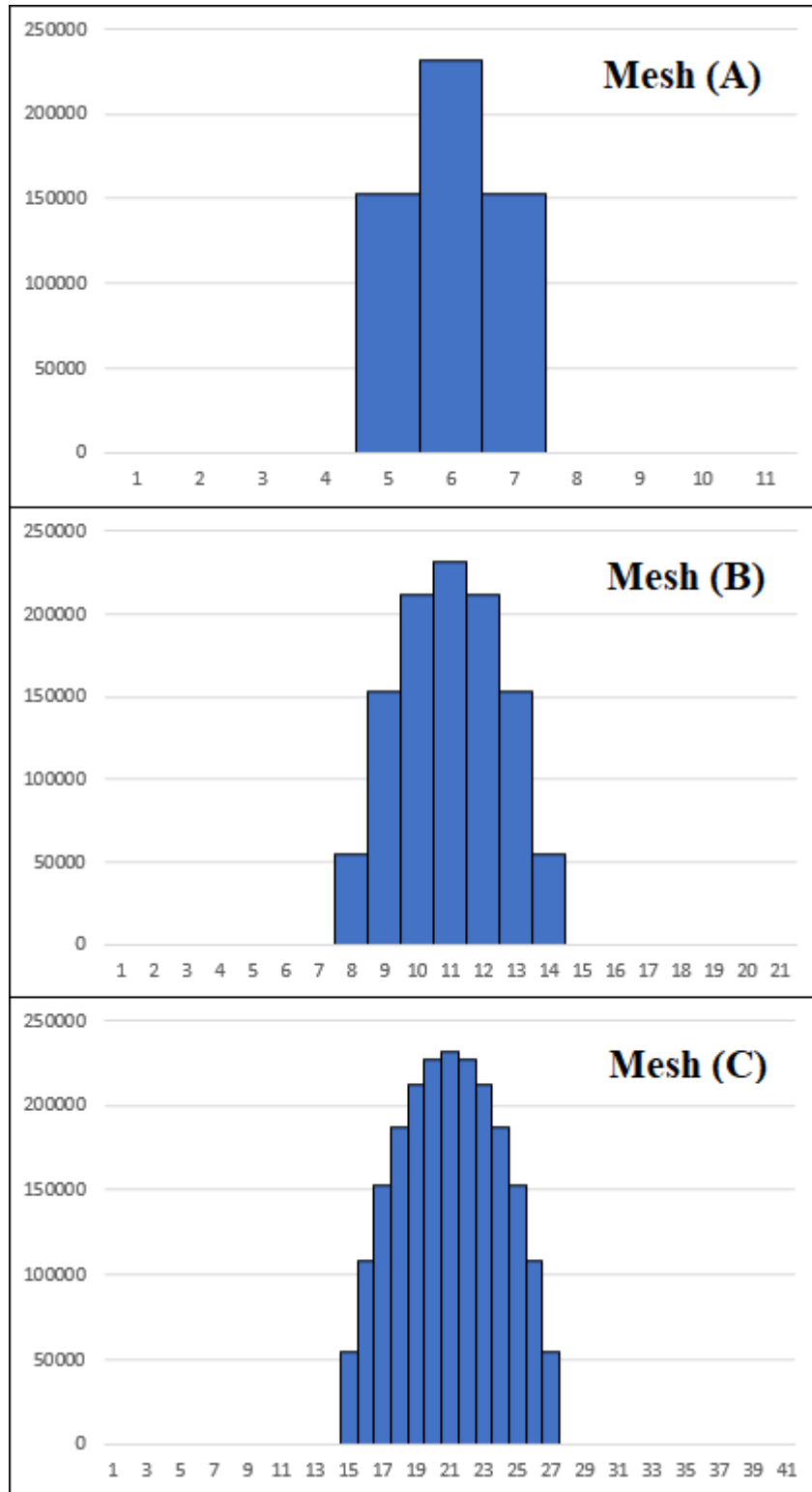


Figure 4-22 Histogram for the frictional heat flux for mesh A, B and C

The values of the heat flux applied at the mesh points, as shown in Figure 4-22, does not correspond to the actual measured friction as the areas under these histograms are different although the bar heights are sampled from the same semi-elliptic distribution. This is because of the variation in resolution from coarse to fine.

The frictional heat flux per metre (circumferential length) for these three mesh tests at time step $t = 1000\text{s}$ is calculated and obtained as following:

Mesh test (A): 512 W/m.

Mesh test (B): 509 W/m.

Mesh test (C): 503 W/m.

The total heat input in mesh test (A) is 1.7% greater than mesh test (C), and the total heat input in mesh test (B) is 1.2% greater than mesh test (C).

The analysis using mesh test (B) was carried out again, however, this time the frictional heat flux q_{fr} values were modified at each time step during the analysis. They were scaled to achieve the same total frictional heat flux as mesh (C)

A comparison between the tests using mesh (B), (C) and the new (B) is made in Figures 4-23, 4-24 and 4-25 which show the temperatures for these tests at the vertical centre line, vertical left line and vertical right line respectively.

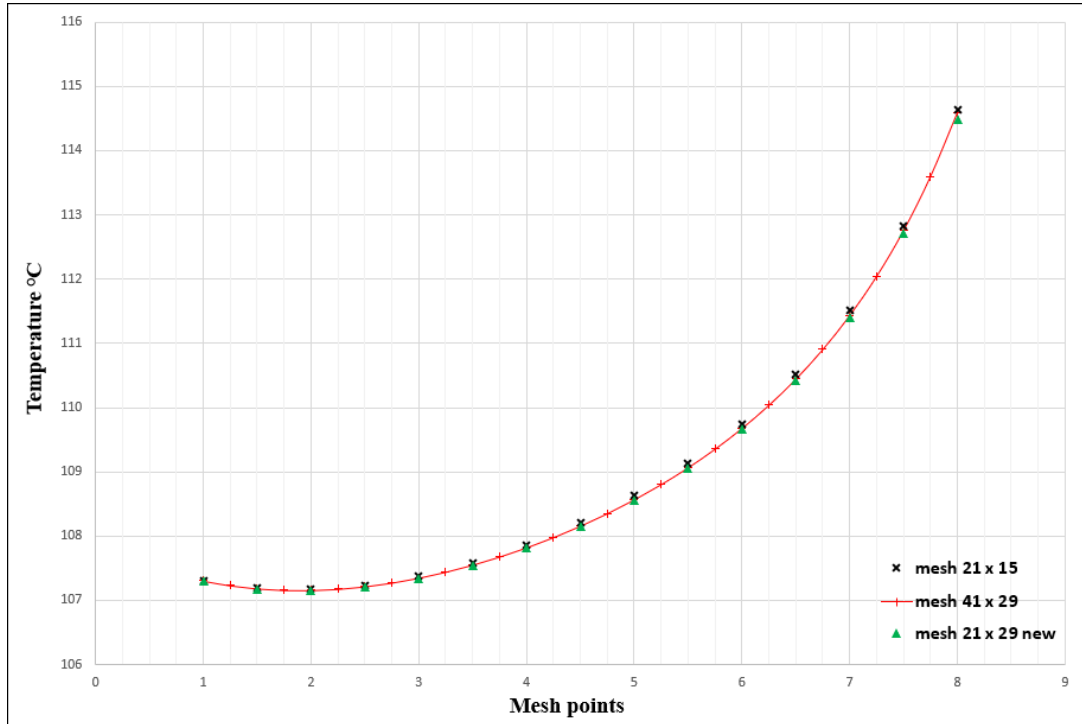


Figure 4-23 Temperatures at $t = 1000s$ along the vertical centre line for mesh B, C and new B

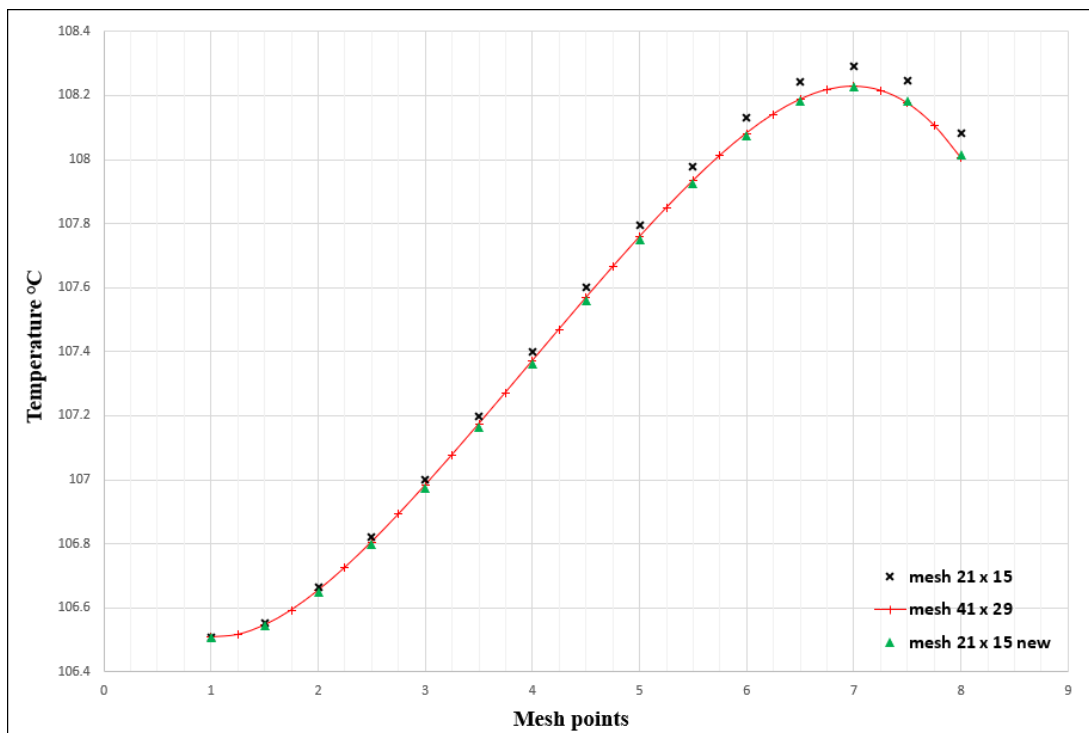


Figure 4-24 Temperatures at $t = 1000s$ along the vertical left line for mesh B, C and new B

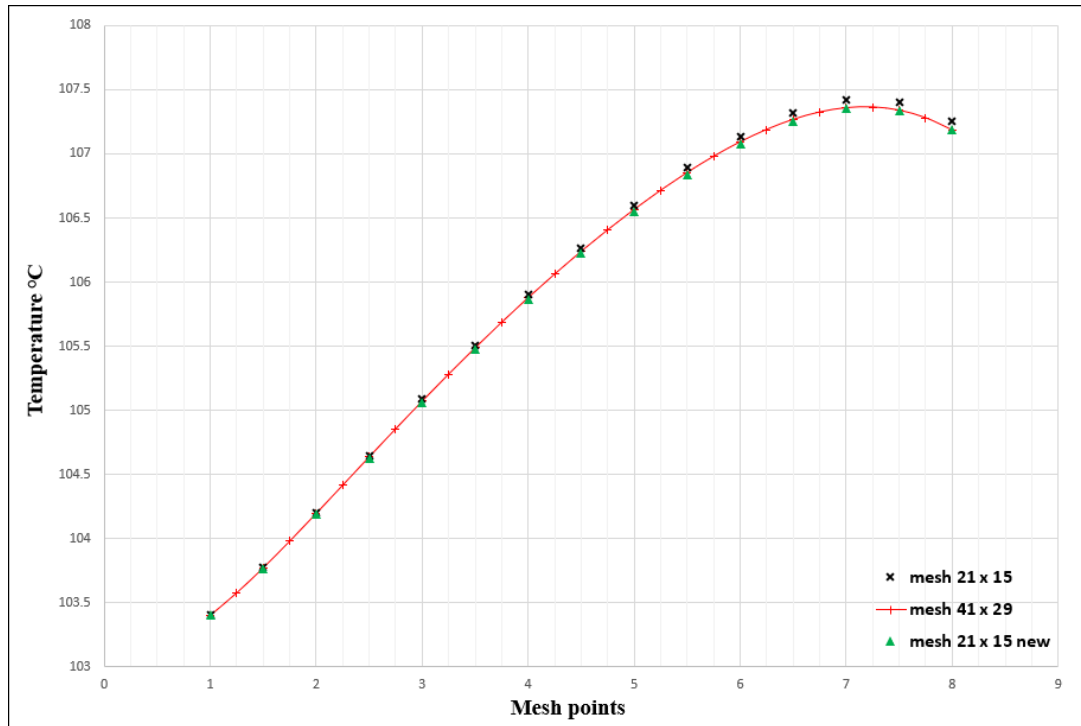


Figure 4-25 Temperatures at $t = 1000s$ along the vertical right line for mesh B, C and new B

Figures 4-23, 4-24 and 4-25 show that the temperatures were lower for the new test (B) compared to the original test of mesh (B), and these new temperatures are on the same temperature curve as mesh (C) where no differences can be observed between them. The differences between the original mesh test (B) analysis and mesh test (C) were therefore due to the different specified heat inputs. There are no significant variations in temperatures between mesh test (B) and mesh test (C) provided that the heat input is the same. This leads to a conclusion that mesh (B) is a mesh independent solution. Hence, mesh (B) is selected as standard in this work, noting that the method for specifying the frictional heat flux on the running track requires minor scaling to ensure the correct total frictional heat flux is applied.

4.4 Analysing an experiment

4.4.1 Analysis method

The solution process previously used by Clarke (2009) and Al-Hamood (2015) was based on using different values of β and h over the range ($0.1 \leq \beta \leq 3$) and ($1 \leq h \leq 1200 \text{ Wm}^{-2}\text{K}^{-1}$) to calculate the temperatures in both discs using the transient analysis method described in Chapter 3. The time varying boundary temperatures measured at points d , b and f were used, and the temperature distributions throughout the experiment were obtained.

The analysis is carried out for both the slow disc and the fast disc for the selected (β , h_s) combination. The values of the calculated temperatures are then compared with the experimentally measured temperatures at points c , a and e to determine the error between the theory and experiment for the (β , h_s) parameters combination. This is quantified by defining errors as:

$$\mathcal{E}_{slow} = \frac{2 \times \left| T_{as_{experiment}} - T_{as_{calculated}} \right| + \left| T_{cs_{experiment}} - T_{cs_{calculated}} \right| + \left| T_{es_{experiment}} - T_{es_{calculated}} \right|}{4} \quad (4.1)$$

$$\mathcal{E}_{fast} = \frac{2 \times \left| T_{af_{experiment}} - T_{af_{calculated}} \right| + \left| T_{cf_{experiment}} - T_{cf_{calculated}} \right| + \left| T_{ef_{experiment}} - T_{ef_{calculated}} \right|}{4} \quad (4.2)$$

Where T_a , T_c and T_e are the temperatures at points a , c and e respectively.

The summations were carried out over the last 200 seconds of the experiment for where it had reached near steady state behaviour.

Figure 4-26 and 4-27 show the results at the last timestep of two analyses for the slow disc that have been carried out by the author with different given (β, h_s) combinations, the first analysis run with $\beta = 0.3$ and $h_s = 300 \text{ Wm}^{-2}\text{K}^{-1}$ for the slow disc, where the second analysis run with $\beta = 0.6$ and $h_s = 800 \text{ Wm}^{-2}\text{K}^{-1}$ for the slow disc.

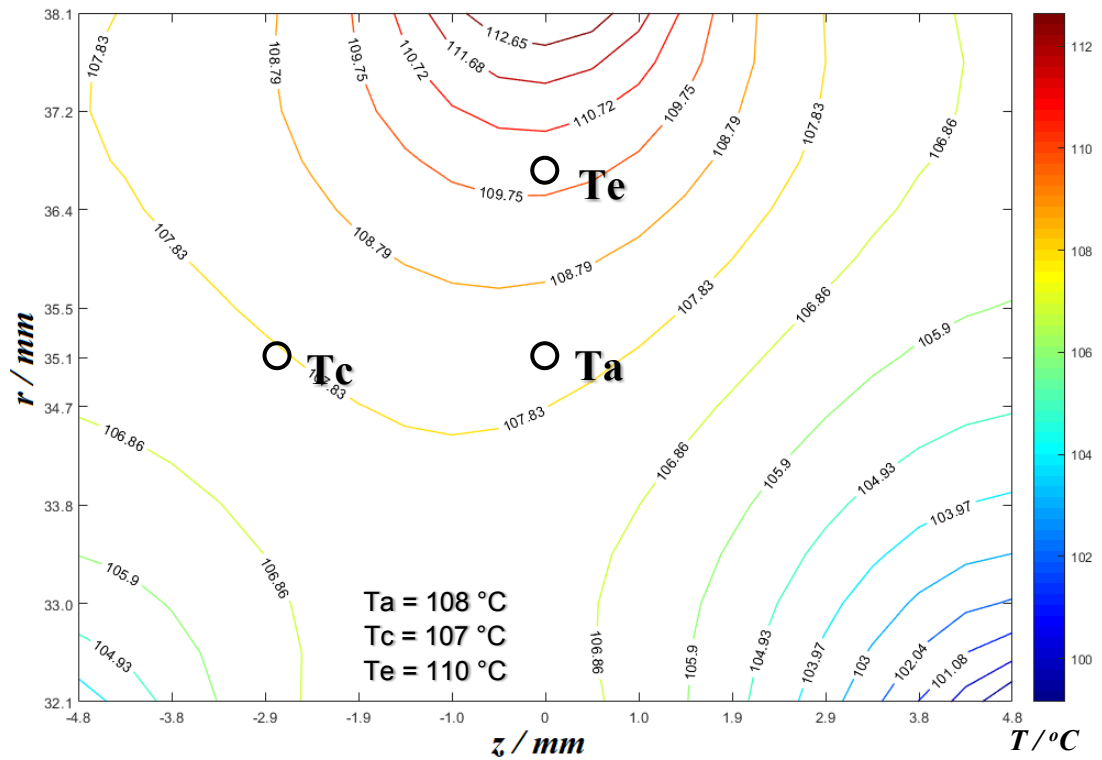


Figure 4-26 Contour plot of temperature distribution in $^{\circ}\text{C}$ of the slow disc at the last timestep for $\beta = 0.3$ and $h_s = 300 \text{ Wm}^{-2}\text{K}^{-1}$

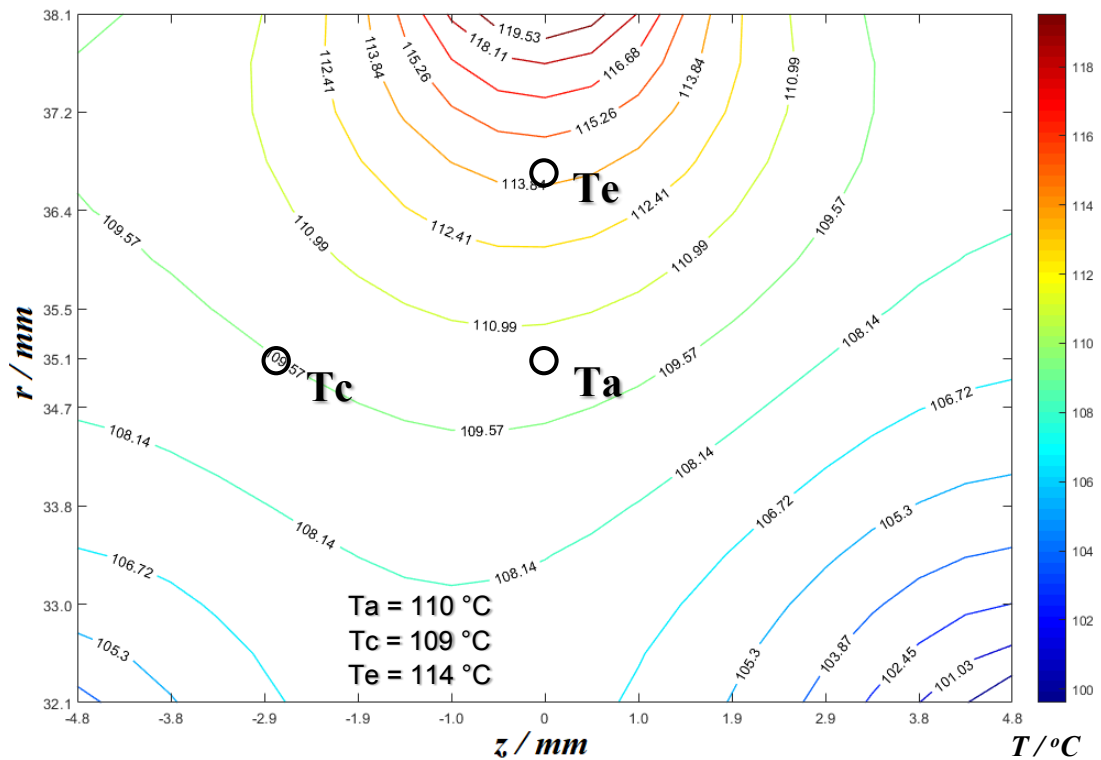


Figure 4-27 Contour plot of temperature distribution in °C of the slow disc at the last timestep for $\beta = 0.6$ and $h_s = 800 \text{ Wm}^{-2}\text{K}^{-1}$

The numerical solution process of the EHL experiment of these two analyses was carried out using a Fortran 90 code written for a single disc with given values of (β , h_s). For each iterative sweep, the error is defined as the maximum value of $|T_{(i,j)_{new}} - T_{(i,j)_{old}}|$ during the sweep, and the process regarded as converged when the error $< 10^{-5}$. At the end of this process, the temperature distribution within the disc at the last timestep was stored and then tabulated in a spreadsheet. The flow chart in Figure 4-28 shows the steps in sequence of this numerical process starting from setting up the (β , h_s) values until obtaining the result where the temperature distribution is tabulated.

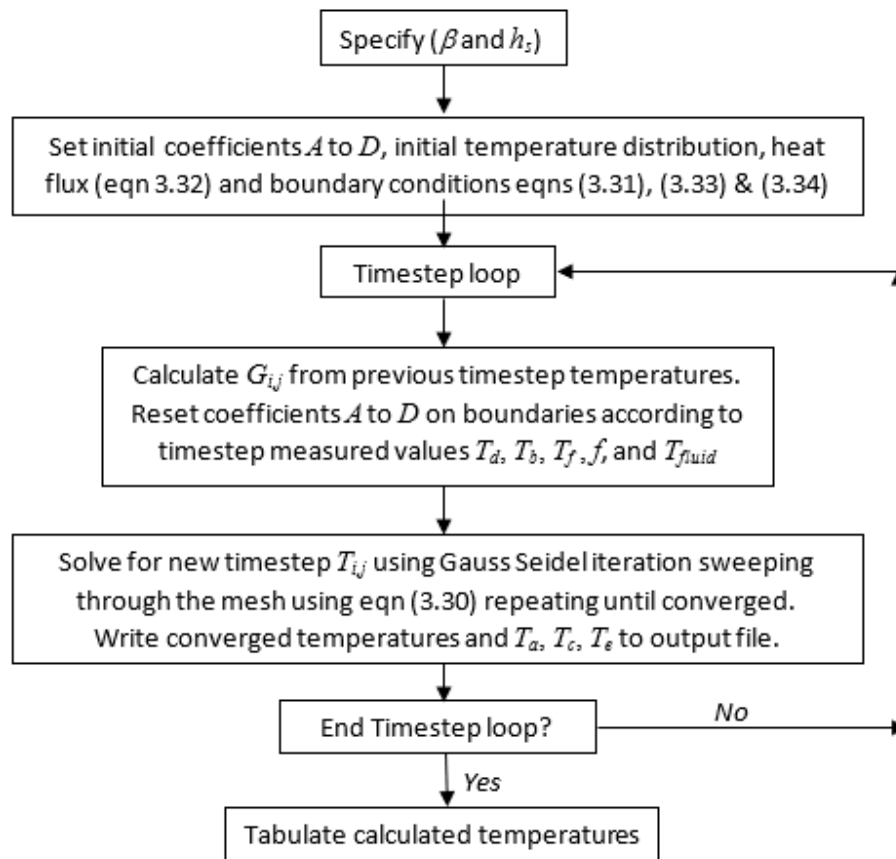


Figure 4-28 Flow chart to calculate temperature distribution for given values of β and h

4.4.2 Relationship between h_s and h_f

Various studies and experimental programmes have been carried out by (Anderson & Saunders, 1953), (Dropken & Carmi, 1957), (Cardone *et al.*, 1997) and (Ozerdem, 2000) to investigate convective heat transfer of a cylinder rotating about its horizontal axis in a fluid in order to identify the value of β as a relationship between h_s and h_f can be expected. During these experiments and studies, the relation between the Nusselt number Nu and the Reynolds number Re was determined as:

$$Nu = C(Re)^n \quad \text{where } C \text{ is a constant}$$

And it can be expressed in the current notation as:

$$\frac{hD}{k_0} = C \left(\frac{uD}{\nu} \right)^n \quad (4.3)$$

Where h is the heat transfer coefficient (W/m²K)

k_0 is the thermal conductivity of fluid (W/mK)

u is the surface speed (m/s)

ν is the kinematic viscosity of fluid (m²/s)

Hence, the heat transfer coefficients for the fast and the slow disc can be expressed as:

$$h_f = C \frac{k_0}{D} \left(\frac{D}{\nu} \right)^n (u_f)^n \quad (4.4a)$$

$$h_s = C \frac{k_0}{D} \left(\frac{D}{\nu} \right)^n (u_s)^n \quad (4.4b)$$

Consequently, the ratio between the heat transfer coefficients h_s and h_f depends only on their peripheral speeds and the power n :

$$\frac{h_f}{h_s} = \left(\frac{u_f}{u_s} \right)^n = \chi \quad (4.5)$$

The analyses carried out by Al-Hamood (2015) to determine the heat partition showed that the minimum error \mathcal{E} position cannot be clearly identified when plotting the error in terms of the (β, h) parameters combination as shown in Figure 4-29. This figure

plots contours of ε_{slow} for varying (β, h_s) , and separately contours of ε_{fast} for varying (β, h_f) .

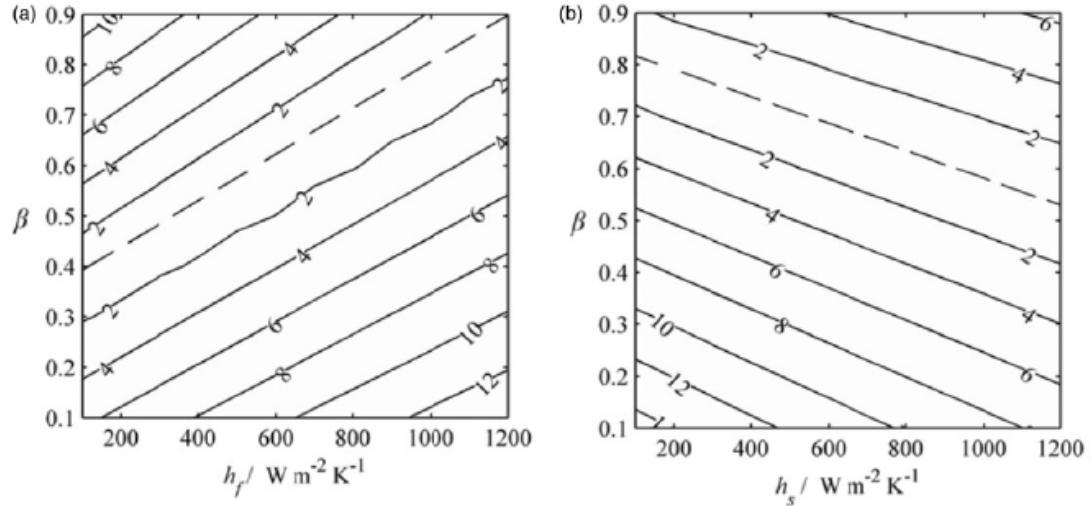


Figure 4-29 Contour plots of error ε (in $^{\circ}\text{C}$) for systematic variation of β and h : (a) for the fast disc and (b) for the slow disc (Al-Hamood, 2015)

This is due to the fact that this error is located on the dashed line between two parallel lines with lower values of ε . The linear equations of the dashed lines from Figure 4-29 which represent the minimum error can be written as:

$$\beta = A + Bh_f \quad (4.6)$$

$$\beta = E + Gh_s \quad (4.7)$$

Where the coefficients A , B , E and G have different values in each analysis.

The red dashed box shown in flow chart in Figure 4-30 is single disc analysis, it was carried out for each disc individually over a specified range of (β, h_s) values. Therefore, the error contour shown in Figure 4-29 was obtained and then plotted using this process twice, once for the slow disc then for the fast disc.

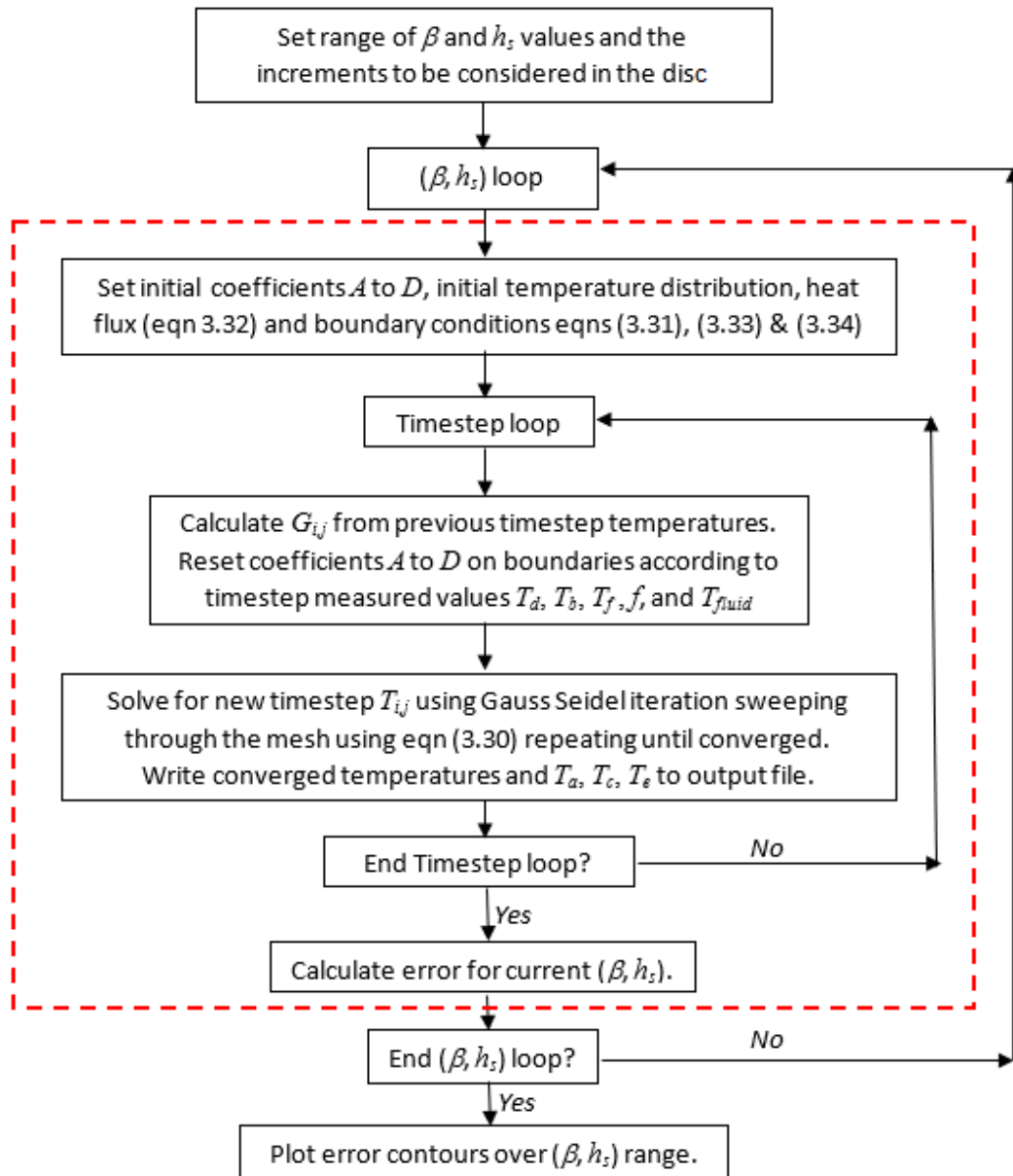
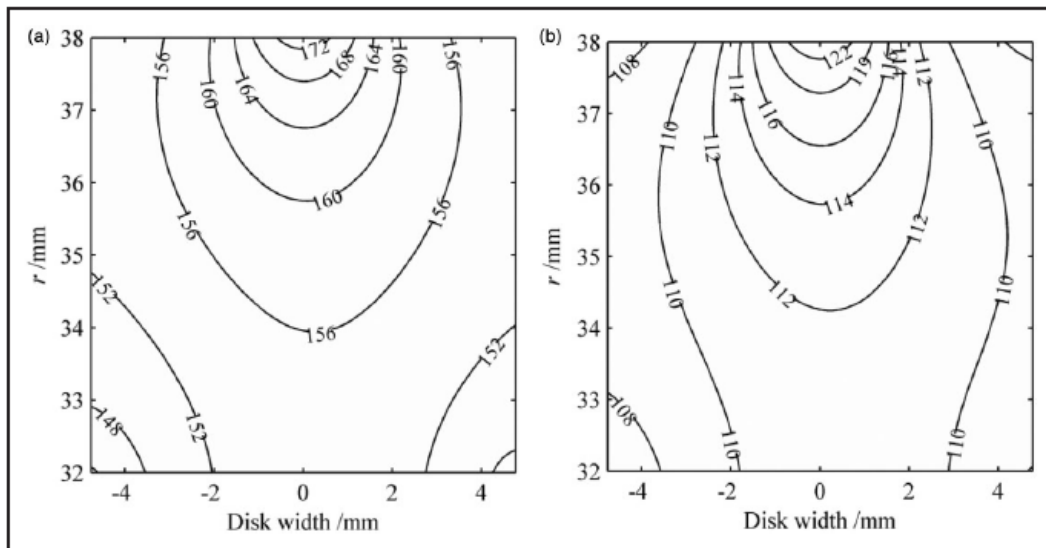
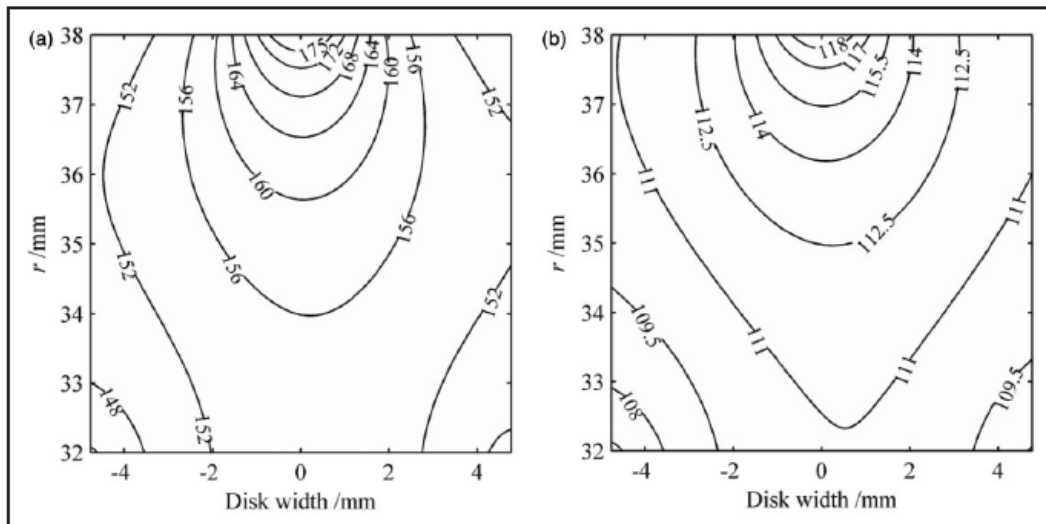


Figure 4-30 Flow chart for single disc analysis. Broken red box is the single disc transient analysis of Figure 4-28

During Al-Hamood's analysis, h_s and h_f were set to $100 \text{ Wm}^{-2}\text{K}^{-1}$ as the smallest value, and from equations (4.6) and (4.7) the largest and smallest β values common to both sets of analyses were obtained as $\beta = 0.53$ and $\beta = 0.82$. The temperature distributions obtained at these values of β are shown in Figure 4-31.



Calculated temperature distributions in °C for: (a) fast disk and (b) slow disk with $\beta = 0.53$.



Calculated temperature distributions in °C for: (a) fast disk and (b) slow disk with $\beta = 0.82$.

Figure 4-31 The calculated temperature distributions for $\beta = 0.53$ and $\beta = 0.82$ (Al-Hamood, 2015)

Making β the subject and solving equations (4.5), (4.6) and (4.7) gives the expression:

$$\beta = \frac{\chi BE - AG}{\chi B - G}$$

The value of power n is found to be between 0.57 and 0.8 in the literature, and Al-Hamood (2015) used the value $n = 0.667$ in his analysis as it is the most accepted value according to the literature. The gearing arrangement in the test rig delivers a

sliding/rolling ratio of 1.24 hence $\frac{u_f}{u_s} = 4.26$.

A series of experiments were carried out with four different sliding speeds 10, 13, 16 and 20 m/s, and four different loads were applied for each of these sliding speeds: 850, 1460, 1850 and 2320N so that is a maximum Hertzian contact pressures of 1, 1.2, 1.3 and 1.4 GPa. During these experiments, β values of between 0.71 and 0.77 were obtained which is generally consistent with those obtained by Clarke *et al.*, (2006).

The experiments were repeated for two tests (rolling/sliding speed 10 and 20 m/s) with different values of power n to examine the sensitivity of β to the n values. Figure 4-32 shows the results where it is clear that β is insensitive to the n values.

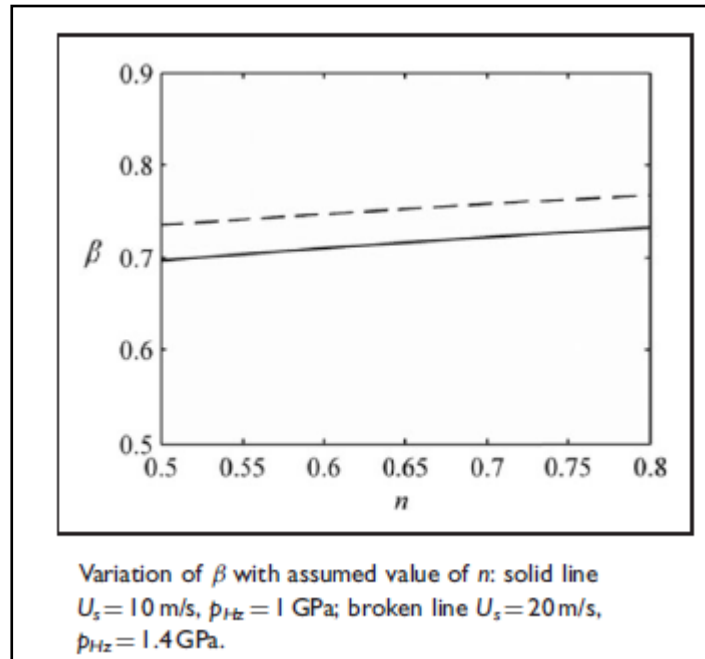


Figure 4-32 results of sensitivity test for β and power n (Al-Hamood, 2015)

In the current research, the error minimisation method was improved by considering the total error rather than that of each individual disc. The initial step was to repeat the analysis method of Al-Hamood for the test temperature data measured. The error analysis was then carried out for set values of (β, h) over the range $(0 \leq \beta \leq 1)$ in steps of 0.1 and $(100 \leq h \leq 1200 \text{ Wm}^{-2}\text{K}^{-1})$ in steps of $100 \text{ Wm}^{-2}\text{K}^{-1}$ with the power n value set to be 0.65.

At the end of these analyses, the resulting error values of each disc are tabulated in output spreadsheets. Figures 4-33 and 4-34 show the contour plot for the resulting error values for the slow disc ε_{slow} and the fast disc error ε_{fast}

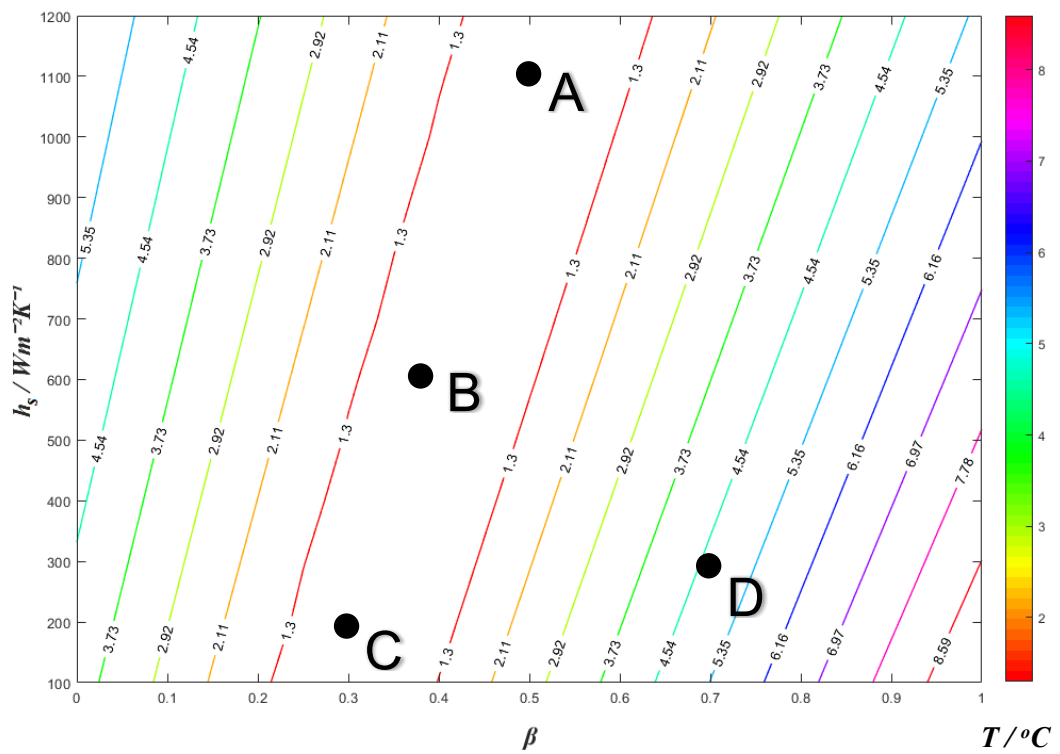


Figure 4-33 Error ε_{slow} values in $^{\circ}\text{C}$ for the slow disc over the last 200 seconds of the steady state

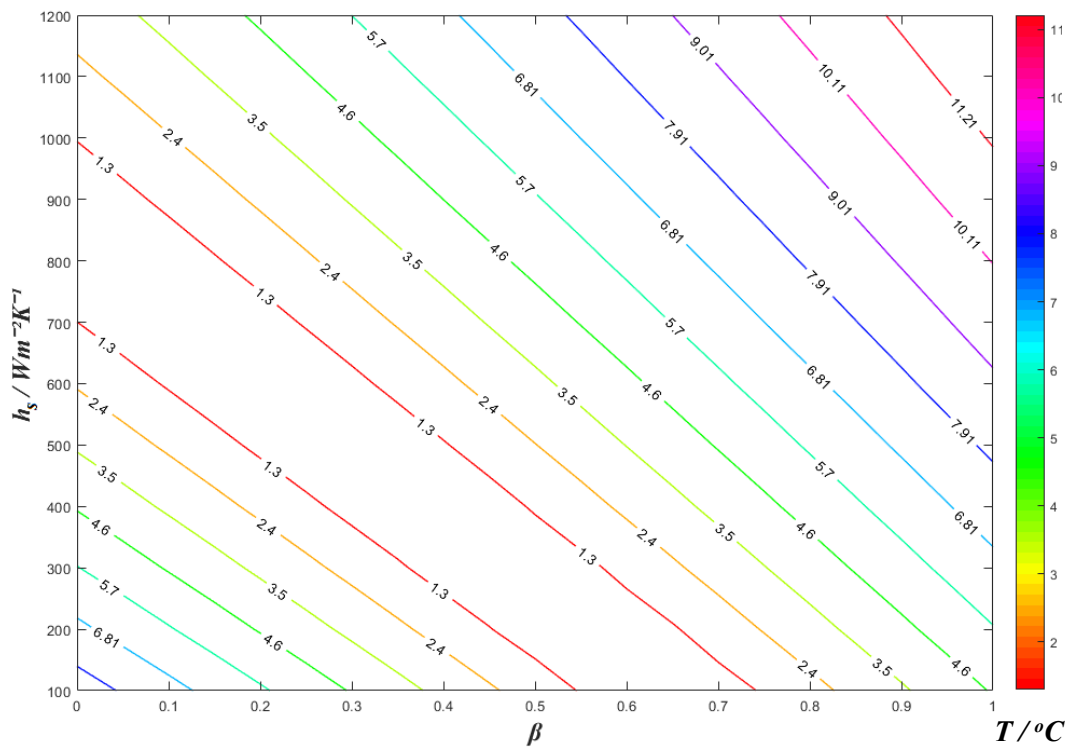


Figure 4-34 Error ε_{fast} values in $^{\circ}\text{C}$ for the slow disc over the last 200 seconds of the steady state

As shown in the figures, the minimum error of the slow disc ε_{slow} is located between the two red lines labelled with error = 1.3 °C and it is clearly not a clear-cut minimum, and the same thing can be observed regarding the minimum error of the fast disc ε_{fast} .

The lack of a clear-cut minimum error position is because different combinations in these analyses, four (β, h_s) combination values for the slow disc were selected as following: $(\beta = 0.5, h_s = 1100 \text{ Wm}^{-2}\text{K}^{-1})$, $(\beta = 0.4, h_s = 600 \text{ Wm}^{-2}\text{K}^{-1})$, $(\beta = 0.3, h_s = 200 \text{ Wm}^{-2}\text{K}^{-1})$ and $(\beta = 0.7, h_s = 300 \text{ Wm}^{-2}\text{K}^{-1})$ and they are represented in Figure 4-33 as points A, B, C and D respectively. The temperature distributions at the last time step of these points are plotted and shown in Figures 4-35, 4-36, 4-37 and 4-381 respectively.

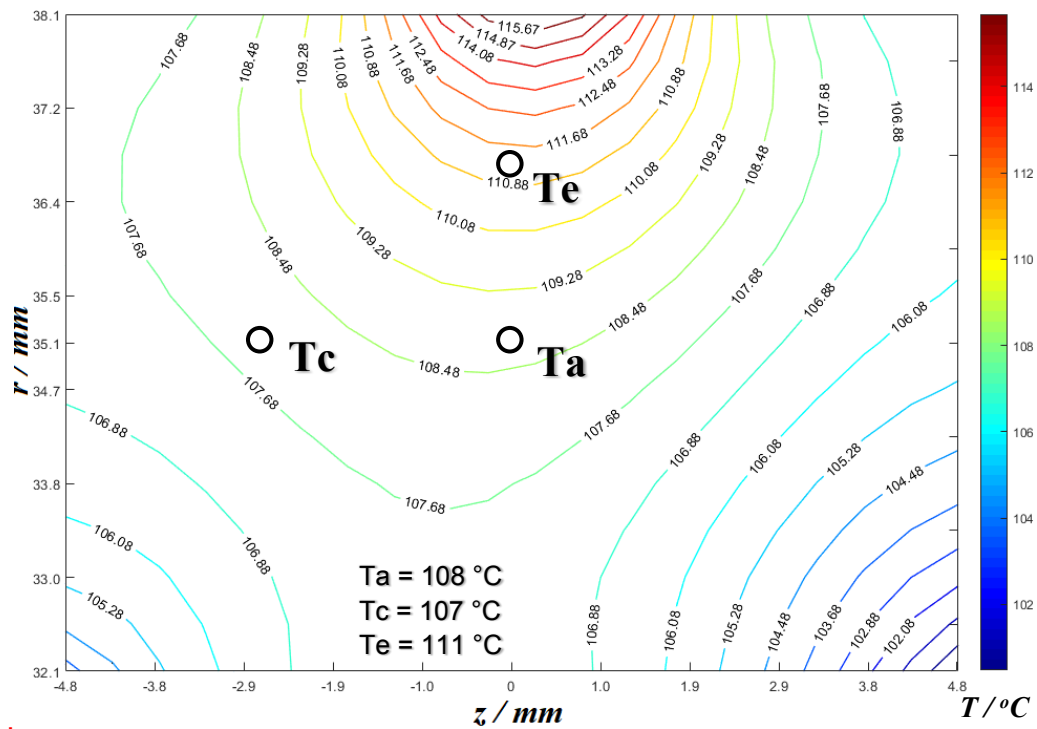


Figure 4-35 Point (A) Temperature distribution in °C within the slow disc at the last time step based on $\beta = 0.5$ and $h_s = 1100 \text{ Wm}^{-2}\text{K}^{-1}$

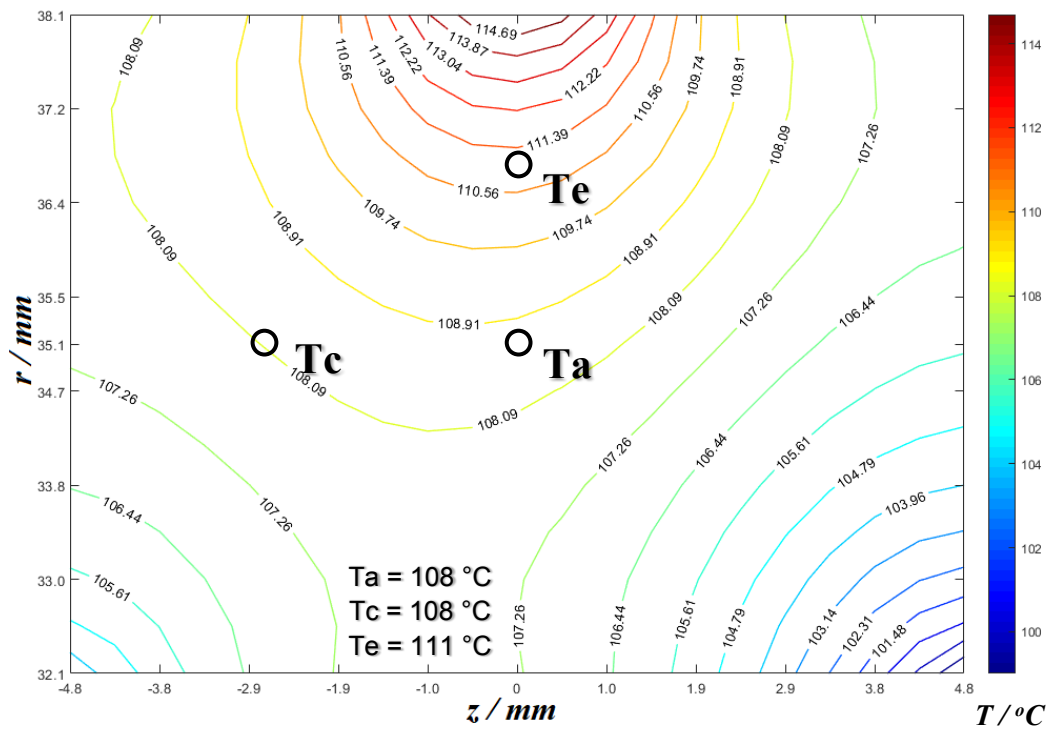


Figure 4-36 Point (B) Temperature distribution in $^\circ\text{C}$ within the slow disc at the last time step based on $\beta = 0.4$ and $h_s = 600 \text{ Wm}^{-2}\text{K}^{-1}$

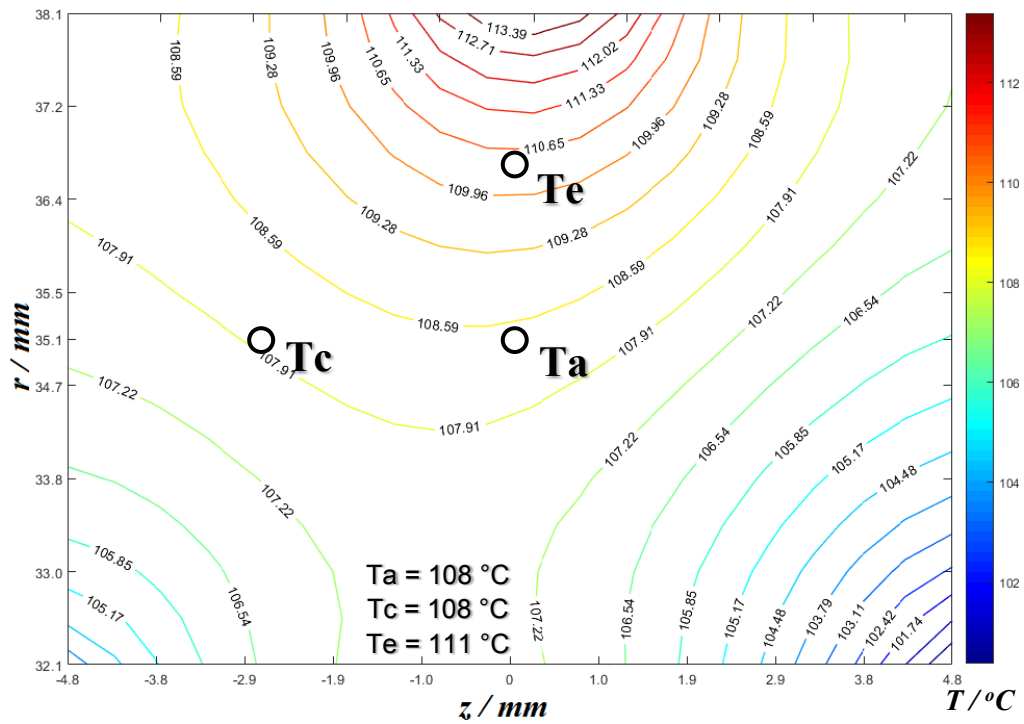


Figure 4-37 Point (C) Temperature distribution in $^\circ\text{C}$ within the slow disc at the last time step based on $\beta = 0.3$ and $h_s = 200 \text{ Wm}^{-2}\text{K}^{-1}$

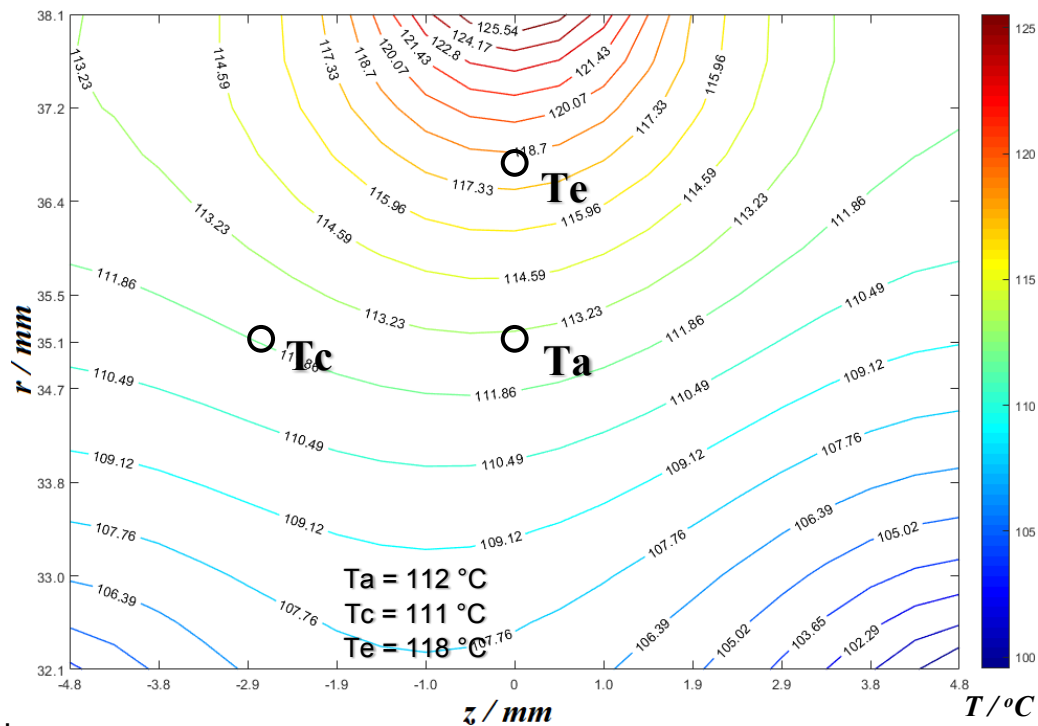


Figure 4-38 Point (D) Temperature distribution in °C within the slow disc at the last time step based on $\beta = 0.7$ and $h_s = 300 \text{ Wm}^{-2}\text{K}^{-1}$

It can be seen from the previous contour plots (points A, B, and C) that the temperature distribution especially near the contact zone is different at any point on the line of minimum error as the temperature behaviour here is governed by the heat flow conducted to the disc and the heat removed at the surface. This means, the temperature near the contact zone is more sensitive to (β, h_s) values. Taking an example a comparison of the temperature distribution between the two extreme points on the line of minimum error which are A and C, the temperature is 116 °C at the contact zone in Figure 4-35, where it is 113 °C in Figure 4-37 at the same location for the (β, h_s) values. This happens because the error is reduced at thermocouples T_a, T_c level (at the 35 mm radius) and the temperature at the 32 mm radius (inner radius) is the same (also at thermocouple T_e level the error is reduced). Consequently, all points along the line of minimum error have the same temperature distribution within the region ($32 \text{ mm} \leq r \leq 35 \text{ mm}$) where it is not the same case with regards to the outer

region. It is also the case that the additional flow of heat conducted into the disc is also removed from the disc by convection before reaching the thermocouples.

The way in which the total error can be used to reduce this uncertainty is explored in Chapter 5.

Chapter 5 Development of the test modelling approach

5.1 Introduction

This chapter highlights the development of the numerical method used for analysing the disc pair total error, initially by a graphical approach and then by adopting a 2-dimensional simplex minimisation method in parameters (β, h_s) . Subsequently investigations were carried out to determine the value of n using the simplex method analysis. These revealed some inconsistencies in temperature measurements causing several investigations to be carried out. This led to a new investigative approach based on generating synthesised experimental temperature datasets for both discs for known (β, h_s, n) values and using the minimisation method and the synthesised temperature to evaluate whether the set (β, h_s, n) values could be determined effectively. Synthesised experiments of this form were used to assess the effect of including noise and losing precision in the temperature datasets and, finally, to determine the optimum positioning of the temperature measurement thermocouples.

5.2 Total error variation (with β and h)

The numerical solution process of the flow chart given in Figure 4-30 calculates the error for an individual disc in terms of the (β, h_s) combination during the last 200 seconds of the transient analysis. The slow disc error ε_{slow} and fast disc error ε_{fast} (equations 4.1 and 4.2) can be calculated for the same (β, h_s) combination, so that when both discs have been analysed the errors can be added together to give the total error ε_{tot}

$$\varepsilon_{tot} = \varepsilon_{slow} + \varepsilon_{fast} \quad (5.1)$$

for both discs using the same (β, h_s) combination values. Repeating this process with a systematic variation of the trial (β, h_s) combination values taking equation (4.5) into account establishes how ε_{tot} varies with (β, h_s) .

The flow chart in Figure 5-1 shows the process of this analysis, where the calculation of the total error for both discs for the same given (β, h_s) combination is carried out within the blue dashed box.

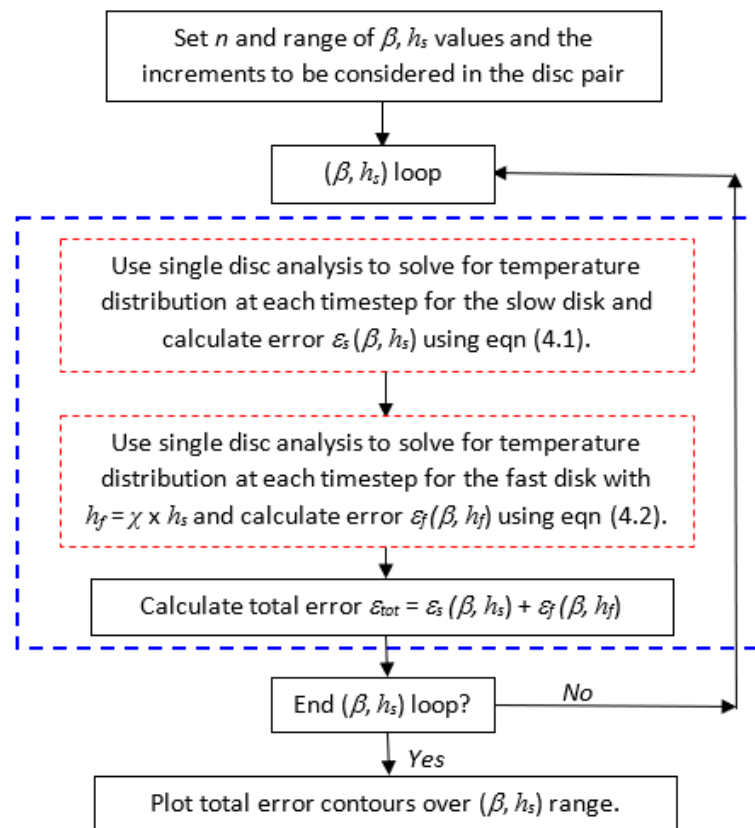


Figure 5-1 Flow chart for disc pair error analysis for given value of parameter n . Broken red box is the single disc transient analysis of Figure 4-30

This disc pair error analysis was carried out for the test data with the power n value set to 0.7. The heat partition coefficient is set over the range ($0 \leq \beta \leq 1$) in steps of 0.1 and the heat transfer coefficient is set over the range ($100 \leq h_s \leq 1200 \text{ Wm}^{-2}\text{K}^{-1}$) in steps of $100 \text{ Wm}^{-2}\text{K}^{-1}$ for the slow disc, where for the fast disc the heat partition is $1 - \beta$ and $h_f = h_s \chi$. For this given n value, χ is equal to 2.76 based on $\chi = \left(\frac{u_f}{u_s}\right)^n = 4.26^{0.7}$. Figure 5-2 shows a contour plot of ε_{tot} and because the total error is used these contours become closed and identify a minimum error at approximately (0.36, 400) in the (β, h_s) parameter space.

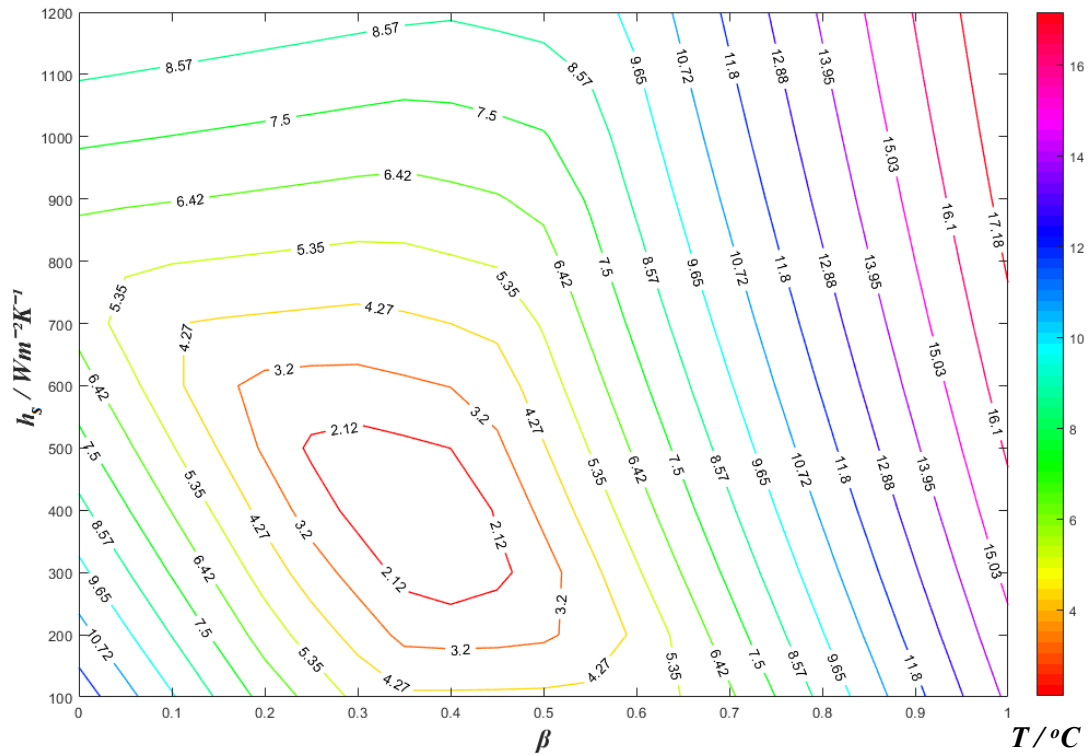


Figure 5-2 Total error plot in °C for both discs, power $n = 0.7$

The minimum total error in this analysis is located inside the red closed contour labelled with error = 2.12 °C near to point $\beta = 0.36$, $h = 400 \text{ Wm}^{-2}\text{K}^{-1}$. With this

improved total error analysis there is a clear-cut minimum. However, it still does not show an exact value of the minimum total error, the smallest contour value here spans the range $\beta = 0.25$ to 0.45 and $h_s = 250$ to $550 \text{ Wm}^{-2}\text{K}^{-1}$. It is not possible to identify the exact (β, h_s) values that correspond to the exact minimum error without having a finer spacing of test points using smaller increments of β and h_s . Hence, another analysis was carried out with finer mesh of (β, h_s) values that enclose the closed red minimum error contour. These new values were set to be: $(0.35 \leq \beta \leq 0.45)$ in steps of 0.01 and the heat transfer coefficient is set over the range $(300 \leq h_s \leq 500 \text{ Wm}^{-2}\text{K}^{-1})$ in steps of $20 \text{ Wm}^{-2}\text{K}^{-1}$. The resulting errors are plotted as shown in Figure 5-3

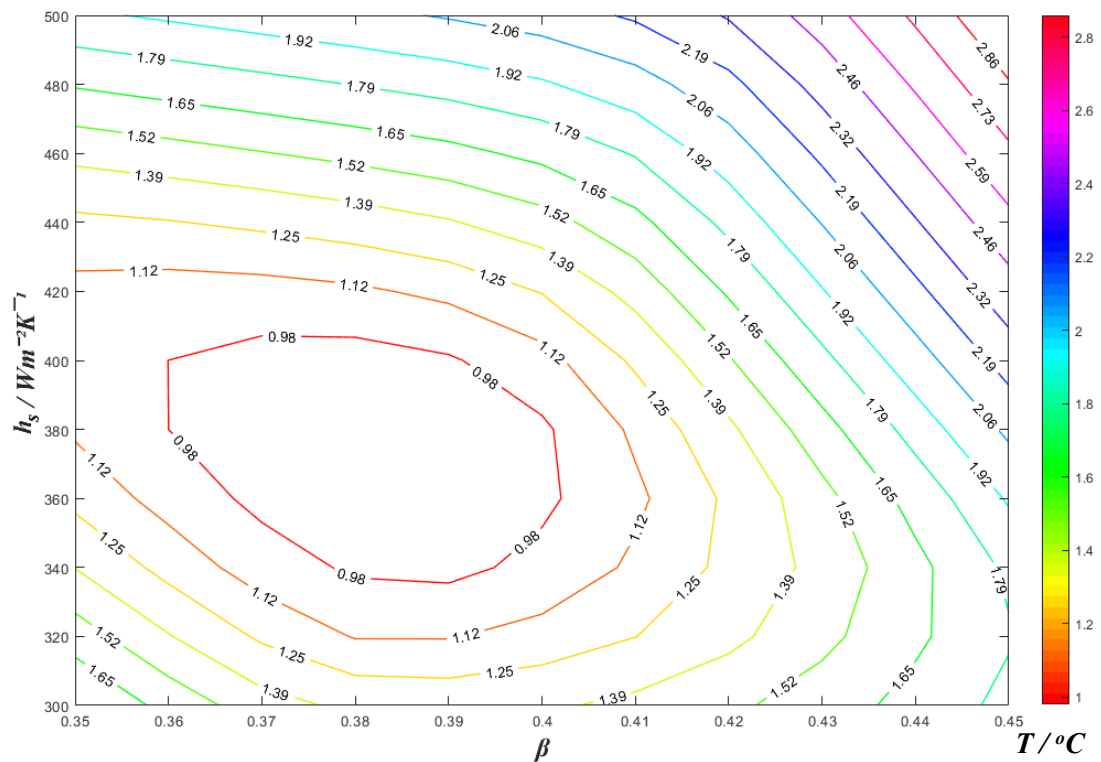


Figure 5-3 Finer mesh for total error plot in $^{\circ}\text{C}$ for both discs, power $n = 0.7$

Here, with this finer mesh error plot, the minimum total error occurs within the new red minimum error contour labelled $\epsilon_{tot} = 0.98^{\circ}\text{C}$. The error has decreased compared

to the previous coarse mesh where it was within error contour 2.12 °C. This approach led to a sequence of analyses, where at the end of each analysis, the resulting total error was plotted and the range of (β, h_s) values that surrounds the new minimum error of the current analysis became the new range values for the finer mesh to be used in the following analysis. Figure 5-4 illustrates a finer mesh analysis that has been carried out using the new range of (β, h_s) values from Figure 5-3.

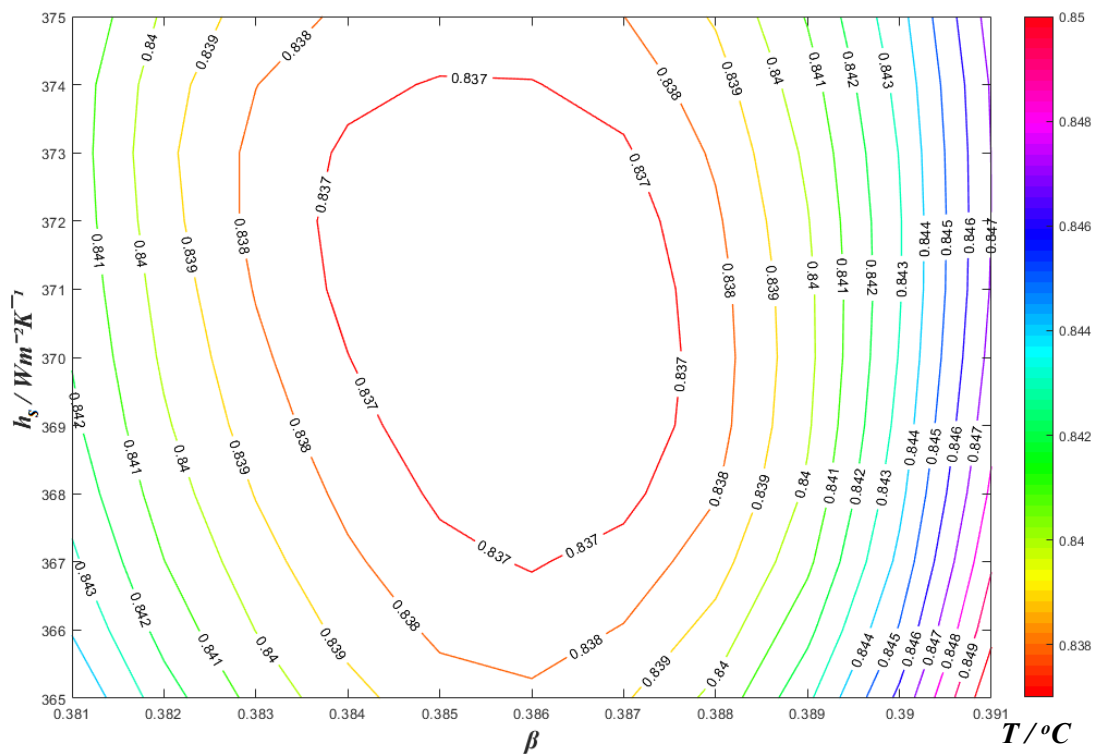


Figure 5-4 Finer mesh for total error plot in °C for both discs, power $n = 0.7$

From the contour of total error in Figure 5-4, the minimum total error is again located inside the new red circle with $\varepsilon_{tot} = 0.837^\circ\text{C}$ and it became smaller. As mentioned, the finer mesh leads to a new range of (β, h_s) values which surrounds a smaller error value. There are limitations in this approach as the contour plot suggests that there are ε_{tot} values in the data that are smaller than 0.837°C although the scale has a

minimum value of 0.837°C. The finer meshes are required to obtain the minimum point as can be seen as the minimum in Figure 5-4 is at point (0.386, 371) whereas the estimated position in Figure 5-2 is (0.36, 400) in term of (β, h_s) parameter space.

This process of finding the minimum total error works well and can be used to establish the (β, h_s) point that has the minimum total error for a given n value. However, a series of analyses needs to be carried out in order to find the minimum total error with its (β, h_s) values for that given power n value. This is time consuming from an organisational point of view and also takes considerable processing time to obtain the final result as at the end of each analysis a new finer mesh analysis needs to be carried out to find the smaller error value and its (β, h_s) values. It would be possible to fit a 2nd order surface to the datapoints within the smallest contour and use calculus to find its minimum position and minimum value, but this would introduce a further step in the process. Since the problem posed in terms of ε_{tot} has a clear well defined minimum it is possible to use a faster method to calculate and find the minimum total error at the end of the analysis without the need of repeating the analysis for all of the (β, h_s) points trialled in the multi stage graphical process. There are a number of possible methods for non-linear optimisation. For the current work the minimum error problem has a single clear minimum as seen from the error contour plots. Also the total error obtained at a (β, h_s) parameter point is a single value and

the gradients of the error surface $\frac{\partial \varepsilon_{tot}}{\partial \beta}$ and $\frac{\partial \varepsilon_{tot}}{\partial h}$ are not available without

approximating based on further analysis points $(\beta+\Delta\beta, h_s)$ and $(\beta, h_s+\Delta h_s)$. In these circumstances the Downhill Simplex method is a reliable choice. It is described in the next section and was implemented using the published code available in Press *et al.*, (1996), which also provides a number of other options together with a critique of the strengths and weaknesses of all the methods.

5.3 Downhill simplex method for non-linear minimisation

The need for function optimization is a common mathematical problem encountered in solving a wide range of real-world problems. In the case of well-defined analytic functions, optimization can be easily obtained through calculating the gradient and evaluating the zero. On the other hand, functions such as ε_{tot} that are not well defined can be optimized through taking the function's derivatives. To do this, various numerical methods for optimization and minimization can be used, one of these methods is the downhill simplex method adopted in this research. A detailed description of this method is given in the following sections.

5.3.1 Basics of the Downhill Simplex method

The downhill simplex method is basically defined as a multidimensional optimization method that is based on utilizing geometric relationships in order to support the process of finding the minimum values of functions. A key feature of this method is that it does not need to take the function's derivatives. It instead generates its own pseudo-derivative through finding adequate points to identify a derivative for every independent variable related to the evaluated function. The overall method revolves around a simplex which is a geometric item which comprises $N + 1$ vertex. The term (N) refers to the number of independent variables in the function. The downhill simplex method does not utilize any one dimensional minimization algorithm and it is only used for multidimensional minimization. Its name comes from the utilization of a simplex in it. For N dimensions, the simplex is presented as geometrical figure that consist of $N + 1$ points and joining lines and planes. Figure 5-5 shows the simplex for low order simplexes.

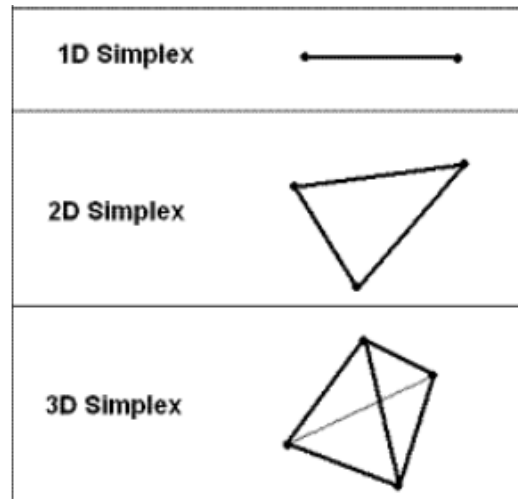


Figure 5-5 Low order simplexes (StudyLib, 2019)

From the figure, the simplex for optimization in one dimension consists two points and appears as a line segment. On the other hand, the two dimensional simplex for optimization takes a shape of a triangle and the three dimensional simplex is a tetrahedron.

In general, the downhill simplex method performs as an algorithm with a starting point or a starting simplex which is defined by selecting the initial $N + 1$ points. However, it is still possible to work with an initial point consisting of a single point P_0 . This can be done through then identifying the additional N points as given in equation 5.2 below (Press *et al.*, 1996)

$$P_i = P_0 + \lambda e_i \quad i = 1, \dots, N \quad (5.2)$$

Where the term e_i refers to N unit vectors while the term λ is a constant which can be guessed by the researchers for the problem's characteristic length scale. Different λ values can be taken for the different vector directions. By utilizing the simplex of the starting point, the downhill method takes a series of steps at each iteration to discover

a (local) minimum point. Four key operations are implemented in this algorithm where the selection of one operation depends on a set of various calculations and criteria. These operations are reflection, expansion, one-dimensional contraction and multiple contractions. In the reflection action, the highest point is taken by the algorithm out of the $N + 1$ points which identifies the simplex and then it is reflected in the conflicting side of the simplex, in a way that conserves its volume. In the expansion action, simplex expands to move in the 'right' direction. In the contraction action, which occurs as the simplex reaches a minimum value or enters a 'valley', the simplex contracts itself in the transposed direction of the valley. Finally, in the multiple contraction or the N -dimensional contraction where all points move towards the current minimum. Figure 5-6 illustrates basic moves in the downhill method with an illustration for each step for a 3D tetrahedron simplex.

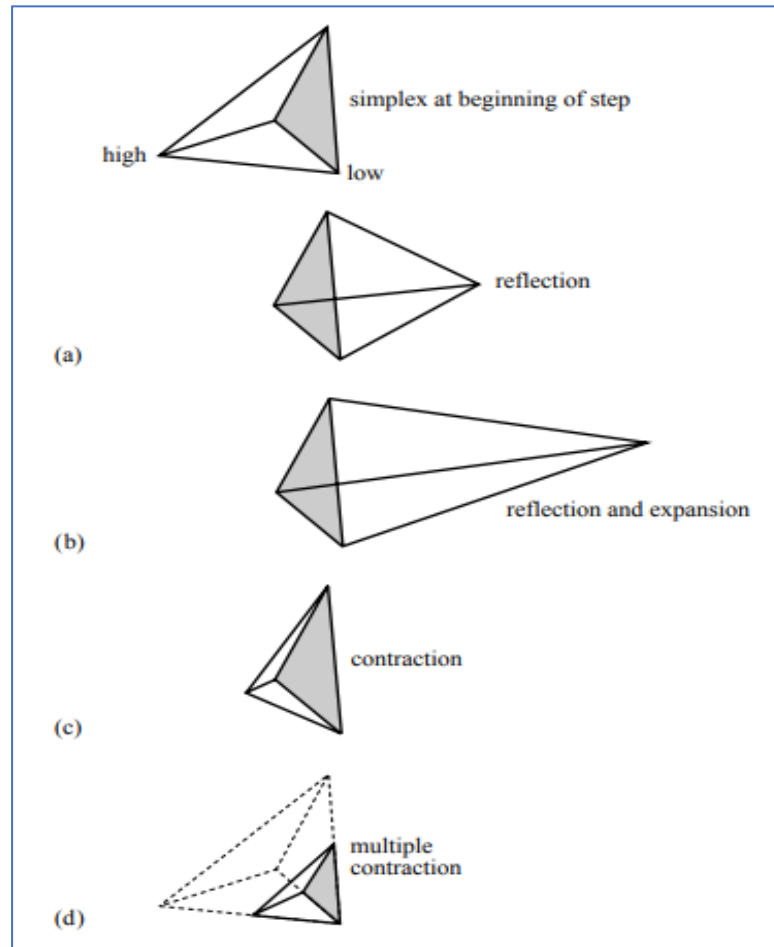


Figure 5-6 The basic moves in the downhill method (Press *et al.*, 1996)

Petersen (2017), also gives an example for the implementation of downhill simplex method in two dimensions as shown in Figure 5-7 below, where it illustrates the steps of this method for the case of a 2D triangular simplex.

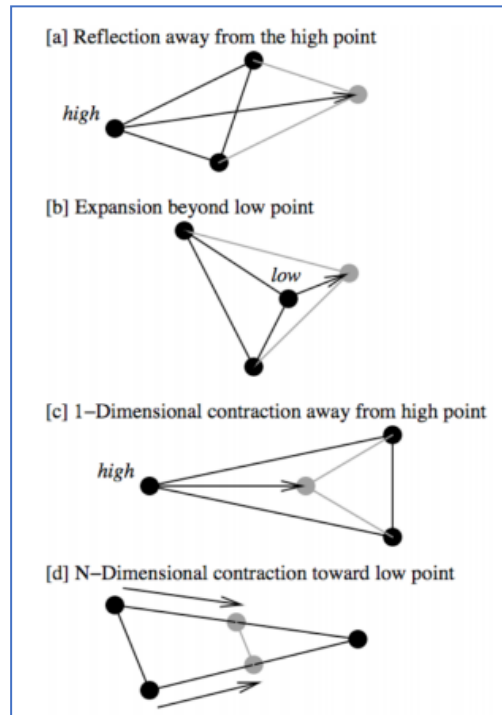


Figure 5-7 The range of changes made to the 2D simplex in the downhill simplex method (Petersen, 2017)

Also, Gavin (2016) concentrated on his study on the utilization of a simplex algorithm in two dimensions where $N = 2$ which means that the simplex is a triangle. He assumes a simplex of three points named as $[u, v, w]$ in the $x_1 - x_2$ plane. These points and planes are connected to form a triangle. The evaluated objective functions at the defined three points were $f(u)$, $f(v)$, and $f(w)$. Figure 5-8 presents the steps followed for iteratively evolving the triangle vertices to minimize the function $f(x)$.

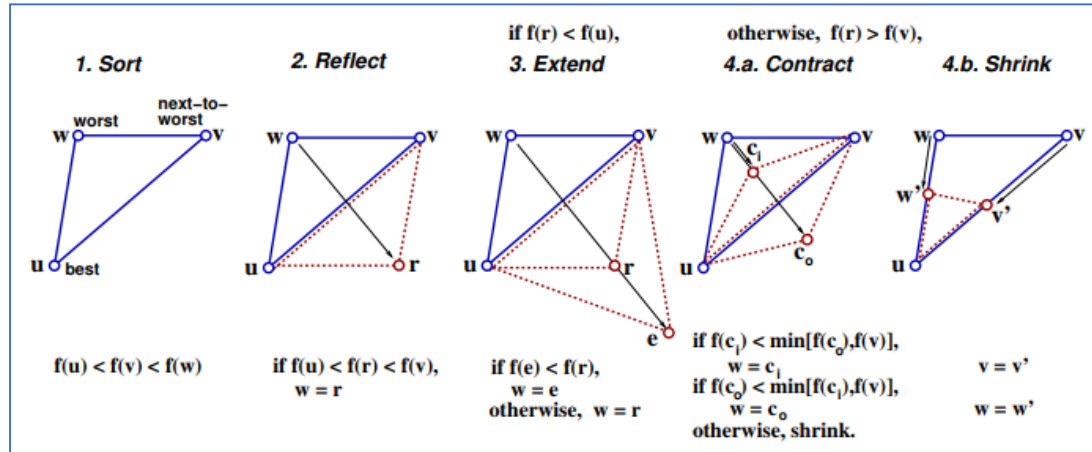


Figure 5-8 Downhill simplex steps in one iteration for N = 2 (Gavin, 2016)

In this research, the downhill simplex method has been implemented to find the minimum total error ε_{tot} for a given n . From Figure 4-32, the n value was found weak in terms of sensitivity to β , it was then used as a fixed parameter and set to $n = 0.7$, where the downhill simplex method has been used in two dimensions, β and h_s . The initial three test points were set as follows:

Point 1: $\beta = 0.2$, $h_s = 100 \text{ Wm}^{-2}\text{K}^{-1}$

Point 2: $\beta = 0.6$, $h_s = 100 \text{ Wm}^{-2}\text{K}^{-1}$

Point 3: $\beta = 0.4$, $h_s = 1000 \text{ Wm}^{-2}\text{K}^{-1}$

The total error for a point in the simplex is ε_{tot} and the three points are denoted *MAX*, *MIN* and *MID* according to the values of ε_{tot} i.e $\varepsilon_{tot_{MAX}} > \varepsilon_{tot_{MID}} > \varepsilon_{tot_{MIN}}$.

The error measure for the simplex is defined as $\varepsilon_s = 2 \times \frac{|\varepsilon_{tot_{MAX}} - \varepsilon_{tot_{MIN}}|}{|\varepsilon_{tot_{MAX}}| + |\varepsilon_{tot_{MIN}}|}$, and the process regarded as converged when $\varepsilon_s < 10^{-5}$.

The flow chart in Figure 5-9 illustrates the process of finding the total minimum error of this method.

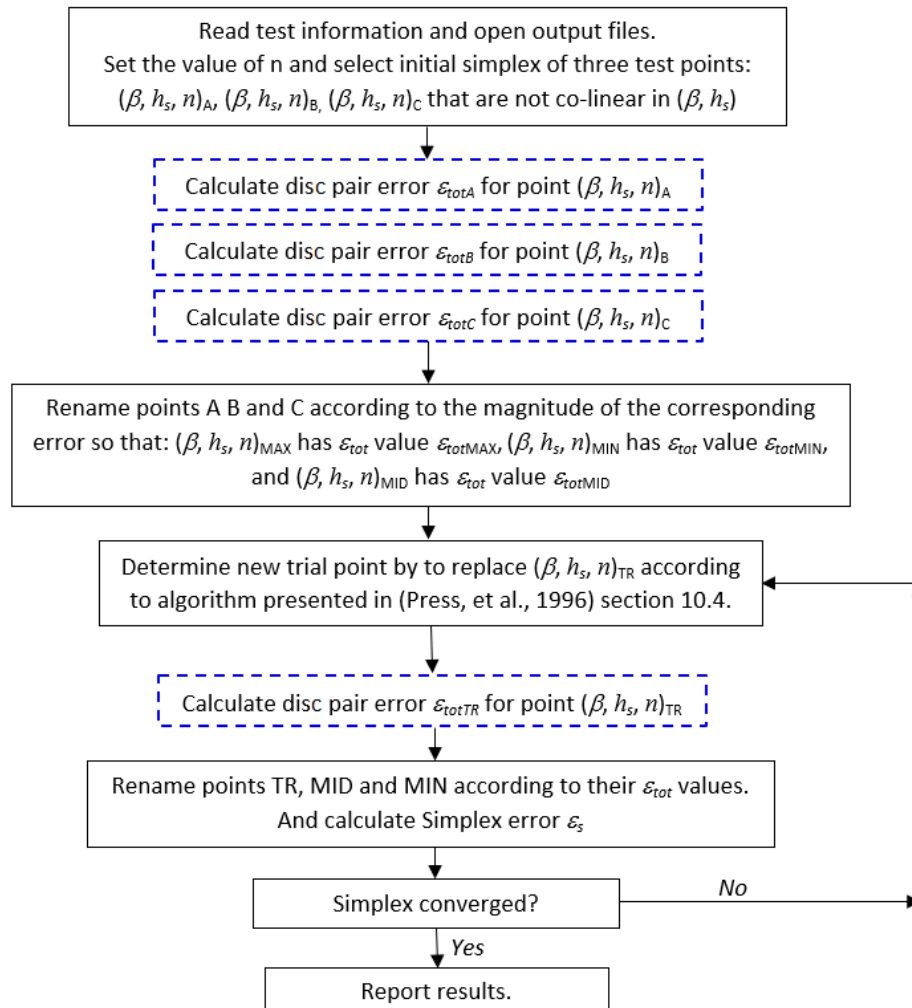


Figure 5-9 Flow chart for simplex minimisation method of disc pair error for given n value. Broken blue box is the disc pair error analysis of Figure 5-1

The time consuming part of this algorithm is the disc pair error analysis which dictates the fundamental cycle time. The disc pair error analysis method which is used in the previous chapter to find β and h_s takes a large number of cycles to calculate the minimum total error because of the multi-stage grid of evaluation points that are used, and is a single process which does not need a succession of finer localised meshes

to be chosen. The downhill simplex method uses less cycles to obtain the minimum. This is because establishing the first simplex requires 3 cycles, and each subsequent simplex in the chain requires one further cycle. This has been validated by carrying out two analyses the first analysis used the disc pair error analysis method, where the second analysis used downhill simplex method for the same given n value. The result shown in Figure 5-10 below is obtained using the first method where it took 504 cycles to reach this result.

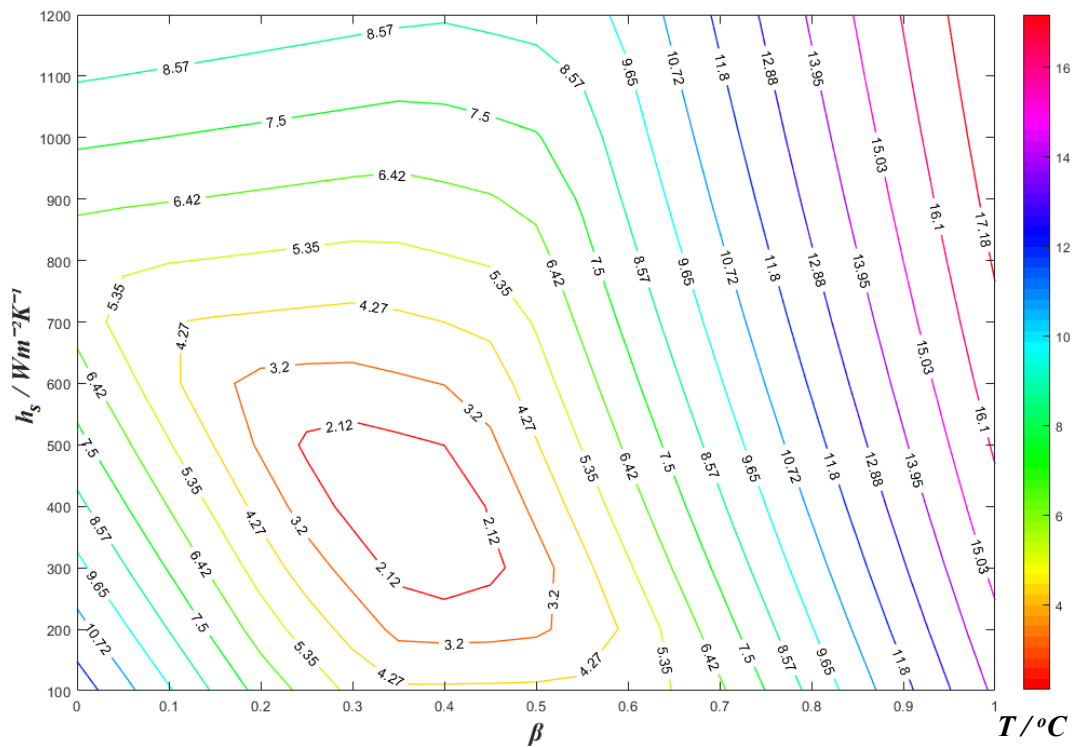


Figure 5-10 Total error plot in °C for both discs using disc pair analysis method, power $n = 0.7$

However, this result is still not showing a clear-cut minimum, it is not possible to find the exact (β, h_s) values. Hence, this method needs to be repeated with finer mesh of (β, h_s) values that are surrounding the red circle until reaching a clear-cut minimum.

The contour plot shown in Figure 5-11 below is obtained after carrying out two more analyses.

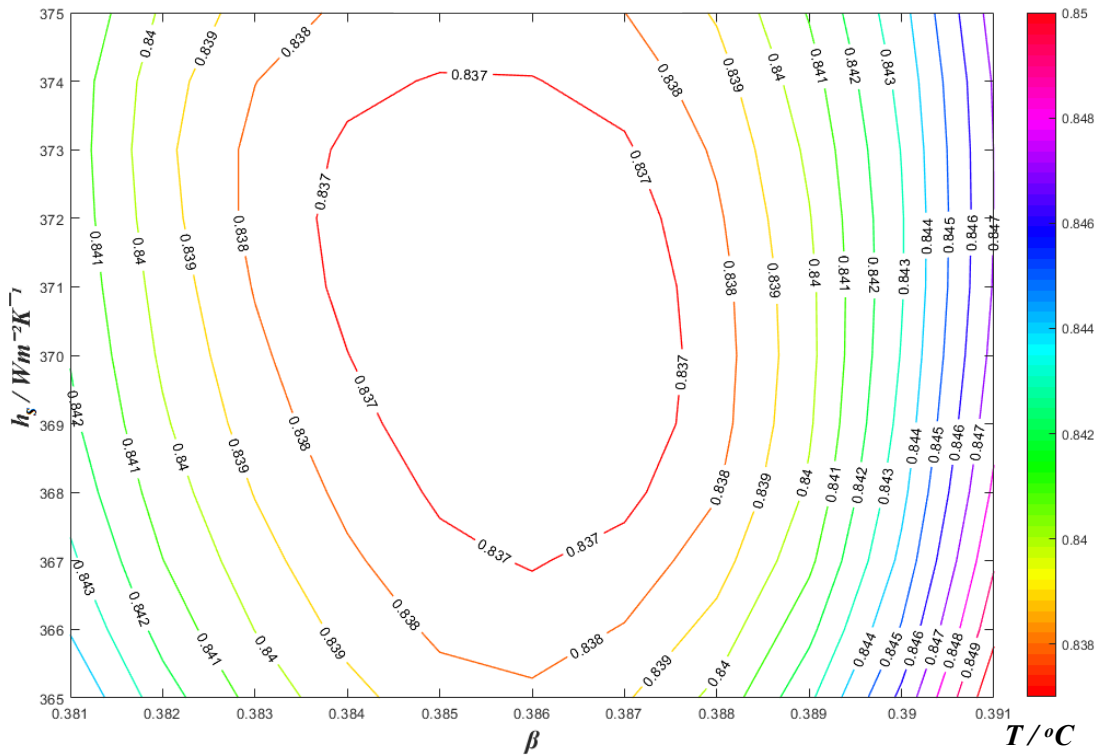


Figure 5-11 Finer mesh for total error plot in $^{\circ}\text{C}$ for both discs using disc pair analysis method, power $n = 0.7$

The first analysis took 504 cycles, the second one took 242 cycles and the last one took 242 cycles. This is 988 cycles in total to find the total minimum error which is located within the red circle labelled with error = 0.837 $^{\circ}\text{C}$.

The downhill simplex method spent less time in calculating the total minimum error, it calculated and found $\varepsilon_{tot} = 0.835$ $^{\circ}\text{C}$ in 61 cycles only. Also, it has found the exact β and h_s values corresponding to this total minimum error, $\beta = 0.386$ and $h_s = 370.6$ $\text{Wm}^{-2}\text{K}^{-1}$. Figure 5-12 below illustrates the triangles movements during the 61 cycles of the simplex method.

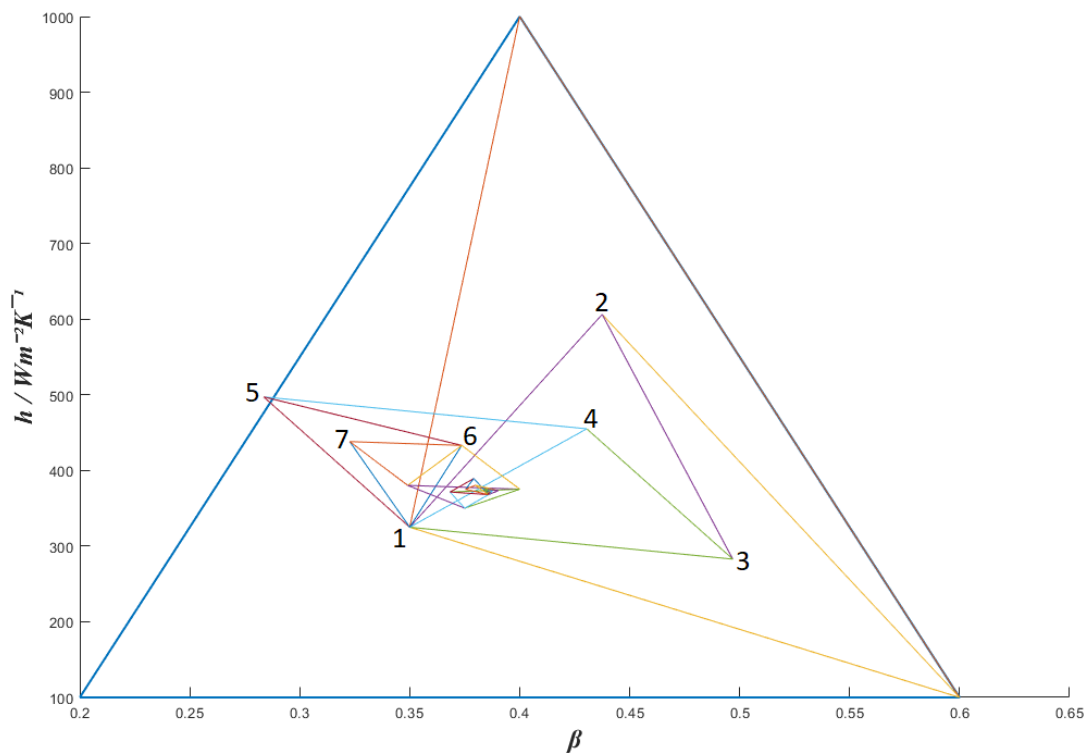


Figure 5-12 movement of the triangles of the simplex method during the 61 cycles of the analysis, power $n = 7$. Sequence of simplexes are \bullet , \circ , \circ , \circ , \circ , \circ , \circ etc.

In Figure 5-12 the first simplex is the outer triangle which covers the area where the minimum error point is found, although this is not a restriction. A larger simplex will take more cycles to reach the same minimum point. For the starting simplex the maximum error is at the apex (0.2, 100). This point is discarded and is replaced by the new vertex labelled 1. The new simplex is the triangle that has the two undiscarded vertices (0.6, 100), (0.4, 1000) and vertex 1. This is Simplex 1. For Simplex 1 the largest apex error is at (0.4, 1000) and this is discarded and replaced by Vertex 2.

This process continues forming new smaller simplex triangles as shown in the figure. The end of the process is illustrated in Figure 5-12a which shows the last 5 simplexes, i.e. Simplex 57, Simplex 58, Simplex 59, Simplex 60, Simplex 61.

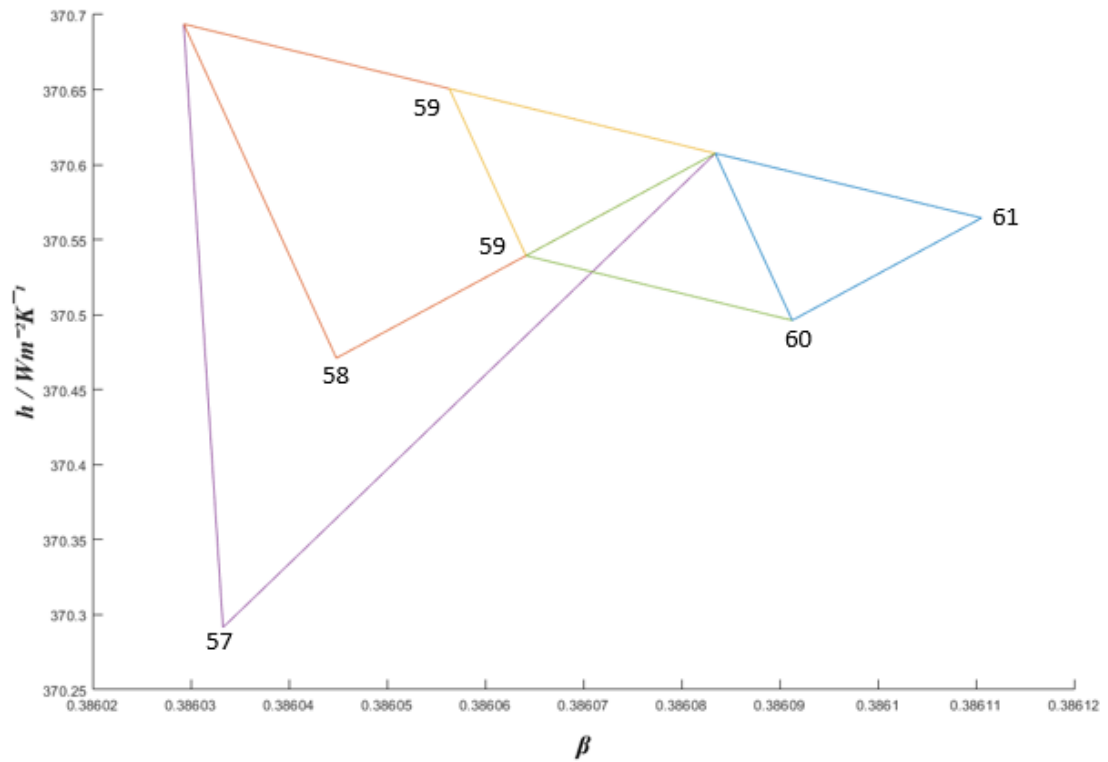


Figure 5-12a movement of the last five simplexes of the analysis, power $n = 7$. Sequence of simplexes are \bullet , \bullet , \bullet , \bullet , \bullet .

For Simplex 61, which is shown in Figure 5-13 the error at each vertex is almost the same and the convergence criterion is satisfied with the process converged and the solution is (β, h_s) at the centroid of the triangle, with the mean vertex error as the minimum value.

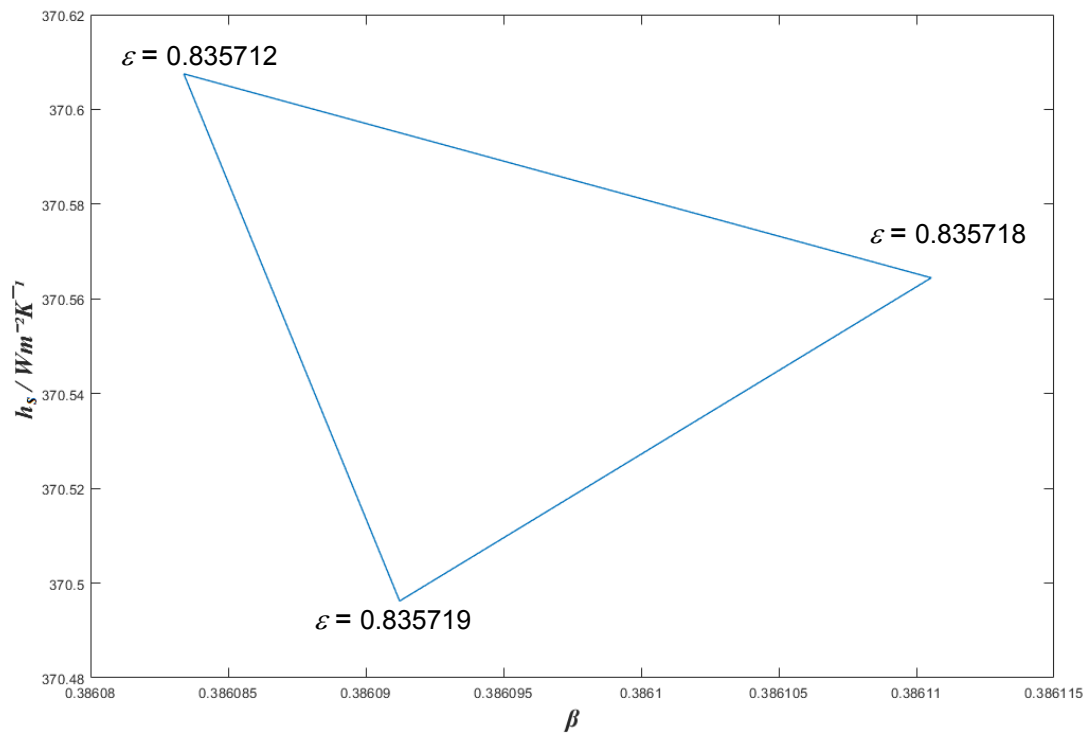


Figure 5-13 The final triangle (cycle 61) of the converged simplex method analysis, power $n = 0.7$, converged result $\beta = 0.386083$, $h_s = 370.6 \text{ W/m}^2\text{K}^{-2}$, $\epsilon_{\min} = 0.835 \text{ }^\circ\text{C}$

5.4 Determining n using Simplex method values for error

In this section, the simplex minimisation method is applied to calculate the minimum total error for both discs, with the power n value set over the range $0.1 \leq n \leq 1.5$. The minimum total error is $\epsilon_{tot} = \epsilon_{slow} + \epsilon_{fast}$. A series of trial models are used to define the total error in terms of the errors at each of measurement points T_a , T_c and T_e in order to examine the way in which the error definition choice influences the variation of the total error with n . The first model, EM1 makes T_c the dominant temperature measurement by giving it a weight of 2 compared to T_a and T_e .

Error model EM1

$$\varepsilon_{slow} = \frac{|T_{as_{experiment}} - T_{as_{calculated}}| + 2 \times |T_{cs_{experiment}} - T_{cs_{calculated}}| + |T_{es_{experiment}} - T_{es_{calculated}}|}{4} \quad (5.11)$$

$$\varepsilon_{fast} = \frac{|T_{af_{experiment}} - T_{af_{calculated}}| + 2 \times |T_{cf_{experiment}} - T_{cf_{calculated}}| + |T_{ef_{experiment}} - T_{ef_{calculated}}|}{4} \quad (5.12)$$

The curve in Figure 5-14 shows the minimum total error ε_{tot} for a range of power n values using the simplex method based on error model EM1 to define the total error.

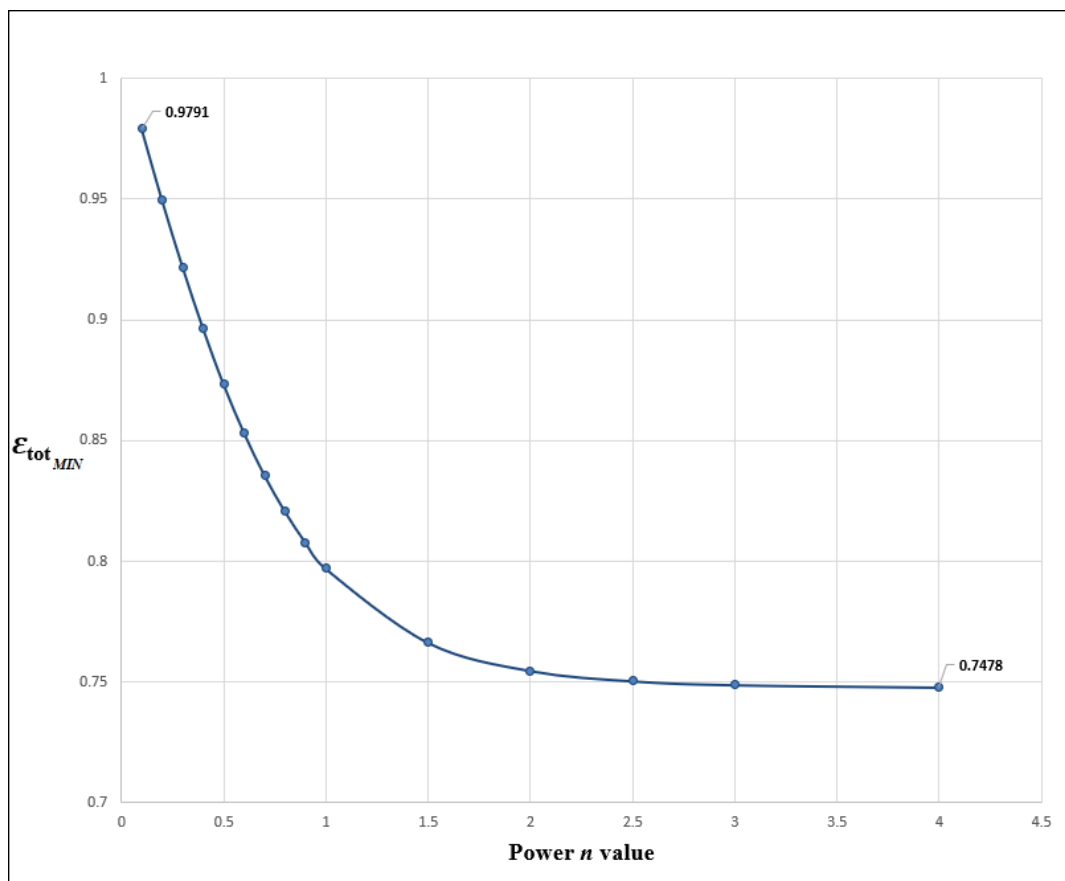


Figure 5-14 Total error of simplex method using error model EM1, equations (5.11) and (5.12)

The other error models used, denoted EM2 to EM7 were as follows

Error model EM2

$$\mathcal{E}_{slow} = \frac{|T_{as_{experiment}} - T_{as_{calculated}}| + |T_{cs_{experiment}} - T_{cs_{calculated}}| + 2 \times |T_{es_{experiment}} - T_{es_{calculated}}|}{4} \quad (5.13)$$

$$\mathcal{E}_{fast} = \frac{|T_{af_{experiment}} - T_{af_{calculated}}| + |T_{cf_{experiment}} - T_{cf_{calculated}}| + 2 \times |T_{ef_{experiment}} - T_{ef_{calculated}}|}{4} \quad (5.14)$$

Error model EM3

$$\mathcal{E}_{slow} = \frac{|T_{as_{exp}} - T_{as_{calculated}}| + 2 \times |T_{es_{exp}} - T_{es_{calculated}}|}{3} \quad (5.15)$$

$$\mathcal{E}_{fast} = \frac{|T_{af_{exp}} - T_{af_{calculated}}| + 2 \times |T_{ef_{exp}} - T_{ef_{calculated}}|}{3} \quad (5.16)$$

Error model EM4

$$\mathcal{E}_{slow} = \frac{2 \times |T_{as_{exp}} - T_{as_{calculated}}| + |T_{es_{exp}} - T_{es_{calculated}}|}{3} \quad (5.17)$$

$$\mathcal{E}_{fast} = \frac{2 \times |T_{af_{exp}} - T_{af_{calculated}}| + |T_{ef_{exp}} - T_{ef_{calculated}}|}{3} \quad (5.18)$$

Error model EM5

$$\mathcal{E}_{slow} = \frac{|T_{as_{exp}} - T_{as_{calculated}}| + |T_{es_{exp}} - T_{es_{calculated}}|}{2} \quad (5.19)$$

$$\mathcal{E}_{fast} = \frac{|T_{af_{exp}} - T_{af_{calculated}}| + |T_{ef_{exp}} - T_{ef_{calculated}}|}{2} \quad (5.20)$$

Error model EM6

$$\mathcal{E}_{slow} = |T_{as_{exp}} - T_{as_{calculated}}| \quad (5.21)$$

$$\mathcal{E}_{fast} = |T_{af_{exp}} - T_{af_{calculated}}| \quad (5.22)$$

Error model EM7

$$\varepsilon_{slow} = |T_{es_{exp}} - T_{es_{calculated}}| \quad (5.23)$$

$$\varepsilon_{fast} = |T_{ef_{exp}} - T_{ef_{calculated}}| \quad (5.24)$$

Error models EM1 and EM2 use the measurements at points T_a , T_c and T_e with a weighting factor 2 for one of the centreline points. These models give very similar behaviour for the variation of ε_{tot} with n as illustrated in Figure 5-14. The further models concentrated on the centreline temperatures in response to concerns about the accuracy of the temperature at point T_c . Models EM3 EM4 and EM5 use temperature measurements T_e and T_a with weights 2:1, 1:2 and 1:1, respectively. Model EM6 uses temperature A only and model EM7 uses temperature E only. The ε_{tot} values obtained reduced as the number of measuring points was reduced, as could be expected, and the range of ε_{tot} values for the individual curves also varied.

To make a comparison of the behaviour of the different models they were scaled so that each curve is plotted on a scale of 0 to 1 for its range. This comparison is made in Figure 5-15 which shows three patterns of behaviour. The maximum and minimum values ε_{tmax} and ε_{tmin} found for ε_{tot} over the range $0.1 < n < 1.5$ are tabulated in Table 5-1. The range for n is considered is centred on the value of $n = 0.7$ found in the literature.

Table 5-1 The maximum and minimum values of ε_{tot} obtained for error models 1 to 7

Error Model	ε_{tmax}	ε_{tmin}	Turning Value
EM1	0.979	0.748	No
EM2	0.955	0.829	No
EM3	0.961	0.960	Yes
EM4	1.22	1.14	No
EM5	1.18	1.17	No
EM6	0.251	0.246	No
EM7	0.432	0.429	No

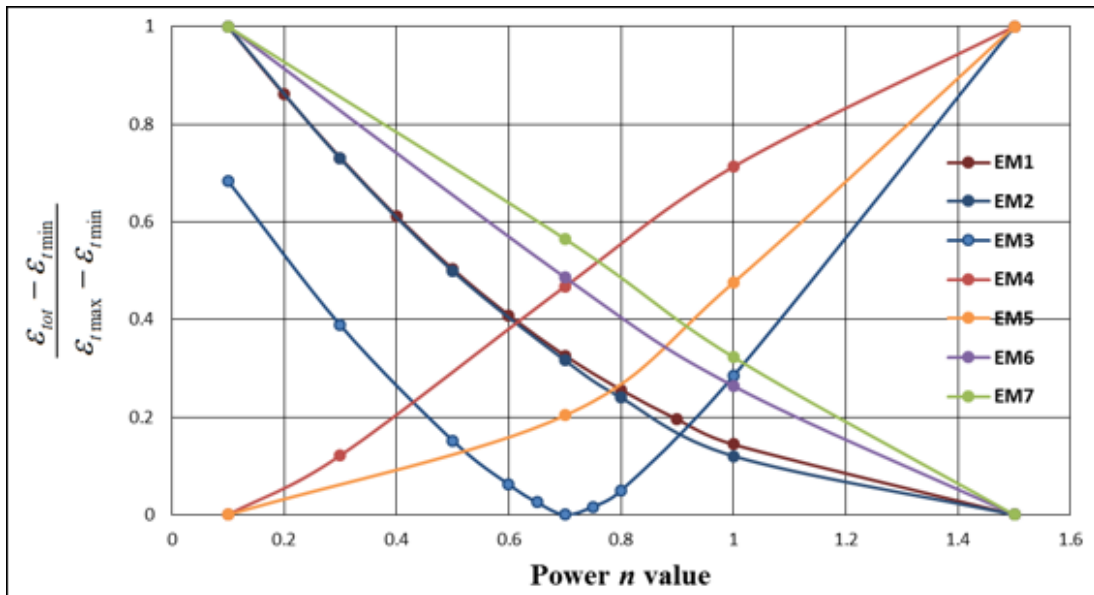


Figure 5-15 Variation of Total error with n for error models EM1 to EM7

Three kinds of behaviour are shown in this comparison. For models EM1, EM2, EM6 and EM7 the ε_{tot} value falls steadily as n increases over the whole range. EM1 and EM2 use T_a , T_c and T_e with weights 1:2:1 and 1:1:2, respectively. These models have

almost identical behaviours when scaled for comparison in Figure 5-15. EM6 and EM7 are single temperature models using T_a and T_e .

Model EM3 which uses T_a and T_e with weights 1:2 is the only model that shows a turning value for ε_{tot} with a near symmetrical increase as n departs from the minimum position.

Models EM4 and EM5 have ε_{tot} values that increase steadily as n increases over the whole range. These models use T_a and T_e with weights 2:1 and 1:1.

These observations show that including the T_c measurement is counterproductive suggesting that its value is inconsistent with those for T_a and T_e , and that it is important to capture the centreline behaviour close to the surface to achieve the desired sensitivity to parameter n .

In summary when modifying the selection of T_a , T_c and T_e in the calculation of total error, the analyses show different results. The variation of ε_{tot} with the n cannot identify the n value, except in the case of error model EM3. These observations led the author to investigate the inconsistencies in the experimental temperature measurements, as described in the following section.

5.5 Inconsistencies in temperature measurements

After carrying out the analyses in Section 5.4, doubts about inconsistencies in the temperature measurements of the discs were reinforced as changes the definitions of $\varepsilon_{\text{slow}}$ and $\varepsilon_{\text{fast}}$ have a significant effect on the results. The temperatures are measured during the experiment by the six thermocouples that are embedded in each disc and arranged as shown in Figure 5-16. The temperatures were recorded during

the test D3 where the sliding speed is set to 20 m/s and the load is set to 1850 N, the temperatures are plotted for the slow disc as shown in Figure 5-17.

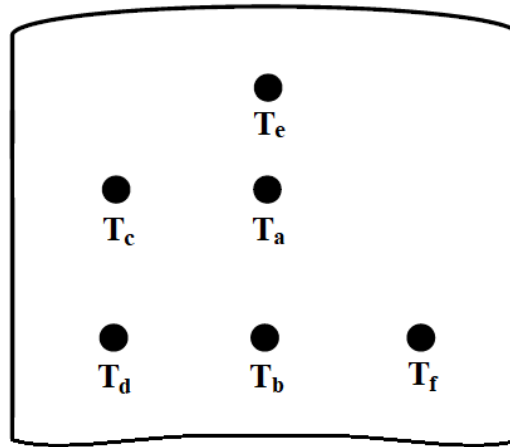


Figure 5-16 thermocouples arrangement in the test disc

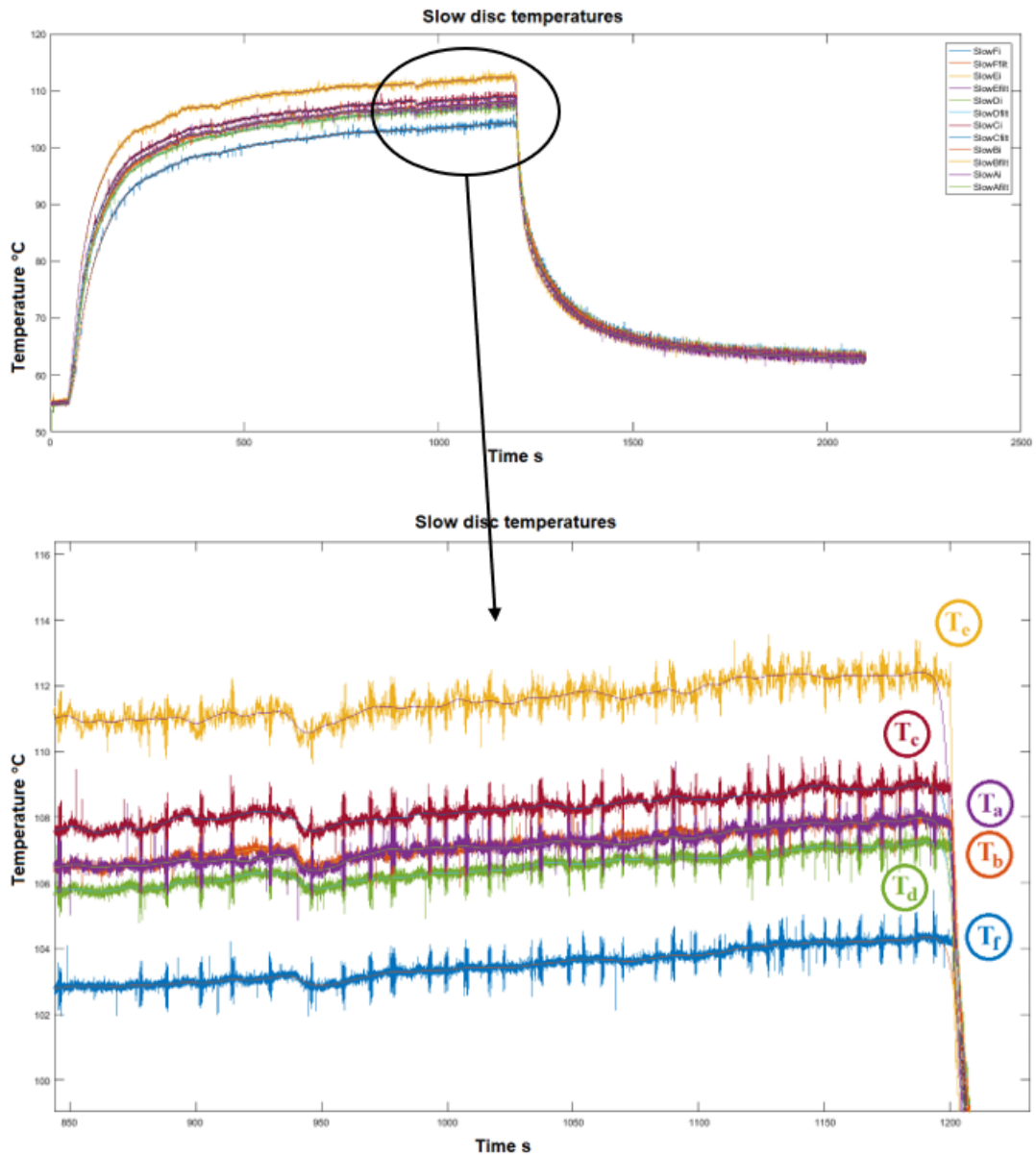


Figure 5-17 temperatures of the slow disc (test D3)

In the previous figure, the slow disc temperature measurements show that T_a and T_b have the same temperature measurements during the steady state, which is not thought to be physically possible. T_a should have higher temperatures due to the fact that it is located at $r = 35$ mm which means it is closer to the heating zone compared to T_b which is located at $r = 32$ mm. If that T_a and T_b are equal it means that there is

no radial temperature gradient in that area which is unlikely as the disc temperatures rise due to conduction from the surface increasing the temperature of the shaft assembly which has a large thermal mass. Also, it is noticed that T_c has higher temperatures than T_a which is again difficult to accept as T_a can be expected to be higher than T_c due to the fact that T_c is located at a closer position to the side where it will lose heat by convection as the disc is rotating. Figure 5-18 below shows the temperature measurements from the six thermocouples at time $t = 1100\text{s}$ as an example, it is shown in part (i) that the temperatures T_a and T_b are not in logical agreement with the heat flow within the disc, and also in part (ii) that T_a and T_c are inconsistent with each other. In addition, T_f in both parts (i) and (ii) is inconsistent with the other temperatures at the lower radius.

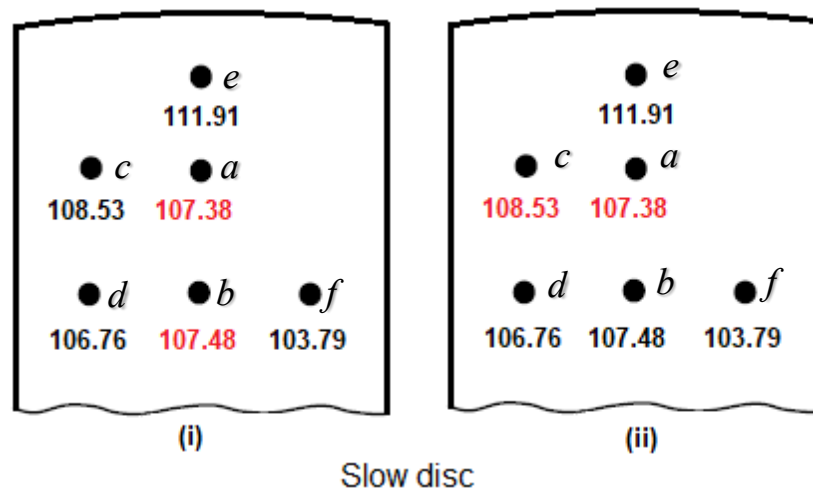


Figure 5-18 temperature recorded by thermocouples at $t = 1100\text{s}$ for the slow disc

For the fast disc, the temperature measurements during the test D3 are shown in Figure 5-19 below. As with the slow disc, the fast disc temperature measurements showed inconsistencies in the temperature measurements. Here, Figure 5-20 identifies these inconsistencies. From part (i) of Figure 5-20 temperature

measurement T_d is higher than T_b , which is again not expected as a result of having T_d located close to the side of the disc where it will lose the heat by convection due to the rotation of the disc. The other inconsistency in temperature measurements for the fast disc is shown in part (ii). Temperatures at T_c and T_f are observed within the same range during the last 200 s of the steady state. In fact T_c should have higher temperatures than T_f even during the last 200 s as it is located at $r = 35$ mm which is closer to the heating zone compared to T_f .

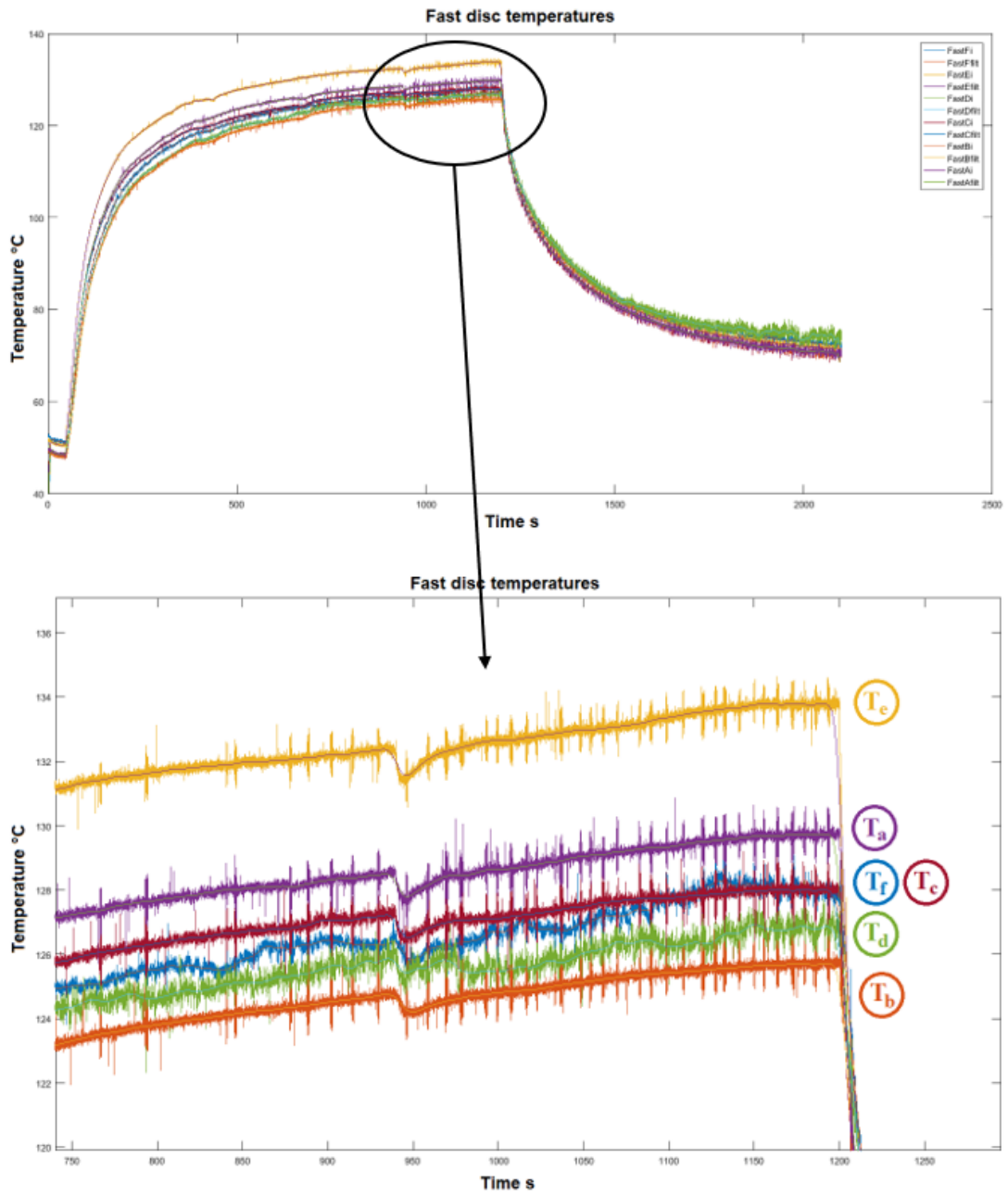


Figure 5-19 temperatures of the slow disc (test D3)

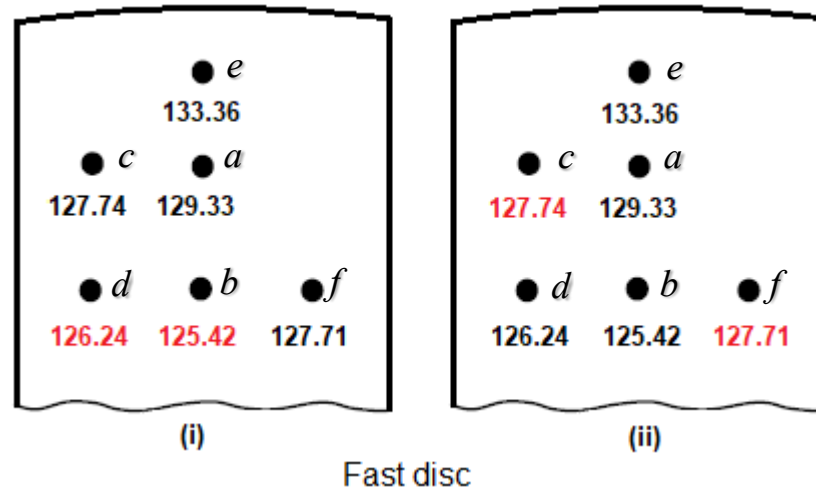


Figure 5-20 temperature recorded by thermocouples at $t = 1100$ s for the fast disc

This section shows that there is clearly an offset in the data recorded by some of the thermocouples, and this observation led to trying to establish which of the thermocouple measurements are mutually consistent in terms of the expected heat flow patterns and to use them as inputs for the error analysis to see whether the pattern of results could be improved. Several comparisons were made in order to find the best combination of mutually consistent temperatures for both discs. At the end, it was found that for the lower boundary of the slow disc, T_f is the weakest (least plausible) measurement and should be replaced with the T_d signal due to the large differences T_f compared to the others. This means in the analysis $T_f = T_d$ so that the lower boundaries of the slow disc ($T_d T_b T_f$) will become ($T_d T_b T_d$). And for the calculation of total error of the slow disc for the last 200 s, equation (5.11) was modified so that only T_c and T_e are included in the calculation and divided by 2, where T_a is not as it showed inconsistency with the other temperatures. This is stated in

As for the slow disc, the lower boundaries of the fast disc were also changed, T_c is changed so that $T_c = \frac{T_d + T_f}{2}$, $T_d = T_b$ and $T_f = T_b$. Thus, the lower boundaries of the

fast disc ($T_d T_b T_f$) became ($T_b T_b T_b$), and the calculation of total error is based on including only T_a and T_e in equation (5.11b) divided by 2 where T_c has been removed from it due to the inconsistency showed in the data recorded. This tuned error model to use the perceived best measurements for each disc is denoted EM8 and it was tested together with error models EM9 to EM12.

Error model EM8

$$\mathcal{E}_{slow} = \frac{|T_{cs_{exp}} - T_{cs_{calculated}}| + |T_{es_{exp}} - T_{es_{calculated}}|}{2} \quad (5.25)$$

$$\mathcal{E}_{fast} = \frac{|T_{af_{exp}} - T_{af_{calculated}}| + |T_{ef_{exp}} - T_{ef_{calculated}}|}{2} \quad (5.26)$$

Error model EM9

$$\mathcal{E}_{slow} = \frac{|T_{cs_{exp}} - T_{cs_{calculated}}| + |T_{es_{exp}} - T_{es_{calculated}}|}{2} \quad (5.27)$$

$$\mathcal{E}_{fast} = \frac{|T_{af_{exp}} - T_{af_{calculated}}| + |T_{cf_{exp}} - T_{cf_{calculated}}| + |T_{ef_{exp}} - T_{ef_{calculated}}|}{3} \quad (5.28)$$

Error model EM10

$$\mathcal{E}_{slow} = \frac{|T_{cs_{exp}} - T_{cs_{calculated}}| + |T_{es_{exp}} - T_{es_{calculated}}|}{2} \quad (5.29)$$

$$\mathcal{E}_{fast} = \frac{|T_{cf_{exp}} - T_{cf_{calculated}}| + |T_{ef_{exp}} - T_{ef_{calculated}}|}{2} \quad (5.30)$$

Error model EM11

$$\mathcal{E}_{slow} = |T_{es_{exp}} - T_{es_{calculated}}| \quad (5.31)$$

$$\mathcal{E}_{fast} = |T_{ef_{exp}} - T_{ef_{calculated}}| \quad (5.32)$$

Error model EM12

$$\mathcal{E}_{slow} = \frac{|T_{c_{exp}} - T_{c_{s_{calculated}}}| + 2 \times |T_{e_{s_{exp}} - T_{e_{s_{calculated}}}|}{3} \quad (5.33)$$

$$\mathcal{E}_{fast} = \frac{|T_{c_{f_{exp}} - T_{c_{f_{calculated}}}| + 2 \times |T_{e_{f_{exp}} - T_{e_{f_{calculated}}}|}{3} \quad (5.34)$$

The variation of \mathcal{E}_{tot} over a range of n values is given in Figure 5-21.

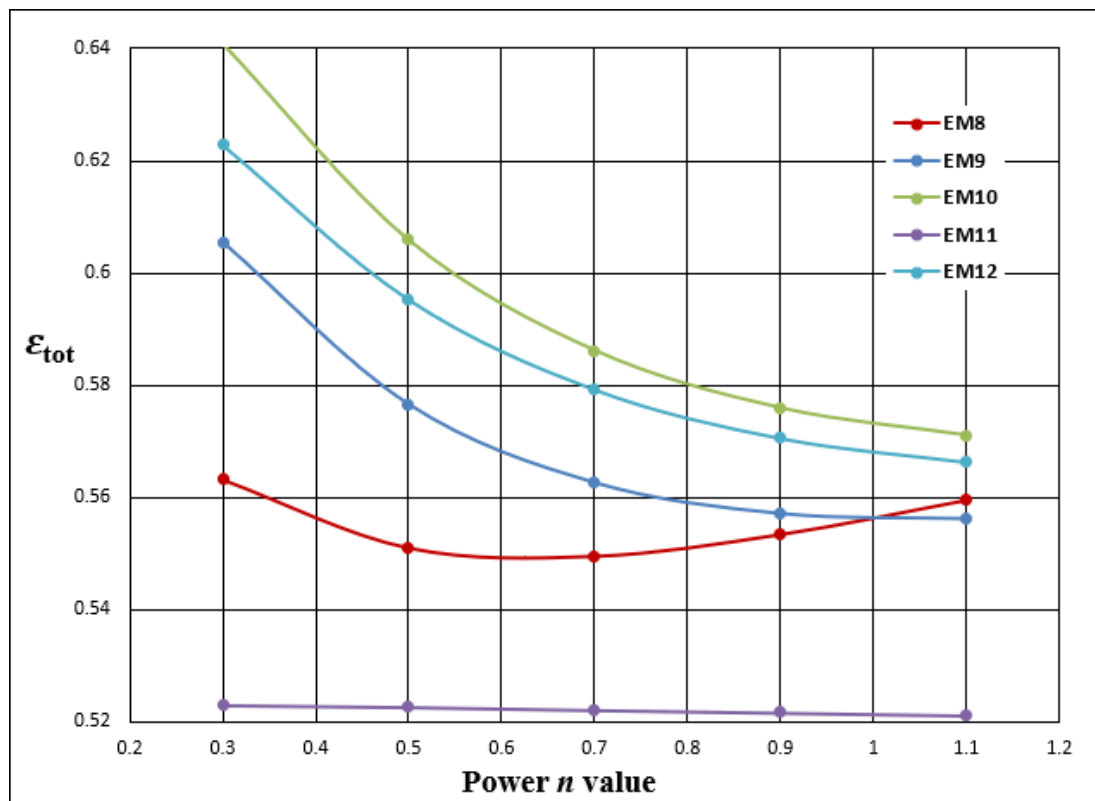


Figure 5-21 variation of \mathcal{E}_{tot} with n for Error models EM8 to EM12. Note that 0.07 is added to \mathcal{E}_{tot} for model EM11 to facilitate comparison.

Error model EM8 has a turning value with the minimum \mathcal{E}_{tot} occurring at around $n = 0.6$. The curve for error model EM11 has almost no dependence on n and has

been offset by 0.07 to facilitate comparison. The other three error models show a reducing trend for ε_{tot} as n increases, without achieving a minimum value.

It has been shown from the analyses carried out in Section 5.4 and in this section that it is difficult to determine the power n value. For the same n value, each case has a different total error value. In addition, some cases do not show a minimum total error where the error continues decreasing as long as n value increases. The difficulty in determining the value of n has also been there when the lower boundaries arrangements have been changed and the definitions of error calculation for the slow and the fast disc have been modified. This means finding which measurements are mutually consistent and using them in the analysis is not possible. Subsequently, it has been concluded that the temperature signal processing has to be reconsidered and improved.

In order to establish what improvements should be made to the test rig in the absence of mutually consistent experimental temperature measurements a synthesised experiment approach was adopted as is described in Section 5.6.

5.6 Optimum positioning and required accuracy of thermocouples

5.6.1 Synthesised experimental data

In order to eliminate the inconsistencies revealed in the previous section, the measured input data should be reliable and correct. This is not possible with the current test rig because of the uncertainty in temperature measurements. These have a noise content and they also show inconsistencies as far as their relative values are concerned. It was decided to generate a set of synthesised experimental data based on the inner radius temperatures measured by the author in the experiment. The

synthesised data should have temperatures that were consistent with the conduction equation as it is a fundamental assumption that the mean circumferential temperature, which the thermocouples measure, satisfies equation (3.27).

The measured temperatures at the lower boundary display an asymmetry that is difficult to explain in terms of heat flow in the disc material. Figure 5-17 shows the filtered central temperature T_b is 107.3 °C, and those ± 2.76 mm away in the axial direction are T_d is 106.6 °C and T_f is 103.7 °C. Figure 5-17 shows that $T_b - T_d$ is consistently less than 1 °C, while $T_b - T_f$ is consistently 1°C or more from time 400 s until the load is removed at time 1200 s. Al-Hamood (2015) investigated possible physical causes for this asymmetry and came to the conclusion that it was probably spurious. For the first of the synthesised datasets the lower boundary temperatures over the time of the experiment was set to the average of the filtered temperature measurements, i.e. $(T_b(t) + T_d(t) + T_f(t)) / 3$. This was done for each disc using the corresponding temperature measurements.

In this way the general heating behaviour measured in the real experiment was imposed on the synthesised data at the lower boundary of the analysis region. The synthesised temperatures at the three other measuring points were specified by carrying out a transient analysis for each disc and extracting the calculated temperatures at points A, C and E at each timestep. The heat input for the analyses was obtained by specifying trial values of parameters (β, h_s, n) and using the measured friction force and the surrounding fluid temperature, T_{ft} . For this synthesis, the parameter values used were $\beta = 0.37$, $h_s = 350 \text{ Wm}^{-2}\text{K}^{-1}$ and $n = 0.7$. The synthesised data obtained was thus consistent with the conduction equation and its boundary conditions and could be used to examine the capability of the minimum error technique to obtain the specified parameters from the dataset.

The generated synthesised temperatures were then used as the input for a standard downhill simplex method for the disc pair error analysis. The research question being considered in this is whether the simplex approach can identify the correct values of the parameters from the error minimisation analysis, or more realistically, how well can it obtain the values?

For this section, the error was defined as:

Error model EM13

$$\mathcal{E}_{slow} = \frac{|T_{as_{exp}} - T_{as_{calculated}}| + |T_{cs_{exp}} - T_{cs_{calculated}}| + |T_{es_{exp}} - T_{es_{calculated}}|}{3} \quad (5.35)$$

$$\mathcal{E}_{fast} = \frac{|T_{af_{exp}} - T_{af_{calculated}}| + |T_{cf_{exp}} - T_{cf_{calculated}}| + |T_{ef_{exp}} - T_{ef_{calculated}}|}{3} \quad (5.36)$$

The three temperatures involved in the error calculation T_a , T_c and T_e thus had equal weights.

5.6.2 Synthesised experiment

Figure 5-22 below shows the results obtained from simplex method analyses for disc pair for different values of n using the generated synthesised temperatures. The result shows that when setting $n = 0.1$, the minimum total error calculated $\varepsilon_{tot} = 0.07$ °C where $\beta = 0.43$ and $h_s = 662.5$ Wm⁻²K⁻¹, and when setting $n = 1.1$, the minimum total error calculated $\varepsilon_{tot} = 0.03$ °C where $\beta = 0.34$ and $h_s = 213.9$ Wm⁻²K⁻¹. On the other hand, when selecting $n = 0.7$, the total error $\varepsilon_{tot} = 0.00005$ °C which is effectively zero, $\beta = 0.370$ and $h_s = 350.0$ Wm⁻²K⁻¹ which are the specified parameter values chosen for the synthesised experiment.

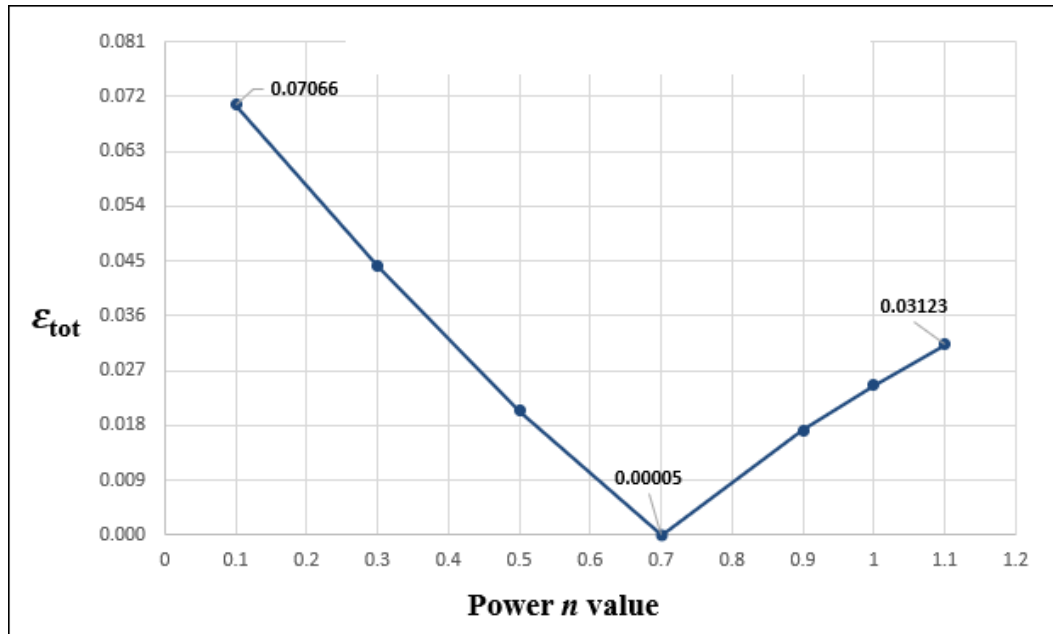


Figure 5-22 Total error of simplex method for disc pair analysis using generated synthesised temperatures

The actual values obtained for the total error at the extreme values of n adopted are $\epsilon_{tot} = 0.10$ for $n = 0.1$ and $\epsilon_{tot} = 0.10$ for $n = 0.7$. This underlines the difficulty in obtaining n from the error minimisation procedure. There is a clear minimum error for any given value of n , and this is obtained effectively by the simplex minimisation. However, the way in which the minimum error varies with n does not necessarily lead to a clear minimum position. Figure 5-22 has been obtained using 'perfect' data but the only information for the analysis are the three temperatures, T_a , T_c and T_e . This raises the question of where the thermocouple temperatures should be measured to obtain the most discerning test.

So, the thermocouple T_c was moved to attempt to improve discernment. Using the synthesised data in this way is advantageous as relocating the thermocouple is a simple matter of obtaining the synthesised temperature at a different point in the analyses. The position of thermocouple T_c was moved closer to the surface so that it

was positioned at the same depth as thermocouple T_e . Thermocouple T_e was located 1.25 mm below the surface. This is as close to the surface as was thought reasonable considering the diameter of the hole and that the peak shear stress occurs at a depth ≈ 0.32 mm as discussed by Al-Hamood (2015). Thermocouple T_c was located 1.43 mm from the disc face and 1.25 mm from the surface for this trial. Located at this position T_c and T_e both respond to the near surface temperatures in a more effective way.

Figure 5-23 represents the new arrangement of thermocouples in the numerical experiment.

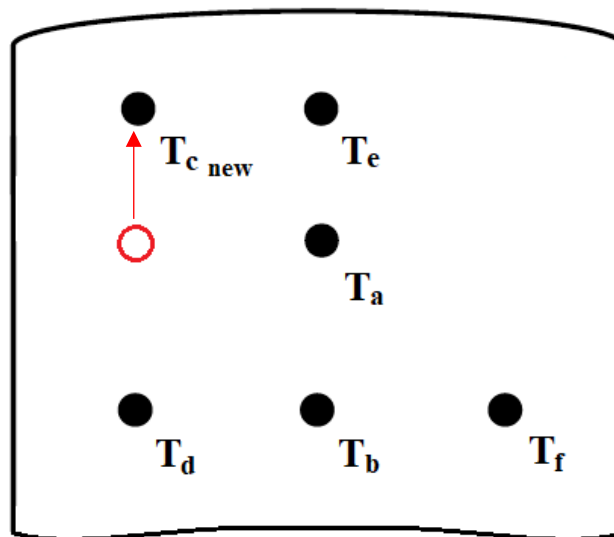


Figure 5-23 New arrangement with the new position of T_c located 1.43 mm from the disc face

After setting this arrangement, the disc pair analysis was repeated, and new generated synthesised temperatures were obtained based on the new location of thermocouple T_c and used as inputs in the simplex method analysis. Figure 5-24 shows the results obtained from this analysis for different values of n . The best fits at $n = 0.1$ and $n = 1.1$ now have errors that are about 4 times larger than in figure 5-22

so that with thermocouple T_c raised to be closer to the surface the error minimisation method is more discerning, as had been hoped. Further discussion regarding the optimum positioning of thermocouples are described in Section 5.6.3.

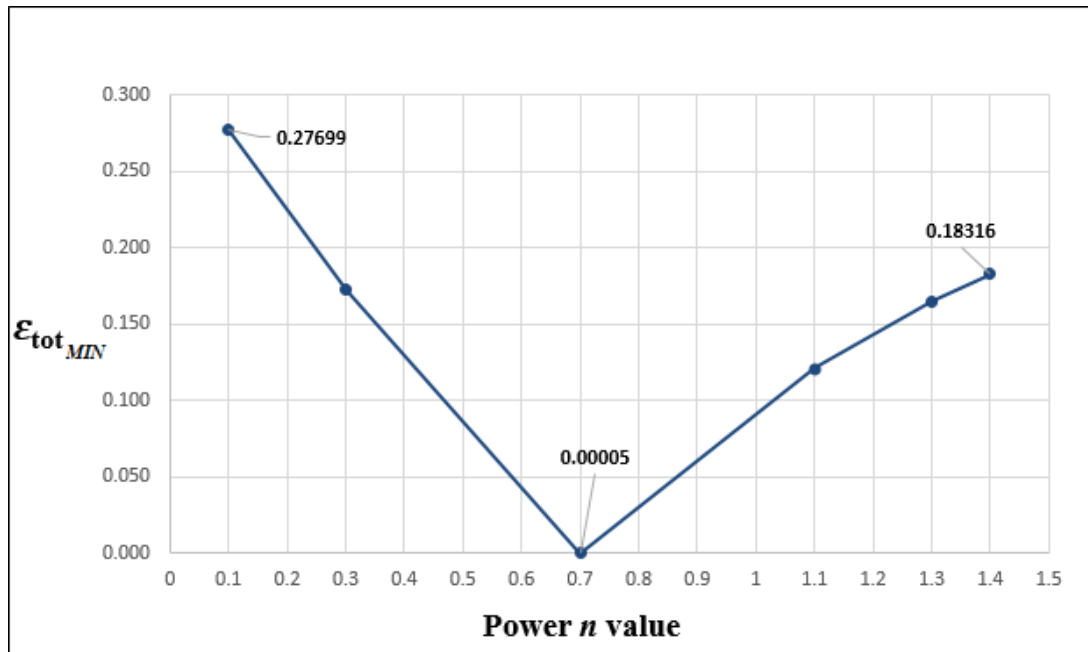


Figure 5-24 Total error of simplex method for disc pair analysis using generated synthesised temperatures

The previous analysis was repeated with different definitions of ϵ_{slow} and ϵ_{fast} to investigate the influence of using two different methods, these methods are the absolute value method which is been used during all previous analysis, and the square root method. The square root method has been applied instead of the absolute value as following:

Error model EM14

$$\varepsilon_{slow} = \sqrt{\frac{(T_{as_{exp}} - T_{as_{calculated}})^2 + (T_{cs_{exp}} - T_{cs_{calculated}})^2 + (T_{es_{exp}} - T_{es_{calculated}})^2}{3}} \quad (5.37)$$

$$\varepsilon_{fast} = \sqrt{\frac{(T_{af_{exp}} - T_{af_{calculated}})^2 + (T_{cf_{exp}} - T_{cf_{calculated}})^2 + (T_{ef_{exp}} - T_{ef_{calculated}})^2}{3}} \quad (5.38)$$

The result obtained from the analysis is shown in Figure 5-25 below. The red curve represents the total error with the new definition using the square root method. It clearly shows that when selecting $n = 0.7$, the minimum total error ε_{tot} has not changed and it is still equal to zero, also β and h_s values are obtained 0.3699 and 349.99 Wm⁻²K⁻¹ respectively. However, the total error becomes larger with other n values. This shows that using the square root method improves the discernment further.

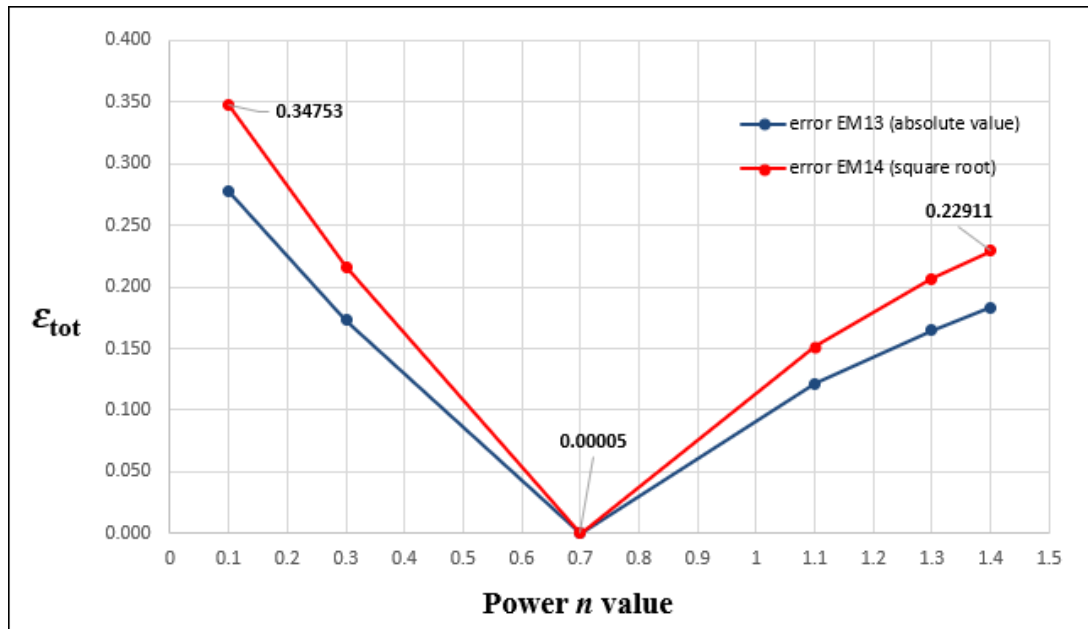


Figure 5-25 Total error of simplex method for disc pair analysis using generated synthesised temperatures with new definition of ε_{slow} and ε_{fast}

To evaluate the effectiveness in calculating the minimum total error using this synthesised experiment, new sets of synthesised data were generated using the disc pair analysis with different values of β , h_s and n for each set. Then each set of the generated synthesised data was used as input in simplex method analysis. The results obtained for each synthesised data set including that from Figure 5-25 (error model EM14) are plotted in Figure 5-26. These synthesised experiments with different parameters showed good results and led to the expected outcome with similar discernment.

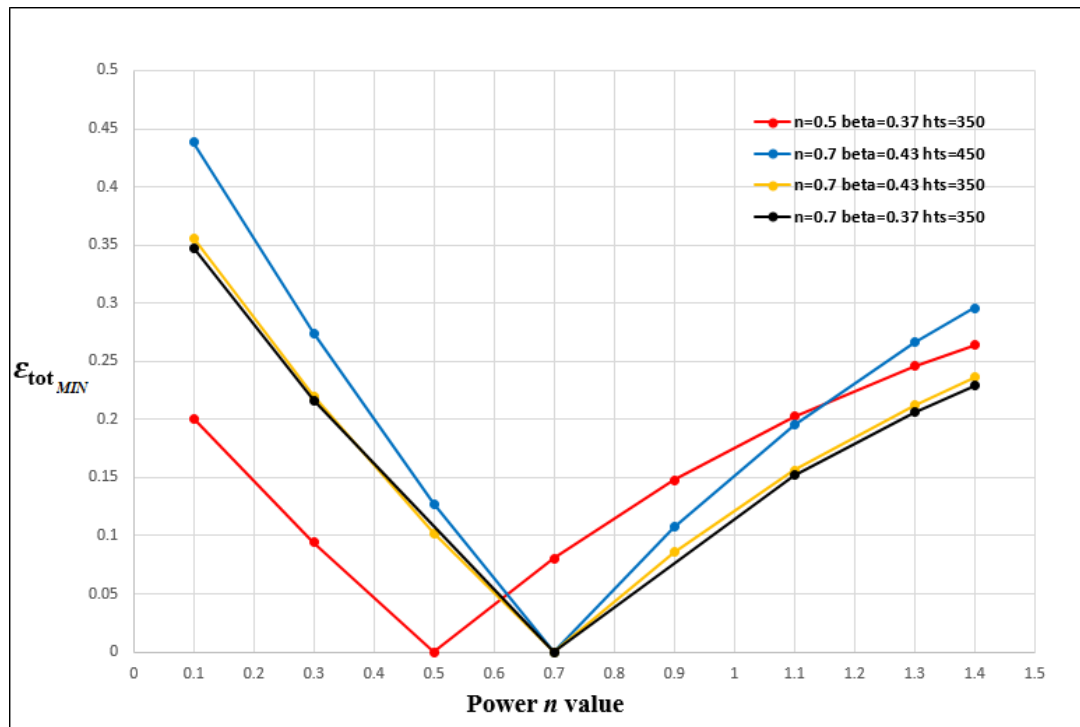


Figure 5-26 Total error of simplex method for disc pair analyses using different synthesised data sets

However, the robustness of this synthesised experiment should be tested and confirmed. To do this, noise was introduced at each time step to the first generated synthesised temperatures obtained from ($\beta = 0.37$, $h_s = 350 \text{ Wm}^{-2}\text{K}^{-1}$ and $n = 0.7$).

This noise was introduced using random number generator in Excel software and it is shown in Figure 5-27 below for the slow disc as an example.

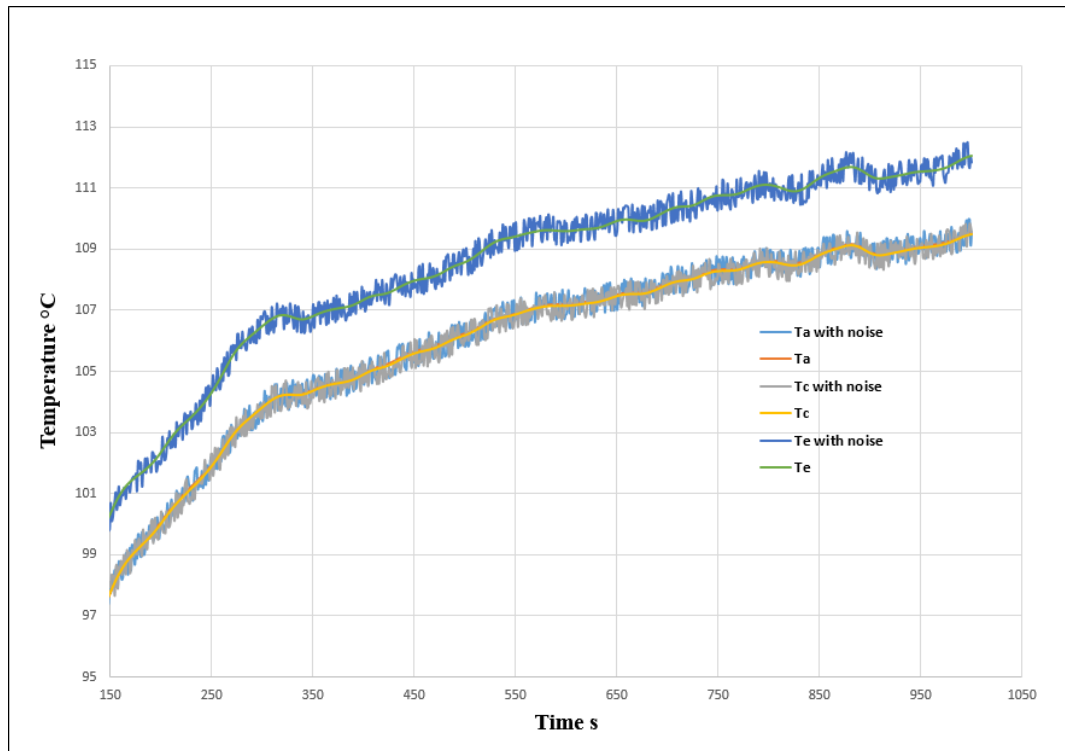


Figure 5-27 section of generated synthesised temperatures for the slow disc with noise added to it from -0.5 to 0.5 °C. Note that T_a and T_c have similar values and that T_c masks T_a in the figure.

After adding noise to the synthesised temperatures, the simplex method analysis was carried out with different amplitudes of noise added to the generated synthesised temperatures. The three amplitudes of noise were: (-0.5 to 0.5 °C), (-0.25 to 0.25 °C) and (-0.125 to 0.125 °C). The three new sets of data with noise give the results shown in Figure 5-28 below.

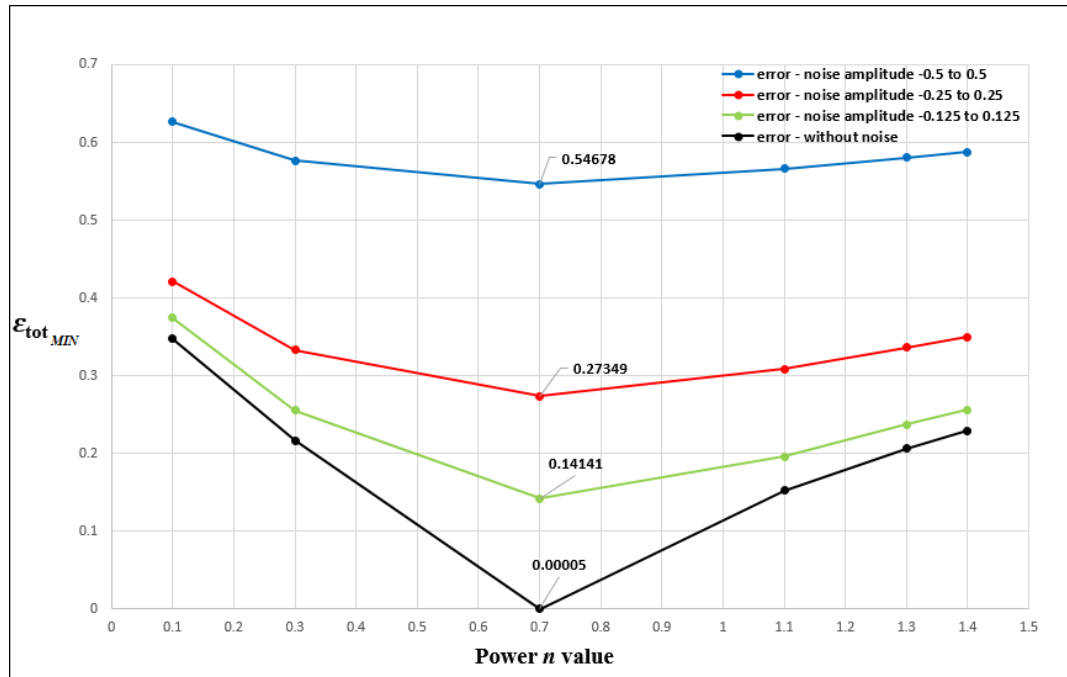


Figure 5-28 Total error of simplex method for disc pair analyses using generated synthesised temperatures with noise at each time step

The noise has a clear influence on the error minimisation results. Introducing a larger amplitude of noise to input data gives larger errors and a flatter curve of total error as represented by the blue curve, this is due to the fact that the synthesised temperatures with noise have larger differences in temperatures compared to the original generated ones. Where while introducing a lower amplitude of noise the error obtained is smaller and the curve becomes steeper toward $n = 0.7$ and has a similar shape to that obtained from the original generated synthesised temperatures.

5.6.3 Thermocouple position investigation

In the previous section, it was confirmed that changing the position of thermocouple T_c has an effect on the result and having T_c closer to the surface leads to results with higher discernment. This section shows how the position can be improved where

more experiments have been carried out to investigate the influence of changing this position on the result and what the optimum position of this thermocouple is.

Firstly, experiment (A) with the position of T_c moved towards the vertical centre line of the disc as shown below in Figure 5-29 and is located 1.9 mm from the disc face.

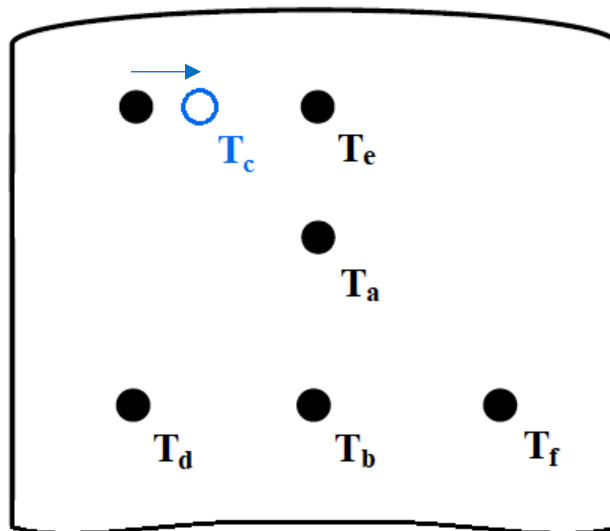


Figure 5-29 New position of thermocouple T_c for experiment (A), moved inwards

A new set of synthesised temperatures were generated with the new position of T_c . The simplex method for disc pair error analysis was carried using these new temperatures as inputs. Several analyses were carried out with different values of n each time.

Secondly, experiment (B) with the position of T_c moved towards the face of the disc as shown below in Figure 5-30 and located 0.95 mm from the disc face.

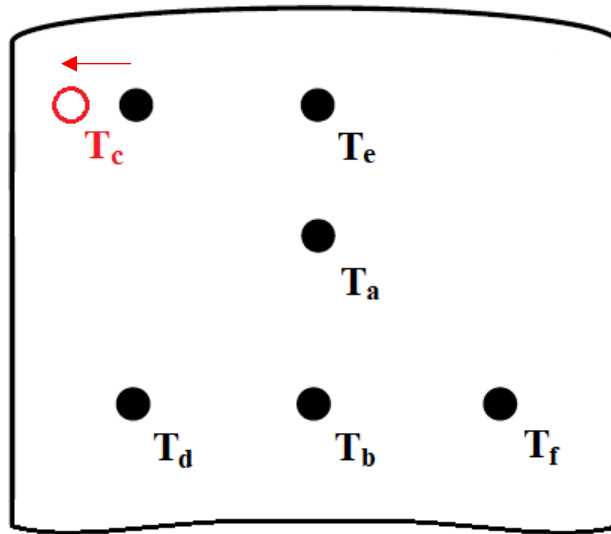


Figure 5-30 New position of thermocouple T_c for experiment (B), moved outwards

The same analysis process used for experiment (A) was used again for experiment (B). At the end of these analyses, the results obtained were compared to those obtained from having T_c located at its original near surface position and they are shown in Figure 5-31 below.

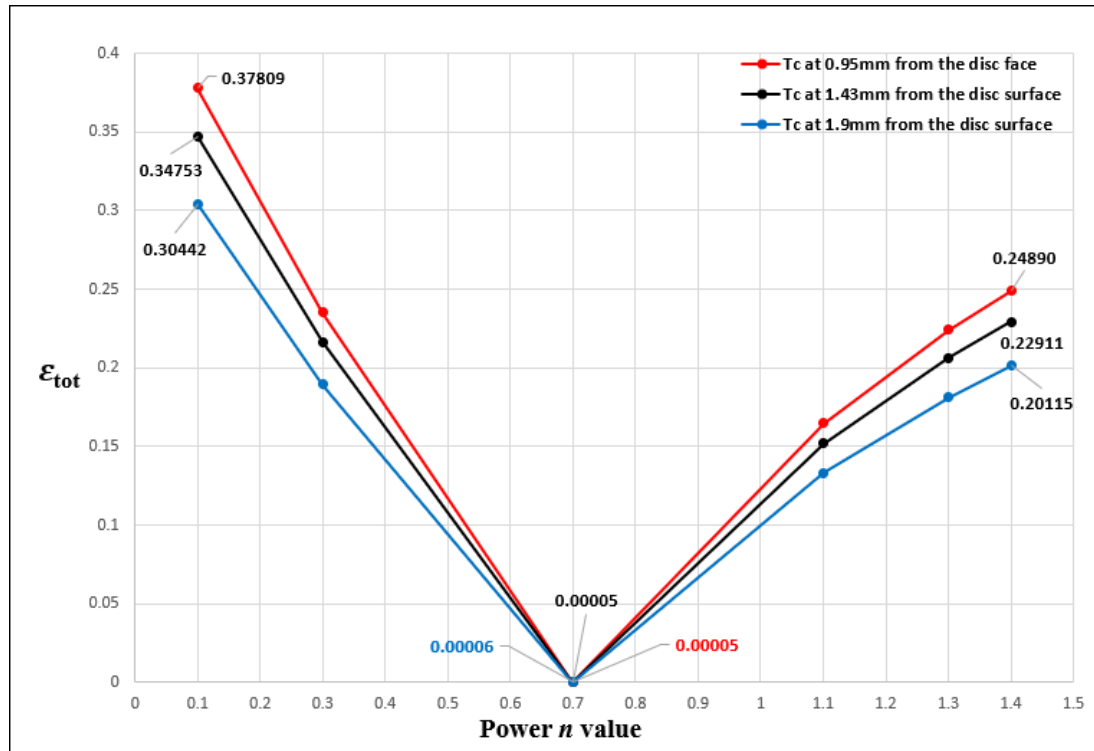


Figure 5-31 Total error using simplex method with different positions of thermocouple T_c

The analyses carried out previously clearly showed that moving thermocouple T_c outwards gives better results in terms of discernment. The best fit for this position of T_c gives errors that are larger when for values of $n \neq 0.7$ compared to those obtained originally, where for the selected value $n = 0.7$ the total error obtained is still zero. On the other hand, moving the position of T_c inwards gives best fits that have smaller errors than those obtained from having T_c at the original position. Hence, having the position of T_c near the side of the disc is better and leads to the best discernment of the value of n .

These results were obtained using the simplex method analysis without adding noise to the three generated synthesised temperatures sets. Therefore random noise with maximum amplitude of $0.5 \text{ }^\circ\text{C}$ was added to the three generated synthesised

temperatures sets at random time steps, the analysis was carried out again using these new temperatures in order to verify and test the effectiveness of this experiment after having the position of T_c modified and having noise added to the data. Figure 5-32 below illustrates a comparison between the analysis with noise and without it for the three different positions of T_c .

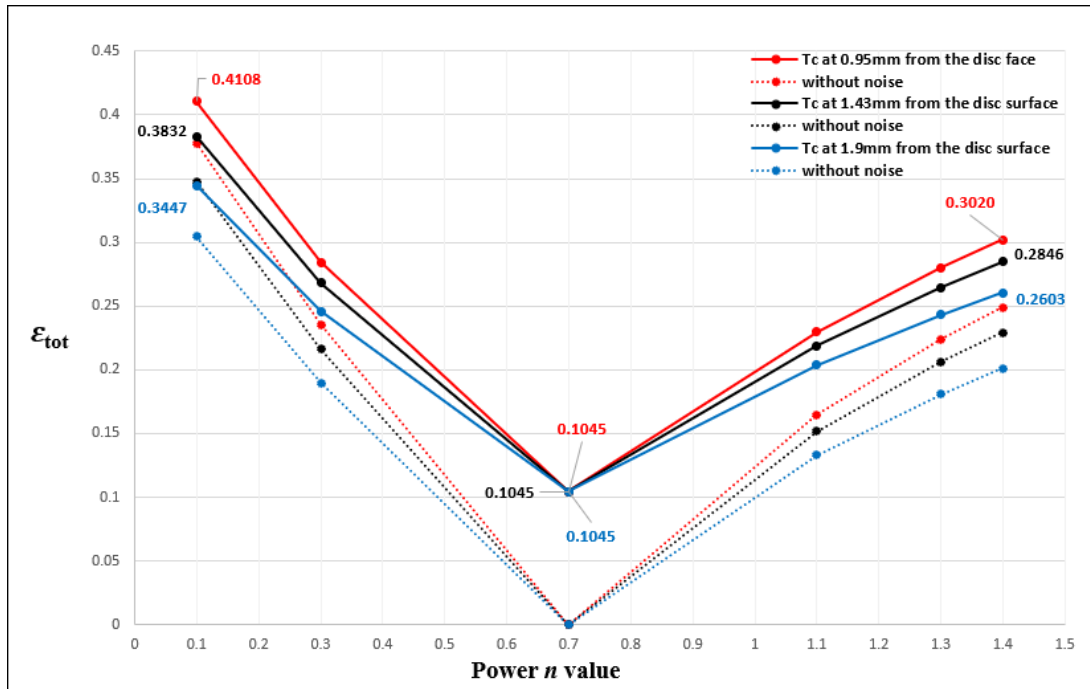


Figure 5-32 Total error using simplex method with noise added to the generated synthesised temperatures for different positions of thermocouple T_c

The solid curves in Figure 5-32 represent the new results obtained by carrying out the simplex method analysis with noise introduced to the three generated synthesised temperatures sets, where the dashed curves are those have been previously shown in Figure 5-31. These results show that the synthesised experiment is still robust and reliable while having this level of noise introduced to the new synthesised temperatures data. The comparisons confirm that discernment is increased as the position of thermocouple T_c is moved further towards the face. **A further experiment**

where point C was located at the face surface had higher discernment but is not practical to implement as the thermocouples need to be located in blind holes to achieve effective thermal contact with the disc.

5.6.4 Synthesised experiments based on Clarke data

The synthesised experiments, which were covered in the previous section, were based on using the data obtained by the author from the test D3, where the sliding speed is set to 20m/s and the load is set to 1850N. In this section, the same synthesised experiments were repeated, however, using new data obtained from tests carried out by Clarke (2009). Two tests were selected, A1 where the sliding speed is 10m/s and the load is 850N. and C3 where the sliding speed is 16m/s and the load is 850N. This selection was made in order to have three tests in total (A1, C3 and D3) which cover a range of loads and sliding speeds.

As for the synthesised experiment of test D3, test A1 and test C3 were carried out using the exact process used in synthesised experiment D3 in terms of:

- Generating synthesised experiments based on the lower boundary temperatures, the temperature of the fluid/surrounding T_{fl} and the frictional force, in addition to specific values of β , h_s and n .
- Carrying out the simplex method analysis for disc pair error using the generated synthesised data for different values of n .
- Adding noise to the synthesised temperatures and repeating the analysis for comparison.

The new synthesised experiments were carried out several times using different values of n and the different positions of thermocouple T_c investigated in Section

5.6.3. Then, noise was added to the generated synthesised temperatures from tests A1 and C3. The results obtained from these two analyses using the simplex method are shown in Figure 5-33 and 5-34 for test A1 and test C3 respectively.

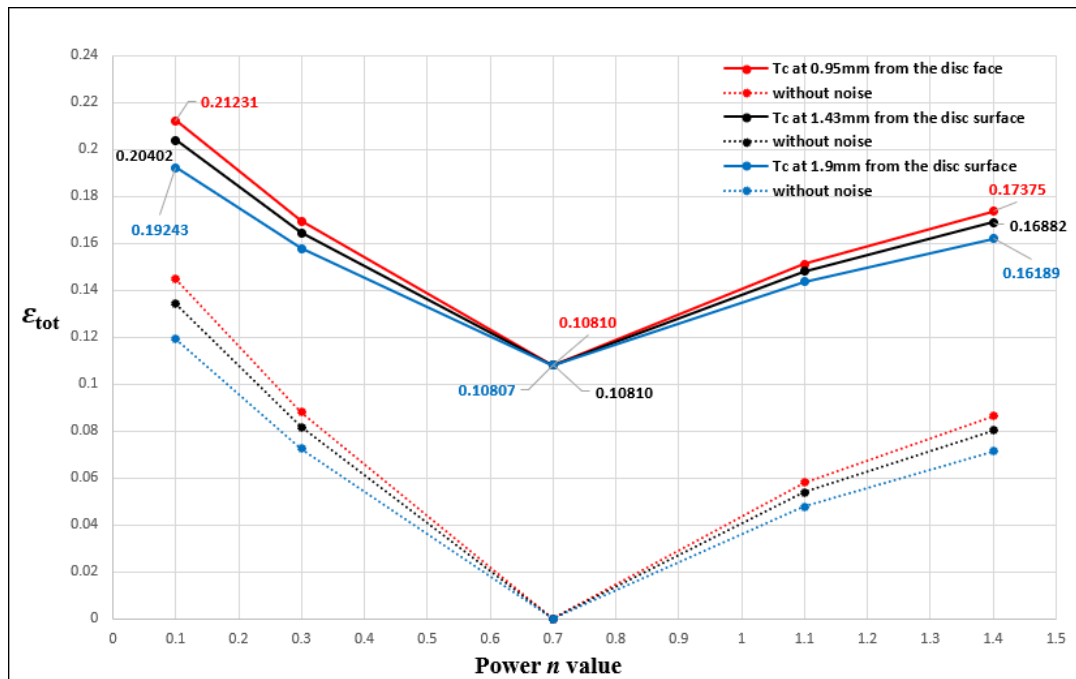


Figure 5-33 Total error using simplex method without and with noise added to the generated synthesised temperatures of test A1 from Clarke data for different positions of thermocouple Tc

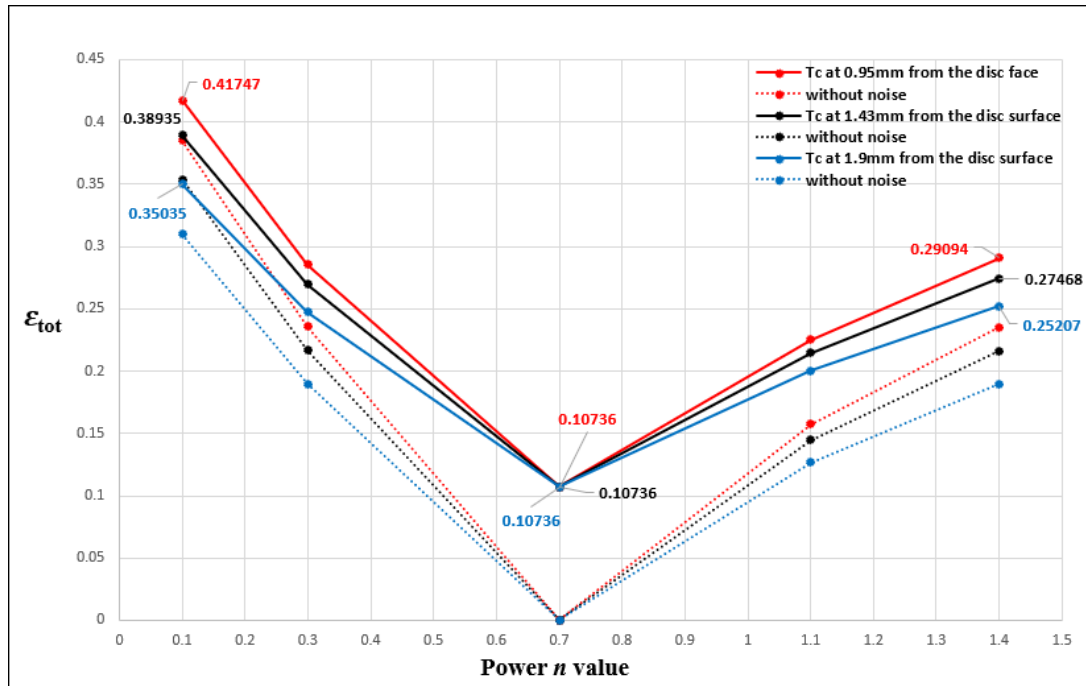


Figure 5-34 Total error using simplex method without and with noise added to the generated synthesised temperatures of test C3 from Clarke data for different positions of thermocouple T_c

The results obtained from the synthesised experiments using Clarke's data for the boundary conditions have a good agreement with those previously obtained using the author's data. The synthesised experiments are always able to find a clear-cut minimum and show a robustness and reliability with three different tests conditions (test A1, C3 and D3) where the sliding speed and the applied load is different for each test, and this gives different temperature measurements and different friction force patterns for each test. Also, the outcomes obtained using the Clarke data with the new different positions of thermocouple T_c showed a good agreement with what was concluded with regard to the optimum position of thermocouples and better results in terms of discernment.

5.6.5 Thermocouples accuracy investigation

During the synthesised experiments, thermocouple accuracy was also examined. Carrying out the analysis using input temperatures that have three decimal digits after the decimal point does not give the same results in terms of accuracy as those when using the same input temperatures rounded to one decimal digit after the decimal point.

Several analyses were carried out in order to determine the influence of changing the accuracy of the data logger on the results and how could the resolution of the measured temperatures change these results. The generated synthesised temperatures from test D3 were rounded to three different levels of precision, 0.05, 0.1 and 0.25 °C. three times, each time to a different decimal numbers after the decimal point. This is to simulate the measurement accuracy of the thermocouples and subsequent rounding by the data logger during each analysis. Each of these three new sets of synthesised temperatures was used as an input in the simplex method analysis.

Figures 5-35, 5-36 and 5-37 below show the synthesised temperatures with T_c at its original position for the slow disc after rounding them to 0.5, 0.1 and 0.25 °C, respectively.

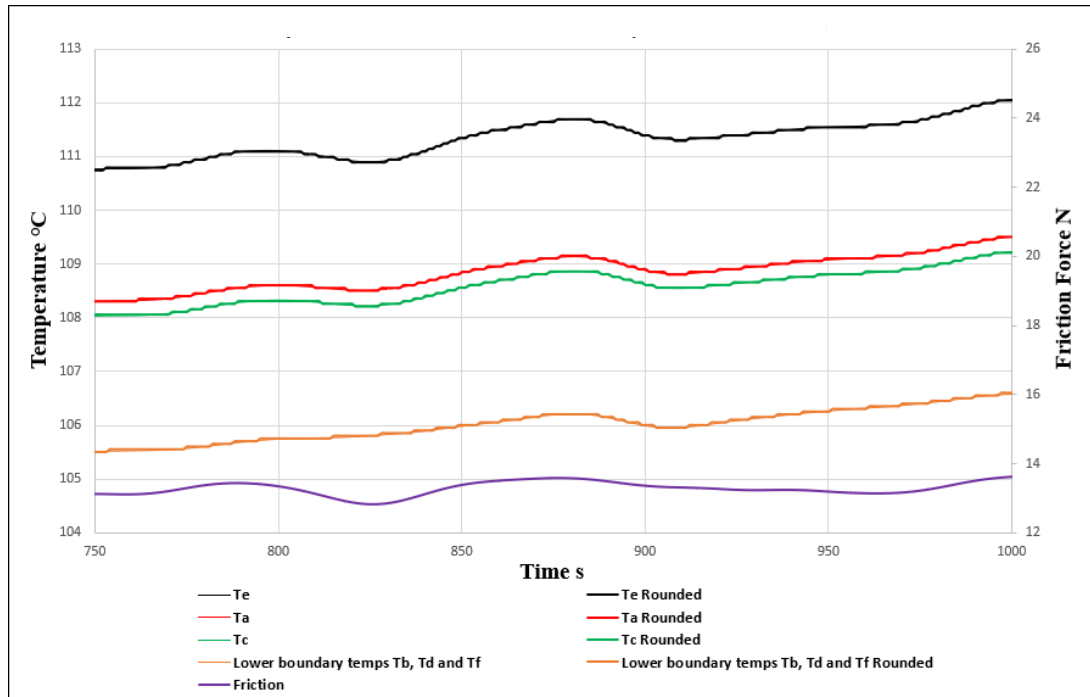


Figure 5-35 Generated synthesised temperatures and rounded to 0.05 temperatures for the slow disc

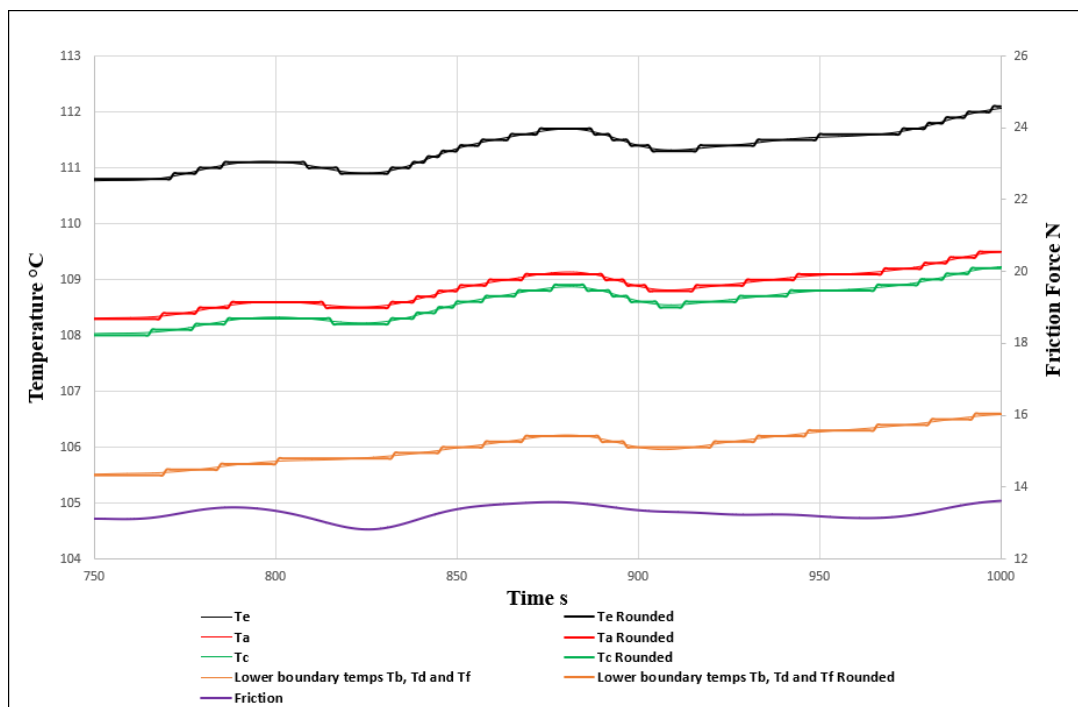


Figure 5-36 Generated synthesised temperatures and rounded to 0.1 temperatures for the slow disc

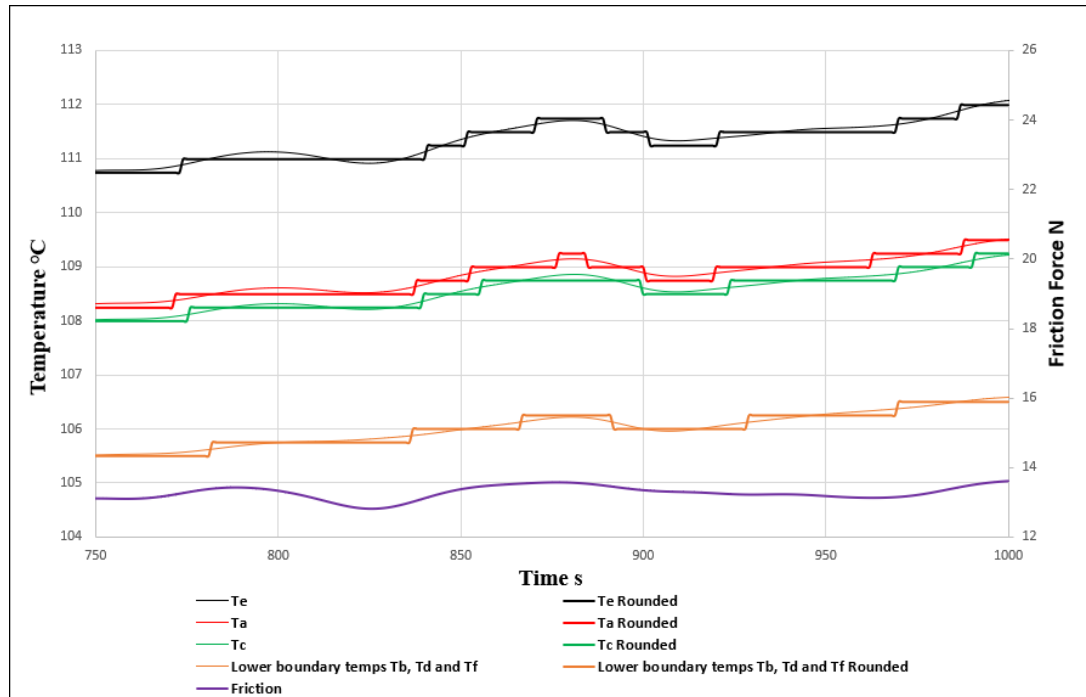


Figure 5-37 Generated synthesised temperatures and rounded to 0.25 temperatures for the slow disc

After carrying out the simplex method analysis with different values of n for these three cases, the results obtained were compared to those obtained from the original generated synthesised temperatures (without rounding them) as shown in Figure 5-38 below.

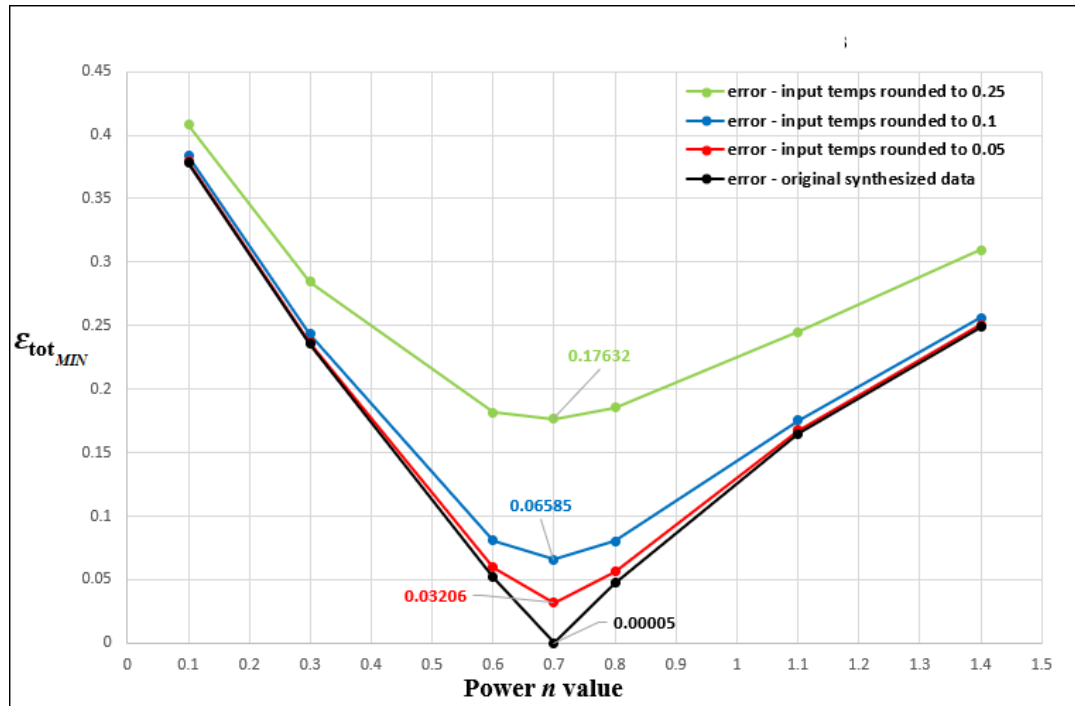


Figure 5-38 Total error of simplex method analysis for synthesised temperatures and rounded ones

The black curve shown in Figure 5-38 represents the total error obtained from the simplex method analysis for $n = 0.7$ using the original synthesised temperatures. The red curve represents the best fit obtained from the same analysis using the input temperatures that are rounded to $0.05\text{ }^{\circ}\text{C}$. There is a clear-cut minimum at $n = 0.7$ and this is also seen for the case of the blue curve with rounding to $0.1\text{ }^{\circ}\text{C}$. However, the green curve for $0.25\text{ }^{\circ}\text{C}$ rounding has a minimum error at $n = 0.7$ but the flattening of the curve at the minimum mean that it is no longer clear cut. Hence, using a measurement processing process that rounds the temperatures to $0.25\text{ }^{\circ}\text{C}$ will introduce some uncertainty into the n value at the minimum.

5.7 Conclusion on requirements

During the experiments and the investigations conducted in this chapter, inconsistencies in the measured temperatures were discovered, and this was confirmed by conducting the synthesised experiment where synthesised temperatures were generated based on the lowest boundary temperatures and were used as input files. In addition, the position of thermocouple T_c was found to be weak in terms of discernment of the dependence on n . Hence, it should be moved to be at the most advantageous position in order to get best discernment. Also, the accuracy of thermocouples, in terms of decimal digits after the decimal point for the measured temperatures was investigated, these temperatures should not be rounded by the recorders to more than 0.1 for better results. This level of accuracy was also achieved by Clarke (2009) when he calibrated each thermocouple in the disc individually by placing the instrumented disc in a temperature-controlled chamber which also had a calibrated high accuracy Platinum Resistance Thermometer with maximum error of ± 0.1 °C. By obtaining individual calibration curves over the expected temperature range he showed that the thermocouple error was less than 0.2 °C for 90% of the calibration measurements and less than 0.1 °C for 70% of them.

Chapter 6 Test rig development design

6.1 Introduction

This chapter covers further developments of the test rig, where two main improvements to the test rig were developed in order to ensure a better performance of test rig during the EHL experiments. The first improvement was designing new integral shafts and test discs to replace the original slow shaft and fast shaft with their test discs, where the second improvement was adding on-shaft thermocouple amplifiers to the test rig in order to adapt the test rig for use in the current work.

6.2 Integral shaft and disc

The shafts and test discs previously used for the EHL experiments in Cardiff University consisted of two main parts, the shaft itself and a test disc that mounted on the shaft by using a heavy press fit. This test disc is also retained on the shaft by the means of a high shoulder and secured using a locking nut. The insulating ceramic washers are fixed on both sides of the test disc. The schematic drawing in Figure 6-1 illustrates how the test disc is mounted on the shaft. In previous work using the rig the temperatures measured by the inner radius thermocouples were not symmetric as discussed in Section 5.5. This is thought to have been due to a temperature measurement problem, but the integral shaft and disc was seen as a method for eliminating two possible sources of thermal asymmetry, the asymmetry in the thermal path from the disc to the shaft, and inconsistency in the thermal resistance at the interference fit between the shaft and disc.

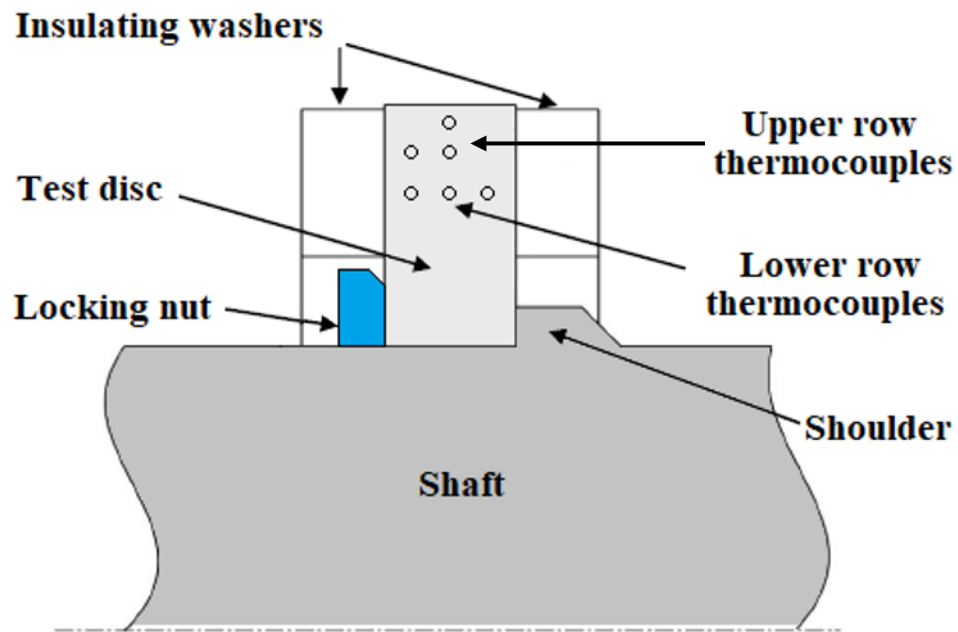


Figure 6-1 Drawing of the configuration of the shaft and the test disc

The existing configuration might cause asymmetric temperature distributions due to the fact that there are three parts involved in conduction (Shaft, locking nut and test disc). Hence, integral shafts and test discs were designed in order to remove the uncertainties of conductance variation. They were designed to be made from a single piece of metal bar and to be as symmetrical as possible. This would lead to a symmetric temperature distribution within the test discs as the contact area is symmetrical about the disc centre plane. SolidWorks software was used for this development design.

Figure 6-2 and 6-3 below shows the developed designs of the slow and the fast integral shafts and test discs respectively. Both shafts consist of a single metal piece. Also, it can be noticed that there is a slight difference between the two integral shafts near the disc area, this is due to the fact that the slower shaft is installed on two bearings mounted on a swinging arm (yoke) as shown in Figure 2-4 which is used to

apply the load during the EHL experiments, and these bearings are located close to the disc. For the faster shaft there are two fixed bearings that are located slightly further from the disc in comparison to those for the slower shaft.

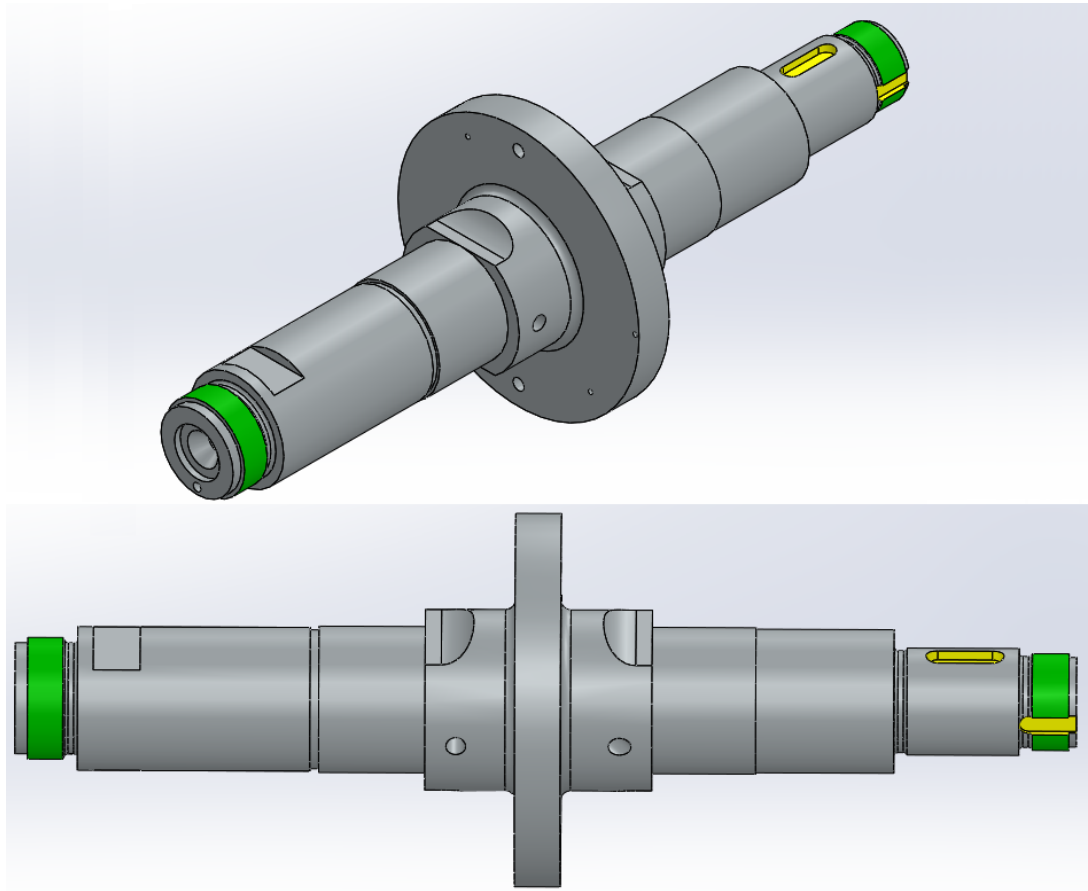


Figure 6-2 The new developed design of the slow integral shaft and test disc

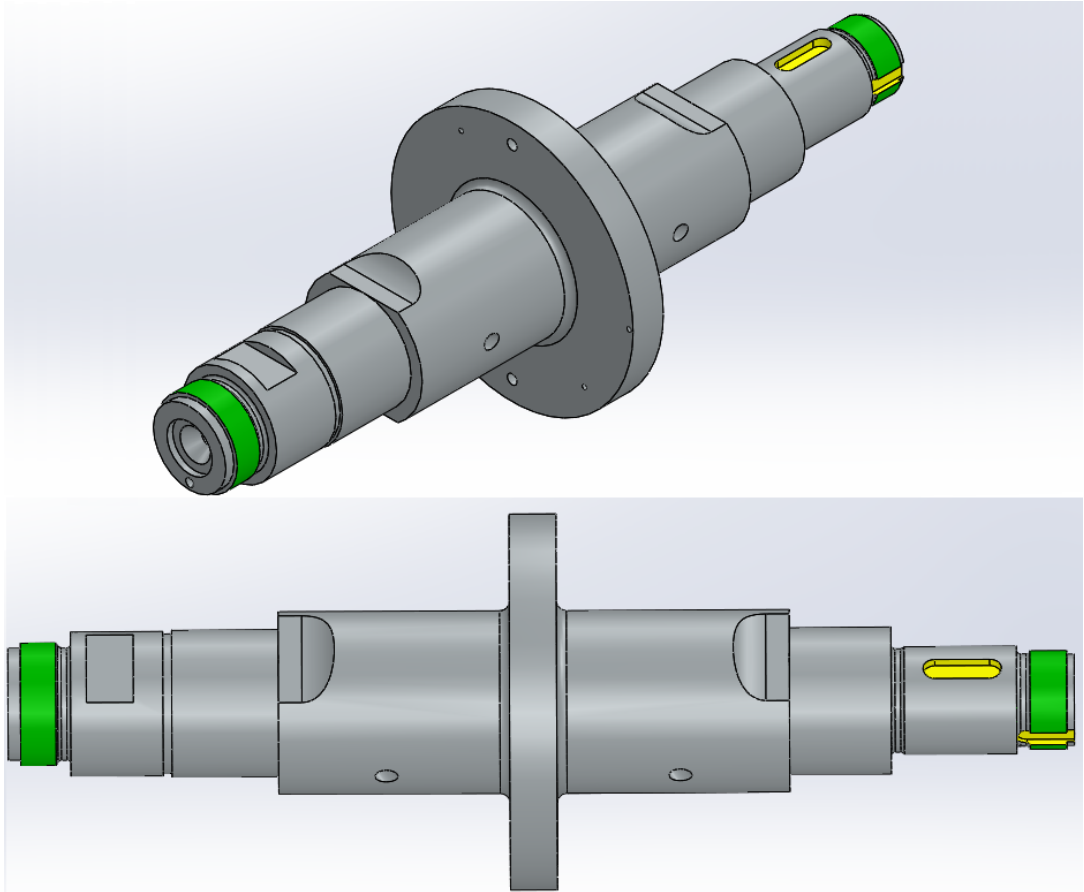


Figure 6-3 The new developed design of the fast integral shaft and test disc

Cross-section drawings for the slow and the fast integral shafts and test discs are shown in Figure 6-4 and 6-5 respectively. These drawings show the hole arrangements that are used for passing the thermocouple wires from the discs to the slip rings.

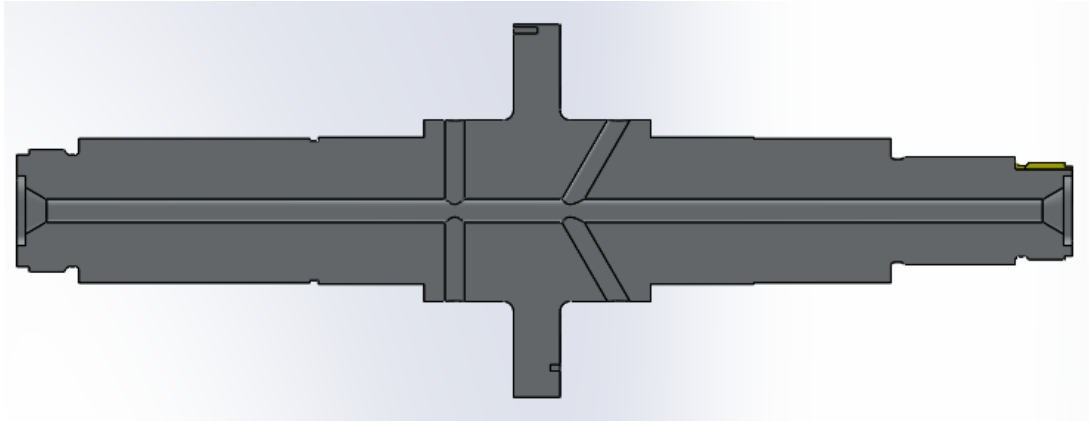


Figure 6-4 Cross-section drawing of the slow integral shaft and test disc

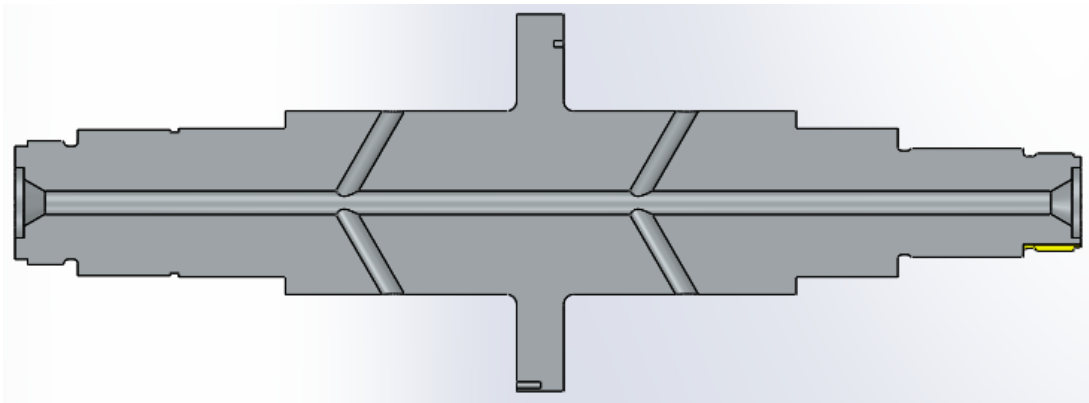


Figure 6-5 Cross-section drawing of the fast integral shaft and test disc

For the integral shaft designs the insulating ceramic washers can be changed so that they contact the whole of the face sides of the integral discs. This would substantially reduce the heat flux from the face sides of the disc that happens with the current shafts at radii lower than the bore radius of the current ceramic discs. Since that heat flux could be asymmetric due to the asymmetric shoulder and retaining nut this is a further advantage of the new design. Figures 6-6 and 6-7 show the proposed positions of the ceramic discs for the slower and faster shafts, respectively.

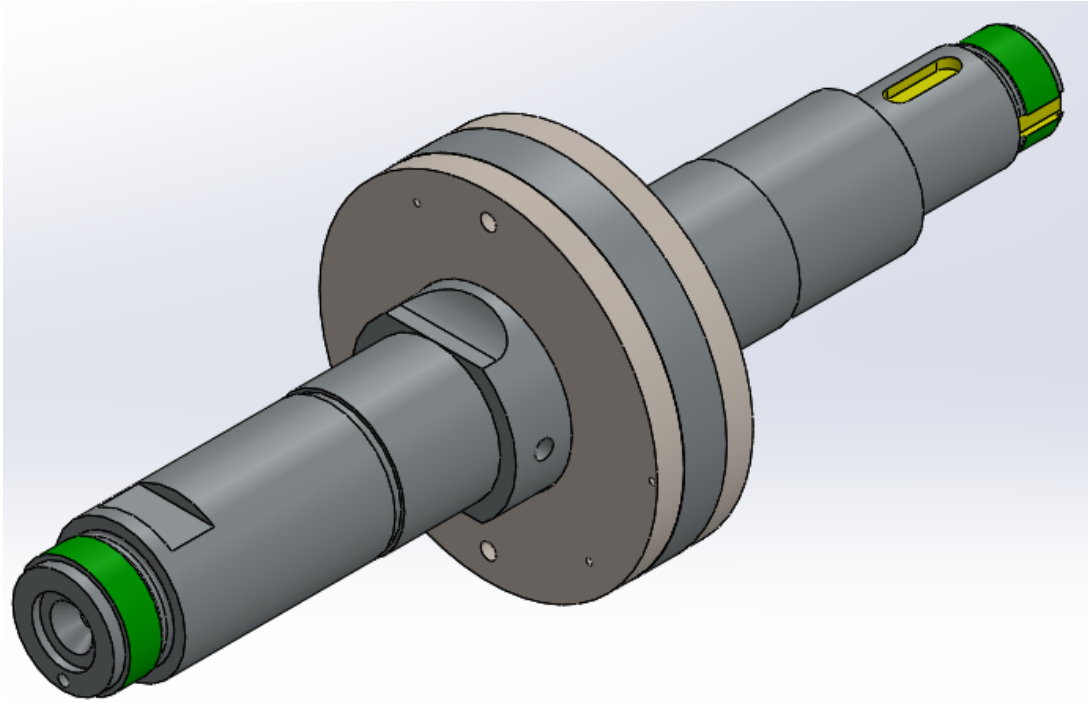


Figure 6-6 The slow integral shaft and test disc with the ceramic washers installed

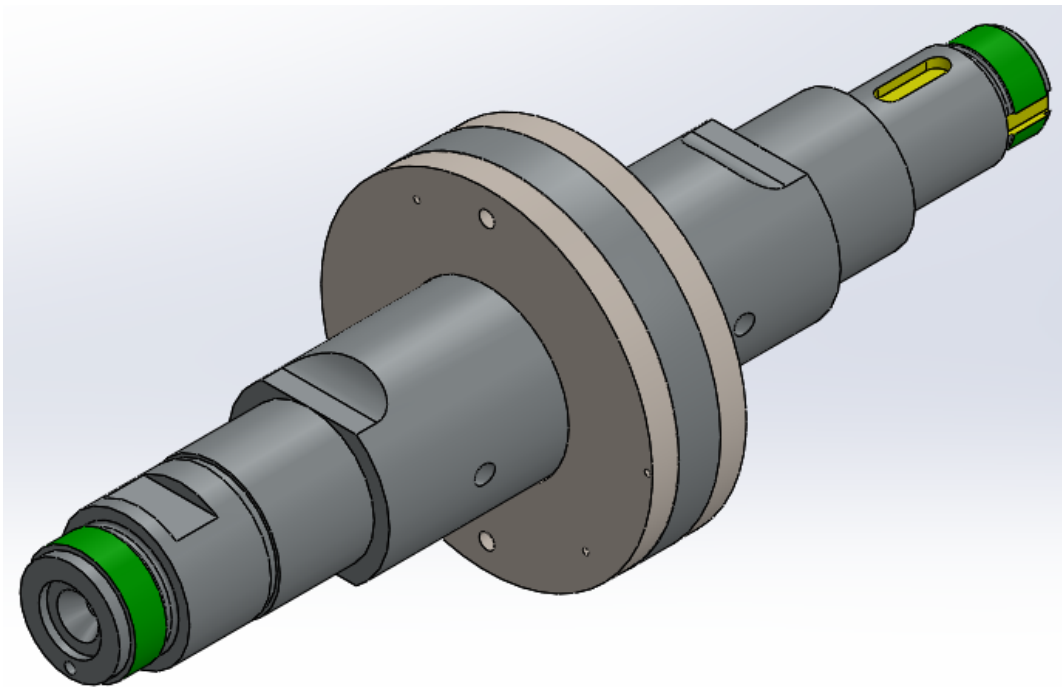


Figure 6-7 The fast integral shaft and test disc with the ceramic washers installed

Figure 6-8 shows both integral shafts and discs assembly. The assembly and disassembly of these new integral shafts and discs will follow exactly the same process of that used for the original shafts. They have been designed so that there is no need to make any modifications to the test rig for installing these new integral shafts and discs as the dimensions of the test rig and the original shafts were taken to be constraints during the design stage of the new integral shafts and discs.

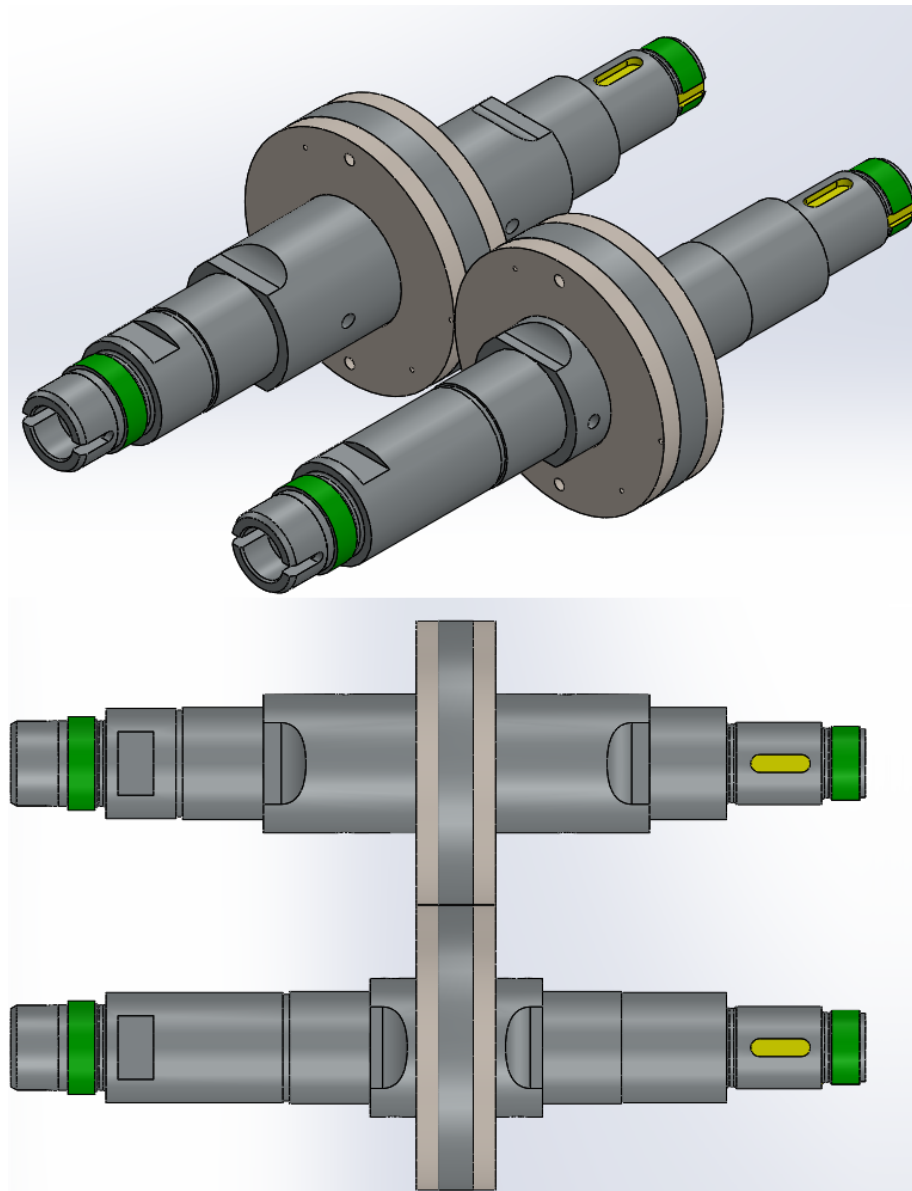


Figure 6-8 Twin disc shaft assembly with the insulating ceramic washers

6.3 Developing on-shaft thermocouple amplifiers

The output signal from the thermocouple travels via the wiring, then it has to pass through the slip rings before reaching the amplifiers. As this is a low voltage signal, in the mV range, it can be easily affected by stray voltages and electrical noise from the surroundings. In addition the slip rings used to transfer the signals from the rotating shafts to the thermocouple signal conditioning modules may also distort the signal causing errors in the measurements obtained. Increasing the output signal by moving the thermocouple signal conditioning modules onto the rotating shafts would significantly reduce the error and also allow the analogue signal to be digitised to provide a more robust signal for transfer through the slip rings to the LabVIEW software.

As the only way to amplify this signal before reaching the slip rings is to have the thermocouple signal conditioning modules mounted on the shaft, two on-shaft thermocouple amplifiers, one per shaft, were developed as shown in Figure 6-9 below.

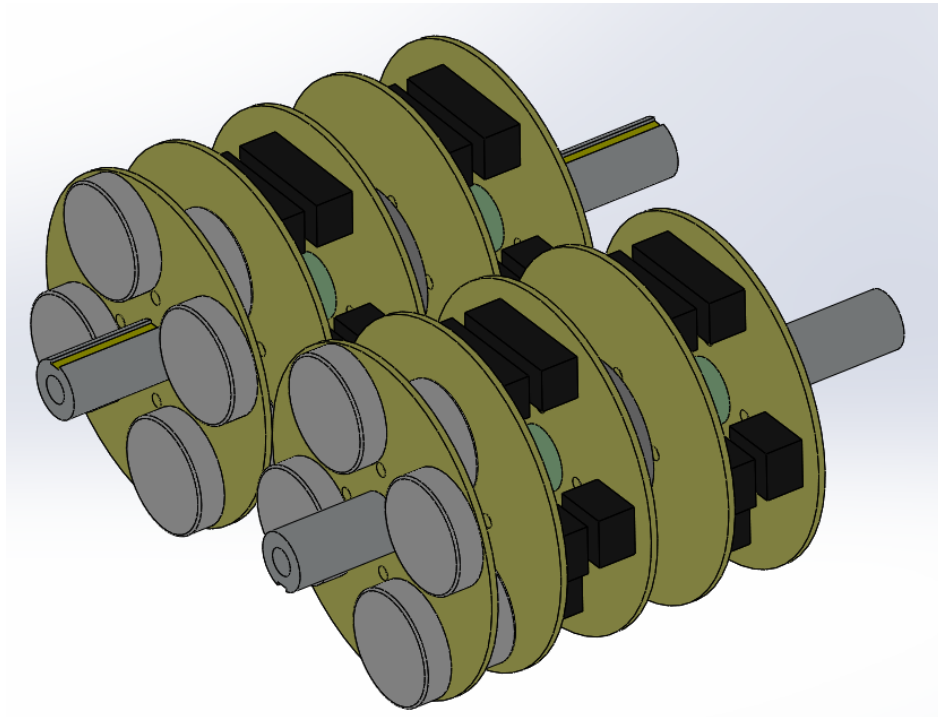


Figure 6-9 On-shaft thermocouple amplifiers design

Each shaft is intended to carry five disc shaped circuit boards. One board is used for mounting the separate power supply batteries. There are eight batteries per board, four on each side of the board. The other boards are to be used for installing the thermocouple amplifiers and the microprocessor to be used to digitise the thermocouple signals and send the measurements through a slip ring to the LabVIEW software. Each of the three amplifier boards includes two J-type thermocouple amplifiers, this gives a total of six thermocouple amplifiers per shaft. Figure 6-10 and 6-11 show the batteries board and the amplifiers board respectively.

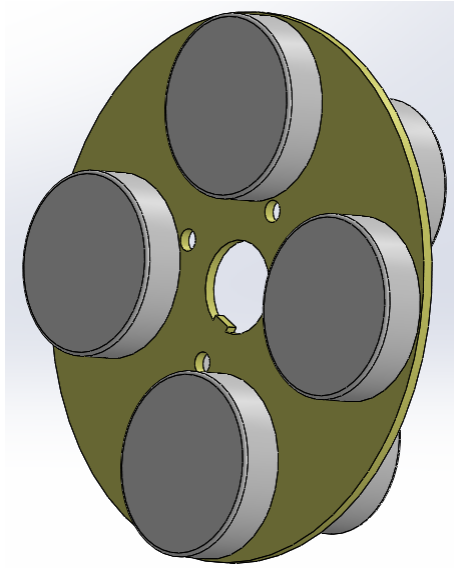


Figure 6-10 Batteries board design

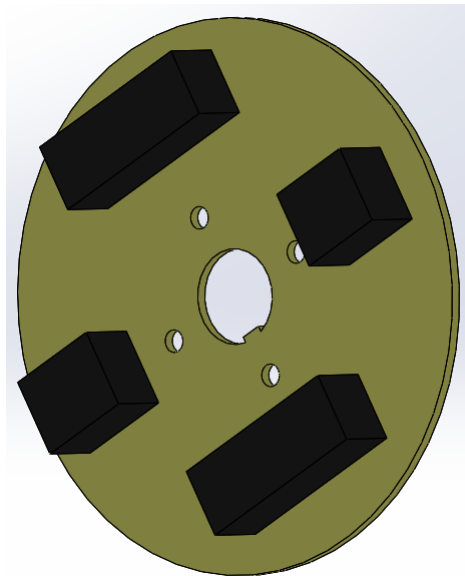


Figure 6-11 Thermocouple amplifiers board design

The mechanical design for the on-shaft amplifiers involves extensions to the test head shafts to carry the electrical boards outside of the test head area of the test rig in order to avoid the heat generated during the EHL experiments. Both on-shaft thermocouple amplifiers will have one end connected to the thermocouple leads that

emerge from the external end of the test shafts. The output from the microprocessors will then be connected to the slip rings. In order to implement this prototype design and install it on the test rig, it was necessary to make new holes at new locations in the test head base plate of the test rig to mount the slip rings at their new position. Figure 6-12 shows the original design of the test head base plate of the test rig. The four larger holes are those for the test head end plate bolts in the current design. The group of four smaller holes are used to attach the slip ring mounting to the base plate. Both of these components are located by dowels in the other holes shown.

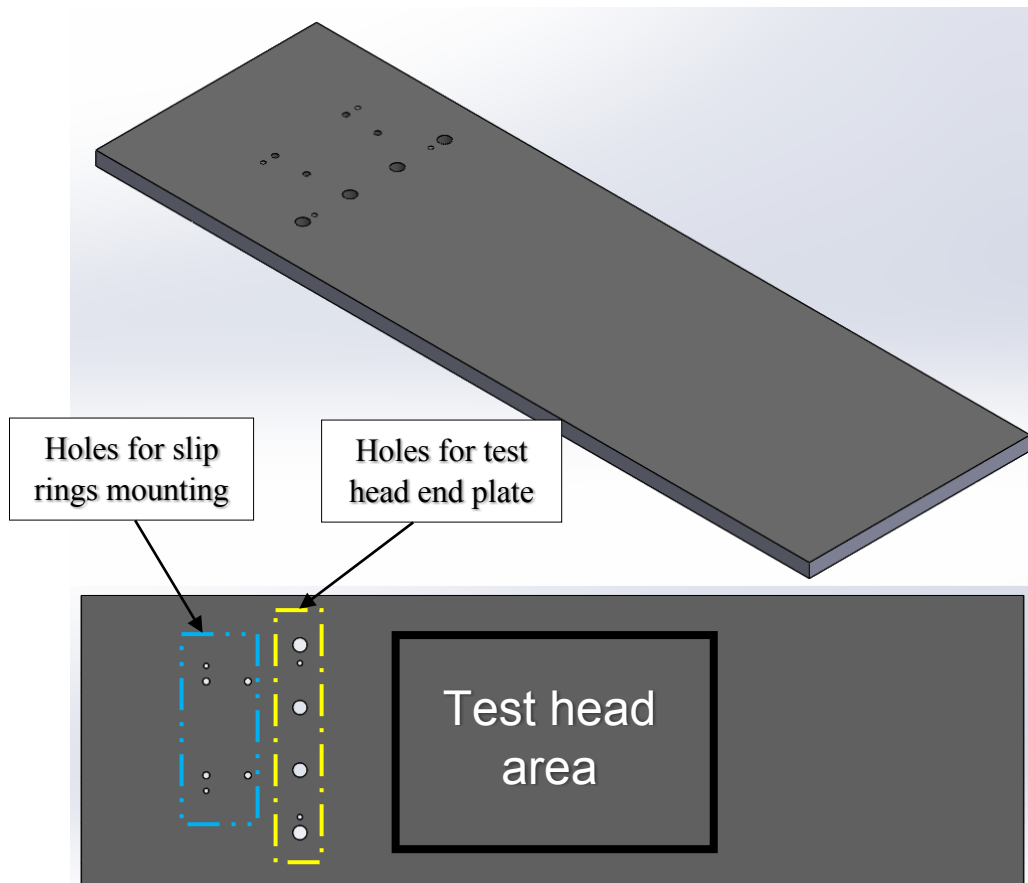


Figure 6-12 The original design of the test head base plate with the original positioning of the holes

Figure 6-13 shows the additional holes made in the test head base plate to accommodate the mounting arrangement for the shaft extensions and circuit boards. These provide an axial offset for bolting the slip ring mounting to the test head base plate so that the shaft extensions can be incorporated.

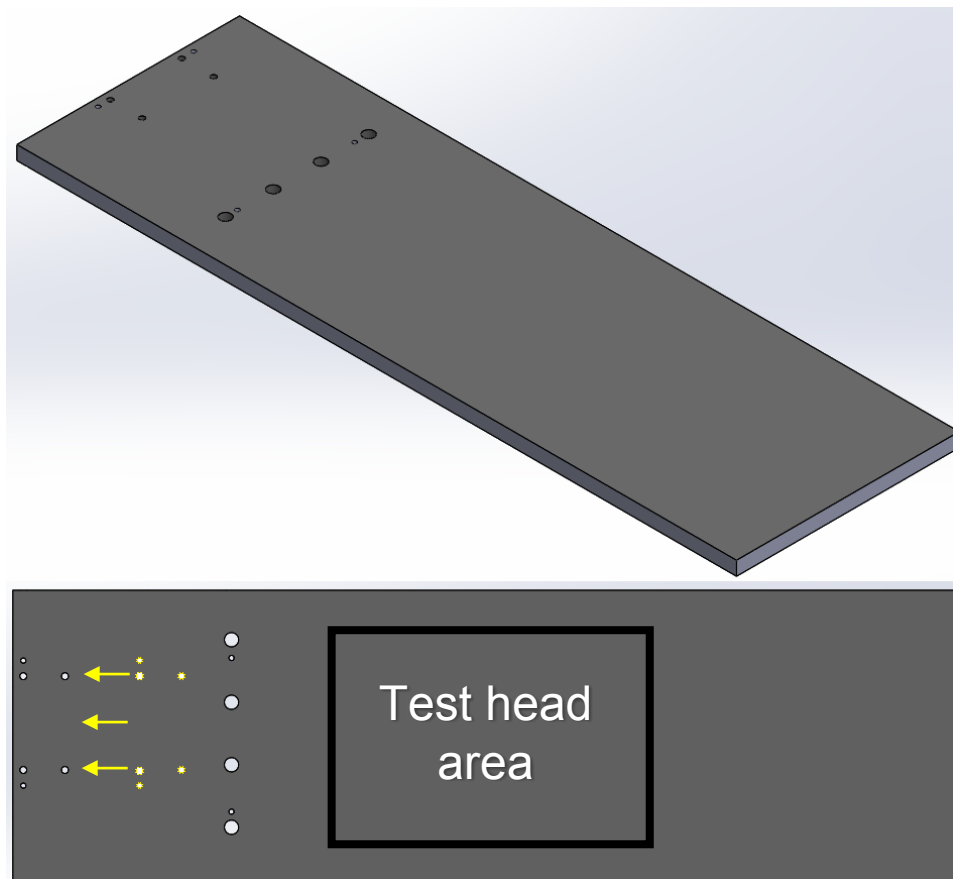


Figure 6-13 The new test head base plate arrangement with offset the slip ring mounting holes

The difference between the original and the modified design is shown in the sectional schematic view of Figure 6-14.

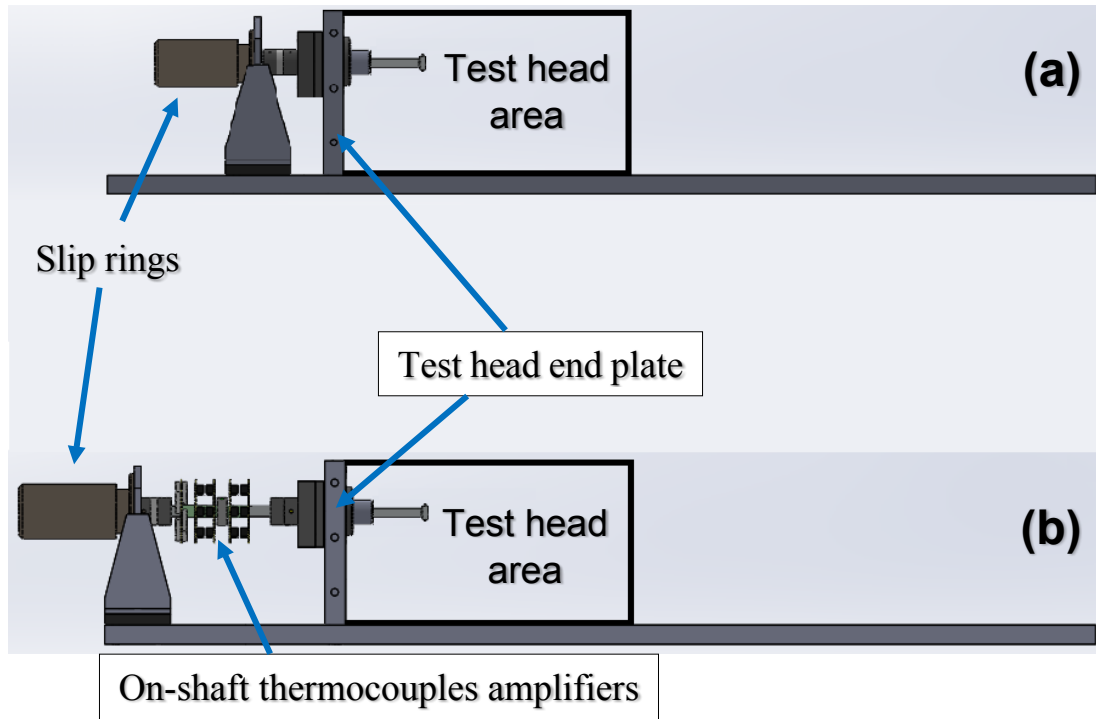


Figure 6-14 Side view of (a) the original design, and (b) the modified design

A more detailed view of the design of the on-shaft thermocouple amplifiers mounted in the test rig is shown in Figure 6-15.

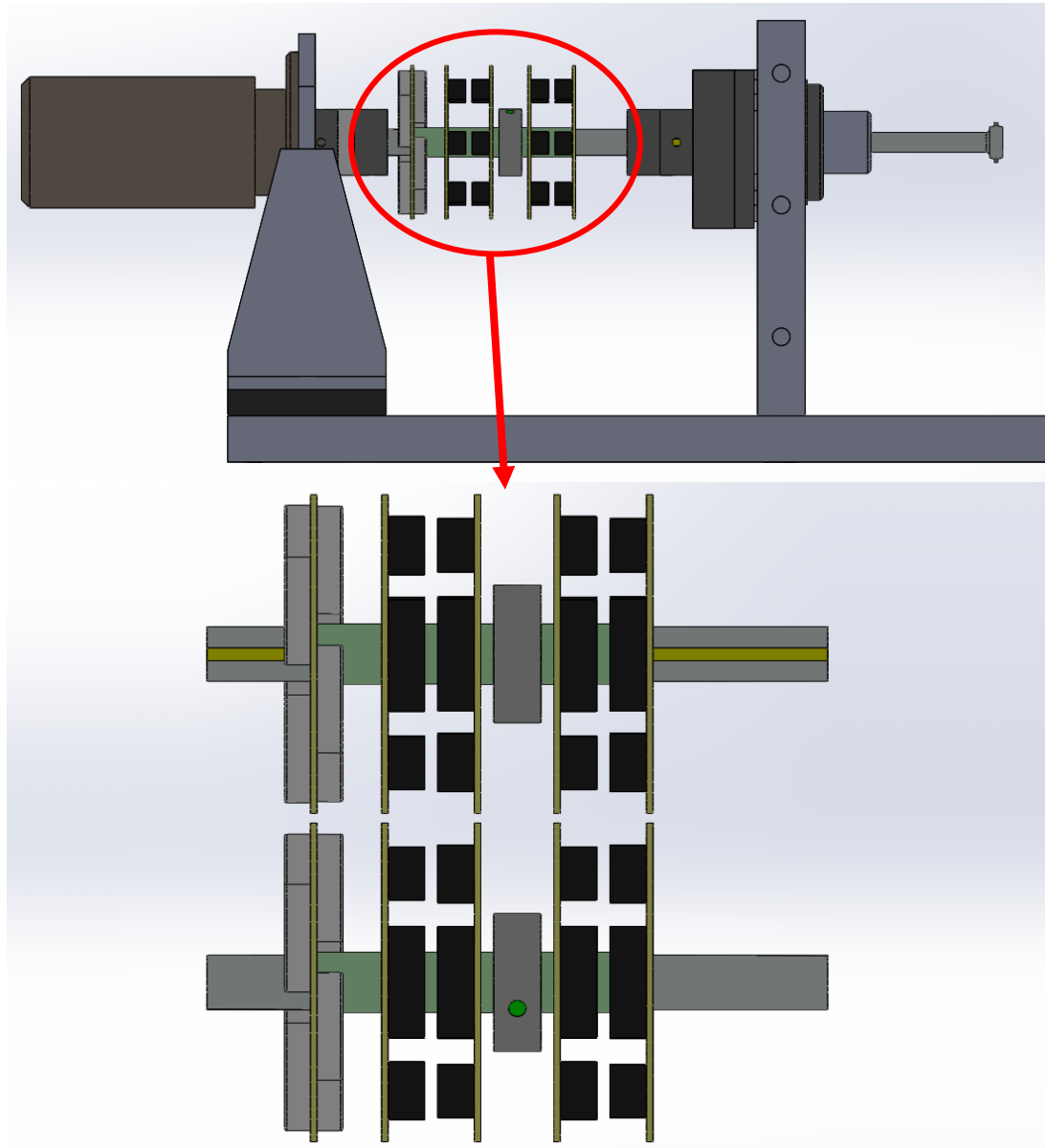


Figure 6-15 Detailed view of the design developed for the on-shaft thermocouple amplifiers.

Figure 6-16, 6-17 and 6-18 show photographs of the batteries board and the prototype thermocouple amplifier board made by the School of Engineering electrical workshop. Unfortunately manufacture of these boards was delayed significantly due to technical staff retirements which led to a much reduced availability of electrical support over the last 18 months of the project.



Figure 6-16 Photograph of the batteries board

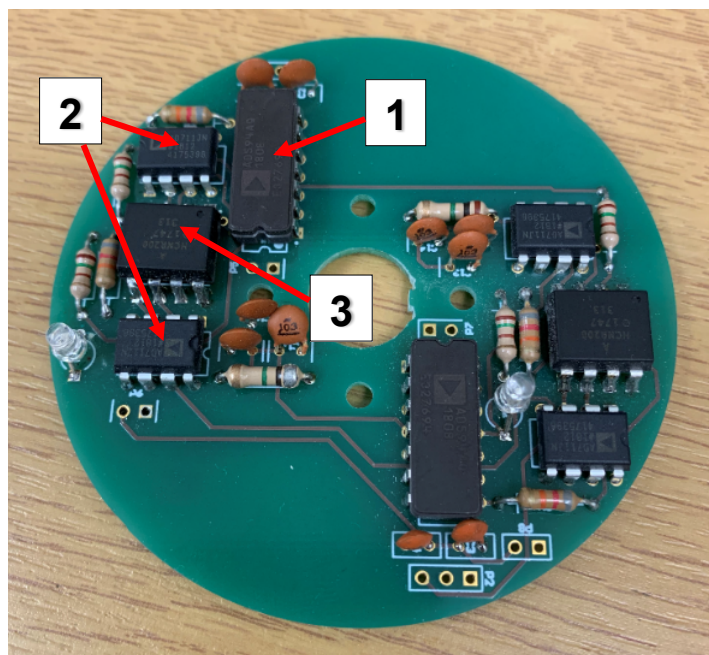


Figure 6-17 Photograph of the thermocouple amplifiers board

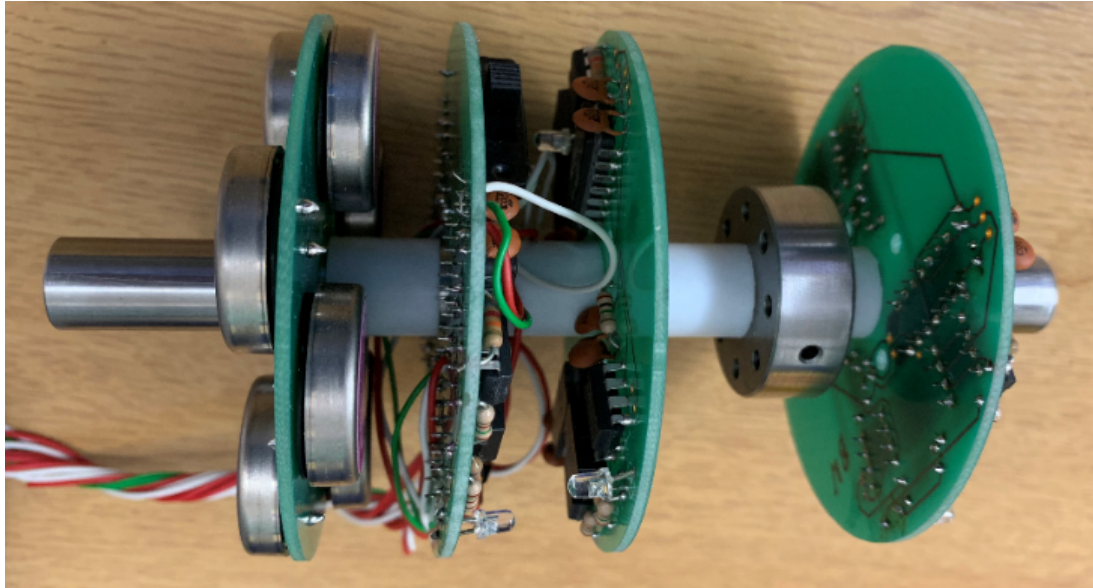


Figure 6-18 Photograph of the on-shaft thermocouple amplifiers

During the specification discussions for the thermocouple amplifiers the problem of galvanic isolation was clarified. In the test circuit shown in figure 6-17 the thermocouple output is passed to a thermocouple amplifier with cold-junction compensation (1) whose output is amplified by an op-amp (2) to provide input to a high-linearity analogue optocoupler (3) to provide thermocouple isolation. The optocoupler output is then amplified by a second op-amp to provide a suitable signal for A to D conversion for microprocessor processing and robust digital transmission through the slip rings to the LabVIEW software. The circuits shown carry out this analogue conditioning and amplification and the circuit diagram for a single thermocouple is shown in Figure 6-19.

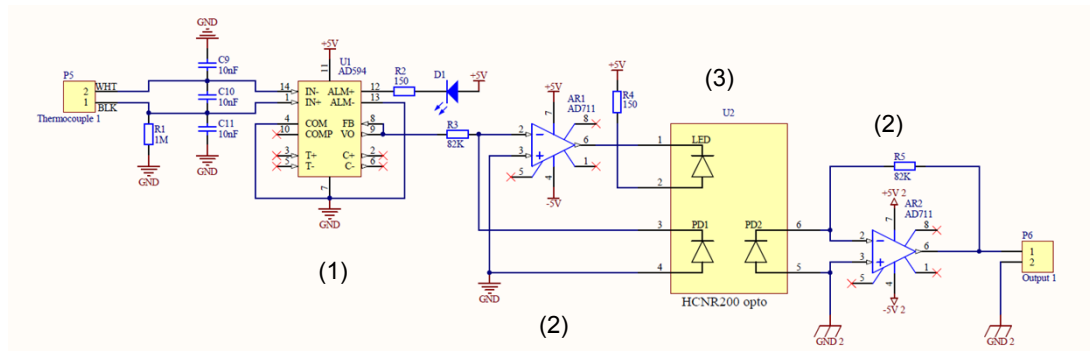


Figure 6-19 Circuit for the on-shaft thermocouple amplifiers developed by school electrical technical support. (1) Thermocouple amplifier with cold junction compensation, (2) Op-amps, (3) Opto isolator.

Tests of galvanic isolation of the manufactured circuits were made by the technical staff on the first two boards and were reported to be satisfactory. A revised more compact circuit arrangement was then designed for the two shaft circuit sets. However, the pressure on technician resource led to a simpler alternative approach being supplied to close the task. These are illustrated in the photographs of Figure 6-20 where miniature thermocouple amplifier boards were used that are 21 mm square.

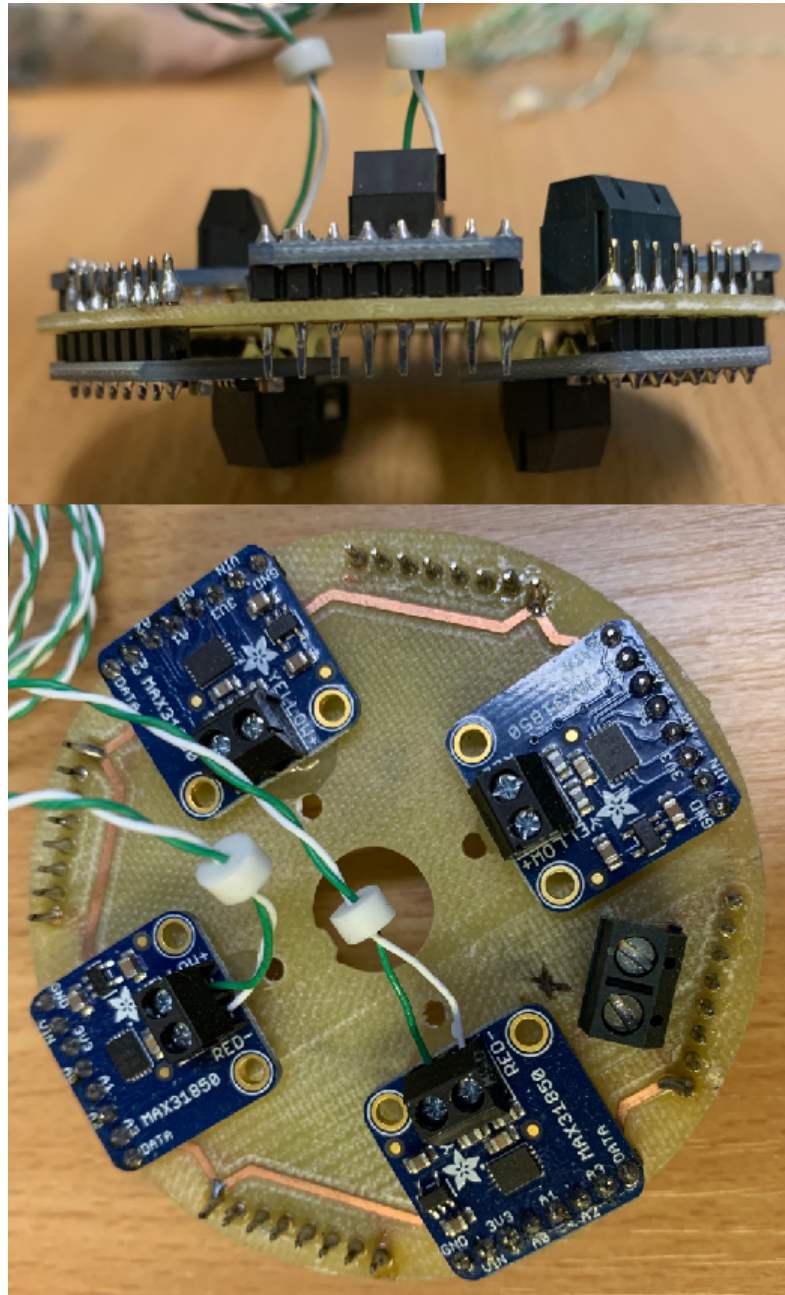


Figure 6-20 New thermocouple amplifiers board, 8 modules mounted on one board

The new type of thermocouple amplifiers supplied have several potential advantages in that they were expected to be able to work successfully from a common power source which could be fed to them by a pair of slip ring channels. This would remove the need for individual batteries. A second advantage is that the amplifiers incorporate

built-in Analogue to Digital conversion of the thermocouple signal. The amplifiers work with K-type thermocouples only, which would not be a problem for the current work as they have the same accuracy as the J-type thermocouples and have a larger temperature range (K-type ≈ -270 to 1250 °C, J-type ≈ -210 to 750 °C). However these factors, taken together, mean that the amplifiers cannot provide the necessary accuracy.

Before implementing the proposed modifications on the test rig, the on-shaft thermocouple amplifiers required testing and calibrating in order to ensure their effectiveness. The first step taken to test them was to place two thermocouples connected to the boards in two different heat sources. One was placed in a container of boiled water and the second was left at the room temperature. It was observed that the temperature measurements obtained from the amplifiers varied with time in 0.25 °C increments. This is an inherent limitation of the miniature thermocouple amplifier boards. As they are general purpose and resolve the whole 1520 °C measurement range of the type K thermocouple the word length of the built-in A to D conversion results in the 0.25 °C resolution limitation. For measuring temperature this is probably perfectly satisfactory, but the essence of the experimental method is of measuring differences of temperature and so they become questionable in this regard. This test was carried out while the earlier investigations of the discrimination of simplex minimisation approach were being carried out, as reported in Chapter 5. This work was therefore extended to consider thermocouple accuracy and to assess the effects of different levels of temperature rounding. The results obtained for the dependence of simplex error minimisation on error and temperature rounding showed that the resolution of 0.25 °C compromised the effectiveness of the experiment. It became clear that resolution of the A to D conversion process was an important factor to consider. The built-in A to D conversion was a poor choice and this part of the signal

processing would need to have the capacity to resolve the measurement down to the resolution of the calibrated thermocouples as a minimum requirement.

Consequently, the miniature thermocouple amplifiers were discarded for the current work and it was clear that the planned experiments could not be carried out effectively until the resolution problem could be overcome.

6.4 Conclusion on requirements

The difficulties with the miniature thermocouple amplifier boards and the subsequent analysis of resolution issues reported in Chapter 5 clarified the requirements for the on-shaft processing in order to exploit the potential of the new simplex error minimisation method developed for analysing the experiments. These are:

- Galvanic isolation of the thermocouples is essential.
- The extent of electrical noise introduced by the test rig environment when the thermocouple signals are amplified and opto-isolated on-shaft needs to be established.
- A to D conversion must have sufficient digits to resolve the analogue signal to better than the thermocouple resolution obtained with individual calibration.
- The processing approach for the digitised signal to provide the transient temperature measurements should ensure that the rig induced noise is removed.

Chapter 7 Conclusions and recommendations for future research

7.1 Summary of the work

This work has been concerned with the study of friction and heat generation in rolling/sliding contacts operation in the Elastohydrodynamic Lubrication (EHL) regime using a twin-disc test rig that was previously modified and developed by previous authors for this purpose.

An EHL experiment was carried out, where the data obtained were filtered and curve fitted in order to model it. A numerical model for the thermal behaviour of the test discs was developed using that EHL experiment data as boundary conditions to calculate and analyse the temperature distribution within the test discs, and to compare these calculated temperatures with those measured during the EHL experiment. The results depend on parameters β , h_s and h_f quantifying partition of the heat generated between the discs and heat transfer from their surfaces. The analysis process to calculate the error was applied over the last 200 seconds of the transient analysis where it had reached near steady state behaviour with the objective of determining the values of β , h_s and h_f .

A new approach for calculating the error was achieved using the downhill simplex method, which has been implemented in two dimensions for the parameters (β and

h_s) for a given ratio $\frac{h_f}{h_s}$. This method was able to find the minimum total error by

calculating the total error for both discs for the same given (β , h_s) combination. The simplex method varies (β , h_s) according to the total error found for three (β , h_s) points

(the simplex). The initial simplex is a triangle in the (β, h_s) plane and the method's strategy adjusts this triangle to enclose and contract around the minimum error point.

During the analyses, inconsistencies in temperature measurements were found which caused further investigations to be carried out. These investigations were: carrying out synthesised experiments, finding the optimum positioning of thermocouples and examining the accuracy of thermocouples and the logging recorders in terms of resolution and significant figures of the measured temperatures.

New integral shafts and test discs were designed to replace the original slow shaft and fast shaft with their test discs, and new on-shaft thermocouple amplifiers were commissioned to be installed on the test rig.

7.2 Conclusions

- The mesh size for the numerical solution can be varied and a mesh independence was determined. The total frictional heat flux on the running track of the test disc is mesh dependent and should be subjected to minor scaling in order to ensure that the correct heat input is applied.
- A new method for calculating the minimum total error has been developed, the error minimisation method was improved by considering the total error for both discs rather than that of each individual disc.
- The new method (disc pair error minimisation method) was applied over the last 200 seconds of the loading stage where the test had reached approximately steady state conditions. The new method can find a clear-cut minimum error for a given ratio $\frac{h_f}{h_s}$.

- The disc pair error minimisation method takes a large number of cycles to find the minimum total error as it is based on error contours. The simplex minimisation method was included in this research in two dimensions (β and h_s) to calculate the minimum total error for both discs, and it was able to find the minimum total error more precisely while reducing the computational load significantly.
- While carrying out the error analyses, the data recorded by the thermocouples during the EHL experiment was seen to be inconsistent with the trends shown by the numerical analyses.
- Various investigations were carried out to identify which measurements are mutually consistent to use them as the lower boundary temperatures, however, this was not possible and led the author to carry out synthesised experiments that use generated synthesised temperatures based on the lowest boundary temperatures. These experiments confirmed that the measured temperature inconsistencies were due to measurement errors.
- The robustness of the synthesised experiments was tested and confirmed. These experiments were then used to assess the effect of including noise, losing precision in temperatures and to find the optimum positioning of the thermocouples.
- A resolution of ± 0.25 °C in the recorded temperatures degrades the error minimisation process and compromises the effectiveness of the experiment. The measured temperatures should not be rounded by the recorders to more than 0.1 °C for better results.
- The new integral shafts and test disc were designed in order to eliminate the asymmetry in the thermal path from the disc to the shaft, and possible inconsistency in the thermal resistance at the interference fit between the shaft and disc.

- The miniature thermocouple amplifiers cannot provide the required accuracy, hence, they cannot be used in the current work as long as the resolution issue is present.
- The temperature signal processing must be reconsidered and improved.

7.3 Recommendations for future work

- **Inconsistency in temperature measurements:** This issue can be overcome using the new designed integral shafts and test discs, which allow symmetric temperature distribution, and also using the on-shaft thermocouple amplifiers to obtain amplified and stronger signals before transferring it through the slip rings to the LabVIEW software.
- **Optimum position of thermocouples:** Re-positioning the side thermocouples outwards for best temperature discernment by having these thermocouples fitted as close as possible to the side of the test disc.
- **Thermocouple accuracy:** Using data recorders that record and log the temperatures at a resolution of ± 0.1 °C or less. This could be achieved by improving the A to D conversion where an accurate determination of the digital temperature should be set, for example, setting the range from 0 to 250 °C in order to allow more bits to be used during the calibration of the thermocouple amplifiers which leads to stronger and more robust digital signal.
- **Integral shafts and test discs:** Replacing the original slow shaft and fast shaft with their test discs by the new integral shafts and test discs to ensure a symmetric temperature distribution and to eliminate the uncertainty of the conductance variation.
- **On-shaft thermocouple amplifiers:** Currently, the sampling of the temperatures is achieved by recording the temperatures by the

thermocouples at high frequency and then averaging them in LabVIEW software to give mean temperature. With the on-shaft thermocouple amplifiers, this process can be carried out before passing the signals through the slip rings to the LabVIEW software, this ensures more robust signals transferred to the LabVIEW software. However, some investigations are required before using the on-shaft processing in the test rig:

- Galvanic isolation test, as it plays an important role, the thermocouple amplifiers have to be galvanically isolated. This means they should not be influenced by grounding or isolating problems with the test rig or with the other thermocouple amplifiers, which can affect on the signals.
- Calibration of thermocouples and analogue circuit should be carried out against a reference PRT thermometer. High frequency measurements should be used to assess the level of ambient noise in the circuit. The signal amplification should be chosen so that resolution will be maintained in the subsequent A to D conversion.
- Noise tests of the calibrated analogue circuit should be carried out in the lab with the circuit near to the actual test rig position. Noise in a cooling test can be measured and A to D processing used to provide digital data. Digital data will allow an appropriate averaging strategy to be developed without running the test rig.
- Further testing with rig running to identify the analogue output noise and reconsider averaging strategy.
- Develop on-shaft averaging and digital data transfer to LabVIEW and test by running a constant temperature signal through a stationary slip ring.

References

Adafruit, n.d. *Adafruit Learning System*. [Online] Available at: <https://cdn-learn.adafruit.com/downloads/pdf/adafruit-1-wire-thermocouple-amplifier-max31850k.pdf>

[Accessed 15 October 2019].

Al-Hamood, A., 2015. *Friction and thermal behaviour in elastohydrodynamic lubrication power transmission contacts*, Cardiff: Cardiff University.

Amontons, G., 1699. de la resistance causee dans les machines (About resistance and force in machines). *Memoires de l'acaemie Royal A*, pp. 257-282.

Anderson, T. & Saunders, O., 1953. Convection from an isolated heated horizontal cylinder rotating about its axis. *Proceedings of the Royal Society of London*, 217(1131), pp. 555-562.

Bair, S., Green, I. & Bhushan, B., 1991. Measurements of Asperity Temperatures of a Read/Write Head Slider Bearing in Hard Magnetic Recording Disks. *ASME Journal of Tribology*, 113(3), pp. 547-554.

Bhushan, B., 1971. *Temperature and Friction of Sliding Surfaces*, Cambridge, MA: Massachusetts Institute of Technology, Department of Mechanical Engineering.

Bhushan, B., 1995. Micro/Nanotribology and its Applications to Magnetic Storage Devices and MEMS. *Tribology international*, 28(2), pp. 85-96.

Bhushan, B., 2000. *Modern Tribology Handbook*. Florida: CRC Press.

Bhushan, B., 2013. *Introduction to tribology*. New York: John Wiley & Sons, Ltd.

Blok, H., 1937. Theoretical study of temperature rises at surfaces of actual contact under oiliness conditions. *Proceedings of the Institute of Mechanical Engineers General Discussion of Lubrication*, Volume 2, pp. 222-235.

Blok, H., 1970. The Postulate About the Constancy of Scoring Temperature. *Interdisciplinary Approach to the Lubrication of Concentrated Contacts*, Issue SP237, pp. 153-248.

Bos, J. & Moes, H., 1995. Frictional Heating of Tribological Contacts. *ASME Journal of Tribology*, 117(1), pp. 171-177.

Cameron, A., 1985. Righting a 40-year-old wrong. *Tribology International*, 18(2), p. 92.

Cardone, G., Astarita, T. & Carlomagno, G. M., 1997. Heat Transfer Measurements on a Rotating Disk. *International Journal of Rotating Machinery*, Volume 3, pp. 1-9.

Carslaw, H. S. & Jaeger, J. C., 1959. *Conduction of Heat in Solids*. London: Oxford University Press.

Chandrasekar, S. & Bhushan, B., 1990. Friction and Wear of Ceramics for Magnetic Recording Applications: Part I - A Review. *ASME Journal of Tribology*, 112(1), p. 1-16.

Chang, L. & Webster, M.N., 1991. A study of elastohydrodynamic lubrication of rough surfaces. *ASME Journal of Tribology*, 113(1), pp. 110-115.

Chu, L., Hsu, H., Lin, J. & Chang, Y., 2009. Inverse approach for calculating temperature in EHL of line contacts. *Tribology International*, 42(8), pp. 1154-1162.

Clarke, A., 2009. *Heat partition in elastohydrodynamic sliding contacts under full film lubrication conditions*, Cardiff: Cardiff School of Engineering, Cardiff University.

Clarke, A., Sharif, K. J., Evans, H. P. & Snidle, R. W., 2006. Heat partition in rolling/sliding elastohydrodynamic contacts. *ASME Journal of Tribology*, 128(1), pp. 67-84.

Clarke, A., Sharif, K. J., Evans, H. P. & Snidle, R. W., 2007. Elastohydrodynamic modelling of heat partition in rolling–sliding point contacts. *Proceedings of the Institution of Mechanical Engineers, Part J: Journal of Engineering Tribology*, 221(3), pp. 223-235.

Coulomb, C.-A. d., 1785. *Theorie des Machines Simples, en ayant regard au Frottement de leurs Parties, et a la Roideur des Cordages*. Mem. Math. Phys. X. Volume 10, pp. 161-342.

Croft, D. R., Stone, J. A. R. & Lilley, D. G., 1977. *Heat Transfer Calculations Using Finite Difference Equations*. London: Applied Science Publishers.

Crook, A. W., 1962. The Lubrication of Rollers III. A Theoretical Discussion of Friction and the Temperatures in the Oil Film. *The Royal Society*, 254(1040), pp. 237-258.

Davidson, C., 1957. Bearings Since the Stone Age. *Engineering*, Volume 183, pp. 2-5.

Dowson, D., 1998. *History of Tribology*. London and Bury St Edmunds: Professional Engineering Publishing Limited, Issue 2nd.

Dowson, D. & Higginson, G., 1959. A numerical solution to the elastohydrodynamic problem. *Journal of Mechanical Engineering Science*, 1(1), pp. 6-15.

Dropken, D. & Carmi, A., 1957. Natural convection heat transfer from a horizontal cylinder rotating in air. *Transaction of the ASME*, 79(4), pp. 741-749.

Ebner, M. et al., 2018. Measurement of EHL temperature by thin film sensors - Thermal insulation effects. *Tribology International*, article 105515(in press, corrected proof).

Gavin, H., 2016. The Nelder-Mead Algorithm in Two Dimensions. *CEE 201L. Duke University*.

Griffioen, J., Bair, S. & Winer, W., 1986. Infrared Surface Temperature Measurements in a Sliding Ceramic contacts. *Mechanisms and Surface Distress: Proc. Twelfth Leeds-Lyon Symp. on Trib*, pp. 238-245.

Grubin, A., 1949. *Investigation of the Contact of Machine Components*. Moscow: Central Scientific Research Institute for Technology and Mechanical Engineering.

Gulino, R., Bair, S., Winer, W. & Bhushan, B., 1986. Temperature Measurement of Microscopic Areas within a Simulated Head/Tape Interface Using Infrared Radiometric Technique. *ASME Journal of Tribology*, 108(1), pp. 29-34.

Habchi, W., et al., 2010. Influence of pressure and temperature dependence of thermal properties of a lubricant on the behaviour of circular TEHD contacts. *Tribology international*, 43(10), pp. 1842-1850.

Hertz, H., 1881. *On the contact of elastic solids*. *J. Reine Angew: Mathematik* 92, pp. 156-171.

Holmes, M. J. A., Evans, H.P. & Snidle, R. W., 2005. Analysis of mixed lubrication effects in simulated gear tooth contacts. *ASME Journal of Tribology*, 127(1), pp. 61-69.

Isaac, G. et al., 2018. Thermal analysis of twin-disc machine for traction tests and scuffing experiments. *Journal of engineering tribology*, 232(12), pp. 1548-1560.

Jaeger, J. C., 1942. Moving Sources of Heat and the Temperature of Sliding. *Proceedings of the Royal Society of New South Wales*, Volume 76, pp. 203-224.

Johnson, 1987. *Contact mechanics*. Cambridge: Cambridge university.

Kannel, J. W. & Bell, J. C., 1972. A Method for Estimation of Temperatures in Lubricated Rolling-Sliding Gear on Bearing Elastohydrodynamic Contacts. *Proceedings of the Institution of Mechanical Engineers, EHD symposium*, pp. 118-130.

Kennedy, F. E., 1984. Thermal and Thermomechanical Effects in Dry Sliding. *Wear*, 100(1-3), pp. 453-476.

Lubrecht, A. A., Ten Napel, W. E. & Bosma, R., 1988. The Influence of Longitudinal and Transverse Roughness on the Elastohydrodynamic Lubrication of Circular Contacts. *ASME Journal of Tribology*, 110(3), pp. 421-426.

Lu, J., Reddyhoff, T. & Dini, D., 2018. 3D Measurements of lubricant and surface temperature within an Elastohydrodynamic contact. *Tribology Letters*, 66(1), pp. 1-16.

Lu, J., Reddyhoff, T. & Dini, D., 2020. A study of thermal effects in EHL rheology and friction using infrared microscopy. *Tribology international*, Volume 146.

Maione, R. & D'Elia, L., 2005. *Lubrication and lubricants*. Italy: ISTITUTO DELLA ENCICLOPEDIA ITALIANA FONDATA DA GIOVANNI TRECCANI S.p.A..

Manton, S. M., O'Donoghue, J. P. & Cameron, A., 1967. Temperatures at Lubricated Rolling/Sliding Contacts. *Proceedings of the Institution of Mechanical Engineers*, 182(1), pp. 813-823.

Marshall, R., Atlas, L. & Putner, T., 1966. The Preparation and Performance of Thin Thermocouples. *J. Sci. Instrum.*, Issue 43, p. 144.

Martin, H., 1916. Lubrication of gear teeth Engineering. Volume 102, pp. 119-121.

Meinders, M., Wilcock, D. & Winer, W., 1983. Infrared temperature Measurements of a Reciprocating Seal test. *Tribology of Reciprocating Engines: Proceedings Ninth Leeds-Lyon Symposium on Tribology*, pp. 321-328.

Merritt, H. E., 1962. Gear-Tooth Contact Phenomena. *Proceedings of the Institution of Mechanical Engineers*, 176(1), pp. 141-163.

Miyata, S., Hohn, B.-R., Michaelis, K. & Kreil, O., 2008. Experimental investigation of temperature rise in elliptical EHL contacts. *Tribology International*, 41(11), pp. 1074-1082.

Morales-Espejel, G. & Lugt, P., 2011. A Review of Elasto-Hydrodynamic Lubrication Theory. *Tribology Transactions*, April 2015, 54(3), p. 470–496.

Nagaraj, H., Sanborn, D. & Winer, W., 1978. Direct Surface Temperature Measurement by Infrared Radiation in Elastohydrodynamic Contacts and the Correlation with the Blok Flash Temperature Theory. *Wear*, 49(1), pp. 43-59.

Olver A.V. & Spikes H.A., 1998. Prediction of traction in elastohydrodynamic lubrication. *Olver AV, Spikes HA. Prediction of traction in elastohydrodynamic lubrication. Proceedings of the Institution of Mechanical Engineers, Part J: Journal of Engineering Tribology*, 212(5), pp. 321-332.

Olver, A. V., 1991. Testing Transmission Lubricants: The Importance of Thermal Response. *Olver AV. Testing transmission lubricants: the importance of thermal response. Proceedings of the Institution of Mechanical Engineers, Part G: Journal of Aerospace Engineering*, 205(1), pp. 35-44.

Ozerdem, B., 2000. Measurement of convective heat transfer coefficient for a horizontal cylinder rotating in quiescent air. *International communication in heat and mass transfer*, 27(3), pp. 389-395.

Patching, M. J., 1994. *The effect of surface roughness on the microelastohydrodynamic lubrication and scuffing performance of aerospace gear tooth contacts*, Cardiff: University of Wales College of Cardiff.

Patching, M. J., Kweh, C. C., Evans, H. P. & Snidle, 1995. Conditions for scuffing failure of ground and superfinished steel discs at high sliding speeds using a gas turbine engine oil. *ASME Journal of Tribology*, 117(3), pp. 482-489.

Petersen, S., 2017. *Methods of Optimization for Numerical Algorithms*, Groningen: University of Groningen.

Popova, E. & Popov, V. L., 2014. On the history of elastohydrodynamics: The dramatic destiny of Alexander Mohrenstein-Ertel and his contribution to the theory and practice of lubrication. *ZAMM Zeitschrift fur Angewandte Mathematik und Mechanik*, 95(7), pp. 652-663.

Press, W., Teukolsky, S., Vetterling, W. & Flannery, B., 1996. *Numerical Recipes in Fortran 77*. 2nd ed. The United States of America: The Press Syndicate of The University of Cambridge.

Qiao, H., 2005. *Prediction of contact fatigue for the rough surface elastohydrodynamic lubrication line contact problem under rolling and sliding conditions*, Cardiff: Cardiff University.

Reed, R., 1982. Thermoelectric Thermometry: A Function Model. *Temperature: Its Measurement and Control in Science and Industry (J.F. Schooley, ed.)*, Volume 5, p. 915–922.

Shaw, M., 2005. *Metal Cutting Principles*. Second edition ed. Oxford, UK: Oxford University Press.

Shore, H., 1925. Thermoelectric Measurement of Cutting Tool Temperatures. *Journal of the Washington Academy of Sciences*, 15(5), p. 85–88.

Smith, G. D., 1985. *Numerical solution of partial differential equations*. Oxford: Clarendon Press.

Snidle, R. W. & Evans, H.P., 1990. *Thermal distress-related failure of high speed gearing*, Cardiff: University of Wales College of Cardiff, Division of Mechanical Engineering and Energy Studies.

Spurr, R., 1980. Temperatures Reached by Sliding Thermocouples. *Wear*, 61(1), pp. 175-182.

Stachowiak, G. & Batchelor, A., 2004. *Experimental methods in tribology*.. Amsterdam: Elsevier.

StudyLib, 2019. *the downhill simplex method*. [Online] Available at: <https://studylib.net/doc/5891575/the-downhill-simplex-method> [Accessed 17 August 2019].

Tian, X., Kennedy, F., Deacutis, J. & Henning, A., 1992. The Development and Use of Thin-Film Thermocouples for Contact Temperature Measurements. *Tribology Transactions*, 35(3), pp. 491-499.

Tian, X. & Kennedy, F. E., 1994. Maximum and Average Flash Temperatures in Sliding Contacts. *ASME Journal of Tribology*, 116(1), pp. 167-174.

Union carbide, 1972. *Technical Bulletin: Optical Properties and Applications of Linde Cz Sapphire*. San Diego, California: F-CPD 72950.

Wang, K. L. & Cheng, H. S., 1981. A Numerical Solution to the Dynamic Load, Film Thickness, and Surface Temperatures in Spur Gears. *ASME Journal of Mechanical Design*, 103(1), pp. 177-187.

Yagi, K., Kyogoku, K. & Nakahara, T., 2006. Measurements of Temperature Distributions around Longitudinally Grooved Rough Surfaces in Sliding Elastohydrodynamic Point Contacts. *Tribology Transactions*, 49(4), pp. 482-489.

Zakaria, N. H., 2010. *Elastohydrodynamic Lubrication for bio-based lubricants in elliptical conjunction*, Johor: Faculty of mechanical engineering, Universiti Teknologi Malaysia.